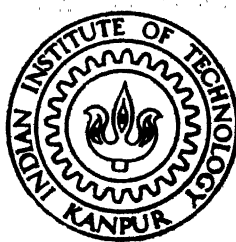


ION-BEAM MIXING IN METAL/Ge SYSTEMS

by
SANKAR DHAR



DEPARTMENT OF PHYSICS

INDIAN INSTITUTE OF TECHNOLOGY, KANPUR

NOVEMBER, 1996

PHY
1996
D
DHA
ION

ION-BEAM MIXING IN METAL/Ge SYSTEMS

A Thesis Submitted
in Partial Fulfillment of the Requirements
for the Degree of
Doctor of Philosophy

by
SANKAR DHAR

to the
DEPARTMENT OF PHYSICS
INDIAN INSTITUTE OF TECHNOLOGY, KANPUR
November, 1996

- 5 AUG 1997
CENTRAL LIBRARY
I. I. T., KANPUR

Acc. No. A 123635

Dedicated to....

my parents & teachers

CERTIFICATE

It is certified that the work contained in this thesis entitled *Ion beam mixing in metal/Ge systems* by *Sankar Dhar* has been carried out under my supervision and that this work has not been submitted elsewhere for a degree.



V. N. Kulkarni
Department of Physics
Indian Institute of Technology
Kanpur

November, 1996

Acknowledgements

I try to express my great feelings, emotion and respect about few personals amongst which I have spent more than six years at IIT, Kanpur and without whom I would not be able to complete this work.

I would like to express my profound gratitude to Dr. V. N. Kulkarni for introducing me in the field of ion-beam physics. I am very grateful to him for his invaluable, sincere and patient guidance throughout this work. From the beginning he has patiently taught and helped me to familiarize with various aspects of the research methodology, explaining various theoretical and experimental aspects of ion beam mixing which nurtured my scientific outlook. I have enjoyed working with him in different areas of physics for the last six years. I sincerely acknowledge that I have learnt many valuable lessons from his personality which help me to think and work independently. I am indebted to him for his timely help in other non-academic matters which made my stay comfortable.

I would also like to express my profound gratitude to Dr. Y. N. Mohapatra for providing me much needed impetus during different circumstances. I am very grateful to him for sparing time for me from his busy schedule for several enlightening discussions.

I am grateful to Prof. S. V. Bhoraskar and Prof. S. B. Ogale, University of Poona, for extending their glancing angle x-ray facility at a very crucial stage of this work.

I am very grateful to Prof. V. A. Singh for valuable discussions and suggestions at various stages of this work. I am also grateful to Prof. R. M. Singru, Prof. Y. R. Waghmare, Dr. S. Saha and Dr. S. Kumar for their constant encouragements. I am also grateful to Prof. A. K. Majumdar for providing me some crucial materials and many useful discussions with him for this work.

I am indebted to Dr. H. C. Verma for extending immense help and useful discussions which assisted me to overcome many unavoidable difficulties.

I have derived an unique help through my lab mate Mr. T. Som by his untiring company (sometimes whole day and night) and active participation during different

experiments throughout this work. I must express my deepest gratitude for various crucial help provided by him. I am also grateful to him for his time to time helps in different matters during the stay at IIT, Kanpur.

I am very grateful to Mr. P. K. Giri for many valuable discussions and active help in some of the important measurements described in this work.

I would like to give my sincere thanks to other lab colleagues Dr. Nobin Banerji, Mr K. Ramakrishnan, Mr. Paritosh Chowdhury, Mr. Rajnish Gupta, Mrs. Bishakha Bhattacharya, Dr. Debashis Bondyopadhyay and Dr. Bidyut Halder.

A large measure of thanks is owed to Mr. M. M. Gupta, Mr. K. Masood and Mr. R. S. Rajput, the technical staff of the Van de graaff laboratory, for their ungrudging help and sincere co-operation (even on holidays) throughout the course of this work. At this point I wish to extend my sincere thanks to Mr. Sivprakash for his help in getting liquid nitrogen and other valuable things throughout this work. I am grateful to Mr. A. K. Srivastava and Mr. S. L. Kanoujia for making my stay cheerful.

I wish to extend my sincere thanks to the technical staff of physics workshop Mr. R. Singh, Mr. B. Singh, Mr. R.M. Singh, Mr. Bhagawandeen for their sincere and hard work in making different experimental apparatus used in this work. I Sincerely thank the staff of the liquid nitrogen plant, Mr. S. Singh, Mr. V. K. Sharma, Mr. J. Singh, Mr R. Asare and others for supplying liquid regularly. I also thank to Mr. P. K. Pal for SEM measurements and Mr. Umashanker for XRD measurements. I also express my sincere thanks to the staffs of physics department Mr. L. Singh, Mr. H. K. Panda, Mr. Ghanshyam, Mr. D.P. Pant, Mr. Salim, Mr. A. K. Srivastava for their helps in official and personal matters. I am thankful to Mr. A. K. Ganguly for preparing neat tracings.

I would like to thank to all of my friends Tapo, Swapan, Deba, Ani, Tapan, Goutam, Sunu, Jal, Dmid, Ctop, Giri, Dinu, Prasen, Rangan, Alok, Rajan, Rahul, Buro, Sayan, Subit, Kishore, Bhargab, Supriti, Sangita, Manoj, Shyamal, Sekhar, Sudhansu, Abir, Rameshan, Shinku, Pattu, Anil, GK, Kak, Johri, Pandeyji, Shreos, Bivash, Sirshendu, Ramki, Ajay, Pari, Sudipta, Mirnda, Sankarda, Gour, Bachha, Samarda, Pra-

bal, Prashanta, Amitda, Tapas, Shantanuda, Sujay, Santi, Bhaba, Nilay, Arun, Jethu, George, Gourav, Sourav, Alok, Pratima, Rahul, Subash, Shibu, Sushanta, Subratada, Indranidi, Soumya, Arnab, Machao. Paddy, Sudip, Porel, Pallab, Dhruva, Raybabu, Tanmay, Kalyanda, Mama, Mami, Goutamda, Banerjida, Gangulyda, Majumdarda, Boseda, Bansida, all Boudi, Sudiptoda, Bishakha, Rebadi, Swapanda, Palda, Boudi, Biswajit, Masima, Mesomasay, and many others who have helped me in innumerable ways and have made my stay at IIT, Kanpur a memorable one.

I would like to express my deepest gratitude to my parents and in-laws, brothers Tukai and Bubai and sister Dola, Tukai. I am also thankful to Debukaka, Madhumita, Deepa, Swathi, Vijayanthi, Pana, Manas, and all other friends and relatives for encouraging me to complete this work. I am very thankful to Ms. Anjali Kulkarni and Ms. Shraddha Mohapatra and their children Vedricha, Apoorva and Stuti for their friendly and homely association. I wish to express my deep appreciation for my wife Indrani for patiently bearing my gloominess, providing mental support during critical period, managing the house all alone, helping in preparation of thesis and never complaining of my regular absence for long hours away from home.

Finally, I cherish the memory of our beloved "*BODHI*", the association which helped me to spend my most of the leisure time in an active way during this long stay at IIT, Kanpur.

Sankar Dhar

SYNOPSIS

Name of Student: SANKAR DHAR

Roll No: 9010979

Degree for which submitted: Ph.D.

Department: Physics

Thesis Title: Ion-Beam Mixing in metal/Ge systems

Name of thesis supervisor: Dr. V. N. Kulkarni

Department of Physics

I.I.T Kanpur-208016

Month and year of thesis submission: November, 1996

It is well known that the process of ion implantation revolutionized the semiconductor industry. In case of metals, ion implantation has been proved to be very effective as a surface treatment technique which reduces wear and friction of the implanted surfaces and improves corrosion resistance and adhesion properties. These properties are the consequences of the stable/metastable/amorphous alloys produced in the near surface region due to ion implantation. However, the major disadvantage of ion implantation in case of metals has been the long irradiation times required to achieve sufficiently high implant concentrations resulting in high cost of the process. Further, the achievable concentrations are limited by the sputtering of surface atoms. Therefore, the process of ion implantation had a limited success in case of metals as compared to semiconductors.

During the past decade new techniques have been developed which combine thin film deposition and heavy ion irradiation processes to synthesize novel and technologically important phases or materials, thereby reducing the process time and cost by an order of magnitude. These techniques utilize the inherent capability of heavy ion irradiation process of displacing the atoms from their normal sites either during thin film deposition

(ion-beam assisted deposition) or after irradiation (ion-beam mixing).

In case of ion-beam mixing (IM), the elements to be alloyed are first sequentially deposited on the metal or semiconductor or inert surface and subsequently irradiated by energetic heavy ions. Ions of inert heavy gases are generally utilized in order to avoid any chemical reaction with the alloy to be formed. The sample configurations which are generally used for IM studies are i) marker ii) bilayer and iii) multilayer. In marker configuration one employs a thin layer (~ 1 nm) of an element in a host matrix to determine the effective diffusion coefficient of impurity resulting from the collision-induced atomic migration. In another configuration a marker layer placed across the interface is used to monitor the atomic movement during the formation of phase. The marker experiments mainly address the basic aspects of ion mixing process. The bilayer configuration involves a film of element A of thickness ranging from a few tens to a few hundreds of nanometer deposited on a bulk material B or on an inert substrate coated with a film of element B. The interest here is focused around the formation of binary phases of different compositions in addition to the understanding of the basic processes involved at the interface. Multilayer configurations are mainly important from the point of view of formation of stable/metastable/amorphous alloys of desired composition having larger thicknesses.

For ion-beam mixing studies, inert gas ions having energy of few hundred kilo electron-volts are mostly used. This is partly due to the wide availability of the ion implanters at these energies. However, these ion energies limit the maximum thickness of the alloyed region to about 100 nm. The use of ion-beams of MeV energies is now gradually increasing for synthesizing thicker surface alloys.

In order to make ion-beam mixing a viable technique for producing desired phases, an important prerequisite is to decipher the latent facet of the physics involved in the basic mechanisms under different processing conditions. Several ion-beam mixing studies have been reported for metal/metal and metal/Si systems which reveal the character of the mixing mechanism under various combinations of the processing parameters. The details of these studies on phase formation and mechanisms of mixing

have been the subject of some excellent review articles by Cheng[1], Was[2], Kelly and Miotello[3], Nastasi and Mayer[4].

It is well known that metal silicides are important as contact and interconnect materials in semiconductor device technology. The interest in the synthesis of silicides by different methods grew in 1970s when it became clear that with decreasing dimension the resistance of the conductors fabricated from polycrystalline silicon would become too high for effective use. The work done in the last decade on metal silicide thin films revealed a large number of interesting properties related to resistivity, electromigration, diffusivity, corrosion resistance, etc. All these properties are important from the point of view of semiconductor and microelectronics industry which require such materials in modern integrated circuits because the packing density, speed, etc. are usually limited by interconnects and contact requirements rather than by decreasing active device dimension. For example, if the circuit size is scaled by a factor k , the interconnect resistance increases by a factor $1/k$ while the contact resistance by $1/k^2$. For the formation of stable and metastable alloys of metal-semiconductor systems ion-beam mixing has been widely used for its several advantages over solid state reaction such as lower processing temperature and higher spatial selectivity. In the last decade a large number of studies on the formation of different near-nobel and refractory silicides have been reported.

In contrast to the silicide systems, which have been widely studied using both thermal and ion-beam processes, the reports on the synthesis of germanides are very few in the literature. Recently the interest in the germanide systems has been triggered by the work of Krusin-Elbaum and Aboelfotoh[5] who report that the ϵ_1 - Cu_3Ge phase possesses lower resistivity (few $\mu\Omega - cm$) than many silicides ($CoSi_2$, $NiSi_2$, etc.). Also it possesses most of the desirable properties required for an interconnect/contact material in the existing GaAs and Si device technology. This copper germanide phase which is formed by thermal annealing at about 680 K, is found to be stable and reproducible. The studies on Cu/Ge system indicates that other germanides which are mostly unexplored might emerge as promising future materials for the semiconductor

industry.

The interesting and technologically important properties of Cu_3Ge , mentioned above, motivated the author to undertake the study of MeV ion-beam mixing in metal/Ge systems. Apart from Cu/Ge, two other systems viz. Ni/Ge and Co/Ge have also been selected for these studies. These systems have been chosen for the following reasons. Firstly, the atomic masses of Cu, Ni and Co being similar it is expected that the ballistic effects produced under ion irradiation in all these three cases would be similar. Also, the equilibrium phase diagrams of Cu/Ge, Ni/Ge and Co/Ge are similar. The main objectives of this work are (i) to explore the directed energy deposition process of ion mixing for producing germanide phases in bilayer and multilayer thin film structures of Cu/Ge, Ni/Ge and Co/Ge systems at different ambient temperatures, using Kr and Ar ions of mega electron-volt energy, (ii) to obtain quantitative information of the parameters viz. mixing rates, mixing efficiencies which are used to understand the basic mixing processes and the activation energies from temperature dependence of mixing (the Q curve) and (iii) to develop a phenomenological model to explain the mixing parameters.

The thesis is divided into seven chapters. The importance of metal/Ge systems and the application of ion-beam mixing techniques are brought out in Chapter 1.

A brief discussion of mechanisms of ion-beam mixing and various phenomenological models for calculating mixing parameters viz. mixing rate, mixing efficiencies, etc. are presented in Chapter 2. A compilation of experimental ion mixing results relevant to this work is also presented in this chapter.

Chapter 3 deals with the methodology of sample preparation along with a description of experimental techniques utilized in this work. High purity (99.99%) Ge, Cu, Ni, Co materials were used for preparing multilayer and bilayer films of M/Ge configuration on quartz substrates where M is one of the above mentioned metallic species. For marker experiments high purity Au was utilized in M/Au/Ge configuration. The multi-hearth electron gun evaporation system which was used for the deposition of thin films has been described.

For ion irradiations, the 2 MeV Van de Graaff accelerator at IIT, Kanpur was utilized. For mixing experiments, an ion irradiation chamber to work in the range of 77 K to 500 K was designed and fabricated along with other ancillaries. Thermal annealing was carried out at various temperatures in the range of 400 - 700 K in vacuum. A brief description of these facilities has been described. Most of the quantitative information viz. layer thickness, composition of the mixed regions and depth profiling were obtained by Rutherford backscattering spectrometry (RBS) using 1.1-1.5 MeV He^+ ions from the same accelerator. The method of backscattering analysis has been explained by giving an example of Cu/Ge system.

The experimental results and analysis on multilayer, marker and bilayer configurations are presented in Chapters 4, 5, and 6 respectively. These chapters deal with the production of specific germanide phases, movement of the atomic species during mixing and the mixing mechanisms respectively.

Chapter 4 describes results of MeV Kr and Ar ion induced mixing effects[4], leading to compound formation in multilayer structures of Cu/Ge, Ni/Ge and Co/Ge samples. The ion mixing was done at various substrate temperatures ranging from 100 to 450 K. Irradiations were performed for several doses in the range of $(2 - 20) \times 10^{15} \text{ ions/cm}^2$. In all the cases films of the metal M and Ge were sequentially deposited to produce multilayer structure of 8 to 10 layers having total thickness in the range of 90 - 300 nm. The thickness of the individual layers of multilayer samples were adjusted such that the average film compositions range from about 60 at.% to 80 at.% of metal M.

The results of ion-beam mixing experiments have been compared with those of thermal annealing experiments performed at various temperatures in the range of 400 - 700 K. The characterization of all treated samples were done by RBS and X-ray diffraction measurements. The surface morphologies of the samples were studied by scanning electron microscope before and after mixing. The resistivity measurements were done by Van der Pauw four-probe method.

It has been observed that MeV heavy ion irradiation is a very efficient low temperature process for producing stable phases in metal/Ge systems namely Cu/Ge, Ni/Ge

and Co/Ge at different temperatures. Cu_3Ge , Ni_2Ge and Co_2Ge have been observed as "first phase" in ion mixed as well as in thermally annealed multilayer Cu/Ge, Ni/Ge and Co/Ge systems respectively. In case of Cu/Ge system another Cu-rich phase (Cu_5Ge) has also been observed only at higher irradiation doses which is not observed in thermally annealed samples.

In case of bilayer samples, the first phase produced by thermal annealing are Cu_3Ge , Ni_2Ge and Co_2Ge in Cu/Ge, Ni/Ge and Co/Ge systems respectively. At higher annealing temperatures NiGe and CoGe phases have been observed as second phase in Ni/Ge and Co/Ge systems. The present studies show that the first phases formed by thermal annealing and ion-beam mixing are identical.

The formation of compound phases has been analyzed on the basis of various existing empirical rules. The composition of the first and subsequent phases have been explained in the light of the effective heat of formation rule which considers both kinetic and thermodynamic aspects.

Chapter 5 deals with marker experiments which give information on the dominantly moving atomic species during ion mixing and thermal annealing. The bilayer structures of metal M and Ge deposited on quartz substrate along with a thin marker layer embedded at the M/Ge interface were used for these studies. The thickness of individual layers was chosen such that it yielded the composition of about $M_{50}Ge_{50}$. The total thickness of bilayer films was in the range of 100-200 nm. These experimental results are discussed on the basis of the present knowledge of the atomic movements in metal/semiconductor systems.

It has been observed that during the formation of Cu_3Ge phase by ion-beam mixing at room temperature, both Cu and Ge are mobile but Cu is the dominant moving species across the interface while for Ni/Ge system both Ni and Ge are equally mobile during the formation Ni_2Ge phase. However, for Co/Ge system only Ge atoms are mobile to produce Co_2Ge phase.

In Chapter 6 the values of different mixing parameters viz. mixing rates, mixing efficiencies, critical temperature for initiating thermally activated process etc. obtained

from bilayer experiments are described. The bilayer configuration was used since accurate quantitative information on these parameters can be obtained in this configuration only. Ion mixing of bilayer samples also leads to the formation of the phases described in Chapter 4 for multilayer samples. The room-temperature mixing rates for Ar ion irradiation in case of Cu/Ge, Ni/Ge and Co/Ge systems are found to be 5.4 nm^4 , 5.6 nm^4 and 1.6 nm^4 respectively. Similarly for Kr ion irradiations the mixing rates are 20.6 nm^4 , 18.5 nm^4 and 7.7 nm^4 respectively. The mixing efficiencies are independent of the deposited energy density in each case and the experimental values for Cu/Ge, Ni/Ge and Co/Ge are obtained to be $13.1 \text{ nm}^5/\text{keV}$, $10 \text{ nm}^5/\text{keV}$ and $5 \text{ nm}^5/\text{keV}$ respectively.

The temperature dependence of ion mixing in all the three systems show that the critical temperature T_c , above which the mixing becomes temperature dependent, is just above room temperature. The value of T_c is about 320 K for both Cu/Ge and Ni/Ge while for Co/Ge system it is about 347 K. There is no distinction between critical and equivalent temperature for crystallization in these systems. Compound formation in all the cases occur around the critical temperature T_c . Empirical models which estimate the critical temperatures have also been discussed.

In this chapter we have also presented a new phenomenological model[7] based on chemical kinetics applicable to reactive systems (such as metal silicides or germanides) to explain the experimentally obtained mixing rates since the existing models underestimate the mixing rates for reactive systems. In this model the mixing rate is enhanced by the compound formation factor retaining the linear dependence on the deposited energy density. The predictions of this model are very close to the experimental results presented in this work. It is also able to explain observed mixing rate of Ni/Si system reported in the literature. Hence it is demonstrated that this model would be applicable to the important class of silicide and germanide systems.

The last chapter, Chapter 7 presents a summary of the work followed by important conclusions and scope of the future studies.

To conclude, the synthesis and characterization of technologically important ger-

manide phases by ion-beam mixing and thermal annealing along with the experimentally determined mixing parameters (to understand mechanisms of mixing) and their successful interpretation with the help of a new phenomenological model, are the main outcome of this work which accomplishes the objectives mentioned above.

Bibliography

- [1] Y. -T. Cheng, *Mat. Sci. Rep.* 5 (1990) 45.
- [2] G.S. Was, *Prog. Sur. Sci.* 32 (1990) 211.
- [3] R. Kelly and A Miotello, *Thin Solid Films* 241 (1994) 192.
- [4] M. Nastasi and J. W. Mayer, *Mat. Sci. and Eng.* R12 (1994) 1.
- [5] L. Krusin-Elbaum and M. O. Aboelfotoh, *Appl. Phys. Lett.* 58 (1991) 1341.
- [6] S. Dhar, T. Som, Y. N. Mohapatra and V. N. Kulkarni, *Appl. Phys. Lett.* 67 (1995) 1700.
- [7] Sankar Dhar, Y. N. Mohapatra and V. N. Kulkarni, *Phys. Rev.* B54 (1996) 5769.

List of Publications

International Journals

1. ¹Room temperature synthesis of copper germanide phase by ion-beam mixing – S. Dhar T. Som, Y. N. Mohapatra and V. N. Kulkarni, *Appl. Phys. Lett.*, 67 (1995) 1700.
2. ¹Compound formation under local thermal spikes during ion-beam mixing: Model and its experimental verification – Sankar Dhar, Y. N. Mohapatra and V. N. Kulkarni, *Phys. Rev. B* 54 (1996) 5769.
3. Electrically active defects due to end-of-ion-range damage in silicon irradiated with MeV Ar ion. – P. K. Giri, S. Dhar, V. N. Kulkarni and Y. N. Mohapatra, *Nucl. Inst. Meth. B* 111 (1996) 285.
4. Electrically active defects in As-implanted deep buried layers in p-type Silicon – P.K Giri, S. Dhar, V. N. Kulkarni and Y. N. Mohapatra, *J. Appl. Phys.* (in press).
5. ERD facility for analysis of hydrogen and deuterium in materials – T. Som, S. Dhar, N. Banerji, K. Ramakrishnan and V. N. Kulkarni, *Bull. Mater. Sci.*, 19 (1996) 73.
6. Hydrogen depletion from KH_2PO_4 under He^+ ion bombardment – Tapobrata Som, Sankar Dhar, Shiraz N. Minwalla and Vishwas. N. Kulkarni, *Nucl. Inst. Meth. B* (in press).

¹Article is based on this thesis work.

International Conferences/Symposia

1. $^{2}\text{Cu}_3\text{Ge}$, a novel contact material for semiconductor device technology : Room temperature synthesis by ion-beam mixing – S. Dhar, T. Som, Y. N. Mohapatra and V. N. Kulkarni, Ed. Krishan Lal, *Semiconductor Devices*, (Narosa, New Delhi 1995) p 502.
2. ^{2}Ar ion induced copper germanide phase formation at room temperature – S. Dhar, T. Som, Y. N. Mohapatra and V. N. Kulkarni *Proc. of Defects in condensed media symposium*, (IGCAR, Kalpakkam, 1995).
3. Ion beam mixing of Si-Ge multilayers using MeV ions – B. Bhattacharya, S. Dhar, Y. N. Mohapatra, T. Som and V. N. Kulkarni, *Proc. of Defects in Condensed Media symposium*, (IGCAR, Kalpakkam, 1995).
4. Characterization of deep level defects in Si irradiated with Ar ions using constant capacitance time analyzed transient spectroscopy – P. K. Giri, S. Dhar, V. N. Kulkarni and Y. N. Mohapatra, *Proc. of Defects in Condensed Media Symposium*, (IGCAR, Kalpakkam, 1995).
5. MeV ion-beam mixing of Au in $\text{Fe}_{78}\text{B}_{13}\text{Si}_9$ amorphous metallic alloy – S. Dhar T. Som, H. C. Verma and V. N. Kulkarni, *Proc. of 7th International Symposium on Radiation Physics, Rajasthan, 1997* (in press).
6. Study of low energy dc plasma ion implanted hydrogen in GaAs – T. Som, S. Dhar and V. N. Kulkarni, *Proc. of 7th International Symposium on Radiation Physics, Rajasthan, 1997* (in press).

National Conferences/Symposia

1. Mixing of Au in $\alpha - \text{SiO}_2$ by Kr ion-beam – S. Dhar, T. Nigam, T. Som, K. Ramakrishnan and V. N. Kulkarni, *Proc of DAE Nuclear Physics Symposium, India*, 37B (1994) 521.

²Article is based on this thesis work.

2. ³Snthesis of copper germanide films by ion-beam mixing – B. Bhattacharya, **S. Dhar**, T. Som, V.N. Kulkarni and Y. N. Mohapatra, *Proc of DAE Nuclear Physics Symposium, India*, 37B (1994) 521.
3. ³Ion induced synthesis of low resistive metal germanide phases – **S. Dhar**, P. K. Giri, T. Som, Y. N. Mohapatra and V. N. Kulkarni, *Proc of DAE Solid State Physics Symposium, 1996 India* (in press).
4. Electrically active defects due to end-of-ion-range in silicon irradiated with MeV Ar ion – P. K. Giri, **S. Dhar**, V. N. Kulkarni and Y. N. Mohapatra, *Conf. on Recent Advances on Semiconductors at IIT, Delhi*, 1995.
5. Ion beam mixing study of Si-Ge system – P. Choudhury, **S. Dhar**, T. Som, Y. N. Mohapatra, and V. N. Kulkarni, *Proc. of DAE Solid State Physics Symposium, India*, 38C (1995) 175.
6. Degradation of physical properties of Indium Tin Oxide films on glass plate due to interaction with water – T. Som, **S. Dhar** and V. N. Kulkarni, *CRYOVAC Conference, VECC, Calcutta*, 1995.
7. Study of hydrogen diffusion in silicon by Elastic Recoil Detection Analysis – T. Som, **S. Dhar** and V. N. Kulkarni, *Conference on Recent Advances on Semiconductors at IIT, New Delhi*, 1995.
8. Low energy DC H and D plasma source ion implantation facility at IIT, Kanpur – T. Som, **S. Dhar** and V. N. Kulkarni, ed. P. K. Ghosh *Proc. of Plasma Science Symposium* ed. P. K. Ghosh (Prentice-Hall, New Delhi, 1996) p 103.
9. Hydrogen depletion from KH_2PO_4 due to interaction with hydrogen – T. Som, S. Minwalla, **S. Dhar** and V. N. Kulkarni, *Proc. of DAE Solid State Physics Symposium, India*, 38C (1995) 395.

³Article is based on this thesis work.

10. Channeling study of low energy DC plasma ion implanted N in Si and GaAs – T. som, R. Paily, **S. Dhar**, Y. N. Mohapatra and V. N. Kulkarni, *Proc of DAE Solid State Physics Symposium, 1996 India* (in press).
11. Trapping characteristics of MeV ion implanted buried layers in silicon – P. K. Giri, **S. Dhar**, Y. N. Mohapatra and V. N. Kulkarni, *Proc of DAE Solid State Physics Symposium, 1996 India* (in press).

Contents

Acknowledgments	vii
Synopsis	xi
List of Publications	xix
List of Tables	xxvii
List of Figures	xxxi
1 Introduction	1
1.1 Preamble	1
1.2 Ion-Beam Mixing	3
1.3 Synthesis of Silicides	4
1.4 Synthesis of Germanides	6
1.5 Motivation and objectives of this work	7
1.6 Organization of Thesis	8
2 Review of ion-beam mixing	9
2.1 Introduction	9
2.1.1 Basic mechanism of mixing	9
2.1.2 Phase formation	12
2.2 Critical temperature	14
2.3 Phenomenological model	19

2.3.1	Ballistic Model	21
2.3.2	Thermodynamic effects	22
2.4	Thermal Spike	24
2.4.1	Global or overlapping spike model	25
2.4.2	Local or non-overlapping spike model	26
2.5	Model for Compound Formation	29
2.6	Formalism based on kinetics	31
3	Experimental	33
3.1	Introduction	33
3.2	Sample preparation	34
3.2.1	Sample cleaning	34
3.2.2	Thin film deposition	34
3.3	Van de Graaff accelerator facility	35
3.4	Ion irradiation	40
3.4.1	Heavy ion-beam line	40
3.4.2	Heavy ion irradiation chamber	41
3.5	Thermal annealing	44
3.6	Rutherford Backscattering Spectrometry	46
3.7	The RBS setup	49
3.7.1	The beam line	49
3.7.2	Pulse shaping electronics and multichannel analyzer	53
3.7.3	Calibration of the MCA ^a	54
3.7.4	Backscattering spectra analysis	54
3.8	X-ray measurements	58
3.9	Scanning electron microscopy	59
3.10	Four probe resistivity measurement technique	59
4	Ion induced phase formation	61
4.1	Introduction	61

4.2	Experimental	62
4.3	Results	63
4.3.1	Cu/Ge system	63
4.3.2	Ni/Ge system	85
4.3.3	Co/Ge system	102
4.3.4	Resistivity measurements	108
4.4	Discussion	114
4.4.1	Phase formaton mechanism	114
4.4.2	Nature of Phase formation	116
4.4.3	Formation of “First phase”	126
4.5	Conclusions	132
5	Mobility of species during ion-beam mixing	135
5.1	Introduction	135
5.2	Experimental	136
5.3	Experimental results	136
5.4	Discussion	141
5.5	Conclusion	145
6	Mechanism of ion-beam mixing	149
6.1	Introduction	149
6.2	Experimental	150
6.3	Results:	151
6.3.1	Cu/Ge system	151
6.3.2	Ni/Ge system	159
6.3.3	Co/Ge system	164
6.4	Discussion	176
6.4.1	Critical temperature	176
6.4.2	Mixing rate: Prediction of existing models	177
6.4.3	Mixing in non-overlapping subcascade	185

6.4.4	Mixing under Overlapping subcascade	185
6.5	Need for a new model	186
6.5.1	Model for compound formation under local spike mixing	187
6.5.2	Comparison with experimental results	190
6.6	Conclusions	196
7	Summary and Conclusions	199
	Bibliography	205

List of Tables

2.1	Comparison of first phase formation by ion-beam mixing and thermal annealing in metal/semiconductor systems	13
2.2	Comparison of experimentally obtained critical temperatures with those calculated from the model of de Raus et al.(after ref 51)	17
3.1	Description of the samples used for present studies	37
4.1	Description of the layer structure used for the simulation of RBS spectrum of as-deposited Cu/Ge multilayer sample shown in Fig 4.1. . . .	65
4.2	Description of the layer structure used for the simulation of RBS spectrum of ion mixed Cu/Ge multilayer sample shown in Fig 4.3.	69
4.3	Description of the layer structure used for the simulation of RBS spectrum of ion mixed Cu/Ge multilayer sample shown in Fig 4.4.	71
4.4	Comparison of experimentally obtained d-values of the observed copper germanide phases with the one reported in literature.	77
4.5	Summary of ion-beam mixing results in Cu/Ge multilayer systems using Kr and Ar ions at various doses and temperatures.	80
4.6	Description of the layer structure used for the simulation of RBS spectrum of thermally annealed Cu/Ge multilayer sample shown in Fig 4.9.	85
4.7	Summary of thermal annealing results of Cu/Ge sample	86
4.8	Description of the layer structure used for the simulation of RBS spectra of as-deposited and ion mixed Ni/Ge multilayer sample shown in Fig 4.12.	88

4.9	Comparison of experimentally obtained d-values of the observed Ni_2Ge phase with the one reported in literature.	92
4.10	Summary of ion-beam mixing results in Ni/Ge multilayer systems using Kr and Ar ions at various doses and temperatures.	94
4.11	Description of the layer structures used for the simulations of RBS spectra of as-deposited and thermally annealed bilayer Ni/Ge bilayer sample shown in Fig 4.18.	99
4.12	Summary of thermal annealing results of Ni/Ge sample	101
4.13	Description of the layer structures used for the simulation of RBS spectrum of ion mixed Co/Ge multilayer sample shown in Fig 4.21a.	106
4.14	Summary of ion-beam mixing results of Co/Ge sample	107
4.15	Summary of thermal annealing results of Co/Ge sample	112
4.16	Resistivities measured on Cu_3Ge , Ni_2Ge and Co_2Ge layers produced by ion-beam mixing and thermal annealing.	113
4.17	Comparison of "first phase" formation in metal silicides and germanides by ion-beam mixing and thermal annealing.	117
4.18	The nature of phases predicted by the existing empirical rules for the present case of metal germanide systems.	118
4.19	The different useful parameters of Cu/Ge, Ni/Ge and Co/Ge systems.	123
5.1	Reported results of marker movements in metal/Si systems during thermal annealing and ion-beam mixing	146
6.1	Description of the layer structure used for the simulation of RBS spectra of as-deposited and ion mixed Cu/Ge bilayer samples shown in Figs 6.1 and 6.2.	155
6.2	Description of the layer structure used for the simulation of RBS spectra of before and after ion mixing in Ni/Ge bilayer sample shown in Fig 6.7.	163
6.3	Description of the layer structure used for the simulation of RBS spectra of as-deposited and ion mixed Co/Ge bilayer samples shown in Fig 6.13.	170

6.4	Compariosn of experimentally obtained critical temperatures with the one calculated from different emperical models	178
6.5	The values of average atomic number Z_{ave} , ξ , atomic density C. displacement energy E_d , heat of formation ΔH_{for} , cohesive energy ΔH_{coh} of Cu/Ge, Ni/Ge, Co/Ge and Ni/Si systems.	180
6.6	The values of deposited energy density F_D , critical energy F_D^c for global spike and the critical energy E_c for spike formation.	181
6.7	Comparison between experimental ($\frac{X^2}{\Phi} ^{exp}$) and calculated mixing rates. The theoretical mixed rates calculated from ballistic model (Eq 6.4) ($\frac{X^2}{\Phi} _{bal}$), model ($\frac{X^2}{\Phi} _{loc}^{Borgesen}$) of Borgesen et al. (Eq 6.7), local spike model of Bolse (Eq 6.8) ($\frac{X^2}{\Phi} _{loc}^{Bolse}$) and global spike model ($\frac{X^2}{\Phi} _{glo}$) (Eq 6.9).	182
6.8	Comparison between experimental ($\frac{X^2}{\Phi F_D} ^{exp}$) and calculated mixing efficiencies from ballistic (Eq 6.4) model ($\frac{X^2}{\Phi F_D} _{bal}$), Borgesen et al local (Eq 6.7) spike model ($\frac{X^2}{\Phi F_D} _{loc}^{Borgesen}$) and Bolse local spike (Eq 6.8) model ($\frac{X^2}{\Phi F_D} _{loc}^{Bolse}$) Global spike (Eq 6.9) model($\frac{X^2}{\Phi F_D} _{glo}$).	183
6.9	Comparison between experimental ($\frac{X^2}{\Phi} ^{exp}$) and calculated mixing rates. The theoretical mixed rates ($\frac{X^2}{\Phi} _{loc}^{com}$) calculated from our model (Eq 6.18) agree well with the experimentally obtained mixing rates. Note the significant departures of the rates calculated from modified ballistic (Eq 6.19) model ($\frac{X^2}{\Phi} _{bal}^{com}$) and global spike ($\frac{X^2}{\Phi} _{glo}^{com}$) model (Eq 6.20).	192
6.10	Comparison between experimental ($\frac{X^2}{\Phi F_D} ^{exp}$) and calculated mixing efficiencies. The theoretical mixing efficiency ($\frac{X^2}{\Phi F_D} _{loc}^{com}$) calculated from our model (Eq 6.18) agree well with the experimentally obtained mixing efficiency. The mixing efficiencies from modified ballistic (Eq 6.19) model ($\frac{X^2}{\Phi F_D} _{bal}^{com}$) and global spike ($\frac{X^2}{\Phi F_D} _{glo}^{com}$) model (Eq 6.20) are also shown for comparison.	193

List of Figures

1.1	Universal stopping power vs. ion energy in solid in Thomson-Fermi (T.F.) unit as predicted by LSS theory. S_n and S_e are the nuclear and electronic stopping powers respectively.	2
1.2	Schematic diagram of sample configurations utilized for ion-beam mixing and thermal annealing studies.	5
2.1	Schematic diagram showing the ion-beam mixing processes.	11
2.2	Plots showing variation of (a) T_c as a function of $\Delta H_{V_{small}}$ and (b) T_{eq} as a function of $\Delta H_{V_{large}}$ (from ref 51 and data given in table 2.2). . .	16
2.3	Variation of mixing rate as a function of F_D for the case of Pd/Si system. . .	20
2.4	Plot of $[d(4Dt)/d\Phi] \times [C^{5/3}(\Delta H_{coh})^2/F_D^2]$ as a function of $\Delta H_{mix}/\Delta H_{coh}$ (from ref 14).	27
2.5	Squared thickness of the mixed layer vs the fluence in Pd/Si irradiated at 80 K with 730 keV Au ions (after ref 31).	30
3.1	Photograph of multi-hearth electron-beam gun evaporation system. . .	36
3.2	Lay out of the Van de Graaff accelerator facility at I.I.T Kanpur. . . .	38
3.3	Photographs of (a) Van de graaff accelerator and (b) the analyzing magnet. . .	39
3.4	Photograph of beam line and irradiation chamber.	42
3.5	Block diagram of irradiation chamber and other accessories.	43
3.6	Photographs of the sample holders used for (a) high temperature ion-beam mixing (b) low temperature ion-beam mixing.	45
3.7	Photograph of the annealing set-up.	47

3.8	Schematic representation of an elastic collision process in laboratory frame. Target of mass M is initially at rest.	48
3.9	Block diagram of RBS chamber along with target, detector and other accessories.	51
3.10	Photograph of RBS chamber along with target and other accessories. .	52
3.11	Experimental RBS spectra of calibration sample (a) thin film of Au on Al substrate (b) Pure Al.	55
3.12	Experimental RBS spectra along with simulation of Cu/Ge bilayer sample deposited on SiO_2	57
4.1	The as-deposited RBS spectrum of Cu/Ge multilayer sample deposited on SiO_2 . The simulated spectrum was obtained using the sample structure given in Table 4.1.	64
4.2	RBS spectra of Cu/Ge multilayer sample in the as-deposited condition and after ion-beam mixing at room temperature for two different doses.	67
4.3	RBS spectrum of ion mixed Cu/Ge multilayer sample at RT for a dose of $8 \times 10^{15} Kr^+/cm^2$ along with simulation.	68
4.4	RBS spectrum of ion-beam mixed Cu/Ge multilayer sample irradiated at RT for a dose of $1 \times 10^{16} Kr^+/cm^2$ along with the simulated spectrum by considering formation of Cu_3Ge and Cu_5Ge phases. Another simulated spectrum obtained by considering formation of only Cu_3Ge layer is also shown for comparison.	70
4.5	RBS spectrum of ion mixed Cu/Ge multilayer sample at 100 K for a dose of $8 \times 10^{15} Kr^+/cm^2$ along with its simulation.	73
4.6	SEM photograph of Cu/Ge multilayer sample a) before and b) after ion-beam mixing at RT for a dose of $8 \times 10^{15} Kr^+/cm^2$	75
4.7	X-ray pattern of Cu/Ge multilayer sample taken before and after ion-beam mixing at RT (a) as-deposited (b) $8 \times 10^{15} Kr^+/cm^2$ (c) $1 \times 10^{16} Kr^+/cm^2$	76

4.8	RBS spectra of Cu/Ge multilayer sample before and after ion-beam mixing at RT for a dose of $1 \times 10^{16} \text{ Ar}^+/\text{cm}^2$. The simulated curves are shown by dashed and continuous line respectively.	79
4.9	RBS spectra of Cu/Ge multilayer sample before and after thermal annealing at 630 K for 150 min along with their simulations. Annealing leads to the formation of homogeneous Cu_3Ge phase.	82
4.10	X-ray pattern of Cu/Ge multilayer sample before and after thermal annealing (a) as-deposited (b) 630 K for 150 min.	83
4.11	RBS spectra of Cu/Ge bilayer sample before and after annealing at 580 K for 60 min along with simulations.	84
4.12	RBS spectra of the as-deposited and ion mixed ($6 \times 10^{15} \text{ Kr}/\text{cm}^2$, RT) Ni/Ge multilayer sample deposited on SiO_2 . The Continuous lines show simulations.	87
4.13	RBS spectra of Ni/Ge multilayer sample before and after ion-beam mixing at 390 K for a dose of $4 \times 10^{15} \text{ Kr}^+/\text{cm}^2$ showing formation of a uniformly mixed region of composition $\text{Ni}_{66}\text{Ge}_{34}$	90
4.14	X-ray pattern of Ni/Ge multilayer sample after ion-beam mixing at for irradiation fluence of (a) $6 \times 10^{15} \text{ Kr}^+/\text{cm}^2$ (b) $1 \times 10^{16} \text{ Ar}^+/\text{cm}^2$	91
4.15	Comparison between the RBS spectra of Ni/Ge multilayer sample after ion-beam mixing at doses of $4 \times 10^{15} \text{ Kr}^+/\text{cm}^2$ and $1 \times 10^{16} \text{ Ar}^+/\text{cm}^2$	93
4.16	RBS spectra of Ni/Ge multilayer sample before and after annealing at 580 K for 60 min. along with simulations.	96
4.17	X-ray pattern of Ni/Ge multilayer sample after thermal annealing at 580 K for (a) 60 min. (b) 180 min.	97
4.18	(a)RBS spectra of Ni/Ge bilayer sample before and after annealing at 480 K for 180 min. along with simulations (b) X-ray diffraction pattern confirms the formation of Ni_2Ge and NiGe phases.	98

4.19 Comparison of RBS spectra of Ni/Ge bilayer samples annealed at three different temperatures (a) 430 K for 90 min. (b) 480 K for 60 min. (c) 530 K for 180 min.	100
4.20 RBS spectra of Co/Ge multilayer sample before and after ion-beam mixing at RT for a dose of $1 \times 10^{16} \text{ Kr}^+/\text{cm}^2$. The simulated curves in both cases are shown by continuous line.	103
4.21 RBS spectra of Co/Ge multilayer sample before and after ion-beam mixing for a dose of $1 \times 10^{16} \text{ Kr}^+/\text{cm}^2$ at 380 K. In this case mixing leads to the formation of Co_2Ge phases. The simulated curve is shown by continuous line.	104
4.22 RBS spectra of Co/Ge multilayer sample before and after ion-beam mixing for a dose of $1 \times 10^{16} \text{ Kr}^+/\text{cm}^2$ at 420 K. In this case mixing also leads to the formation of Co_2Ge phases.	105
4.23 RBS spectra of thermally annealed Co/Ge multilayer samples (a) 530 K for 180 min. and (b) 680 K for 120 min. Simulated spectra are given by continuous lines.	109
4.24 Comparison between RBS spectra of Co/Ge multilayer sample taken after ion-beam mixing at 380 K for a dose of $6 \times 10^{15} \text{ Kr}^+/\text{cm}^2$ and after thermal annealing at 580 K for 60 min.	110
4.25 Comparison of RBS spectra of thermally annealed Co/Ge bilayer samples at three different temperatures (a) 480 K for 180 min. (b) 530 K for 120 min. (c) 580 K for 120 min.	111
4.26 Equilibrium phase diagram of Cu-Ge system.	120
4.27 Equilibrium phase diagram of Ni-Ge system.	121
4.28 Equilibrium phase diagram of Co-Ge system.	122
4.29 Hagg radii ratio diagram	124
4.30 Effective heat of formation diagram for (a) Cu/Ge (b) Ni/Ge and (c) Co/Ge systems.	130

- 5.1 The RBS spectra of Cu/Ge sample embedded with Au marker layer at the interface. The continuous line shows RBS spectrum of as prepared sample while the dashed line spectrum is taken after ion-beam mixing. The Au marker shifts towards low energy side suggesting dominating motion of Cu atoms. 137
- 5.2 The plot of energy displacement ΔE of the marker versus thickness of the Cu_3Ge layers. The upper (lower) continuous line is obtained from the theoretical calculations by considering that only Ge (Cu) atoms are mobile. 139
- 5.3 The RBS spectra taken before and after ion-beam mixing at RT for a dose of $6 \times 10^{15} Kr^+/cm^2$ of Ni/Ge sample with a Au marker. 140
- 5.4 The RBS spectra of Co/Ge sample with a Au marker taken before and after ion-beam mixing at RT for a dose of $1 \times 10^{16} Kr^+/cm^2$ 142
- 5.5 The plot of energy displacement ΔE vs. thickness of the cobalt germanide layers. The upper (lower) continuous line is obtained from the theoretical calculations by considering that only Ge(Co) atoms are mobile. 143
- 5.6 The comparison of RBS spectra of Co/Ge marker sample taken before and after thermal annealing at two different temperatures of 480 K and 580 K. 144
- 5.7 The distribution of damage energy due to 1 MeV Kr ion bombardment as a function of depth in (a) Cu/Ge and (b) Ni/Ge and (c) Co/Ge systems. Each point (x) corresponds to energy deposition in 10 nm. 147
- 6.1 Rutherford backscattering spectra of Cu/Ge bilayer thin film on quartz substrate for as-deposited condition (○) and after room-temperature mixing (▲) with 1 MeV Kr ions at a dose of $6 \times 10^{15} Kr/cm^2$. The corresponding simulated spectra are shown by solid lines. The arrows show the surface position of different elements. 153

6.2	Rutherford backscattering spectra of Cu/Ge bilayer thin film on quartz substrate for as-deposited condition (○) and after room-temperature mixing (▲) with 1 MeV Kr ions at a dose of $8 \times 10^{15} \text{ Kr/cm}^2$. The corresponding simulated spectra are shown by solid lines.	154
6.3	Dose dependence of squared thickness of mixed layers of composition Cu_3Ge formed across the interface of Cu/Ge bilayer system irradiated at room temperature with 1 MeV Ar ions (○) and Kr ions (●) respectively.	156
6.4	The squared thickness of the reacted layer of composition Cu_3Ge formed across the interface of Cu/Ge bilayer system after thermal annealing is shown as a function of annealing time for different temperatures (after ref 48).	157
6.5	The variation of mixing rate measured in Cu/Ge bilayer system for different deposited energy F_D at the interface.	158
6.6	Rutherford backscattering spectra of Cu/Ge bilayer film on quartz substrate for as-deposited condition and after mixing for a dose of $4 \times 10^{15} \text{ Kr/cm}^2$ at 100 K, RT and 350 K.	160
6.7	(a)The variation of mixing rate for Cu/Ge bilayer system as a function of reciprocal of substrate temperature for a dose of $4 \times 10^{15} \text{ Kr/cm}^2$ (b) Arrhenius plot of the mixing rate as a function of reciprocal of substrate temperature extracted from Fig.6.6a.	161
6.8	Rutherford backscattering spectra of Ni/Ge bilayer thin film on quartz substrate for as-deposited condition and after room-temperature mixing with 1 MeV Kr ions at a dose of $8 \times 10^{15} \text{ Kr/cm}^2$. The corresponding simulated spectra are shown by solid lines.	162
6.9	Dose dependence of squared thickness of mixed layers of composition Ni_2Ge formed across the interface of Ni/Ge bilayer system irradiated at room temperature with 1 MeV Ar ions (○) and Kr ions (●) respectively.	165

6.10	The squared thickness of the reacted layer of composition Ni_2Ge formed across the interface of Ni/Ge bilayer system after thermal annealing is shown as a function of annealing time.	166
6.11	The variation of mixing rate measured in Ni/Ge bilayer system for different deposited energy F_D at the interface.	167
6.12	Rutherford backscattering spectra of Ni/Ge bilayer thin film on quartz substrate for as-deposited condition and after mixing for a dose of $6 \times 10^{15} Kr/cm^2$ at 410 K.	168
6.13	The variation of mixing rate for Ni/Ge bilayer system as a function of reciprocal of substrate temperature for a dose of $6 \times 10^{15} Kr/cm^2$ (b) Arrhenius plot of the mixing rate as a function of reciprocal of substrate temperature extracted from Fig.6.12a.	169
6.14	Rutherford backscattering spectra of Co/Ge bilayer thin film on quartz substrate for as-deposited condition and after room-temperature mixing with 1 MeV Kr ions at a dose of $1 \times 10^{16} Kr/cm^2$. The corresponding simulated spectra are shown by solid lines.	171
6.15	Dose dependence of squared thickness of mixed layers of composition Co_2Ge formed across the interface of Co/Ge bilayer system irradiated at room temperature with 1 MeV Ar ions (○) and Kr ions (●) respectively.	172
6.16	The squared thickness of the reacted layer of composition Co_2Ge formed across the interface of Co/Ge bilayer system after thermal annealing is shown as a function of annealing time.	173
6.17	The variation of mixing rate measured in Co/Ge bilayer system for different deposited energy F_D at the interface.	174
6.18	The variation of mixing rate for Co/Ge bilayer system as a function of reciprocal of substrate temperature for a dose of $1 \times 10^{16} Kr/cm^2$ (b) Arrhenius plot of the mixing rate as a function of reciprocal of substrate temperature extracted from Fig.6.17a.	175

6.19	Bilayer sample configuration of two elements A and B where compound A_aB_b grows across the interface under ion bombardment.	188
6.20	Determination of average value of the proportionality constant K , used in Eq 6.18 from the experimental mixing rates. The best fit gives a value $0.99 \times 10^{-6} \text{ keV} - \text{nm}^3$	195

Chapter 1

Introduction

1.1 Preamble

Prior to 1960 the research interests in ion-matter interaction were confined to the radiation damage studies of the surfaces of reactor materials exposed to neutrons and energetic fission fragments. The understanding of the impact phenomena improved when Bohr's theory of energy loss of energetic ions in solids was modified by Lindhard, Scharff and Schiott (LSS)[1] in early sixties. The LSS theory presented the energy loss of an ion in a solid by universal stopping curves. These curves helped in delineating the energy regions useful for the purpose of materials modification and materials analysis as illustrated in Fig 1.1. The revolution in the field of ion-matter interaction occurred when it was realized that ion beams could be used for doping of semiconductors and could modify the tribological properties of metals[2] and that the light ions viz. He^+ , H^+ etc. could be used for materials analysis[3]. Subsequently, a dramatic growth in the use of energetic ion beams took place for studying materials science and solid state physics problems[4-8]. In fact, ion beams of almost all stable elements of energies ranging from a few keV to a few MeV have been put to use.

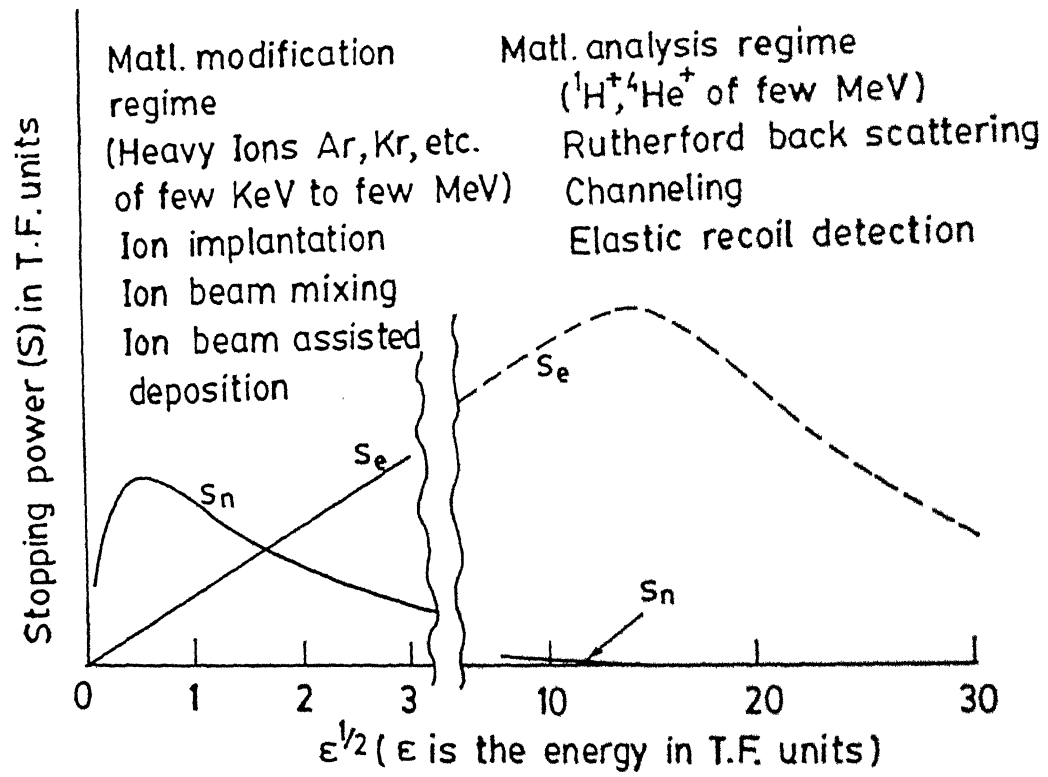


Figure 1.1: Universal stopping power vs. ion energy in solid in Thomson-Fermi (T.F.) unit as predicted by LSS theory. S_n and S_e are the nuclear and electronic stopping powers respectively.

It is well known that the process of ion implantation revolutionized the semiconductor industry[4, 9]. In case of metals, ion implantation has been proved to be very effective as a surface treatment technique which reduces wear and friction of the implanted surfaces and improves corrosion resistance and adhesion properties[10, 11]. These properties are the consequences of the stable/metastable/amorphous alloys produced on the surface due to ion implantation. However, the major disadvantage of ion implantation in case of metals has been the long irradiation times required to achieve sufficiently high implant concentrations resulting in high process cost[6]. Further, the achievable concentrations are limited by the sputtering of surface atoms. Therefore, the process of ion implantation had a limited success in case of metals as compared to semiconductors.

During the past decade new techniques have been developed which combine thin film deposition and heavy ion irradiation processes to synthesize novel and technologically important phases or materials, thereby reducing the process time and cost by an order of magnitude[6, 12–17]. These techniques utilize the inherent capability of heavy ion irradiation process of displacing the atoms from their normal sites either during thin film deposition (ion-beam assisted deposition) or after irradiation (ion-beam mixing).

1.2 Ion-Beam Mixing

In case of ion-beam mixing (IM)[17], the elements to be alloyed are first sequentially deposited on the surface of a material and subsequently irradiated by energetic heavy ions. Ions of inert heavy gases are generally utilized in order to avoid any chemical reactions with the alloy to be formed. The sample configurations which are generally used for IM studies are shown in Fig 1.2. Multilayer configurations shown in Fig 1.2a are mainly important from the point of view of formation of stable/metastable/amorphous alloys of desired composition. The bilayer configuration involves a film of element A of thickness ranging from a few tens to few hundred nanometer deposited on the bulk material B (Fig 1.2b) or on an inert substrate coated with a film of element

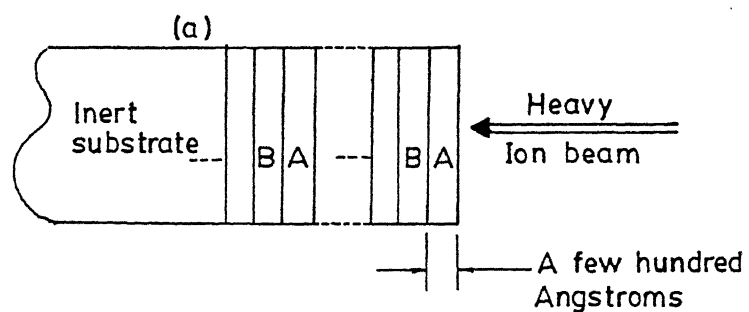
B (Fig 1.2c). The interest here is focused around the formation of binary phases of different compositions in addition to the understanding of the basic processes involved at the interface. In marker configuration (Fig 1.2d) one uses a thin layer (~ 1 nm) of an element in a host matrix. This configuration is used to determine the effective diffusion coefficient of impurity resulting from the collision induced atomic migration. In another configuration (Fig 1.2e), a marker layer placed across the interface is used to monitor the atomic movement during the formation of phases. These studies mainly address the basic aspects of ion-beam mixing process.

For ion-beam mixing studies, inert gas ions having energy of few hundred kilo electron-volt are mostly used[11]. This is partly due to the wide availability of ion implanters at these energies. However, these ion energies limit the maximum thickness of the alloyed region to about 100 nm. The use of ion-beams of MeV energies is now gradually increasing for synthesizing thicker surface alloys[11].

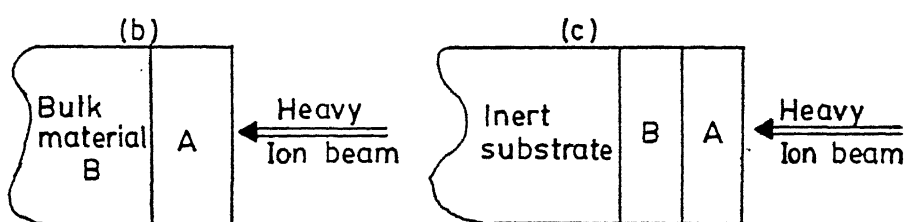
In order to make ion-beam mixing a viable technique for production of different phases, an important prerequisite is to decipher many a latent facet of the physics involved in the basic mechanisms under different processing conditions. Several ion-beam mixing studies have been reported for metal/metal[17-26], metal/Si[27-31] systems which reveal the character of the mixing mechanism under various combinations of the processing parameters. The details of these studies on phase formation and mechanisms of mixing have been the subject of some excellent review articles by Was[6], Cheng[14], Nastasi and Mayer[15], Kelly and Miotello[26].

1.3 Synthesis of Silicides

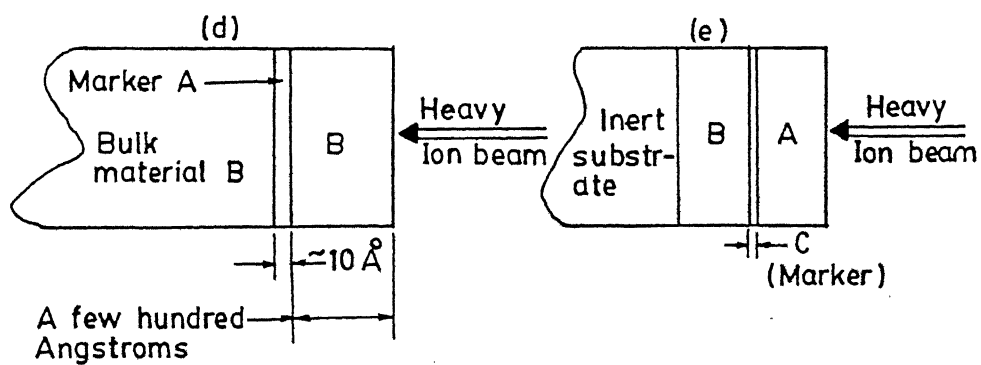
It is well known that metal silicides are important as contact and interconnect materials in semiconductor device technology. The interest in the synthesis of silicides by different methods grew in 70s[32] when it became clear that with decreasing dimension the resistance of the conductors fabricated from polycrystalline silicon would become too high for effective use. The work done in the last decade on metal silicides thin films



MULTILAYER CONFIGURATION



BILAYER CONFIGURATION



MARKER CONFIGURATION

Figure 1.2: Schematic diagram of sample configurations utilized for ion-beam mixing and thermal annealing studies.

revealed a large number of interesting properties related to resistivity, electromigration, diffusivity, corrosion resistance etc.[33, 34]. All these properties are important from the point of view of semiconductor and microelectronics industry which require such materials in modern integrated circuits because the packing density, speed etc. are usually limited by interconnects and contact requirements rather than by decreasing active device dimension[35, 36]. For example, if the circuit size is scaled by a factor k , the interconnect resistance increases by a factor $1/k$ while the contact resistance by $1/k^2$ [36]. For the formation of stable and metastable alloys of metal-semiconductor systems ion-beam mixing has been widely used for its several advantages over solid state reaction such as lower processing temperature and higher spatial selectivity[5, 6, 13, 15]. In the last decade a large number of studies on the formation of different near-nobel and refractory silicides have been reported[15, 17, 29, 30, 37-39].

1.4 Synthesis of Germanides

As compared to the silicides systems, which have been widely studied using both thermal and ion-beam processes[37, 40-43]. The reports on the synthesis of germanides are very few in the literature. Recently, the germanide systems have attracted attention of many researchers[44-48]. This interest in the germanide systems has been triggered by the work of Krusen-Elbaum and Aboelfotoh[49] who report that the ϵ_1 - Cu_3Ge phase possesses lower resistivity (few $\mu\Omega - cm$) than many silicides ($CoSi_2$, $NiSi_2$ etc.). Also it possesses most of the desirable properties required for an interconnect/contact material in the existing GaAs and Si device technology[44, 49]. This copper germanide phase which is formed by thermal annealing at about 680 K, is found to be stable and reproducible. The studies on Cu/Ge system indicates that other germanides which are mostly unexplored might emerge as promising future materials for the semiconductor industry.

1.5 Motivation and objectives of this work

The interesting and technologically important properties[44, 49] of Cu_3Ge , mentioned above, motivated the author to undertake the study of MeV ion-beam mixing in metal/Ge systems. Apart from Cu/Ge, two other systems viz., Ni/Ge and Co/Ge have also been selected for these studies. These systems have been chosen for the following reasons. The atomic masses of Cu, Ni and Co being similar, it is expected that the ballistic effects[14] produced under ion irradiation in all these three cases would be almost same. Also, the equilibrium phase diagrams of Cu/Ge, Ni/Ge and Co/Ge are similar. The main objectives of this work are summarized below :

- To explore the directed energy deposition process of ion mixing for producing germanide phases in bilayer and multilayer thin film structures of Cu/Ge, Ni/Ge and Co/Ge systems at different ambient temperatures, using Kr and Ar ions of mega electron-volt energies.
- To obtain quantitative information of the parameters viz. mixing rates, mixing efficiencies, activation energies from the dose dependence, temperature dependence of mixing (the Q curve) etc. for the above systems.
- To compare the results of ion induced phase formation in the above metal/Ge systems with those obtained by solid state reactions at elevated temperatures, especially concerning the formation of the first phase.
- To study the atomic movements of different species during ion-beam mixing using marker layer at the interface.
- To understand the mixing mechanism responsible for the growth of the compound layer across the interface and to develop a formalism to explain the experimentally obtained mixing rates and efficiencies.

For ion irradiations, the 2 MeV Van de Graaff accelerator at IIT, Kanpur was utilized. Most of the quantitative information viz. layer thicknesses, composition of the

mixed regions and depth profile was obtained by Rutherford backscattering spectrometry[7] using MeV He^+ ions from the same accelerator. X-ray diffraction technique was utilized to identify the phases produced by ion-beam mixing or by thermal treatment.

1.6 Organization of Thesis

A brief review of different aspects of ion-beam mixing is presented in Chapter 2. The details of sample preparation and the experimental techniques utilized in this work are described in Chapter 3. Chapter 4 describes the MeV Kr and Ar ion induced mixing effects, leading to the compound formation in multilayer structures of Cu/Ge, Ni/Ge and Co/Ge samples held at various ambient temperatures. It also shows the comparison of these results with those of thermal annealing experiments. Also, the nature of the phases formed in these systems has been examined on the basis of the existing rules. Chapter 5 deals with the marker experiments which reveal the information on the dominantly moving atomic species during ion-beam mixing and thermal annealing. The mixing rates, mixing efficiencies etc. are determined using bilayer configurations in Chapter 6. In this chapter a new phenomenological model based on chemical kinetics and applicable to reactive systems (such as metal silicides, germanides) has been proposed to explain the experimentally obtained mixing rates. The work has been summarized in the last chapter giving summary, conclusions and scope for future studies.

Chapter 2

Review of ion-beam mixing

2.1 Introduction

In this chapter some basic aspects of ion-beam mixing which are relevant to this work will be reviewed. These include the influence of collisional and thermodynamic effects in the mixing process and temperature dependence of mixing. The various empirical rules reported in the literature for predicting the nature of mixed regions, will be mentioned. Also a brief description of the various phenomenological models used for quantitative calculation of different mixing parameters will be given.

2.1.1 Basic mechanism of mixing

The basic processes involved in ion-beam mixing are illustrated schematically in Fig 2.1. When the energetic heavy ion penetrates a top layer A to reach the bulk material B, it loses energy due to collision with target atoms. Due to these collisions the target atoms receive sufficient energy to get displaced from their original positions and thus produce a displacement cascade[5, 6]. The displacement of atoms occur near the interface of

layer A and the bulk material B resulting into a mixed region of A and B. The effects of the vehement collisions of the incident ion with the target atoms have been broadly divided into two categories based on the time scales[14, 17] compared to the time taken by the incident ion to come to rest in the target which is of the order of pico-second. These are called as prompt and delayed processes.

In the prompt process, the generation of primary recoils by the incident ion and the evolution of a cascade by the secondary collisions occur on a time scale of few pico-second. The prompt process tend to the mixing of A and B by direct recoil of the target atoms or by generation of cascade of secondary atoms called as cascade mixing. The direct recoil process takes the atom of layer A deep inside the bulk B (Fig 2.1b) and is called as recoil implantation[14, 15, 50]. The probability of direct recoil is very small and it cannot quantitatively explain the amount of experimentally observed mixing of A and B in most of the cases[14, 15]. In case of cascade mixing[14], the secondary collisions along the track of the incident ion produce a collision cascade which involves many atoms with kinetic energies much smaller than the incident ion energy and the multiple relocations of the atoms occur resulting in the mixing of dissimilar atoms of A and B across the interface. Such collision cascades are also called as thermal spikes[5, 6, 14, 15]. Thus, each incident ion can be assumed to give rise to a small volume across the interface containing both atoms A and B (Fig 2.1b). The effect of the individual cascades overlap as a function of incident ion dose results in a continuous mixed region as shown in Fig 2.1c. Both processes namely the primary recoil and the collision cascade are essentially temperature independent.

In the delayed process, further mixing of A and B occurs due to the thermally activated motion of defects produced after the cascade dies. The resulting atomic motion persists for a time period exceeding several nanosecond and depends on the temperature of the target[14, 15, 21, 23]. Mixing occurring due to these delayed effects follows an Arrhenious behavior. It has been experimentally observed that for a binary system there exist two critical temperatures T_c [20, 51] and T_{eq} [51]. Above T_c , the mixing is temperature dependent and below it mixing is temperature independent. The critical

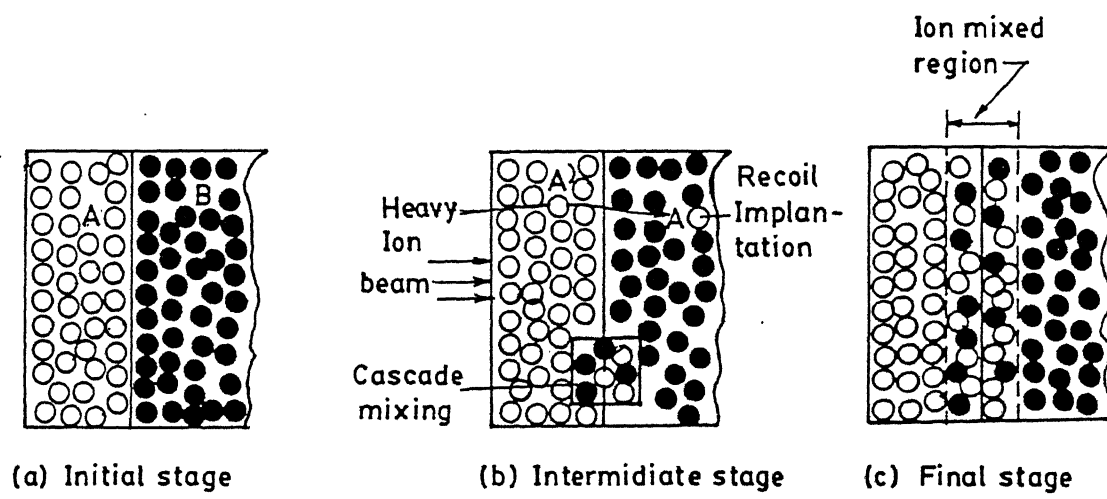


Figure 2.1: Schematic diagram showing the ion-beam mixing processes.

temperature T_{eq} , above which normally stable compound phases form, is known as the equilibrium temperature. It is always greater than or equal to T_c [51]. However, there are many reports of equilibrium phase formation at relatively lower temperature around T_c in case of some metal silicides and aluminides systems[15, 25, 31, 41, 42]. For technological applications it is essential to know the nature of the final phase and its stability. In general, amorphous, crystalline metastable or stable phases form after ion-beam mixing. To predict the nature of the mixed region (amorphous/crystalline) several empirical rules[52–56] have been proposed which will be discussed in the following section.

2.1.2 Phase formation

The phase formation in metal/semiconductor systems by ion-beam mixing can be discussed on the basis of metal/Si systems for which ion-beam mixing have been extensively studied using both bilayer (unlimited source) and multilayer (limited source) structures. The results[17, 31, 42, 57] of these are summarized in Table 2.1. The ion induced silicide formation characteristic can be compared with those obtained by steady-state thermal annealing. The results of silicide formation[33, 34, 57]) by thermal annealing are also given in Table 2.1. It can be clearly seen from this table that the first silicide phase induced by ion-beam mixing in unlimited supply (bilayer) samples is same as that obtained by thermal annealing. Although some of the layers that were ion mixed at room temperature do not exhibit a distinct crystal structure due to low intensity X-ray diffraction patterns[57], the composition of the mixed layers is invariably same as that obtained by thermal annealing. This correlation concerning the first phase formation by ion-beam mixing *vis a vis* the first phase formation by thermal treatment does not hold true for metal/metal systems[15].

In solid state reactions, the kinetic constraints play a dominant role, whereas in ion-beam mixing it is normally assumed that the kinetic restrictions are relaxed[27]. Thus, both the reaction kinetics as well as the thermodynamic driving forces play

Table 2.1: Comparison of first phase formation by ion-beam mixing and thermal annealing in metal/semiconductor systems

Metal/Semiconductor system	Phase formed by IBM		Phase formed by thermal annealing
	composition	phase	
Ni/Si	Ni_2Si	Ni_2Si	Ni_2Si
Co/Si	Co_2Si	Co_2Si	Co_2Si
Pd/Ge	Pd_2Ge	Pd_2Ge	Pd_2Ge
Pd/Si	Pd_2Si	Pd_2Ge	Pd_2Ge
Cr/Si	$\sim CrSi_2$	-	$CoSi_2$
V/Si	$\sim VSi_2$	-	VSi_2
Ti/Si	$TiSi_2$	-	$TiSi_2$
Nb/Si	$NbSi_2$	$NbSi_2$	$NbSi_2$
Pt/Si	Pt_2Si	Pt_2Si	Pt_2Si

-weak x-ray reflection

an active role during mixing. Extensive efforts have been made experimentally as well as theoretically to understand the effect of thermodynamic driving forces[15, 27, 31], mobilities[31, 56], composition[6, 13] etc. to predict phase formation during ion-beam mixing and thermal annealing in metal/metal aluminides[25, 58, 60, 61] and metal/Si[31, 57–60] thin films.

Several empirical rules have been suggested to predict the formation of crystalline compound by ion-beam mixing[52–56]. Similar rules concerning the formation of amorphous phases are also relevant to compound formation since the former can preclude the later[61]. Amongst these the most widely used rules are simple structure rule[52], modified structure rule[53], negative heat of compound formation rule[62], Hagg’s rule[55] and Lau’s rule[57]. All these rules have also been applied to metal/semiconductor systems by several authors. However, In many cases the formation of first and the successive phases in metal/Si systems cannot be predicted by the above mentioned rules[27]. Recently Pretorius et al.[56] have formulated effective heat of formation rule which successfully predicts the sequence of phase formation by thermal annealing and ion-beam mixing in many systems. There are also many other factors which influence the final phase formation which are not considered in these rules. In general, the factors which most likely influence the formation of phase are the structure of the terminal solution, complexity of the compound phase, width of phase field, mobility, effect of substrate temperature etc. These rules will be discussed in detail in the fourth chapter while explaining the present studies of phase formation in metal/Ge systems.

2.2 Critical temperature

The results of temperature dependent mixing show that the mixing is divided in temperature independent and temperature dependent regimes[14, 15, 21, 23, 51]. As mentioned above in most of the systems it has been observed that, in general, there exist two critical temperatures T_c and T_{eq} with $T_c \leq T_{eq}$ such that metastable phases are expected between T_c and T_{eq} and equilibrium phases are expected above T_{eq} . de

Reus et al.[51] have correlated T_c and T_{eq} with the energies required for creating \bullet holes in the compound. The smaller hole formation energy is related with T_c while for the larger one with T_{eq} . These temperatures are given by the following empirical relations.

$$T_c = 4.0 \times \Delta H_{Vsmall} \quad (2.1)$$

and

$$T_{eq} = 3.8 \times \Delta H_{Vlarge} \quad (2.2)$$

where the temperatures are given in K and the hole formation enthalpies in kJ/mole. The plots of T_c or T_{eq} (Fig 2.2) as a function of ΔH_V gives a straight line. In several systems the difference between T_c and T_{eq} is not so pronounced and in those cases there is only one transition temperature[51]. Table 2.2 contains many reported data[51] for metal/metal and metal/semiconductor systems. The hole formation enthalpies ΔH_V for an alloy $A_{1-x}B_x$ are calculated from Miedemman's model[63] and are given by

$$\Delta H_V^A = c_A \Delta H_{IV}^A + (1 - c_A)(V_A/V_B)^{5/6} \Delta H_{IV}^B \quad (2.3)$$

and

$$\Delta H_V^B = c_B \Delta H_{IV}^B + (1 - c_B)(V_B/V_A)^{5/6} \Delta H_{IV}^A \quad (2.4)$$

where ΔH_{IV}^A and ΔH_{IV}^B are the mono vacancy formation enthalpies in pure A and B. The molar volume ratio V_A/V_B can be regarded as a measure to which degree the atoms are surrounded by both constituents. The effective concentrations c_A and c_B depend on x .

Cheng et al.[20] have correlated T_c with average cohesive energy of mixing elements. Since the cohesive energy is proportional to the melting temperature of solids, Rossi and Nastasi[23] have correlated T_c with the melting temperature. Cheng et al.[20] have plotted T_c values obtained experimentally against ΔH_{coh} and obtained a straight line whose slope is 100 K/eV. Thus

$$T_c = 100 \Delta H_{coh} \quad (2.5)$$

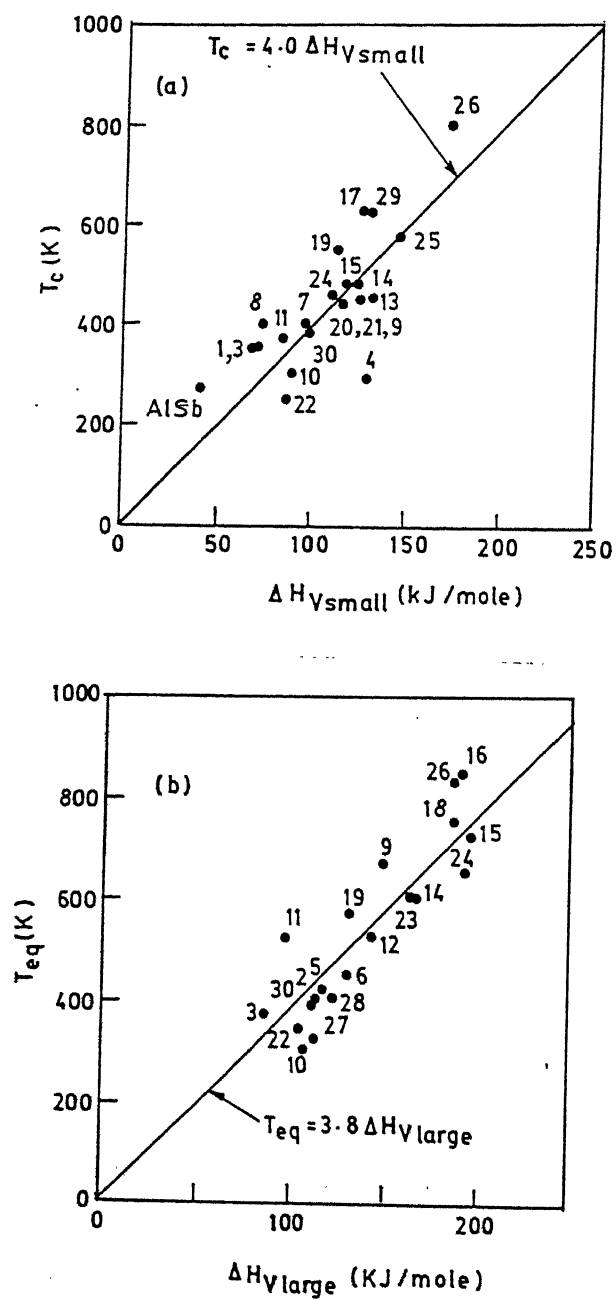


Figure 2.2: Plots showing variation of (a) T_c as a function of ΔH_{Vsmall} and (b) T_{eq} as a function of ΔH_{Vlarge} (from ref 51 and data given in table 2.2).

Table 2.2: Comparison of experimentally obtained critical temperatures with those calculated from the model of de Raus et al.(after ref 51)

Bilayer system	Critical temperature T_c in K		Eq. temperature T_{eq} in K	
	Exp.	Calculated from	Exp.	Cal. from
1) Al-Cu	350	284	-	353.4
2) Al-Fe	-	356	400	433.2
3) Al-Mn	350	272	370	326.8
4) Al-Mo	290	516	-	501.6
5) Al-V	-	408	420	448.4
6) Al-Zr	-	412	450	497.8
7) Au-Ni	400	384	-	520.6
8) Au-Si	400	292	-	326.8
9) Au-Zr	450	504	620	566.2
10) Co-Si	300	356	300	410.4
11) Cr-Si	370	336	520	368.6
12) Cu-Ti	-	428	525	547.2
13) Fe-PT	454	528	-	638.4
14) Fe-Ti	480	496	600	634.6
15) Fe-Zr	480	468	720	744.8
16) Mo-Ni	-	572	830	710.6
17) Mo-Si	630	500	-	509.2

- not available

continue...

...continue (Table 2.2)

Bilayer system	Critical temperature T_c in K		Eq. temperature T_{eq} in K	
	Exp.	Calculated from	Exp.	Cal. from
18) Nb-Ni	-	516	750	710.6
19) Nb-Si	550	448	570	501.6
20) Ni-Pd	440	464	-	570
21) Ni-Pt	450	500	-	630.8
22) Ni-Si	250	344	340	399
23) Ni-Ti	-	468	600	623.2
24) Ni-Zr	460	440	650	733.4
25) Pd-Pt	575	580	-	566.2
26) Pd-Ta	800	684	820	725.8
27) Pt-Si	-	416	320	429.4
28) Ru-Si	-	484	400	467.4
29) Si-Ta	625	520	-	585.2
30) Si-Ti	380	392	390	425.6

- not available

Cheng has shown that the T_c values of other systems specifically metal/metal systems also follow the above relation. However, there are quite a few studies especially concerning metal/semiconductor systems, which report experimental values of T_c which are significantly different than the one predicted by the above relationship[64].

2.3 Phenomenological model

For quantitative understanding of mixing it is important to estimate some of the useful mixing parameters like (i) mixing rate (X^2/Φ): rate at which the squared thickness X^2 of the mixed region increases as a function of irradiation dose (Φ) at given temperature for a particular incident ion beam, (ii) mixing efficiency ($X^2/\Phi F_D$): normalized mixing rate with respect to the deposited energy density F_D . For theoretical prediction of these parameters, several phenomenological models have been proposed which depend on different experimental conditions viz. atomic number of incident ion and target atoms, energy deposited in collisions, nature of the thermal spike (whether local or global), thermodynamic parameters, nature of the final phase etc.[19, 22–24, 31].

The experimental data of mixing rates in various systems reported in the literature reveal that the mixing rate increases linearly with F_D up to certain critical damage energy (F_D^{gr})[24, 65] above which it increases much more rapidly exhibiting a square dependence on F_D . Obviously, the mixing efficiency is constant in the linear region. For example[66], in the case of Co/Ti system, the mixing rate varies linearly with F_D up to 2.25 keV/nm after which it becomes quadratic. For Pd/Si system (shown in Fig 2.3), this linearity is seen for F_D values up to 1.5 keV/nm[31]. For systems with $Z_{ave} > 20$ this dependence comes from the nature of the thermal spikes. For systems having $Z_{ave} < 20$ the concept of thermal spike is not applicable[14]. Different phenomenological models have been developed to explain the mixing rates in the linear and quadratic region of the mixing rate vs. F_D curve. In the next section we shall describe some of the models frequently used for the calculation of mixing rates and efficiencies.

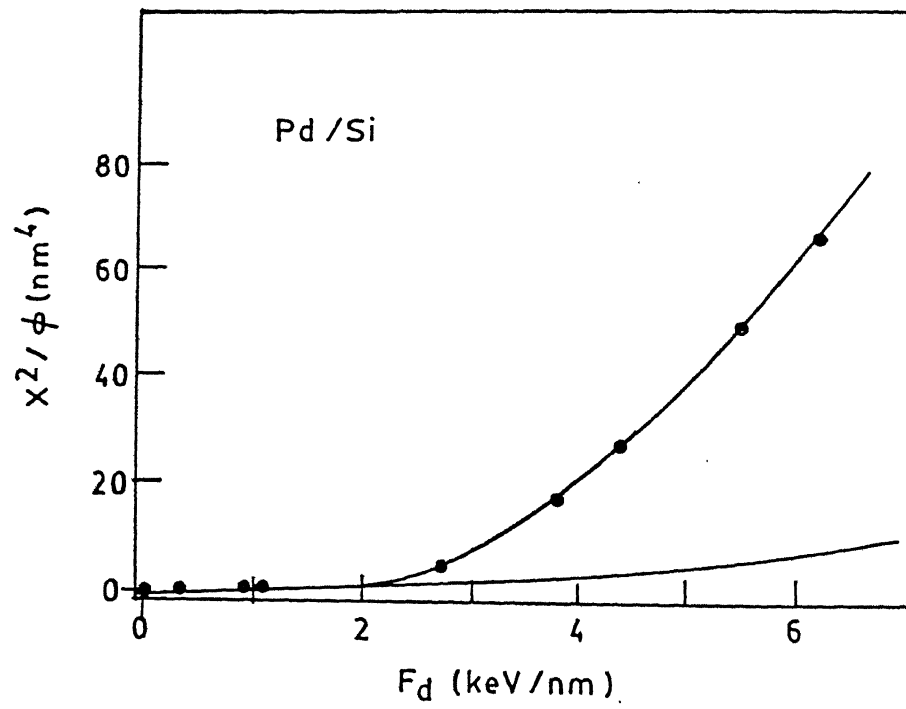


Figure 2.3: Variation of mixing rate as a function of F_D for the case of Pd/Si system.

2.3.1 Ballistic Model

Sigmund and Gras Marti[50] studied the effect of ion bombardment in a dilute solution ($< 1\%$) of an impurity in a homogeneous matrix at low temperature and low current density limit. This implies that the mixing occurs due to linear superposition of elementary events which are associated with individual ion impacts. This approach has been followed by several authors to model mixing rate. The formulae developed by Sigmund and Gras Marti to evaluate the effects of recoil mixing and cascade mixing are given below.

Recoil Mixing

The effect of recoil mixing can be identified in the RBS spectrum as a tail in the low energy side of the impurity peak[50]. The probability of such an event is given by relocation cross-section $d\sigma[E_o(x), T]$ where $E_o(x)$ is the energy of the incoming ion at a depth x and $T \leq \left[\frac{4mM}{(m+M)} \right] E_o$. Where m and M are the masses of incident and target atoms.

The probability density $P(z)$ for an impurity at depth x to get relocated at depth z is given by

$$P(\Delta z)d(\Delta z) = \Phi d\sigma(x, z)$$

where Φ is the irradiation dose. The long-range recoil implantation is mainly due to single ion-impurity knockon events whose cross section $d\sigma$ is of the order of the square of the atomic radius, which is about 10^{-16} cm^2 . Thus long-range recoil implantation at typical dose $\Phi \leq 10^{16} \text{ ions/cm}^2$ is a rare event[14, 50].

Cascade Mixing

As mentioned above, a cascade is formed when a large number of atoms are displaced from their lattice positions and move very small distances in random directions. This motion occurs due to the secondary collisions between impurity and matrix atoms. If

the impurity concentration is very low ($\ll 1\%$) or if the deposited energy density (F_D) is low then the spread in the concentration profile is given by [14, 50],

$$\Omega^2 = \frac{1}{3} \frac{\Gamma}{C} \Phi F_D \xi^{1/2} \frac{R_c^2}{E_c} \quad (2.6)$$

where $\Gamma = 0.608$, $\xi^{1/2} = [\frac{4M_1M_2}{(M_1+M_2)^2}]$, M_1 and M_2 being the masses of the two target atoms, C = average of atomic density, E_c = threshold or cut off energy (8 eV) [14, 15], R_c = mean square range at E_c .

For stable Frenkel pair formation E_c should be replaced [14] by the displacement energy E_d [67] and R_c should be equal to the minimum distance λ (~ 1 nm) where recombination does not occur. Setting $\Omega^2 = 4Dt$, the effective diffusion coefficient can be written as

$$D_{eff} = \frac{1}{4} \frac{d\Omega^2}{d\Phi} \dot{\Phi} = \frac{1}{3} \frac{\Gamma}{C} \dot{\Phi} F_D \xi^{1/2} \frac{\lambda^2}{E_d} \quad (2.7)$$

From the above relation we get $\Omega^2 \propto \Phi$, i.e. $\Omega \propto \Phi^{1/2}$ which is similar to the thermal annealing process in which $\Omega \propto t^{1/2}$. The ballistic mixing rate for a mixed layer of thickness X is given by

$$\frac{X^2}{\Phi} = \frac{D_{eff}}{\dot{\Phi}} = \frac{1}{3} \frac{\Gamma}{C} F_D \xi^{1/2} \frac{\lambda^2}{E_d} \quad (2.8)$$

The main limitation of this theory is that no general result can be derived from the relocation profile without approximation [68, 69]. Also the numerical solutions of the transport equations are very complicated. However, this kinetic view point of cascade mixing provides a good description of broadening and shift of the concentration profile of dilute impurity ($\leq 1\%$) in solid matrix.

2.3.2 Thermodynamic effects

The above mentioned ballistic approach ignores the thermodynamic effects which are important for large atomic concentration. Recently, Miotello and Kelly [26] incorporated chemically guided defect motion in the ballistic approach of mixing. Due to this

reason ballistic model described above could not properly describe ion-beam mixing especially the mixing rates and efficiencies in many systems[14, 15, 70]. For example[71], if only the ballistic effects are considered the Hf-Ni and Hf-Ti systems should show similar mixing behavior. Contrarily, it has been found that the Hf-Ni system mixes much more efficiently than Hf-Ti system. For equal atomic concentrations, the heat of mixing for Hf-Ni is -62 kJ/g at while for Hf-Ti it is 0 kJ/g at. The difference in the mixing was believed to result from the large difference in the heat of mixing between these two systems. The large ion-beam mixing effects in the miscible Au-Cu and the negligible mixing of immiscible W-Cu system is another such example[14]. It has also been realized that thermodynamic driving forces also play a dominant role along with the ballistic effects in the formation of various phases during mixing.[14, 15, 70]. On the basis of studies reported for various systems the dependence of mixing on ΔH_{mix} and ΔH_{coh} can be summarized as follows.

- The Mixing rate varies linearly with the heat of mixing ΔH_{mix} [14, 70]. The slope of this curve gives the effective temperature of mixing and hence the kinetic energy of the moving atom which is found to be of the order of 1 eV/atom.
- The mixing rates and the mixing efficiencies are very low, moderate and high for binary systems having high positive, zero and negative values of heat of mixing respectively[14, 15].
- The mixing rate varies inversely as the square of ΔH_{coh} [18].

Several phenomenological models[14, 15, 19, 22, 24, 31] which consider the effect of the chemical driving force, nature (overlapping and non-overlapping subcascades) and geometry (cylindrical or spherical) of the thermal spike have been developed to explain above experimental results. Although there is no direct experimental evidence of a thermal spike, the concept of which has been found useful in explaining the ion-beam mixing effects. In the following we shall describe the characteristics of a thermal spike followed by brief discussion of different models utilized for calculating mixing rates.

2.4 Thermal Spike

A spike is defined as a limited volume inside a solid within which the majority of atoms are temporarily in motion[14]. A thermal spike is a spike where atomic motion reaches a state of quasi-equilibrium, so that the law of equipartition of energy holds in the spike volume and the velocity distribution can be described by Maxwell-Boltzmann statistics. The characteristics of such spike are

- The average energy density is very high and exceeds the melting temperature.
- The local temperature is as high as 1000-3000 K.
- The cooling time of the spike is 0.1 psec to 10 psec.

The thermal spikes are distributed at random inside the cascade volume. The cascade displacement energy, that is, the number of displacement per unit volume is not homogeneous in space. The density is locally very high in the spike and low in the other part of the cascade. The density of spikes depends on the amount of energy deposition which in turn depends on mass and energy of the incident ion and the ballistic properties of target atoms. Depending on the stopping power of the target and ion energy, the distance between the primary collision can be larger than ^{the} size of the cascade initiated by the secondary recoils[14]. It is to be noted that a cascade may contain several well separate subcascades each of which may have a separate spike or local spike. The ideas about spike have been recently quantified by Cheng[14]. On the basis of fractal geometry approach Cheng has argued that space filling fractals is a necessary condition for spike formation. He has shown that an atom will initiate a space filling cascade or spike, only if its kinetic energy is smaller than E_c . This critical energy E_c is given by

$$E_c = 3.929 \times 10^{-2} Z_{ave}^{2.23} \text{ ev} \quad (2.9)$$

Cheng also calculated that spikes cannot form in a matrix consisting of elements with Z values less than 20[14]. He has proposed the following conceptual picture for

spike formation:

1. When E_c is smaller than the threshold displacement energy E_d , a collision cascade will stop before reaching the space-filling condition. The formation of spike is thus impossible.
2. When $(E_c > E_o > E_d)$, where E_o is the incident ion energy, the space-filling condition is satisfied. Here, the formation of spike is possible.
3. When $(E_o > E_c > E_d)$, the initial kinetic energy of the incident ion E_o is shared by the displaced atoms. Each displaced atom is capable of generating a space-filling sub-cascade, or a local spike, if this displaced atom has a kinetic energy just below E_c . A global spike will form if local spikes overlap.

It is to be noted that the formation of spikes takes place only by higher generation recoils and is determined by E_c , not the incident ion energy E_o .

2.4.1 Global or overlapping spike model

Johnson et al.[19] have developed this model under the condition of overlapping of the subcascades producing a single cascade or global spike for higher deposition energies. The development of this model is based on Vineyard's spike model[72]. In Vineyard's model it is assumed that the energy is deposited instantaneously in a very small volume, producing a localized increase of temperature which spreads according to the classical laws of heat conduction in a homogeneous medium. Vineyard has calculated the jumping rate η for the atoms in a spike of cylindrical geometry as

$$\eta = \frac{AK^2 F_D^2}{8\pi\kappa C Q^2} \quad (2.10)$$

Here the heat capacity κ and thermal conductivity C are independent of temperature, Q is the internal energy per unit volume and A is the proportionality constant. Johnson et al.[19] modified this formula, assuming that the mixed region is in the form

of a regular solution, by empirically including in it the heat of mixing and the cohesive energy (ΔH_{coh}) which is related with Q [18]. The jump frequency η is then given by[18, 19]

$$\eta = \frac{AK^2F_D^2}{8\pi\kappa CQ^2} \left[1 - \frac{4\Delta H_{mix}}{Q} \right] \quad (2.11)$$

where ΔH_{mix} is the heat of mixing.

Considering the spikes to be independent of each other Johnson et al.[19] have postulated the following equation for calculating the mixing rate.

$$\frac{X^2}{\Phi} \Big|_{glo} = \frac{d(4Dt)}{d\Phi} = K_1 \frac{F_D^2}{C^{5/3}\Delta H_{coh}^2} \left[1 + K_2 \frac{\Delta H_{mix}}{\Delta H_{coh}} \right] \quad (2.12)$$

where K_1 and K_2 are constants, C is the average atomic density. Using this formula, Cheng[14] has plotted the quantity $[d(4Dt)/d\Phi] \times [C^{5/3}(\Delta H_{coh})^2/F_D^2]$ versus $\Delta H_{mix}/\Delta H_{coh}$ which is shown in Fig 2.4. Here Cheng has used experimentally measured values of $[d(4Dt)/d\Phi]$ and the tabulated values for ΔH_{mix} and ΔH_{coh} reported by Miedema[63] and Kittel[73] respectively. From this curve the values of K_1 and K_2 are found to be 0.035 \AA and 27.5 respectively. The above relation is valid for infinitely thick layers where the composition of the intermixed region is not influenced by the limited supply of one of the constituents[14, 74]. The experimental values of the mixing rates in the region where it exhibits a quadratic dependence on F_D can be explained fairly well by this model.

2.4.2 Local or non-overlapping spike model

The linear dependence of mixing rate on damage energy cannot be explained by Johnson et al. model. Alford et al.[74, 75] have found that the mixing rate and efficiency do not possess the same energy dependence as predicted by Johnson et al. model and is higher by a factor of about 5. The constancy of the mixing efficiency or the linear dependence of the mixing rate on F_D has been explained by Borgesen et al.[22] and Bolse[24] by considering well separated local spikes. The higher degree of mixing in

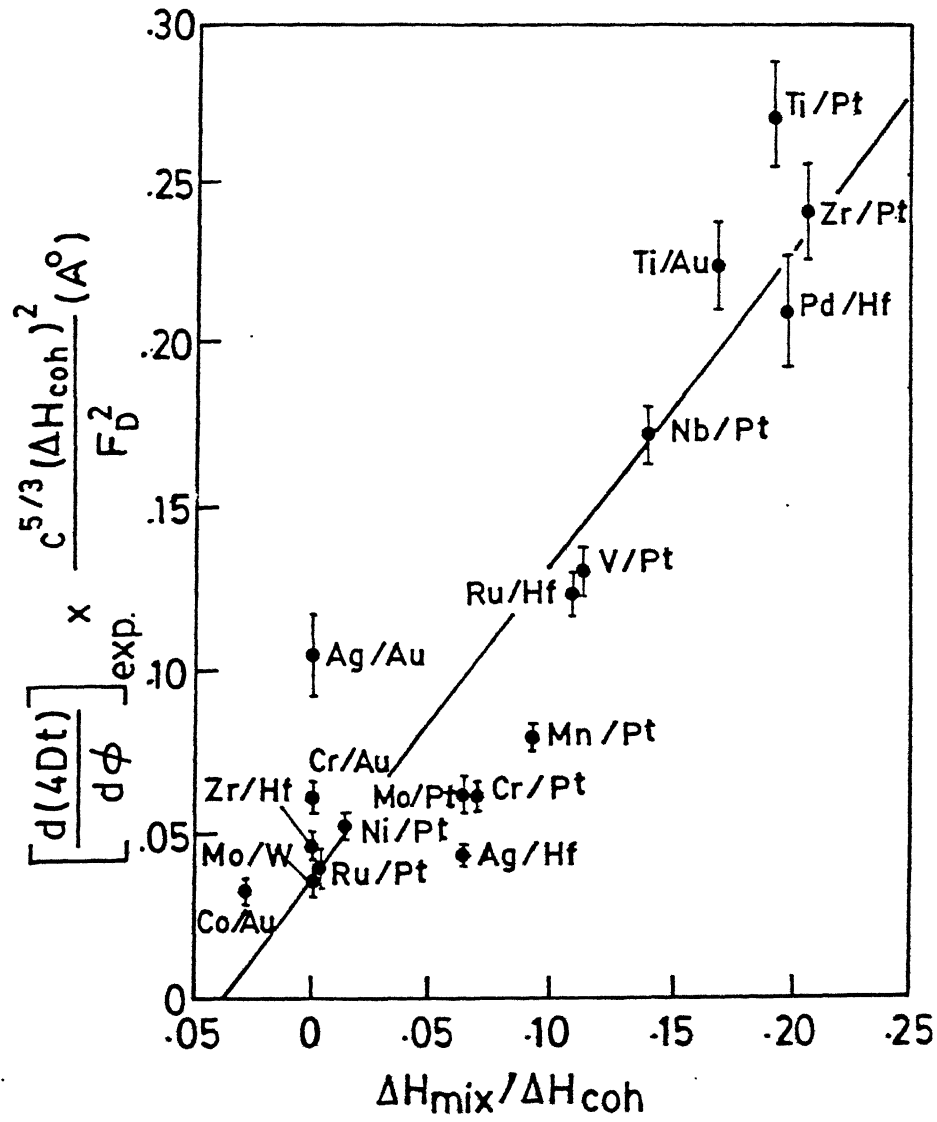


Figure 2.4: Plot of $[d(4Dt)/d\Phi] \times [C^{5/3}(\Delta H_{\text{coh}})^2/F_D^2]$ as a function of $\Delta H_{\text{mix}}/\Delta H_{\text{coh}}$ (from ref 14).

these cases has been taken into account as follows. A local thermal spike would cool much slowly as compared to the global spike because the local spikes are isolated from each other in a cold lattice. A larger cooling time implies a greater degree of atomic motion and hence a larger amount of mixing.

According to Borgesen et al.[22], for medium Z materials the subcascades and hence local spikes are well separated to prevent mutual overlapping. Assuming a spherical non-overlapping spike they deduced the mixing rate as,

$$\frac{X^2}{\Phi} \Big|_{loc}^{Borgesen} = \frac{K_b Z_{ave}^{1.5} F_D}{C^{4/3} \Delta H_{coh}^{5/3}} \left[1 + \frac{5}{6} K_2 \frac{\Delta H_{mix}}{\Delta H_{coh}} \right] \quad (2.13)$$

where K_b is $0.034 \text{ nm-eV}^{2/3}$ and $K_2 = 27.4$ are used[75]. Using this relation they have explained the experimental mixing rates of many medium Z ($20 < Z_{ave} < 40$) bilayer systems.

However, Bolse[24] has argued that the local spikes are cylindrical in nature and not spherical as assumed by Borgesen et al.[22]. According to Bolse, the mixing rate is given by

$$\frac{X^2}{\Phi} \Big|_{loc}^{Borse} = \frac{K_B Z_{ave}^{1.77} F_D}{C^{2/3} \Delta H_{coh}^2} \left[1 + K_2 \frac{\Delta H_{mix}}{\Delta H_{coh}} \right] \quad (2.14)$$

where $K_B = 0.0163 \text{ nm}^3 \text{ eV}$ and $K_2 = 41$ are empirical constants obtained from experimental results[76].

Bolse has also estimated the critical damage[24] energy density F_D^{cr} , for a given ion-target combination, above which the nonlinear dependence of mixing rate on F_D begins. In other words the subcascades begin to overlap. The F_D^{cr} is given by

$$F_D^{cr} = K_m C \left[\frac{Z_i Z_t}{Z_i^{0.23} + Z_t^{0.23}} \right] \left[\frac{m_i}{m_i + M_t} \right] \quad (2.15)$$

where, Z_i and m_i = Atomic number and mass of the incident ion, Z_t and M_t = atomic number and mass of the target atom and $K_m = 2.5 \text{ keV nm}^2$ [24, 65] is the proportionality constant.

All the above mentioned models satisfactorily predict the mixing rates for most of the metal/metal systems. However, many metal/semiconductor systems where growth of a compound occurs by ion-beam mixing exhibit high value of mixing rates which could not be predicted by the above formulas (Eq 2.12 or Eq 2.13 or Eq 2.14). For example, the recent results of Pd/Si bilayer system (shown in Fig 2.5) cannot be explained by the above models. These metal/semiconductor systems are generally considered as a highly reactive systems. The models which explain the formation of phases or compound are described in the next section.

2.5 Model for Compound Formation

Desimoni and Traverse[31] have proposed an ion-beam mixing model that accounts for compound formation at a boundary between two materials during ion irradiation. Their model is based on Fick's law which incorporates a chemical driving force to simulate the chemical reaction at the boundary. The model reproduces the two fluence regimes, linear and quadratic found in several ion beam experiments. When the square of the mixed thickness (X^2) is plotted as a function of the irradiation fluence (Φ) the plot exhibits a quadratic variation of X^2 until a critical dose Φ_c is reached above which it shows a linear dependence. This is illustrated in Fig 2.5 for Pd/Si systems. The critical fluence Φ_c in this case is $1.5 \times 10^{15} \text{ ions/cm}^2$. According to Compound formation model of Desimoni and Traverse the critical dose of Φ_c is proportional to $D\Phi/k^2$ where k is reaction rate and D is diffusion coefficient under ion irradiation. For highly reactive systems for which k is very large. The critical fluence Φ_c is quite low ($< 10^{12} \text{ ions/cm}^2$). Therefore in these systems the linear dependence of X^2 on Φ is only seen. On the other hand, for systems for which k is low the Φ_c is quite high, therefore the quadratic dependence is only observed. For example in Cr-Si case the k rate is $1 \times 10^{-2} \text{ nm/s}$ and the Φ_c value turns out to be $8 \times 10^{18} \text{ ions/cm}^2$. This quadratic regime is called reaction control process while the linear regime is called diffusion control process. When diffusion is the limiting process, D is enhanced by a

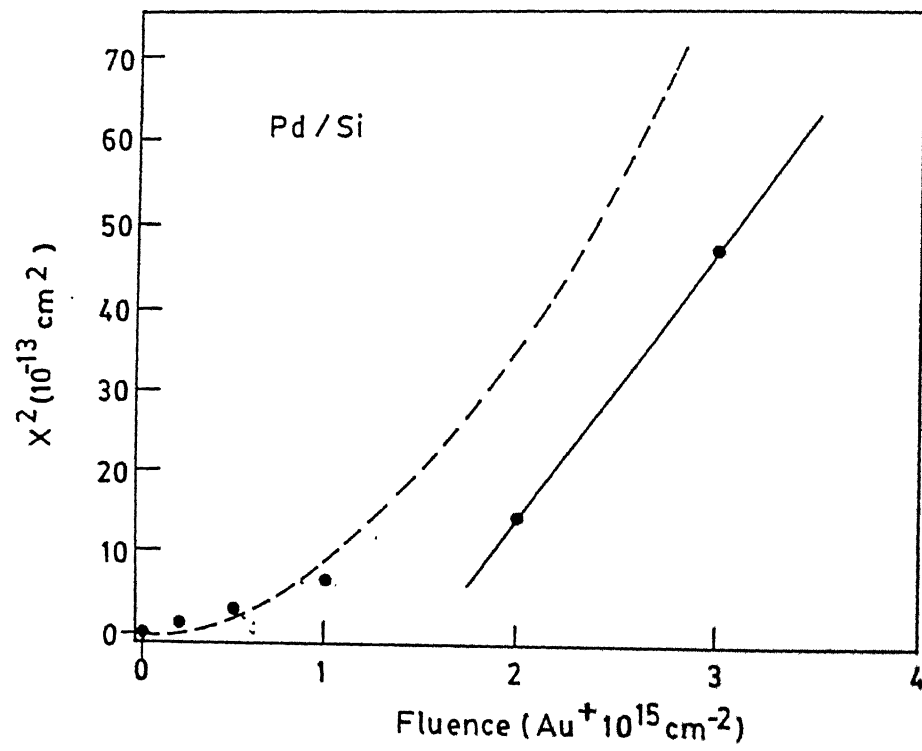


Figure 2.5: Squared thickness of the mixed layer vs the fluence in Pd/Si irradiated at 80 K with 730 keV Au ions (after ref 31).

factor which accounts for the formation of a compound in the mixed layer. Desimoni and Traverse have incorporated this enhancement of D in the ballistic and global spike models of mixing mentioned above and reported the following relations for calculating mixing rates.

$$\frac{X^2}{\Phi} \Big|_{bal}^{com} = 2 \left[\frac{C_A}{a/(a+b)} + \frac{C_B}{b/(a+b)} \right] \frac{1}{3} \frac{\Gamma}{C^2} F_D \xi^{1/2} \frac{\lambda^2}{E_d} \quad (2.16)$$

and

$$\frac{X^2}{\Phi} \Big|_{glo}^{com} = \frac{D_{TS}}{\Phi'} = 2 \left[\frac{C_A}{a/(a+b)} + \frac{C_B}{b/(a+b)} \right] K_1 \frac{F_D^2}{C^{8/3} \Delta H_{coh}^2} \quad (2.17)$$

Here C is the atomic density of compound A_aB_b formed across the interface. C_A and C_B are the atomic densities of layers A and B respectively.

2.6 Formalism based on kinetics

Miotello and Kelly[26] have followed a different approach to address the compound formation in ion-beam mixing. The phase formation has been viewed as a kinetic rather than thermodynamic phenomenon. They have developed a general formalism to describe ion-beam mixing by introducing a chemically guided defect motion to obtain the diffusion flux J_i of a component i in a bilayer system. The diffusion equation

$$\frac{d\alpha_i}{dt} = D_i^t \frac{\partial^2 \alpha_i}{\partial x^2} \quad (2.18)$$

where $D_i^t = (D_i^b + D_i^{ng} + D_i^g)$, can be numerically solved for a bilayer geometry. Here $(D_i^b, D_i^{ng}$ and $D_i^g)$ are diffusivities due to ballistic mixing, chemical non-guided and guided mixing. In order to reproduce the different region of the experimentally obtained concentration profile the diffusivity values are adjusted according to the binary phase diagram. The diffusivity must be high when ΔH_m is strongly negative, and low when strongly positive. Also the value of D_i^t changes significantly at the boundaries of the phase. The growth of a phase is given by,

$$\alpha^* \frac{dX}{dt} = D_i^{t(-)} \frac{\partial \alpha_i}{\partial x} |_X - D_i^{t(+)} \frac{\partial \alpha_i}{\partial x} |_X \quad (2.19)$$

where α^* is the concentrate of the phase and $D_i^{t(-)}$ and $D_i^{t(+)}$ indicate diffusivity at the two sides of the growing layer. This is a generalization of the model presented by Desimoni and Traverse which is described above.

Chapter 3

Experimental

3.1 Introduction

The ion-beam mixing studies presented in this thesis typically involved the following experimental steps : (i) preparation of clean substrates (ii) vacuum deposition of elements to be mixed in the desired geometry (iii) irradiation of the sample kept at a fixed temperature, in the range of 77K to 500 K, with MeV Ar or Kr ions, (iv) compositional analysis by Rutherford backscattering spectrometry (RBS) (v) surface morphological study by scanning electron microscopy (SEM) and (vi) identification of phases by X-ray diffraction technique. In some cases, to study the thermal stability of the mixed region, the ion-beam mixed samples were annealed in vacuum and steps (iv) to (vi) were carried out. On the other hand, for comparing the effects of ion-beam mixing with thermally induced reactions, step (iii) was replaced by thermal annealing of the sample in vacuum.

The 2 MeV Van de Graaff accelerator laboratory at IIT, Kanpur was used for RBS measurements using He^+ ion as well as ion-beam mixing experiments using Ar and Kr ions. For performing mixing experiments in the temperature range of 77-500 K,

an ion irradiation set-up was designed and fabricated along with other ancillaries. A water cooled multi-hearth electron gun evaporation system was used for the deposition of thin films and the heat treatments were performed in high vacuum.

This chapter describes the experimental steps mentioned above along with the description of the accelerator facility.

3.2 Sample preparation

3.2.1 Sample cleaning

The detailed studies of phase formation and the mechanism of ion-beam mixing requires mainly three kinds of sample configurations (described in Chapter 1) namely multilayer (Fig 1.1a), bilayer (Fig 1.1c) and marker (Fig 1.1e) thin films of two elements on inert substrate. In the case of ion-beam mixing studies of metal/Ge systems, experiments were performed using all the three geometries. Experiments involving movements of atomic species may be significantly influenced in the presence of foreign atoms and hence it is essential to prepare as clean a sample as possible[77]. Substrates of size 10 mm x 10 mm were cut from a high purity quartz plate of thickness 0.5 mm. Standard cleaning procedures were employed using high purity acetone, trichloroethylene and ethyl alcohol to de-grease the surface of the substrate using ultrasonic cleaner.

3.2.2 Thin film deposition

Thin films were deposited using a multi-hearth electron gun evaporation unit shown in Fig 3.1. It is equipped with a liquid nitrogen trap to have a clean vacuum in the deposition chamber. The working principle of the electron-beam apparatus involves the generation of thermionic electrons from a tungsten filament and the bending of these electrons towards the water cooled graphite crucible which contains the material to be deposited. The thermionic electrons are generated by passing current through

a tungsten filament held at a negative potential of few kV. The emitted electrons are bent and focused with the help of a permanent magnet on to the material. The unit is also equipped with a quartz crystal controlled digital thickness monitor for *in situ* measurement of film thickness. The monitor was independently calibrated by measuring the thickness of several films by RBS measurements[7]. The major advantages of this deposition system are the accurate control of rate of deposition which is an important parameter associated with film adherence[77] and the ability to perform deposition of a number of layers of different materials without breaking the vacuum which provides a clean interface between two layers.

High purity (99.99%) material of Ge, Cu, Ni and Co were used for preparing multilayer or bilayer films of M/Ge configuration on quartz substrate where M is one of the above mentioned metallic species. A thin Au layer was used as a marker at the interface of M/Ge bilayer samples. In order to make the Kr and Ar ions pass completely through bilayer or multilayer structures, the total thickness of the film was always kept in the range of 100-300 nm. which is much lower than the range of 1 MeV Ar or Kr ions in these materials[78]. A number of samples were prepared for the present studies of ion-beam mixing of metal/Ge as described in Table 3.1.

3.3 Van de Graaff accelerator facility

The Van de Graaff accelerator is the most widely used among the commonly available electrostatic accelerators. A schematic diagram of the accelerator system is shown in Fig 3.2, and photographs of the same are presented in Fig 3.3a and Fig 3.3b. The accelerator (Model AN-2000), High Voltage Engineering Corporation make USA, and is a precision 2-MeV high intensity source of positive ions. The accelerator produces a beam of ions which is homogeneous, stable and controllable over a wide range of energies. It is provided with three gas bottles and presently they are filled with three different gases namely He, Ar and Kr. An r.f. ion source is used to produce positive ions.



Figure 3.1: Photograph of multi-hearth electron-beam gun evaporation system.

Table 3.1: Description of the samples used for present studies

Geometry geometry	Sample	Thickness of individual layers	No. of metal & Ge layers each
Metal/Ge multilayer films deposited on SiO_2	$SiO_2/Cu/Ge$	each Ge layer thickness 11-15 nm each Cu layer thickness 23-27 nm	5
	$SiO_2/Ni/Ge$	each Ge layer thickness 16-26 nm each Ni layer thickness 32-40 nm	5
	$SiO_2/Co/Ge$	each Ge layer thickness 22-27 nm each Co layer thickness 22-25 nm	4
Metal/Ge bilayer film with a Au layer as a marker	$SiO_2/Cu/Au/Ge$	Ge layer thickness 80-85 nm Cu layer thickness 23-27 nm	2 (Thickness of Au marker < 1 nm)
	$SiO_2/Ni/Au/Ge$	Ge layer thickness 120-130 nm Ni layer thickness 65-70 nm	
	$SiO_2/Co/Au/Ge$	Ge layer thickness 95-100 nm Co layer thickness 55-60 nm	
Metal/Ge bilayer films diposited on SiO_2	$SiO_2/Cu/Ge$	Ge layer thickness 110-170 nm Cu layer thickness 50-100 nm	2
	$SiO_2/Ni/Ge$	Ge layer thickness 95-105 nm Ni layer thickness 55-70 nm	
	$SiO_2/Co/Ge$	Ge layer thickness 110-120 nm Co layer thickness 50-60 nm	

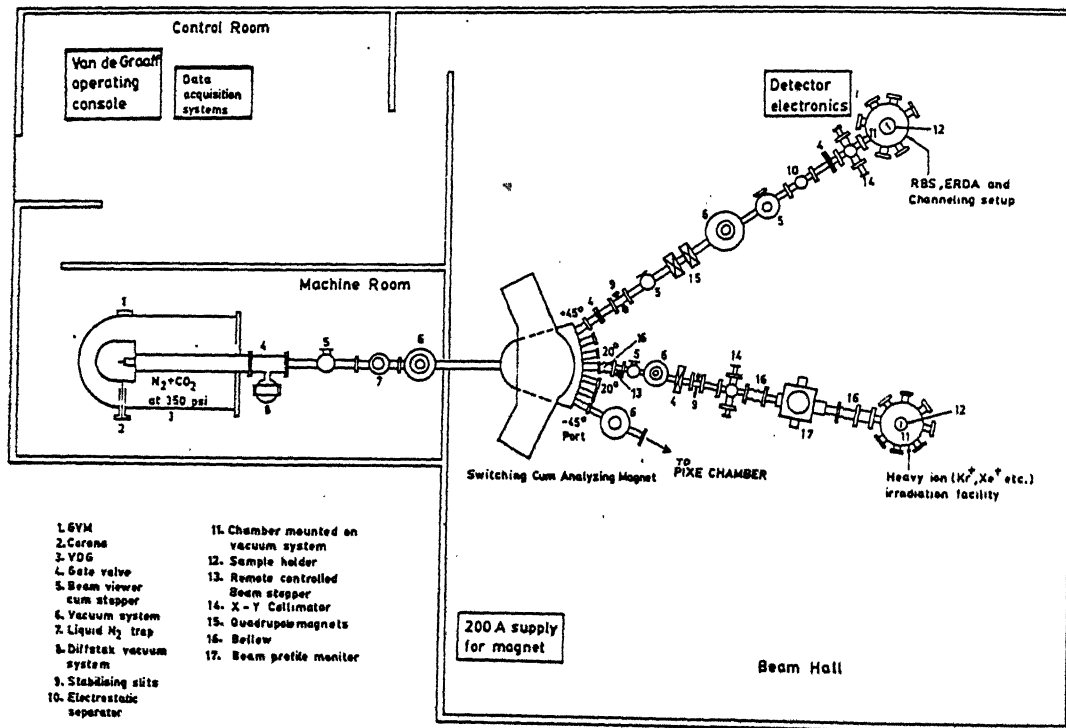
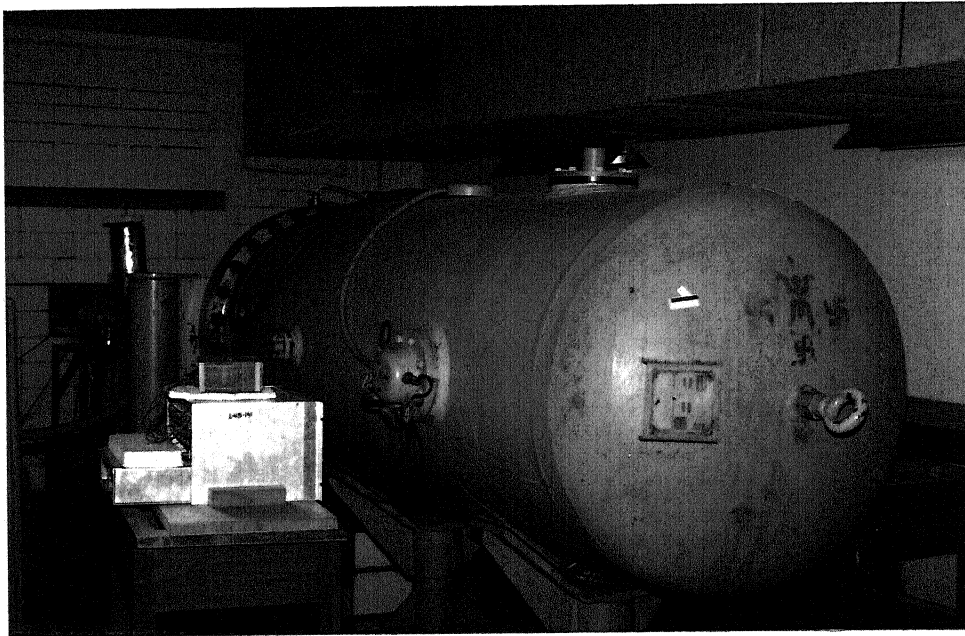


Figure 3.2: Lay out of the Van de Graaff accelerator facility at I.I.T Kanpur.

(a)



(b)



Figure 3.3: Photographs of (a) Van de graaff accelerator and (b) the analyzing magnet.

The mass and energy analysis of the accelerated ion-beam is done by an analyzing cum switching magnet which is a 16 KGauss electro- magnet having a d.c. regulated (0-30 V) power supply which has a capability of supplying current up to 250 A[79]. During operation the magnet is cooled to 10 °C, by circulating de-mineralized water through the coils. However to operate the magnet at currents of less than 140 A, air cooling is done by passing air instead of water through the tubular aluminum coils. The stainless steel switching chamber has five ports at angles 0° , ±20° and ±45° . The energy and mass analyzed beam can be directed to the experimental chamber through any one of the five ports.

3.4 Ion irradiation

The detailed physical processes occurring during irradiation have already been discussed in the previous chapter. Here we describe the beam line containing important ancillaries such as sample manipulator, beam stopper, beam defining slits, beam profile monitor etc. which were developed and installed (for this work) for carrying out uniform irradiations on a sample in the temperature range of 77- 500 K.

3.4.1 Heavy ion-beam line

The accelerated ions obtained from the accelerator reach the experimental chamber through a clean and highly evacuated beam line as shown in Fig 3.4. The beam line has a specially adapted liquid nitrogen trap placed in between the accelerator and the analyzing magnet to achieve clean vacuum in that region. The ion- beam after leaving the analyzing magnet passes through beam stopper followed by a beam profile monitor. The beam stopper is made up of a 'flat plunger' which moves in or out of a coil when it is energized or de-energized. The plunger can thus stop the beam from falling on the sample when a predetermined dose on the sample is achieved. The beam profile monitor (Model 522, DANFYSIK) is used to monitor the position, shape and uniformity of

the beam. The beam then passes through a specially designed beam defining X-Y slit arrangement mounted on a double cross chamber (as shown in Fig 3.4a). This arrangement is used for the purpose of selecting a uniform portion of the beam of required size onto the target placed in the irradiation chamber.

3.4.2 Heavy ion irradiation chamber

The chamber used for irradiation is shown in Fig 3.5. The chamber is mounted on a turbo molecular pump (BALZERS) to obtain a hydrocarbon free clean vacuum. In the center of the chamber there is a movable sample holder as shown in Fig 3.5 on which a number of samples can be mounted and by moving the holder vertically by a predetermined distance, the required sample can be introduced in the path of the beam. The holder is electrically isolated from the rest of the chamber. A current integrator (ORTEC model 439) which measures the total charge accumulated during irradiation is connected to the sample holder.

The sample holder is surrounded by a cylinder made up of aluminum sheet which has an opening for the passage of the heavy ion-beam. This cylinder is maintained at a potential of nearly -260 volt relative to the grounded chamber. The arrangement, called as secondary electron suppressor, inhibits the interference of secondary electrons emitted from the sample surface during ion irradiation.

The arrangement described above is suitable for room temperature irradiations. For performing irradiations at high and low temperatures, specially designed sample holders were fabricated. Figure 3.6a shows the photograph of the sample holder along with the heating arrangements for the high temperature irradiations. This sample holder is made up of high purity Copper for good thermal conduction. The heat loss by conduction via the sample holder is prevented by connecting the sample holder with a ceramic insulator. Temperature measurements are done by placing a chromel-alumel thermocouple junction as close to the sample as possible. With the help of a temperature controller the temperature of the sample can be maintained to within ± 3

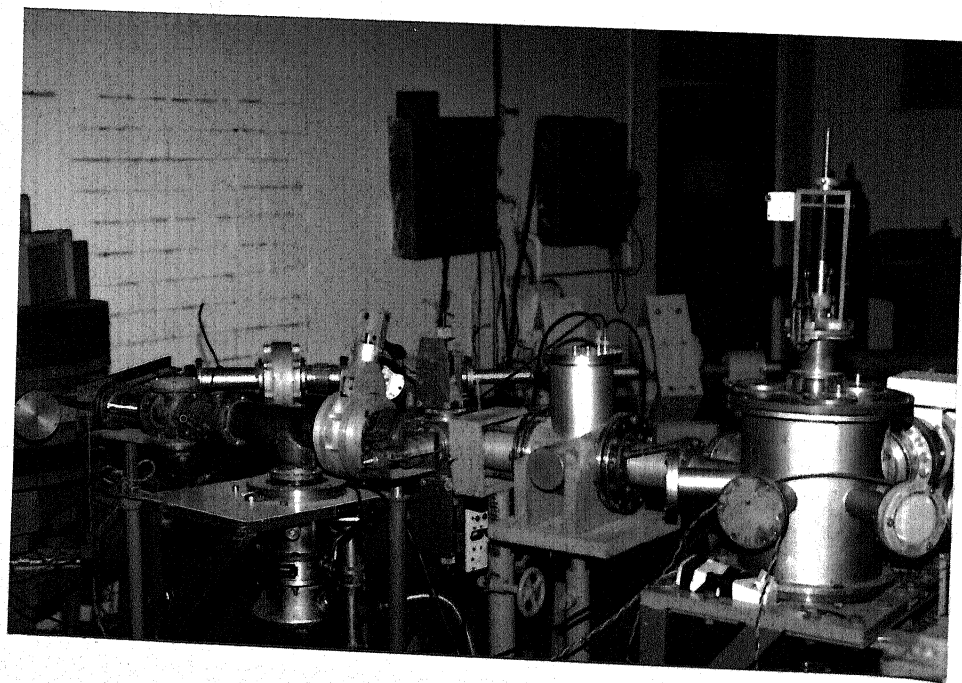


Figure 3.4: Photographs of beam line and irradiation chamber.

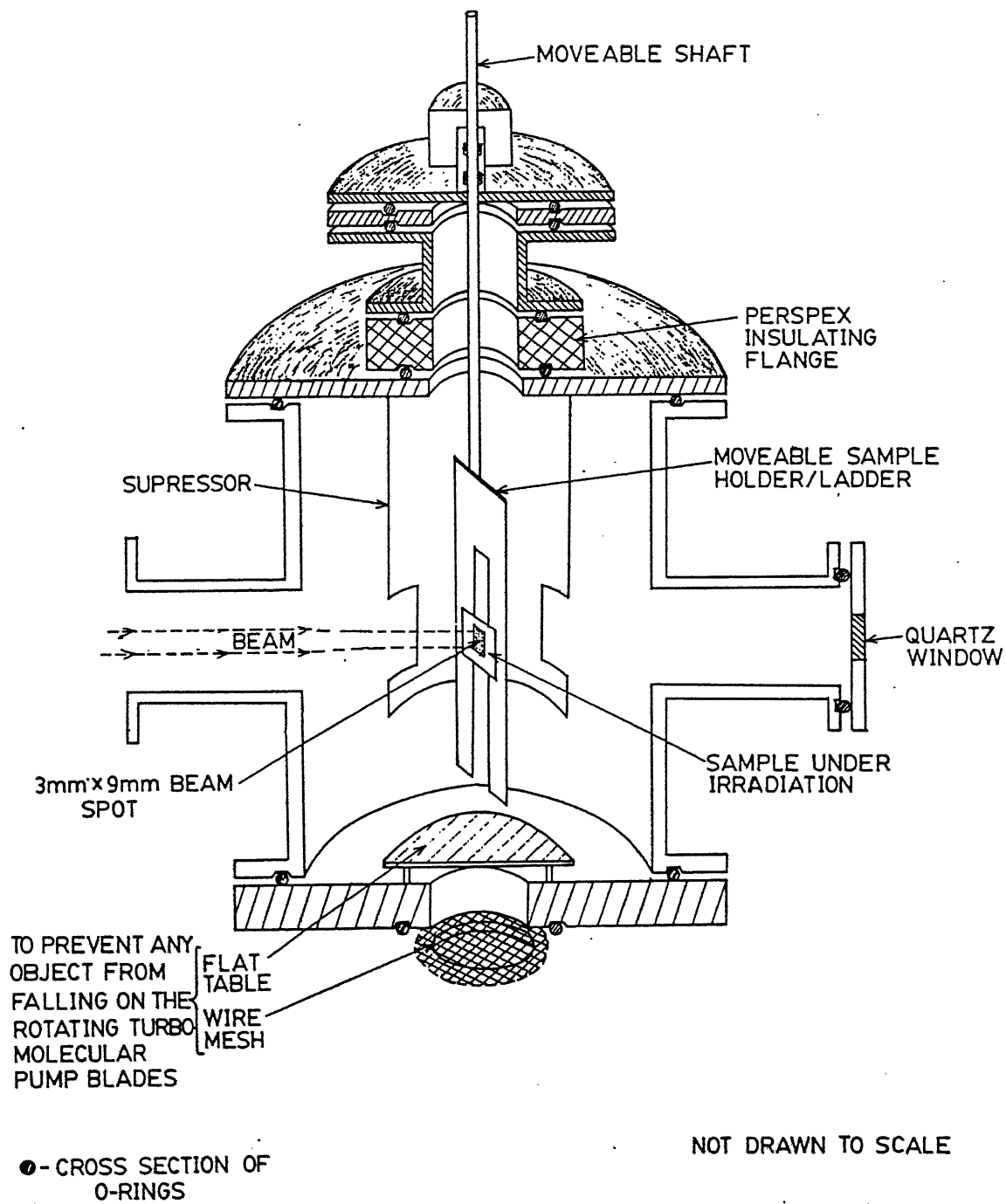


Figure 3.5: Block diagram of irradiation chamber and other accessories.

K of the set temperature. Mica sheets are used to electrically insulate the thermocouple junction from the sample holder. The heating arrangement designed for heating the sample up to 550 K consists of a tungsten filament lamp (25 V, 10 A) which is placed on the sample holder to give uniform heating. A reflector made of stainless steel sheet is mounted to focus the light on to the sample. The reflector also serves the purpose of protecting the chamber walls from getting heated.

The sample holder fabricated for low temperature experiments is shown in Fig 3.6b. It is made up of a rectangular copper block and a stainless steel container which store liquid nitrogen. The Copper block on which samples are mounted comes under direct contact with the liquid nitrogen stored in the stainless steel container. A copper-constantan thermocouple is attached with the copper block to measure the temperature. The sample holder can reach a minimum temperature of 90-100 K and stays for about 2 hours once the trap is filled with liquid nitrogen.

3.5 Thermal annealing

A photograph of the annealing set-up is presented in Fig 3.7. The furnace used for annealing has a ceramic tube (i.d.=2 in.), wound with nichrome wire. A uniform temperature (maximum 1300 K) zone of 4 in. length can be obtained in the central portion of the ceramic tube. The furnace temperature is measured by a chromel-alumel thermocouple. The furnace temperature can be controlled to within ± 2 K using a temperature controller (Indotherm Model 400). The furnace is kept on a horizontal movable platform. The sample to be annealed are kept in the quartz tube (i.d.=1 in.) which is continuously evacuated by a diffusion pump equipped with a liquid nitrogen trap. After reaching the desired temperature, furnace is moved such that the quartz tube containing the samples enter in the central portion of the furnace. The temperature of the sample is measured with a chromel-alumel thermocouple kept directly in contact with the samples in the quartz tube. To achieve thermal equilibrium, on an average, it takes three minutes during heating and six to ten minutes while

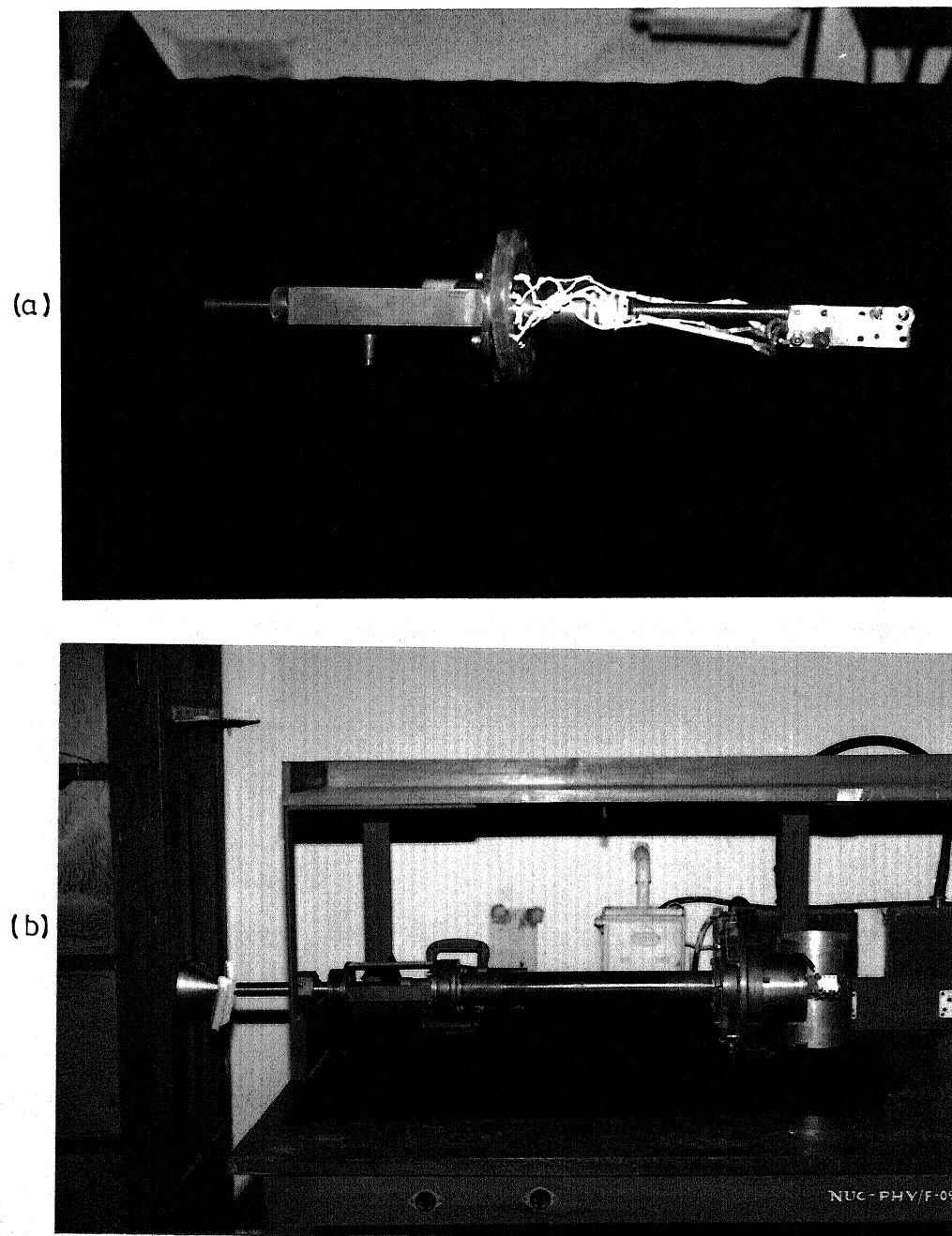


Figure 3.6: Photographs of the sample holders used for (a) high temperature ion-beam mixing (b) low temperature ion-beam mixing.

cooling the sample. The thermal annealing was done at various temperature ranging from 400-700 K for duration of 30-300 minutes.

3.6 Rutherford Backscattering Spectrometry

Rutherford Backscattering Spectrometry (RBS) is a well established method for determining the composition at the interface of two layers, identifying the mass of the impurity and host atoms and thickness of the films etc. RBS is well suited for characterization of thin films or near surface region of bulk samples specially when the sample contain atoms of heavier species. It is based on the framework of the discoveries of Rutherford [1911] and Geiger and Marsden [1913]. In general, H^+ , He^+ etc. ions in the energy range of 0.5 to 3 MeV are used for RBS. The well collimated ion beam of size 1 mm^2 is made to impinge the surface of the sample making a suitable angle of the surface normal as shown in Fig 3.8. The backscattering particle are detected using a semiconductor detector subtending a small solid angle. The signals and energy analyzed using conventional nuclear electronics. The frequency of occurrence of the scattering as a function of energy of the backscattered particles, known as "spectrum" is recorded by performing multi-channel analyzer.

The basic physical phenomena occurring at the target are:

1. The process of energy transfer from the particle to the target nucleus in an elastic collision. This leads to the concept of kinematic factor (K_e) and the capability to determine the mass of the target nucleus.
2. The process of probability of occurrence of a two-body collision, which leads to the concept of scattering cross-section (σ) and the capability to quantitatively analyze the atomic composition of the target.
3. The process of average energy loss of the projectile ions through the target, leading to the concept of stopping cross-section (ϵ) and to the capability of depth perception.

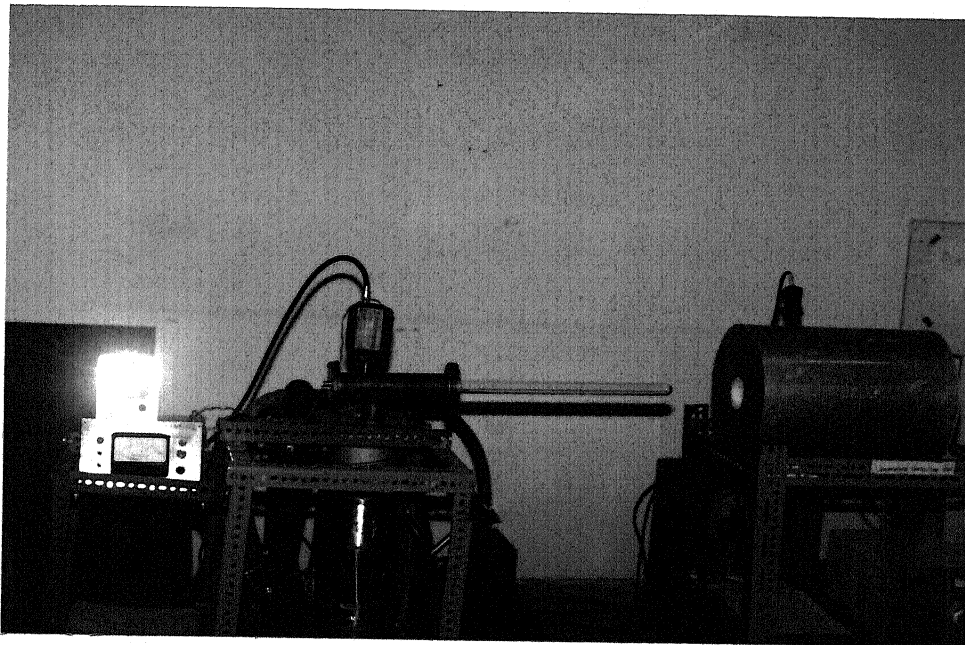


Figure 3.7: Photograph of the annealing set-up.

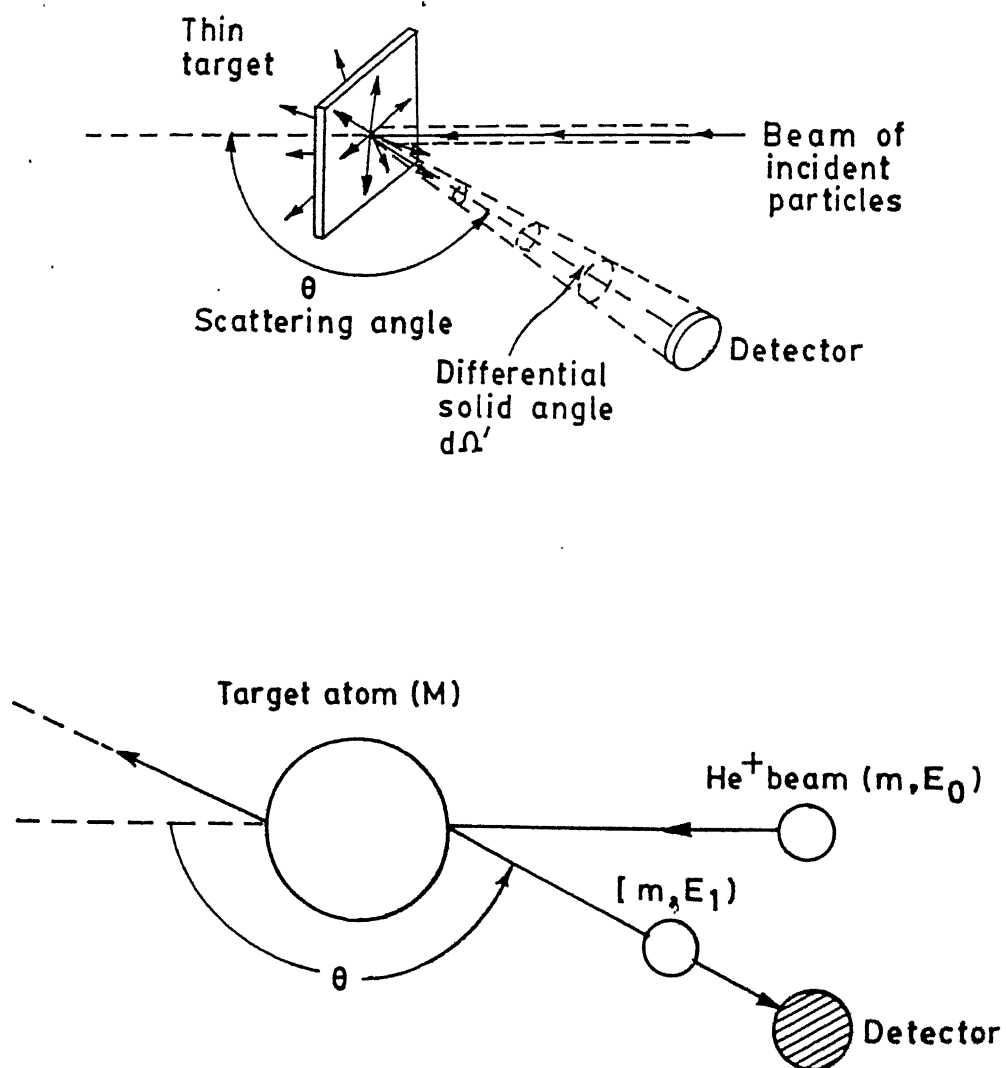


Figure 3.8: Schematic representation of an elastic collision process in laboratory frame. Target of mass M is initially at rest.

4. The process of statistical fluctuations in the energy loss of the projectile in the target. This phenomenon leads to the concept of energy straggling (Ω') and to a limitation in the ultimate mass and depth resolution of backscattering spectrometry.

The RBS measurements are usually carried out in high vacuum (pressure in the range of 10^{-5} to 10^{-6} Torr). An ultra high vacuum may be needed if prolonged measurement on the same spot (to prevent carbon build up on the target due to the breaking up of residual hydrocarbons in the chamber under ion bombardment) is required. The method has been described in detail by Chu et al.[7].

3.7 The RBS setup

The complete backscattering spectrometry set-up used in the present study consists of the following main stages

1. Production of ions and acceleration using the 2-MeV Van de Graaff accelerator
2. Mass and energy analysis of the accelerated ions using an electromagnet.
3. Focusing of the energy analyzed beam and separation the O^{++} ions from the He^+ ions of the same energy
4. Experimental setup for backscattering analysis.

3.7.1 The beam line

The backscattering set up is situated at the $+45^\circ$ beam port. After deflection the beam passes through energy stabilizing slits and quadruple magnets. This focused and collimated ion-beam then passes through an uniform electric field generated by parallel plates (electrostatic beam separator) in order to separate out O^{++} from the

He^+ beam[80] of the same energy. The ion-beam collimating unit placed between the RBS chamber and the ion-beam separator has horizontal and vertical slits, which define the beam size, so that a beam spot of required dimension (a minimum size of 0.5 mm X 0.5 mm) be made incident on the target. Beam viewers and beam stoppers are placed strategically along the beam path to see the ion-beam for diagnosing the beam alignment problem and to block the ion-beam from entering the chamber as and when required.

The backscattering chamber used in this work has six ports as shown in the Fig 3.9 and Fig 3.10. The sample holder is mounted on the top of a flange in such a way that the ion-beam entering from one of the ports is incident perpendicularly on the sample surface. The sample holder is a plate of dimensions 130 mm X 25 mm X 2.5 mm. Five to six samples can be mounted on it at a time. It can be moved in the vertical direction, such that the region of interest of a sample can be brought in front of the incident beam for analysis, with an accuracy of ± 0.5 mm. In this way several measurements on different regions of the same sample and measurements on various samples are possible without breaking vacuum. An aluminum grid is placed around the holder (inside the chamber) and a negative voltage of -260 V is applied to it, to suppress the secondary electrons emitted from the samples due to the primary ion-beam. Beam currents of 5-10 nA were utilized for the present analysis. Currents more than 10 nA increased the detector dead-time and pulse pile-up effect, and hence it was maintained at all times below 10 nA. The target or beam current was measured and integrated to obtain the total fluence or charge (which relates the number of incident He^+ ions incident on the target) using a current integrator (Ortec, Model-401). Backscattering spectra, in the present study, were obtained for a total charge collection of 2-10 μC for each target.

The partially passivated ion implanted or silicon surface barrier detector is placed at a scattering angle (θ) of 150° to the incident beam, and is fixed at one of the ports of the chamber. The experimental geometry for RBS is shown in the inset of Fig 3.9. The detector surface area is decreased by about 80% by inserting a plate having a small

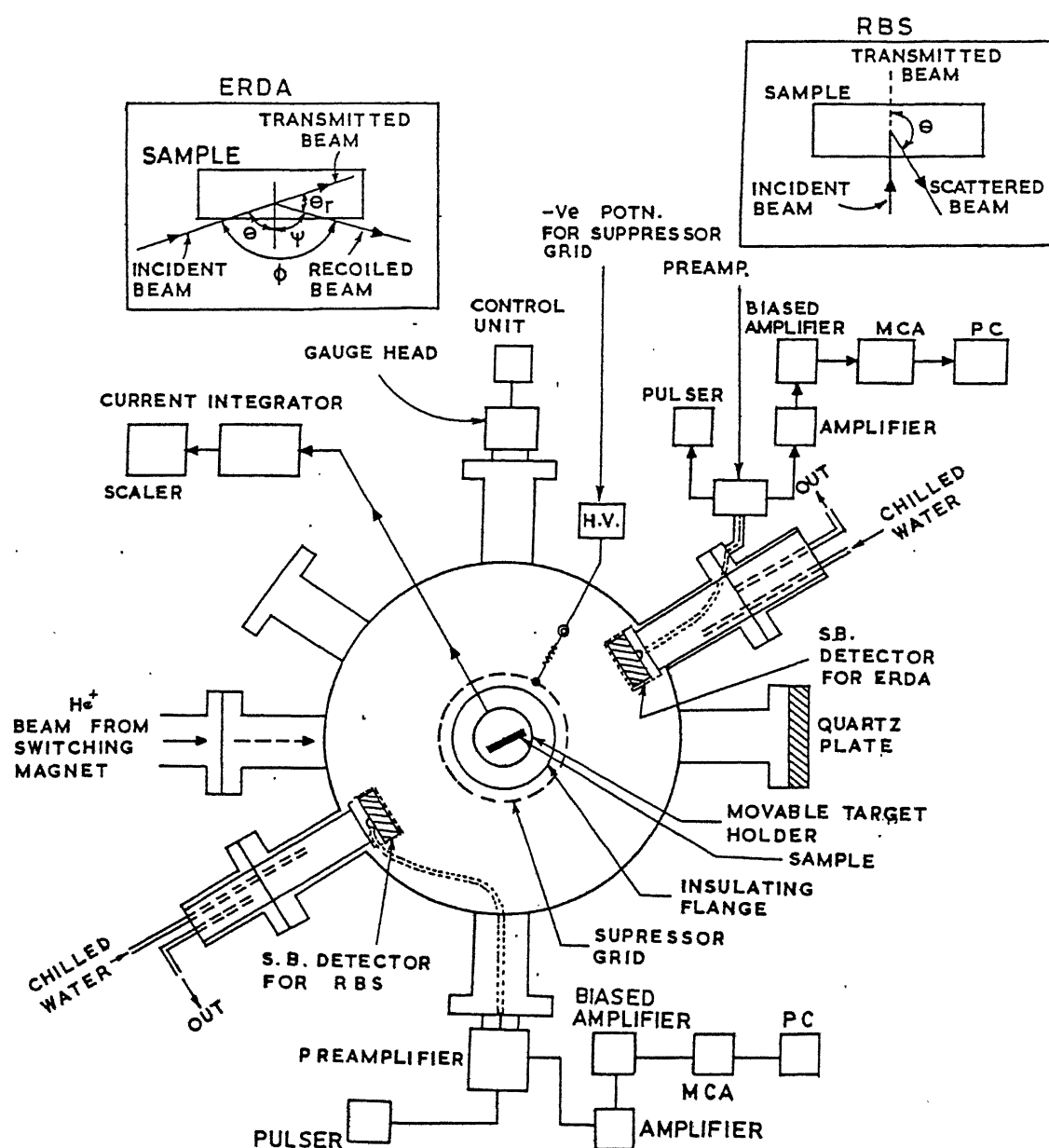


Figure 3.9: Block diagram of RBS chamber along with target, detector and other accessories.

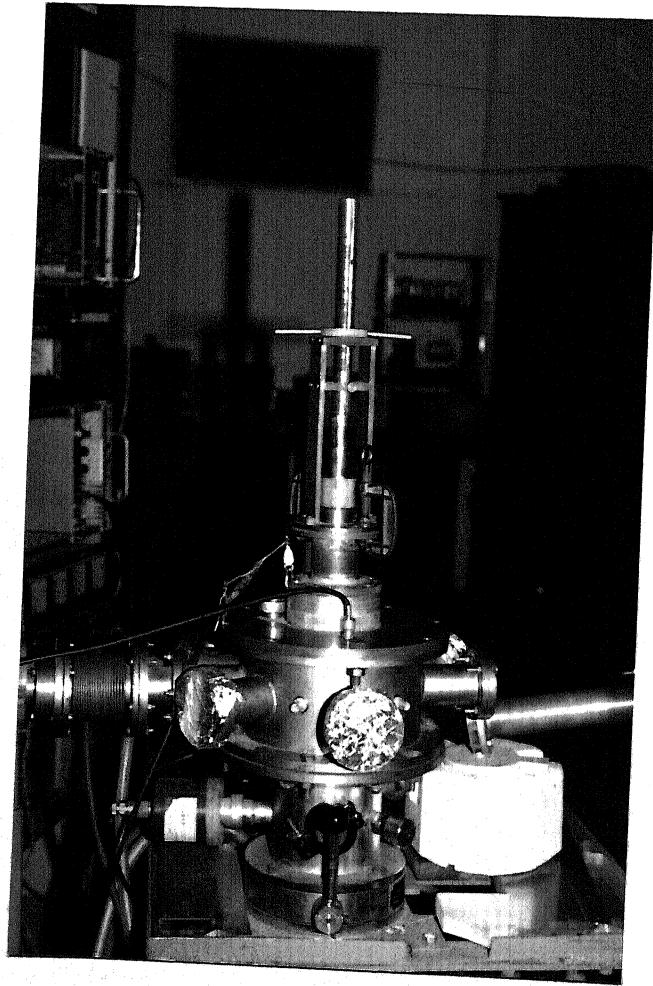


Figure 3.10: Photograph of RBS chamber along with target and other accessories.

aperture in front of the detector. The detector to sample distance was approximately 10 cm. The solid angle of 2.57 mSr subtended by the detector was measured by taking several RBS spectra of standard samples.

3.7.2 Pulse shaping electronics and multichannel analyzer

The signals from the detector are initially amplified by a charge sensitive preamplifier [Ortec Model-142]. The bias circuit (in the preamplifier), for the detector is dc-coupled as it has very high resolution. The preamplifier is specially designed to accept the detector signal and amplify it with some shaping so as to preserve the maximum signal-to-noise ratio. In backscattering, the useful information in the preamplifier output signal is the amplitude of each pulse. The subsequent main amplifier [Ortec Model-572] amplifying this signal creates a suitable pulse shape (rise time of 1 μ C) thus optimizing resolution and count rate capability. The pulse shaping is done to avoid pulse pile-up and to enhance signal-to-noise ratio. Each individual detector signal has to be terminated in a shorter time compared to the time interval between two pulses. Otherwise pulses will overlap causing pulse pile-up, which leads to erroneous amplitude measurements.

The CR-RC (differentiating-integrating) pulse shaping circuit of the amplifier operates with time constants much shorter than the decay of the preamplifier signal and much longer than its rise time. This effectively removes the slow component of the preamplifier signal preventing the pile-up error. It also removes the low and high frequency signals and noise components which significantly enhance the signal-to-noise ratio. Hence the amplifier finally produces individual pulses whose amplitudes convey the quantity of interest, i.e., the energy of the detected particles. The signal output from the main amplifier is then fed to a biased amplifier [Ortec Model-444]. With the help of this, the amplifier signals are compressed or stretched and the edges are cut off as desired, for more efficient analysis in the multichannel analyzer (MCA). The signals from the biased amplifier are then collected, either in the MCA [Model-ND65, Nuclear

Data Inc.], or a PC-based MCA. The MCA has two distinct data analysis modes: the pulse height analysis (PHA) mode and the multichannel scaling (MCS) mode. The PHA mode is exclusively used for RBS measurements.

3.7.3 Calibration of the MCA

The MCA is calibrated by determining the calibration factor (δE) from the channel position of the elements from the experimental RBS spectrum. For this reason, backscattering spectra of pure elements (or calibration samples) were taken in every run. In each run three to four metal/Ge samples were analyzed along with the calibration samples. A set of calibration spectra are depicted in Fig 3.11, for thin film of pure Au on pure Al substrate and pure Al. In these spectra, the surface position of the Au is at channel number 494 and that of Al is at channel number 278. The backscattered energy $E_{1,e}$ for each of these elements (e) is calculated from the following equation

$$E_{1,e} = K_{1,e} \times E_o \quad (3.1)$$

where $K_{1,e}$ is the kinematic factor of the element e and E_o is the incident energy of the He^+ beam (in this case 1.34 MeV). The calibration factor can be calculated from the following equation

$$\delta E = \frac{(K_{1,e} K_{2,e}) E_o}{(ch_1 ch_2)} \text{ keV/ch.} \quad (3.2)$$

considering two calibration samples (e_1 and e_2) at a time. If we calculate for the present case the calibration factor is obtained as 2.212 keV/ch.

3.7.4 Backscattering spectra analysis

A backscattering spectrum obtained from the same run as that of calibration spectrum shown in Fig 3.11, for thin bilayer film of Cu and Ge on quartz substrate is shown in Fig 3.12. This spectrum was obtained using He ions of 1.34 MeV at a scattering angle (θ) of 150° , the detector solid angle (Ω) equal to 2.57 mSr and for a beam dose of 5

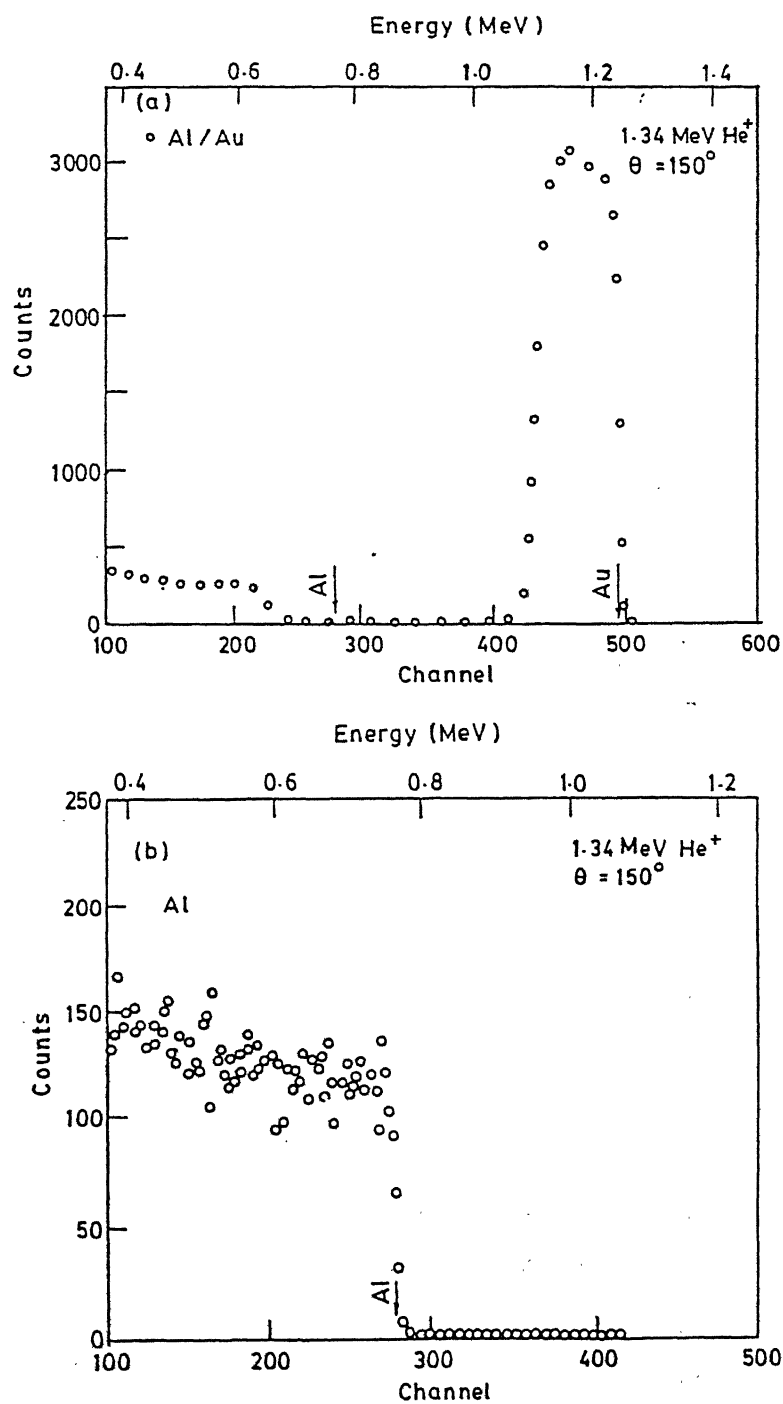


Figure 3.11: Experimental RBS spectra of calibration sample (a) thin film of Au on Al substrate (b) Pure Al.

μC . This RBS parameter description is also given below the figure. It is useful to plot the backscattering yield by normalizing it with respect to some of the above mentioned parameters, by using the following equation

$$\text{Normalized yield} = \frac{\text{raw counts} \times \text{corr}}{Q \times d\Omega \times \delta E} \quad (3.3)$$

where 'raw counts' are the actual counts recorded; 'corr' is the correction factor to compensate for inaccuracies during charge integration; Q is the beam dose in μC ; $d\Omega$ is the solid angle in milli-steradian (mSr); and δE is the calibration factor of the MCA in keV/channel . The normalized yields are utilized for comparison of experimental spectra for which beam energy and scattering geometry are same but the dose solid angle and calibration values are different. The information about the thickness of the film and the depth distribution of the diffusing element (in the case where diffusion has taken place) can be obtained from such a spectrum. The backscattering spectra in the present study have been analyzed by RUMP simulation package[81] as described in the following.

Recently, RBS simulation programs using computers have been developed at several places. One such simulation program developed at the Cornell University by Doolittle[81], has been used in the present studies for the analysis of the backscattering spectra. The simulation program makes use of almost the same equations which have been described By Chu et al.[7]. In simulation, a theoretical sample structure consisting of several layers of varying thickness is first prepared. The experimental parameters are also fed into the program. A backscattering spectrum is then constructed using this sample structure and the experimental parameters. This theoretical profile is then compared with the experimentally obtained RBS spectrum. This procedure is utilized in an iterative manner to arrive at a best set of parameters (sample structure) using which the given sample spectrum compares quite well with the experimental spectrum. We will now illustrate the analysis of the RBS spectrum of Fig 3.12, by the simulation program. The theoretical layer structure of the sample is given below the Fig 3.12. The first two layers comprising of Cu and Ge having thicknesses 660 nm and 1240 nm respectively and are further divided into sublayers of 2 nm each. The third layer is the

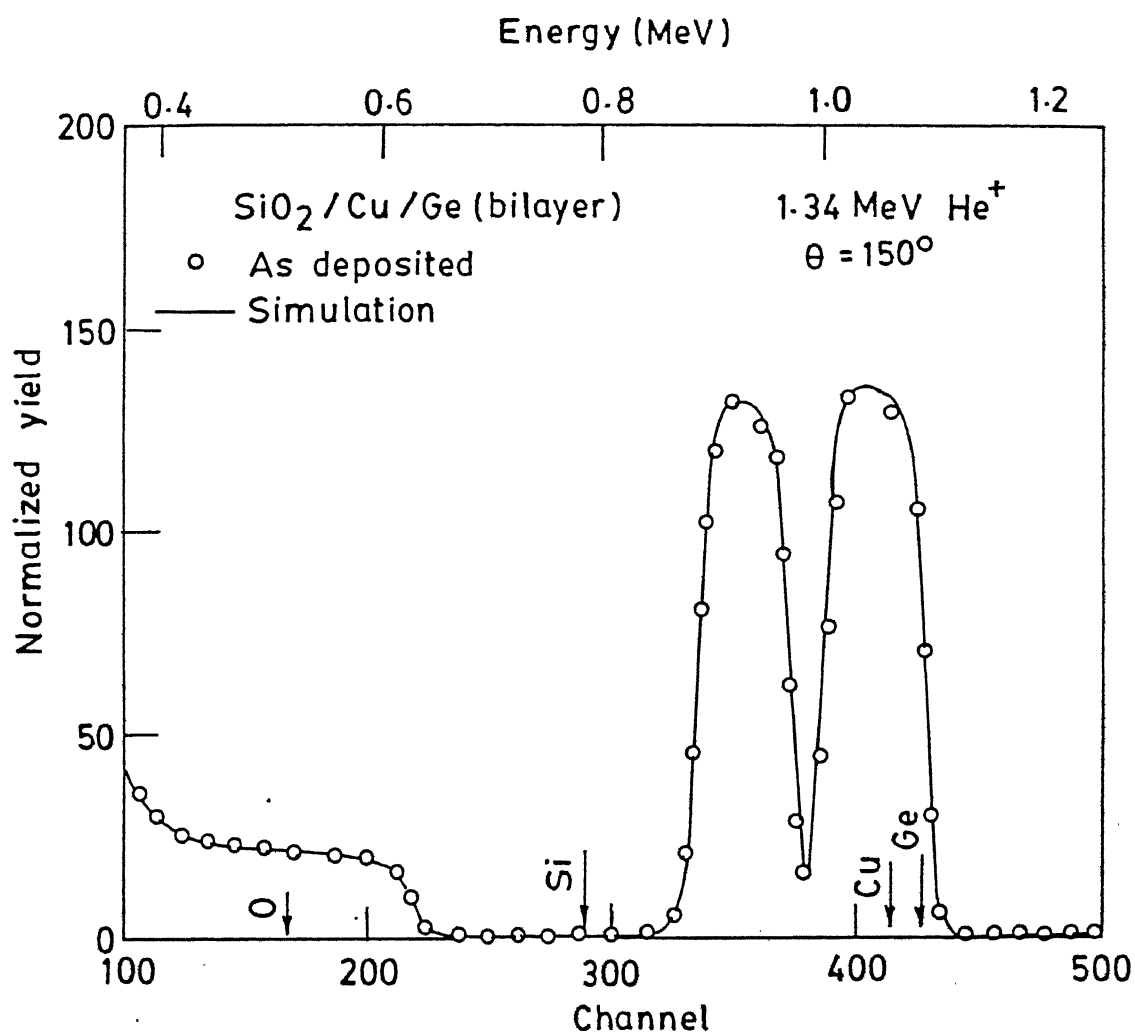


Figure 3.12: Experimental RBS spectra along with simulation of Cu/Ge bilayer sample deposited on SiO_2 .

substrate(quartz SiO_2) of thickness 1000 nm, which is further divided into sublayers of 50 nm each. The program requires this information along with the experimental parameters (as defined below Fig 3.12). The simulated profile is then compared (as shown in Fig 3.12), with the experimental profile. One of the important features of this simulation programme is that it is an extremely powerful tool for understanding complex spectra involving overlap of numerous elements. It also takes into account the detector resolution as well as energy straggling of the ions. Thus the thick target yield for quartz has been simulated very correctly giving the analysis of the substrate as well. Such analysis of the multi-elemental target as mentioned above is not possible by hand calculations.

3.8 X-ray measurements

The nature of reacted layers after ion-beam mixing and thermal annealing were also investigated by the X-ray diffraction (XRD) method to supplement the findings and analysis of Rutherford backscattering spectroscopy. The XRD measurements were done using a X-ray powder diffractometer [Model ISO-Debyeflex-1001], generating $Cu - K_\alpha$ radiation along with a graphite monochromator attached to the goniometer. Some of the samples were measured by glancing angle x-ray diffraction technique in Seeman-Bohlin geometry using CuK_α radiation from University of Poona. A diffractometer in general consists of the following main units: (i) power supply; (ii) X-ray generator; (iii) goniometer, with monochromator, scintillation counter or proportional counter and preamplifier; (iv) amplifier unit; (v) rate meter, and (vi) X-Y chart recorder. The spectral lines obtained in the X-ray spectra of the samples in units of 2θ is converted into d-values using the Bragg's rule i.e.,

$$2d\sin = n\lambda \quad (3.4)$$

On comparing these values with standard tables of d-values of various alloys and phases available in literature, the presence of the suggested or probable phases were confirmed

in the samples.

3.9 Scanning electron microscopy

In Scanning Electron Microscopy (SEM) the area to be examined is irradiated with a focused electron beam, which is swept in a raster across the surface of the specimen. The types of signals which are produced when the focused beam impinges on a specimen surface include secondary electrons, backscattered electrons, characteristic X-rays, Auger electrons and photons of various energies. They are obtained from specific emission volumes within the sample and are used to measure many characteristics of the sample including surface topography.

The Auto Scan model JEOL-JSM 840A having 10 nm resolution, about 10X to 300000X magnification and operating voltage up to 40 KV was used in secondary electron mode.

3.10 Four probe resistivity measurement technique

The four point probe comprises four equally spaced metal probes which are pressed onto the surface under measurement. The probes are usually set in-line or at the corner of a square. For the present work a square probe was used. The sheet resistivity of an infinite thin layer in which the current flow is parallel to the surface is [82]

$$\rho_S^{12,34} = (\pi / \log_e^2) \times (V_{3,4} / I_{1,2}) \quad (3.5)$$

The resistivity measured by a square probe with the current I flowing between two probes and the voltage V measured across the other two probes is given by

$$\begin{aligned} \rho &= \rho_S^{12,34} X \\ &= 4.532 (V_{3,4} / I_{1,2}) \cdot (X) \end{aligned} \quad (3.6)$$

where X is the thickness of implanted layer. This formula can be used for calculating the resistivity of the modified layers because it meets the requirement of $X/S < 0.4$ for probe spacing $S = 1.5$ mm.

Chapter 4

Ion induced phase formation

4.1 Introduction

This chapter¹ describes the mixing effects, leading to the formation of compounds, induced by Ar and Kr ions of megaelectron volt energy in multilayer structures of Cu/Ge, Ni/Ge and Co/Ge samples, held at various ambient temperatures in the range of 100 - 450 K. For comparing the ion induced mixing effects with those induced by thermal reactions. results of thermal annealing experiments performed at temperatures in the range of 400 - 700 K are also presented. We then examine the nature (amorphous/crystalline) of the ion induced phases in these systems in the light of the existing rules, which are based on composition and crystal structure of the reacting elements, ratio of the atomic radii, equilibrium phase diagram and heats of formation of the possible stable/metastable phases.

¹Part of this work is published in Appl. Phys. Lett. 67 (1995) 1700.

4.2 Experimental

In preparing multilayer samples (as shown in Fig.1.1a), alternate layers of metal M ($M = \text{Cu, Ni, Co}$) and Ge were deposited sequentially on clean quartz substrates without breaking vacuum by e-beam evaporation system equipped with a digital thickness monitor as described on chapter 3. The deposition of the films was controlled to 0.4 - 0.6 nm/s to obtain uniform film of good quality. In all the cases four to five layers of metal M and Ge each were deposited. The thicknesses of the layers were adjusted such that the average film compositions range from about 60 at% to 80 at% of metal M. The average individual layer thickness of metal M was not more than 40 nm with total thickness of 90-300 nm.

The bilayer structures of metal M and Ge were prepared on quartz substrates with Ge as the top layer. The thickness of individual layer was chosen such that it yielded the composition of about $M_{50}Ge_{50}$. The total thickness of bilayer films was in the range of 100-200 nm.

Ion-beam mixing was done at various substrate temperatures ranging from 100 to 450 K using 1 MeV Kr and Ar ions. The temperature of the substrate was controlled to ± 3 K during irradiation. Irradiations were performed for several doses in the range of $(2 - 20) \times 10^{15} \text{ ions/cm}^2$. The ion flux was kept low ($\leq 1 \times 10^{13} \text{ ions/cm}^2\text{s}^{-1}$) to prevent the sample temperature rise during irradiation. A uniform portion of the beam was selected by a X-Y beam defining slit arrangement such that the samples got irradiated uniformly over an area of 5 mm x 5 mm. The beam position and uniformity of the beam were monitored *in situ* by a beam profile monitor. The projected range of the incident ions were calculated using TRIM program[78]. For the incident ion energy of 1 MeV, most of the implanted ions pass through the multilayer and bilayer structures. The thermal annealing in vacuum was done for different annealing durations at various temperatures in the range of 400 - 700 K. The amount of mixing, the composition of the ion mixed or thermally reacted layers were determined by theoretically simulating (RUMP code)[81] the experimental Rutherford backscattering (RBS) spectra obtained using 1.1-1.5 MeV He^+ beam. The RBS spectra of the treated samples did not show

any visible oxygen or carbon concentrations. The phases were identified by standard X-ray diffraction (XRD) using a $Cu - K\alpha$ source. A few X-ray measurements were also performed in the Seeman-Bohlin geometry using the glancing angle XRD facility at University of Poona[83]. The surface topography of the samples was studied under scanning electron microscope before and after mixing. The resistivity measurements were done by Van der Pouw four-probe method[82].

4.3 Results

The results of ion-beam induced effects at different temperatures and those induced by thermal annealing alone are presented separately for each metal-Ge system in multilayer and bilayer configurations in the following subsections.

4.3.1 Cu/Ge system

Ion-beam induced effects

A typical experimental RBS spectrum (open circles) of as-deposited Cu/Ge multilayer sample is shown in Fig 4.1. The spectrum of the as-deposited sample shows a multi-peak structure. The peaks corresponding to individual Cu and Ge layers are not completely resolved because of the small mass difference between Cu and Ge atoms. The surface positions of elements are shown by arrows. The RBS spectra of all as-deposited samples were simulated using layer structures of the kind $SiO_2/Cu/Ge/Cu/\dots Cu/Ge$ as the input to the simulation programme RUMP till best visual fits were obtained in each case. One such theoretical simulated spectrum is shown in Fig 4.1 by continuous line and the detailed simulated structure is given in Table 4.1. This sample consists of five pairs of copper and germanium layers with an overall thickness of Cu and Ge equal to 130 nm and 75 nm respectively.

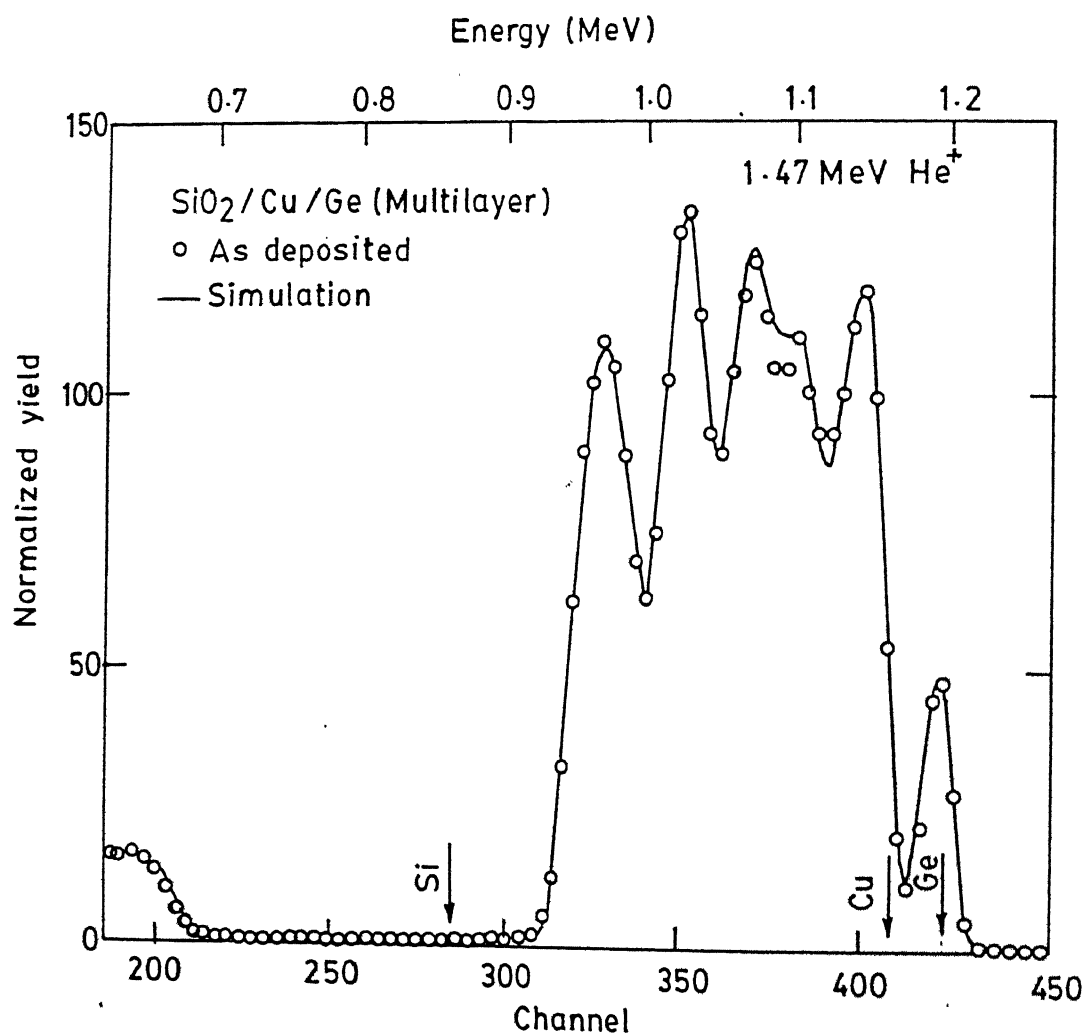


Figure 4.1: The as-deposited RBS spectrum of Cu/Ge multilayer sample deposited on SiO_2 . The simulated spectrum was obtained using the sample structure given in Table 4.1.

Table 4.1: Description of the layer structure used for the simulation of RBS spectrum of as-deposited Cu/Ge multilayer sample shown in Fig 4.1.

Sample description	Layer structure used for simulation			
	Layer no.	Thickness (nm)	Composition	
Cu/Ge Multilayer films deposited on SiO_2	1	15	Ge	1
	2	23	Cu	1
	3	15	Ge	1
	4	23	Cu	1
	5	11	Ge	1
	6	23	Cu	1
	7	17	Ge	1
	8	25	Cu	1
	9	17	Ge	1
	10	37	Cu	1
	11	1500	Si	1 O 2

The effect of ion-beam mixing at room temperature (RT), induced by Kr ions at doses of $4 \times 10^{15} \text{ Kr}^+/\text{cm}^2$ and $1 \times 10^{16} \text{ Kr}^+/\text{cm}^2$, is depicted in Fig 4.2. It shows that the mixing progresses as a function of increasing dose and is indicated by a systematic decrease in the peak to trough ratios of the RBS signal. In order to determine the composition of the mixed layer of irradiated samples, the experimental RBS spectra were simulated using structures of the kind $\text{SiO}_2/\text{Cu}/\text{Cu}_x\text{Ge}_{1-x}/\text{Ge}/\text{Cu}_x \cdots / \text{Cu}_x\text{Ge}_{1-x}/\text{Ge}$ as input to the simulation program. A typical result of such type of analysis for an irradiated sample is presented in Fig 4.3 for Cu/Ge multilayer sample irradiated at a dose of $8 \times 10^{15} \text{ Kr}^+/\text{cm}^2$. The detailed layer structure used for simulation is given in Table 4.2 and the simulated spectrum is shown in Fig 4.3 by a continuous line. The complete structure can be visualized as a layer of thickness 200 nm consisting of a film of composition $\text{Cu}_{75}\text{Ge}_{25}$ and unreacted Ge and Cu atoms. The simulated spectrum shown by continuous line in the Fig 4.3 is the the best visual fit that could be obtained. Mostly, the simulation analysis gives unique result and is significant as no two entirely different types of compositions and structures can give rise to same backscattering spectrum.

The effect of Kr irradiation at a higher dose of $1 \times 10^{16} \text{ Kr}^+/\text{cm}^2$ is depicted by the experimental and theoretical RBS spectra in Fig 4.4. Here the wiggles in the experimental backscattering spectrum in comparison to Fig 4.3 have almost disappeared indicating the formation of a homogeneous mixture of Cu and Ge. The peak at the surface position of Ge indicates that the surface Ge layer has not reacted completely. First, the simulation was tried using a single layer of thickness 190 nm having a composition of $\text{Cu}_{75}\text{Ge}_{25}$ along with an overlayer of 12 nm of Ge. This simulated profile is shown by the continuous line in Fig 4.4. The fit appears reasonable except for the small hump around channel number 400. For fitting this hump a thin layer of composition $\text{Cu}_{83}\text{Ge}_{17}$ was introduced in the layer structure as shown in Table 4.3 which gives a better simulation fit shown by dashed line.

It may be noted that the compositions of $\text{Cu}_{75}\text{Ge}_{25}$ and $\text{Cu}_{83}\text{Ge}_{17}$ used in simulation resemble the Cu_3Ge and Cu_5Ge phases shown in the Cu-Ge equilibrium phase

Figure 4.2: RBS spectra of Cu/Ge multilayer sample in the as-deposited condition and after ion-beam mixing at room temperature for two different doses.

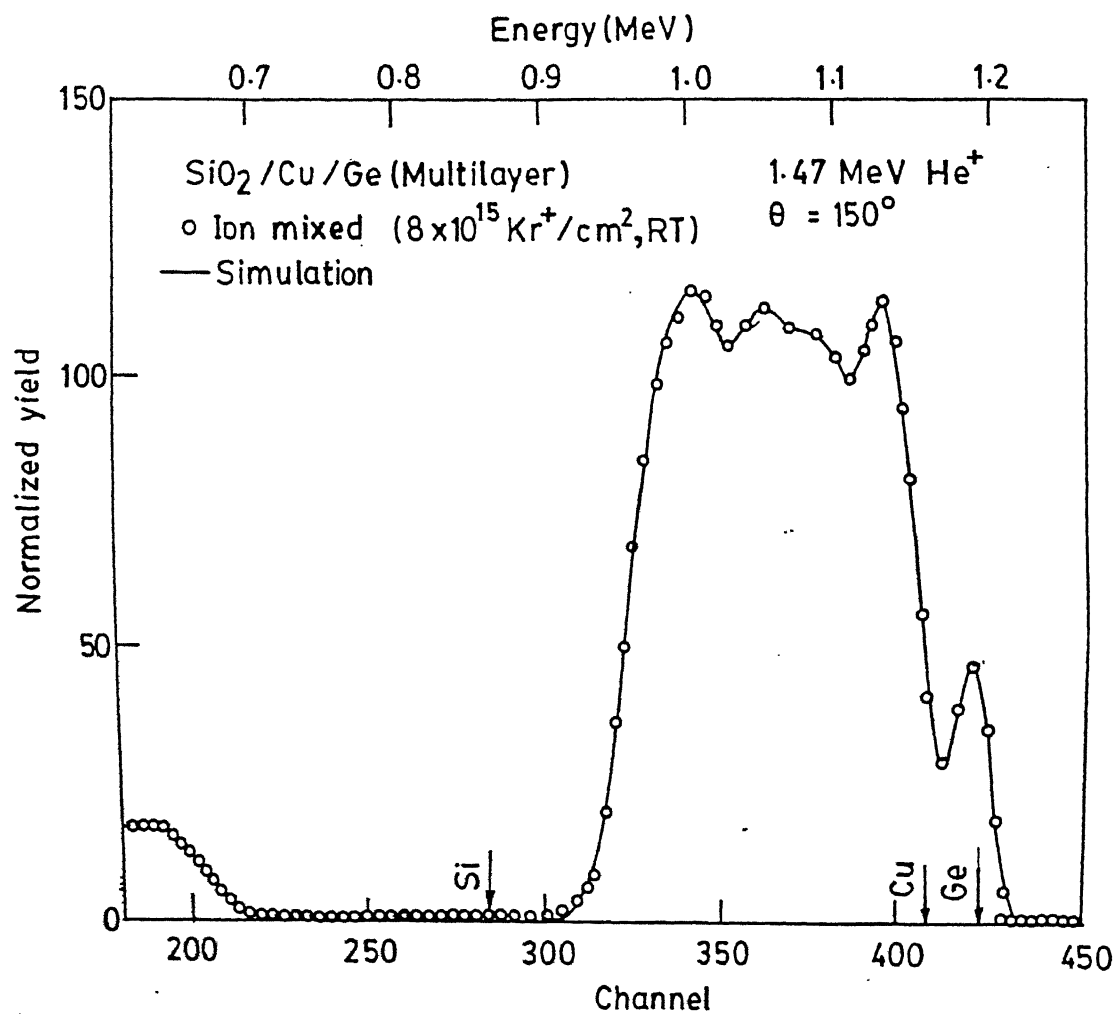


Figure 4.3: RBS spectrum of ion mixed Cu/Ge multilayer sample at RT for a dose of $8 \times 10^{15} \text{ Kr}^+/\text{cm}^2$ along with simulation.

Table 4.2: Description of the layer structure used for the simulation of RBS spectrum of ion mixed Cu/Ge multilayer sample shown in Fig 4.3.

Sample description	Layer structure used for simulation					
	Layer No.	Thickness (nm)	Composition			
Cu/Ge Multilayer films after ion mixing at RT for a dose of $8 \times 10^{15} \text{ Kr/cm}^2$	1	12	Ge	1.00		
	2	16	Ge	0.25	Cu	0.75
	3	7	Cu	1.00		
	4	13	Ge	0.25	Cu	0.75
	5	4	Ge	1.00		
	6	17	Ge	0.25	Cu	0.75
	7	2	Cu	1.00		
	8	20	Ge	0.25	Cu	0.75
	9	1	Ge	1.00		
	10	15	Ge	0.25	Cu	0.75
	11	2	Cu	1.00		
	12	17	Ge	0.25	Cu	0.75
	13	2	Ge	1.00		
	14	25	Ge	0.25	Cu	0.75
	15	3	Cu	1.00		
	16	19	Ge	0.25	Cu	0.75
	17	1	Ge	1.00		
	18	20	Ge	0.25	Cu	0.75
	19	1000	Si	1.00	O	2.00

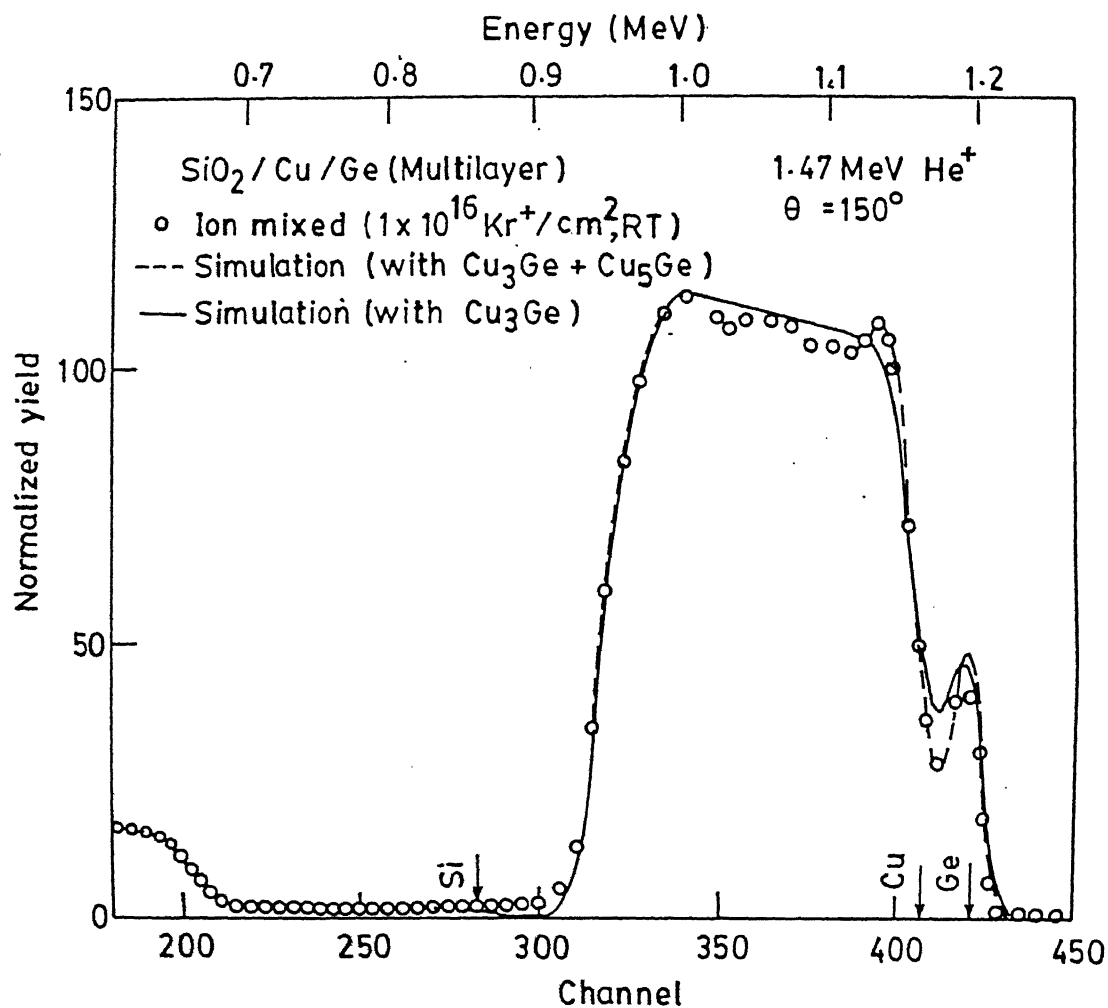


Figure 4.4: RBS spectrum of ion-beam mixed Cu/Ge multilayer sample irradiated at RT for a dose of $1 \times 10^{16} \text{ Kr}^+/\text{cm}^2$ along with the simulated spectrum by considering formation of Cu₃Ge and Cu₅Ge phases. Another simulated spectrum obtained by considering formation of only Cu₃Ge layer is also shown for comparison.

Table 4.3: Description of the layer structure used for the simulation of RBS spectrum of ion mixed Cu/Ge multilayer sample shown in Fig 4.4.

Sample description	Layer structure used for simulation						
	Layer No.	Thickness (nm)	Composition				
Cu/Ge multilayer films after ion mixing at RT for a dose of $1 \times 10^{16} \text{ Kr/cm}^2$	1	12	Ge	1.00			
	2	20	Ge	0.25	Cu	0.75	
	3	170	Ge	0.25	Cu	0.75	
	3	1500	Si	1.00	O	2.00	

diagram (see Fig 4.26) Therefore, one can predict from the RBS analysis that at room temperature, Kr ion irradiation up to dose of $8 \times 10^{15} \text{ Kr}^+/\text{cm}^2$ results in the formation of a Cu_3Ge phase and higher Kr doses result in the formation of both Cu_3Ge and Cu_5Ge phases.

It is interesting to note that the ion-beam mixing carried out with Cu/Ge multilayer samples at a temperature of 100 K (near liquid nitrogen temperature) also shows the formation of a mixed layer having composition of $\text{Cu}_{75}\text{Ge}_{25}$ resembling the Cu_3Ge phase. This is illustrated by the experimental and simulated RBS spectra presented in Fig 4.5. The irradiated area on this sample appears dark to naked eyes unlike the RT irradiations where the irradiated region appears reddish. The dark appearance of the irradiated region is due to the deposition of carbon film caused by the cracking of hydrocarbon on the surface. The carbon film thickness is negligible in case of RT irradiations while ion-beam mixing at 100 K, carbon deposition of as thick as 70 nm has been observed. This leads to the shift in the surface position of Ge as shown in the RBS spectrum of Fig 4.5. As mentioned in Chapter 3, the experimental chamber is equipped with a turbo molecular pump to get high vacuum which is almost free of hydrocarbons. Therefore there is almost negligible deposition of carbon at RT irradiation. It is felt that, when the sample is taken at 100 K, the small quantity of residual hydrocarbons which is still present in the chamber condenses on the sample at such low temperature and gets decomposed under irradiation forming a carbon layer on the sample.

For definite inference about the nature of phases formed, it is necessary to perform experiments which are sensitive to the atomic structure of the mixed region viz. X-ray diffraction (XRD), transmission electron microscopy (TEM) etc., the results of which can in turn be used to improve the quality of the simulation analysis by incorporating them in constructing the theoretical layer structures. The changes in surface topography, viz. formation of globules on the surface etc. can also affect the simulation analysis. The scanning electron microscopy (SEM) pictures taken for the as-deposited Cu/Ge multilayer sample and the one taken after irradiating the sample for a dose of $1 \times 10^{16} \text{ Kr}^+/\text{cm}^2$ are shown in Fig 4.6. Note that the surface topography of the

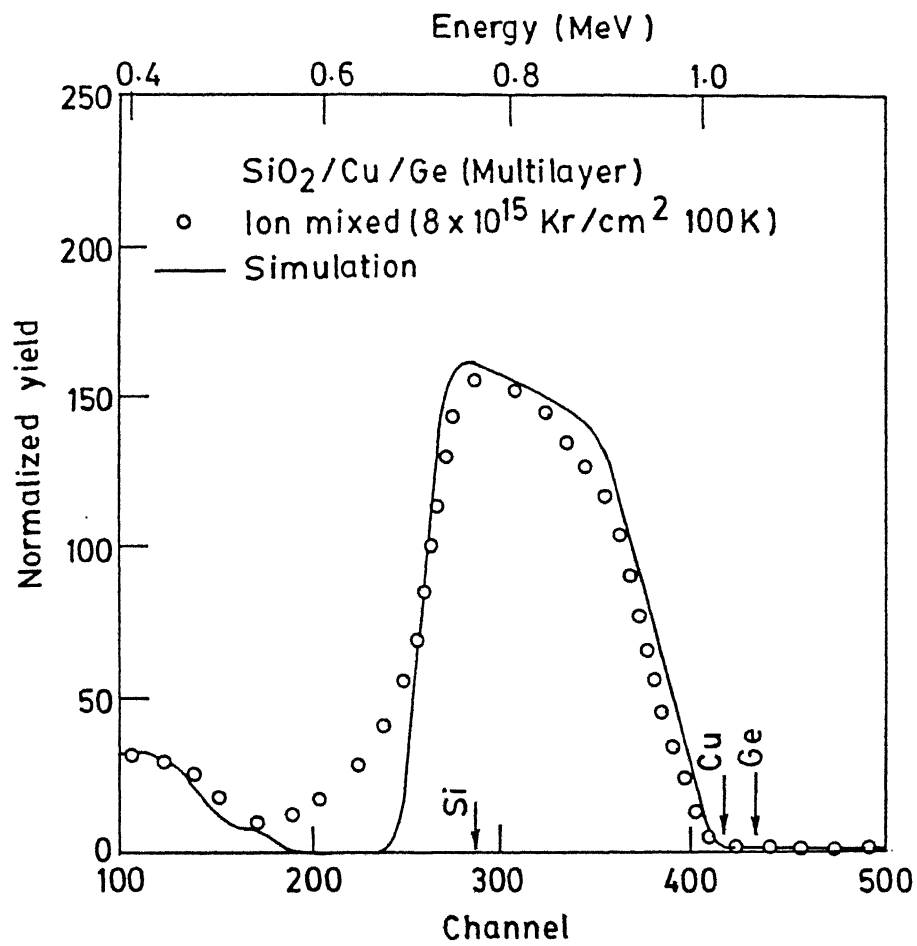


Figure 4.5: RBS spectrum of ion mixed Cu/Ge multilayer sample at 100 K for a dose of 8×10^{15} Kr⁺/cm² along with its simulation.

as-deposited sample is featureless and it remains so after irradiation.

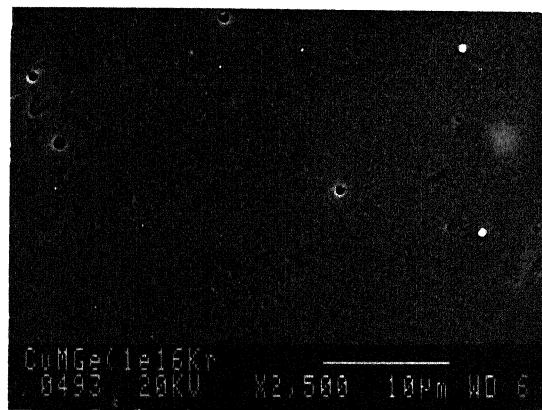
The x-ray diffraction pattern for the as-deposited Cu/Ge multilayer structure sample whose RBS spectrum is shown in Fig 4.1 is depicted in Fig 4.7a. The figure shows diffraction peaks for 2θ values at 43.45° and 48.55° due to copper (111) and (200) planes respectively[84]. The Ge peaks are not seen in the entire diffractogram. This might be due to the amorphous nature of Ge layers which is caused by the fast quenching during the deposition process. The amorphous nature of Ge films prepared by vacuum deposition has been reported by Chopra et al.[85]. After irradiating the sample at RT by Kr ions for a dose of $8 \times 10^{15} \text{ Kr}^+/\text{cm}^2$, the diffraction peaks belonging to copper disappear and the diffraction pattern (Fig 4.7b) exhibits an intense and sharp peak at $2\theta = 42.75^\circ$ along with a weak peak at $2\theta = 45.47^\circ$. These peaks are found to correspond with the (020) and (012) planes of monoclinic $\epsilon_1 - \text{Cu}_3\text{Ge}$ phase having $a=0.2631 \text{ nm}$, $b=0.42 \text{ nm}$, $c=0.4568 \text{ nm}$ and $\beta = 89.68^\circ$ [47]. The observed diffraction peaks and the ones reported in the literature are compared in Table 4.4.

Note that the RBS analysis of this sample presented in Fig 4.3 showed the formation of mixed layer of composition $\text{Cu}_{75}\text{Ge}_{25}$ which is the composition of the compound Cu_3Ge . Thus both RBS and XRD measurements confirm the synthesis of Cu_3Ge phase at RT at this dose as well as for lower doses of $6 \times 10^{15} \text{ Kr}^+/\text{cm}^2$ and $4 \times 10^{15} \text{ Kr}^+/\text{cm}^2$.

The sample irradiated at 100 K up to a dose of $8 \times 10^{15} \text{ Kr}^+/\text{cm}^2$ does not show any clear peak (weak reflection) to confirm the formation of a compound phase. The XRD plot for the sample irradiated at room temperature for a higher dose of $1 \times 10^{16} \text{ Kr}^+/\text{cm}^2$ is shown in Fig 4.7c. Here, in addition to Cu_3Ge diffraction peaks, two distinct peaks at 2θ values of 40.40° and 43.30° also appear which belong to the hexagonal Cu_5Ge phase also termed as ζ phase having $a=0.2582 \text{ nm}$ and $c/a = 0.1632$ nm[47]. The expected and observed diffraction lines are tabulated in Table 4.4. Thus the predictions of RBS analysis, that the Cu_3Ge phase forms up to a dose of $8 \times 10^{15} \text{ Kr}^+/\text{cm}^2$ and both Cu_3Ge and Cu_5Ge phases form at higher doses are confirmed by the X-ray diffraction studies.



(a)



(b)

Figure 4.6: SEM photograph of Cu/Ge multilayer sample a) before and b) after ion-beam mixing at RT for a dose of $8 \times 10^{15} \text{ Kr}^+/\text{cm}^2$.

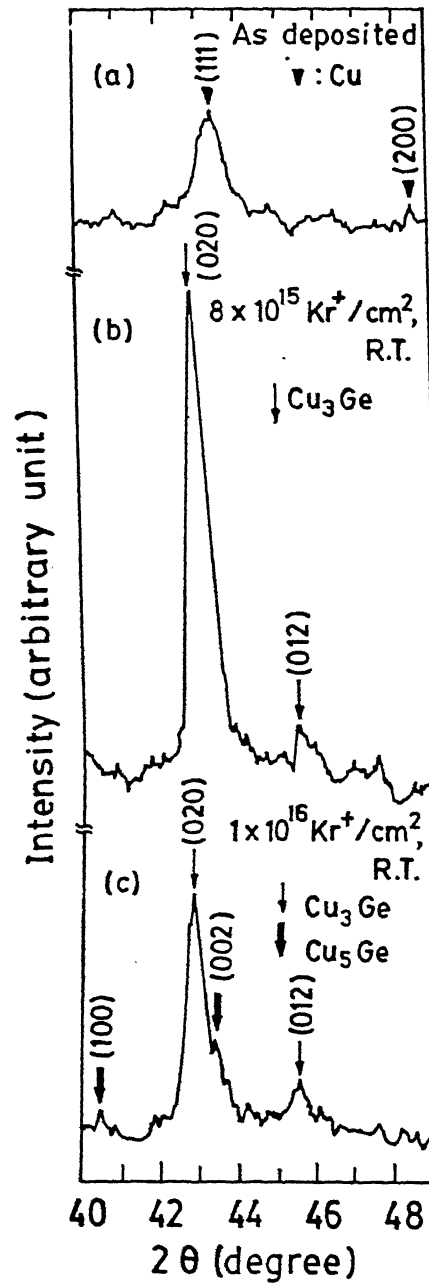


Figure 4.7: X-ray pattern of Cu/Ge multilayer sample taken before and after ion-beam mixing at RT (a) as-deposited (b) $8 \times 10^{15} \text{ Kr}^+/\text{cm}^2$ (c) $1 \times 10^{16} \text{ Kr}^+/\text{cm}^2$.

Table 4.4: Comparison of experimentally obtained d-values of the observed copper germanide phases with the one reported in literature.

Cu/Ge multilayer sample	$d^{Exp.}$ (Å)	$d^{Rep.}$ (Å)	(hkl)	Phase
As-Deposited	2.08	2.08	(111)	Cu
	1.87	1.808	(200)	„
Ion mixed at RT, $8 \times 10^{15} Kr/cm^2$	2.11	2.10	(020)	Cu_3Ge
	1.99	2.01	(020)	„
Ion mixed at RT, $1 \times 10^{16} Kr/cm^2$	2.23	2.24	(100)	Cu_5Ge
	2.11	2.10	(020)	Cu_3Ge
	2.08	2.12	(002)	Cu_5Ge
	1.99	2.01	(020)	Cu_3Ge

The effect of ion-beam mixing in the Cu/Ge multilayers using 1 MeV Ar ions for a dose of $1 \times 10^{16} \text{ Ar}^+/\text{cm}^2$ is compared with the as-deposited sample as shown by the RBS spectra in Fig 4.8. It is clear that complete mixing has not occurred in this case. The simulation analysis shows the formation of a mixed layers of composition $\text{Cu}_{75}\text{Ge}_{25}$ across each Cu/Ge interface indicating synthesis of a Cu_3Ge compound. The XRD analysis also confirms the formation of Cu_3Ge compound. Although the mixing effects observed using Ar ions are qualitatively similar to the those seen in case of Kr irradiation, the rate of mixing is lower as compared to the Kr ion irradiation for the same dose and incident energy. The amount of mixing obtained with Ar ions at a dose of $1 \times 10^{16} \text{ ions}/\text{cm}^2$ is almost same as that obtained with Kr ions at a dose of $4 \times 10^{15} \text{ ions}/\text{cm}^2$. The formation of these copper germanide phases has also been observed in bilayer samples. The detailed comparison of mixing rates and efficiency values obtained using both these ions is dealt with in Chapter 6. The results of RBS and XRD analysis of these ion mixed multilayer samples are summarized in Table 4.5.

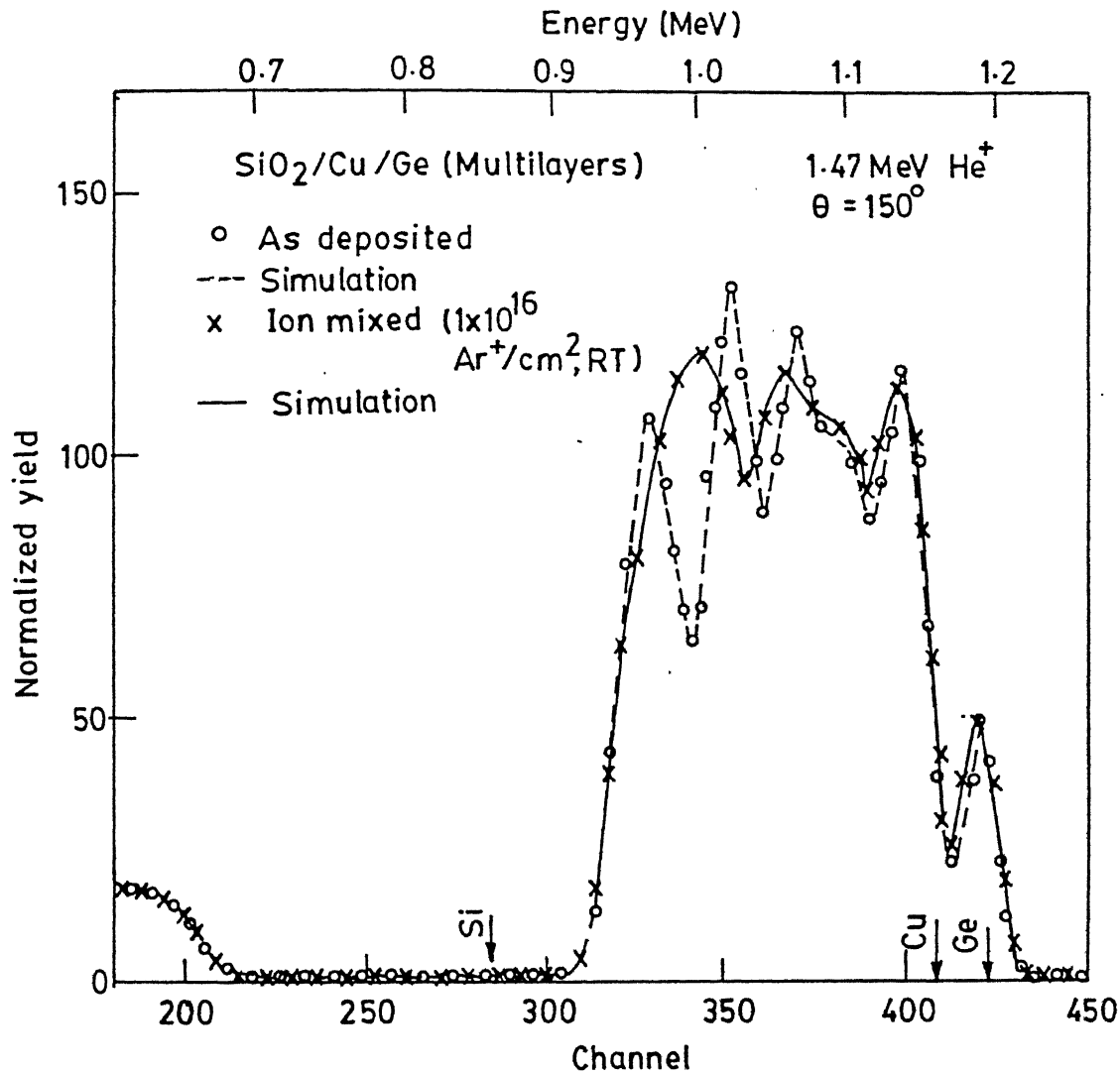


Figure 4.8: RBS spectra of Cu/Ge multilayer sample before and after ion-beam mixing at RT for a dose of $1 \times 10^{16} \text{ Ar}^+/\text{cm}^2$. The simulated curves are shown by dashed and continuous line respectively.

Table 4.5: Summary of ion-beam mixing results in Cu/Ge multilayer systems using Kr and Ar ions at various doses and temperatures.

Sample description	Ion species	Temperature of Irrad. (K)	Dose ions/ cm^2	Phase observed after IM	
				composition	Phase
Cu/Ge multilayer sample deposited on SiO_2	Kr	300	$(2 - 8) \times 10^{15}$	$Cu_{75}Ge_{25}$	Cu_3Ge
			$(1 - 2) \times 10^{16}$	$Cu_{75}Ge_{25}$ + $Cu_{83}Ge_{17}$	Cu_3Ge + Cu_5Ge
	Kr	100	$(4 - 8) \times 10^{15}$	$Cu_{75}Ge_{25}$	*
	Ar	300	$(4 - 10) \times 10^{15}$	$Cu_{75}Ge_{25}$	Cu_3Ge

*Weak X-ray reflection of Cu_3Ge phase

Thermal annealing effects

The thermal annealing experiments have been performed at 630 K for different annealing durations from 30-180 min. After annealing, the peaks and troughs in the as-deposited spectrum start reducing just as in the case of ion mixed samples. Figure 4.9 shows RBS spectra of a multilayer sample before and after annealing for 150 min. which shows the formation of a homogeneous layer of $Cu_{75}Ge_{25}$. The RBS analysis shows that the composition of the reacted region is $Cu_{75}Ge_{25}$ and is similar to the one obtained in ion-beam mixed samples. The simulated structures used for annealed sample is shown in Table 4.6. It is seen from the table that a single layer of thickness 190 nm of composition $Cu_{75}Ge_{25}$ was used for the simulation of the reacted layer. Similar results were also found for other annealed samples. The X-ray studies of this multilayer samples annealed at 630 K (Fig 4.10) show diffraction peaks of Cu_3Ge phase while it does not show any peak corresponding to the copper rich Cu_5Ge phase.

Figure 4.11 shows a RBS spectrum of a bilayer sample before and after annealing at 580 K for 60 min. The simulation analysis gives the stoichiometric composition of $Cu_{75}Ge_{25}$. The X-ray studies also show diffraction peaks from Cu_3Ge crystalline compound. The results of thermal annealing of multilayer and bilayer samples are summarized in Table 4.7.

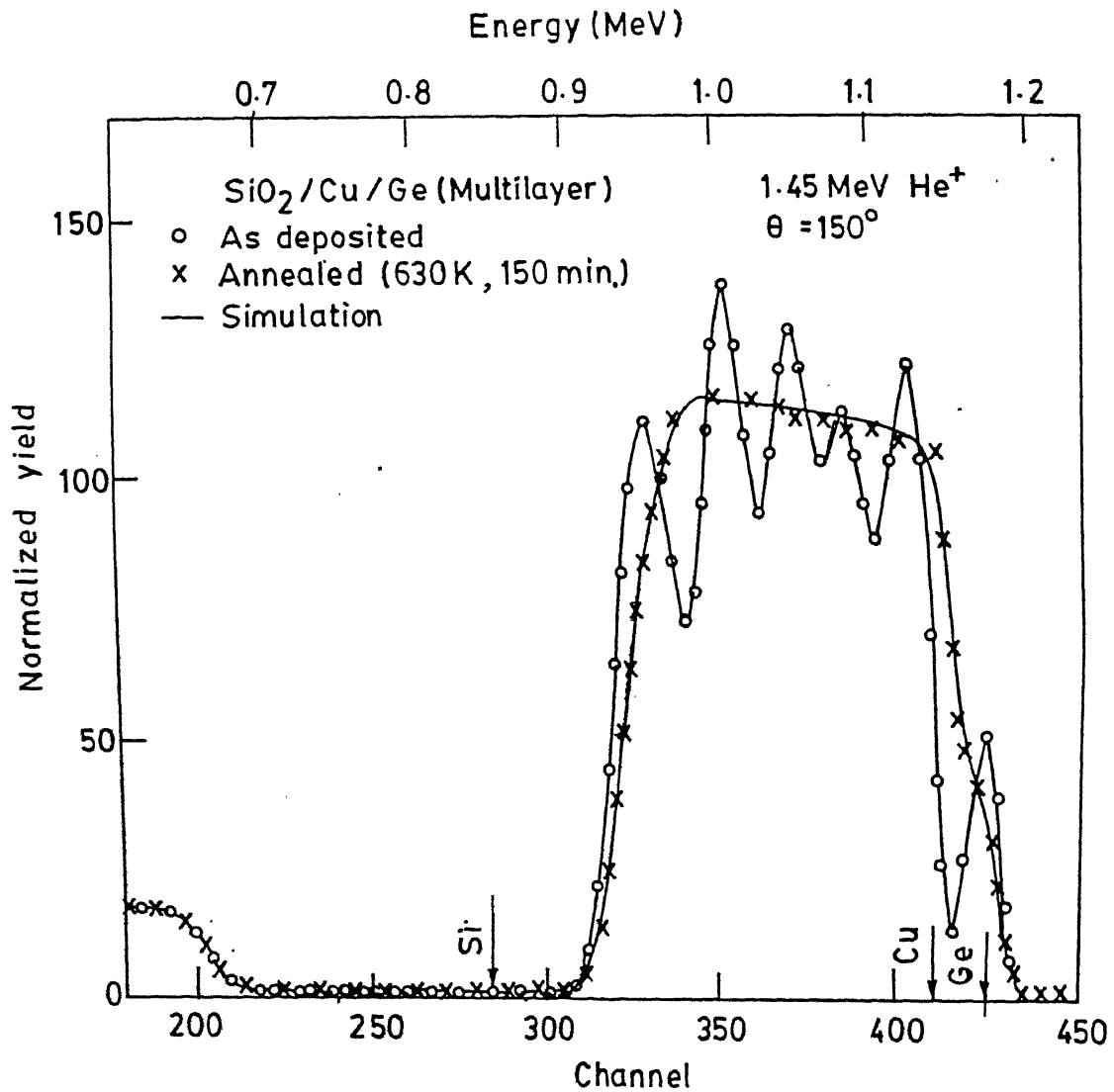


Figure 4.9: RBS spectra of Cu/Ge multilayer sample before and after thermal annealing at 630 K for 150 min along with their simulations. Annealing leads to the formation of homogeneous Cu_3Ge phase.

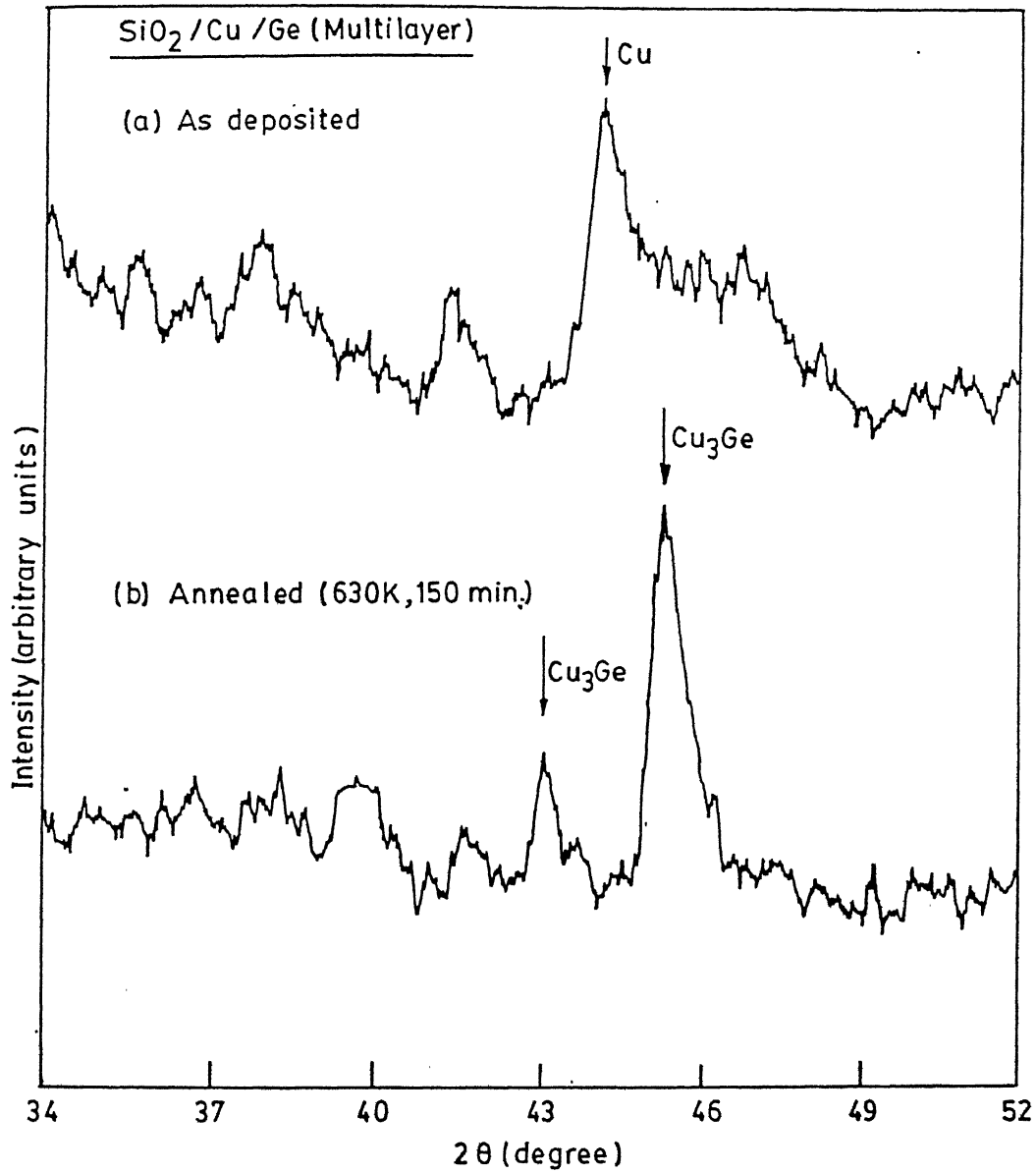


Figure 4.10: X-ray pattern of Cu/Ge multilayer sample before and after thermal annealing (a) as-deposited (b) 630 K for 150 min.

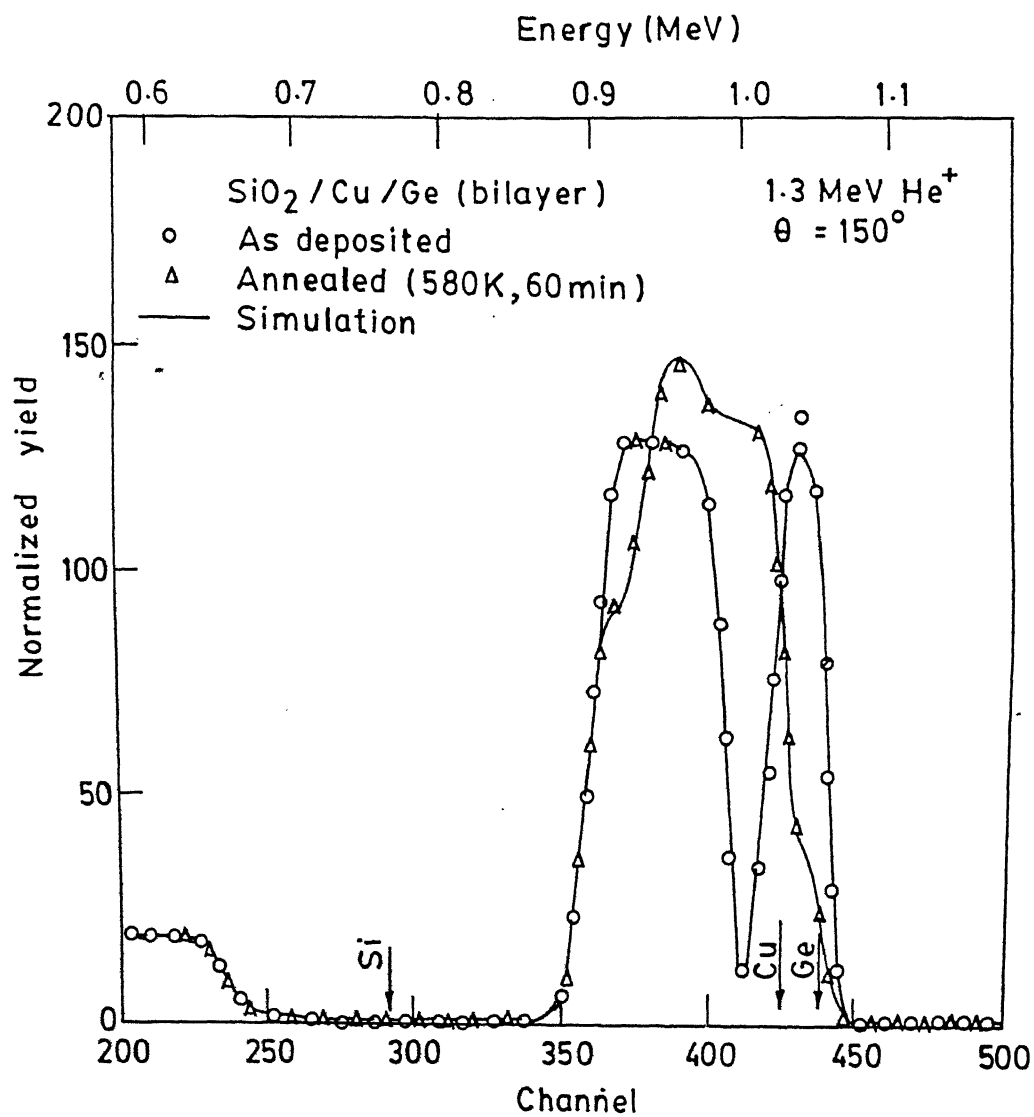


Figure 4.11: RBS spectra of Cu/Ge bilayer sample before and after annealing at 580 K for 60 min along with simulations.

Table 4.6: Description of the layer structure used for the simulation of RBS spectrum of thermally annealed Cu/Ge multilayer sample shown in Fig 4.9.

Sample description	Layer structure used for simulation					
	Layer No.	Thickness (nm)	Composition			
Cu/Ge multilayer samples after annealing at 630 K for 150 min.	1	190	Ge	0.25	Cu	0.75
	2	1500	Si	1.00	O	2.00

4.3.2 Ni/Ge system

Ion-beam induced effect

For Ni/Ge system, the Kr and Ar ion-beam mixing experiments were performed at sample temperatures ranging from 100 K to 425 K. The RBS spectrum of as-deposited multilayer sample (open circle) is shown in Fig 4.12 along with the simulated spectrum. The sample consists of five pairs of nickel and germanium layers with an overall thickness of Ni and Ge equal to 170 nm and 120 nm respectively. The detailed simulated structure is shown in Table 4.8.

The RBS spectrum after irradiation with Kr ions (triangle) for a dose of $6 \times 10^{15} \text{ Kr}^+/\text{cm}^2$ along with the simulated spectrum (continuous line) are also shown in Fig 4.12. This spectrum could be simulated using the structure shown in Table 4.8 consisting of a single layer of thickness 240 nm and composition $\text{Ni}_{66}\text{Ge}_{34}$ for the mixed region. This composition corresponds to Ni_2Ge phase present in the Ni-Ge equilibrium phase diagram (shown in Fig 4.27). Irradiations up to a dose of $1 \times 10^{16} \text{ Kr}^+/\text{cm}^2$ do

Table 4.7: Summary of thermal annealing results of Cu/Ge sample

Sample Geometry	Summary of thermal annealing results in Cu/Ge sample			
	Temperature in K	Annealing time in min.	Composition given by RBS	Phase identified by X-ray
Cu/Ge multilayer sample deposited on SiO_2	630	30	$Cu_{75}Ge_{25}$	Cu_3Ge
		90	"	"
		120	"	"
		150	"	"
		180	"	"
Cu/Ge Bilayer film deposited on SiO_2	580	30	$Cu_{75}Ge_{25}$	Cu_3Ge
		60	"	"

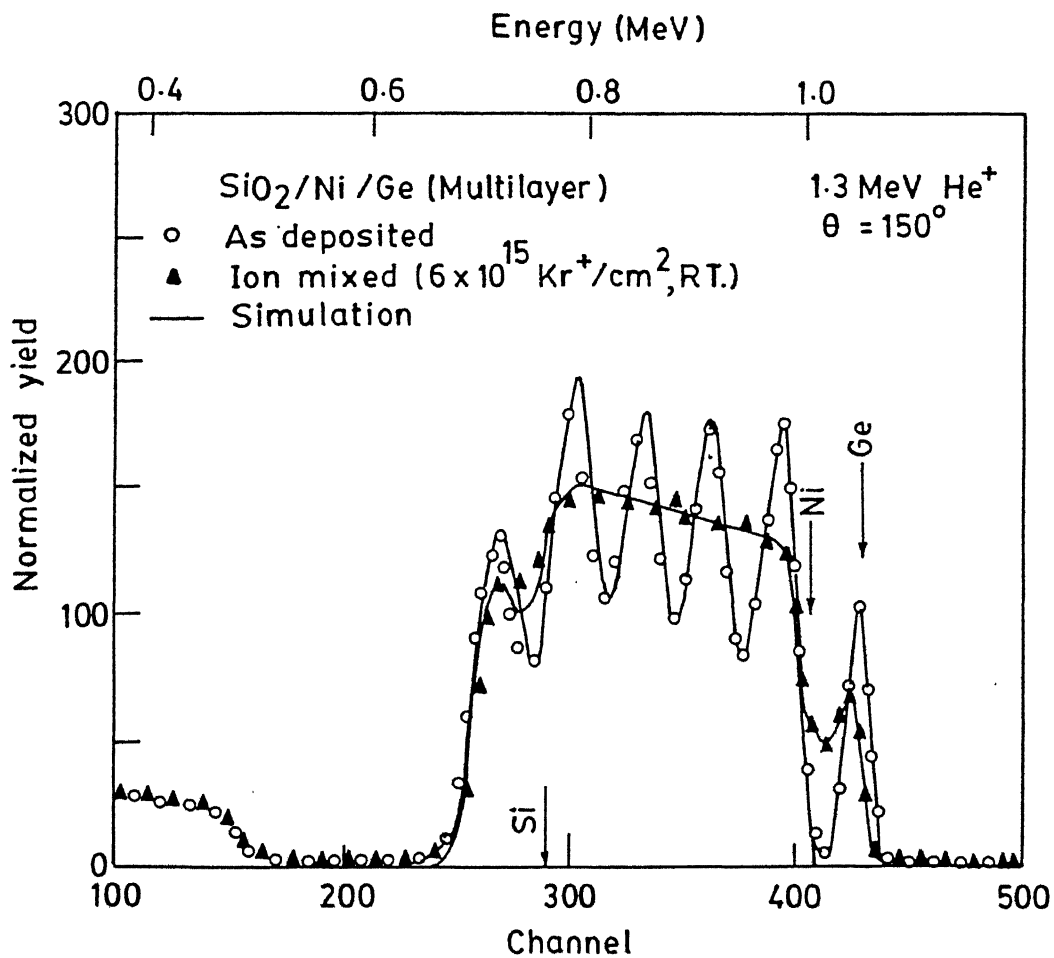


Figure 4.12: RBS spectra of the as-deposited and ion mixed ($6 \times 10^{15} \text{ Kr}/\text{cm}^2$, RT) Ni/Ge multilayer sample deposited on SiO_2 . The Continuous lines show simulations.

Table 4.8: Description of the layer structure used for the simulation of RBS spectra of as-deposited and ion mixed Ni/Ge multilayer sample shown in Fig 4.12.

Sample description	Layer structure used for simulation						
	Layer No.	Thickness (nm)	Composition				
Ni/Ge multilayer films deposited on SiO_2	1	26	Ge	1			
	2	32	Ni	1			
	3	24	Ge	1			
	4	34	Ni	1			
	5	22	Ge	1			
	6	34	Ni	1			
	7	22	Ge	1			
	8	35	Ni	1			
	9	24	Ge	1			
	10	35	Ni	1			
	11	1000	Si	1	O	2	
Ni/Ge multilayer films after ion mixing at RT for a dose of $6 \times 10^{15} Kr/cm^2$	1	10	Ge	1.00			
	2	240	Ge	0.34	Ni	0.66	
	3	15	Ni	1.00			
	4	1000	Si	1.00	O	2.00	

not change the composition of the mixed regions. For irradiation performed at higher sample temperature of 390 K the mixing in Ni/Ge system proceeds rapidly with the formation of a uniform composition corresponding to the Ni_2Ge phase. This is illustrated by the experimental and simulated RBS spectra given in Fig 4.13 corresponding to a dose of $4 \times 10^{15} \text{ Kr/cm}^2$. Ion-beam mixing at a sample temperature of 100 K the mixed region leads to the same composition across the individual Ni/Ge interface. The temperature dependence of mixing and ion induced phase formation have been discussed in detail in Chapter 6.

Conventional X-ray diffraction measurements as well as those performed in Seeman-Bohlin geometry did not show any peak for the as deposited Ni/Ge multilayer sample indicating the amorphous/highly disordered state of the individual Ni and Ge layers[85, 86]. The Seeman-Bohlin X-ray diffraction spectra recorded after irradiating the sample at RT with a dose of $6 \times 10^{15} \text{ Kr}^+/\text{cm}^2$ is shown in Fig 4.14a, which shows diffraction peaks at 2θ values 45.14° and 46.68° belonging to Ni_2Ge phase. The observed and reported[84] d values for Ni_2Ge phase are given in Table 4.9. The irradiations at other doses also show the formation of Ni_2Ge phase. No other Ni-Ge phase has been observed after ion-beam mixing.

Irradiations with Ar ions also lead to the formation of Ni_2Ge phase. The X-ray diffraction spectrum taken after irradiating the Ni/Ge multilayer sample at RT with Ar ions for a dose of $1 \times 10^{16} \text{ ions/cm}^2$ is shown in Fig 4.14b which also shows diffraction peaks at $2\theta = 47.6^\circ$ and 49.68° belonging to Ni_2Ge phase[84]. However, the sample irradiated at 100 K dose not show any prominent peak although the composition corresponding to Ni_2Ge phase has been obtained from RBS analysis. The experimental and reported d-values are also compared in Table 4.9. It should be noted that the effect produced due to RT irradiation for $1 \times 10^{16} \text{ ions/cm}^2$ of Ar is obtained at a much lower dose of $4 \times 10^{15} \text{ ions/cm}^2$ of Kr ions for RT irradiations and is clearly illustrated in Fig 4.15. The results of ion-beam mixing presented here are summarized in Table 4.10.

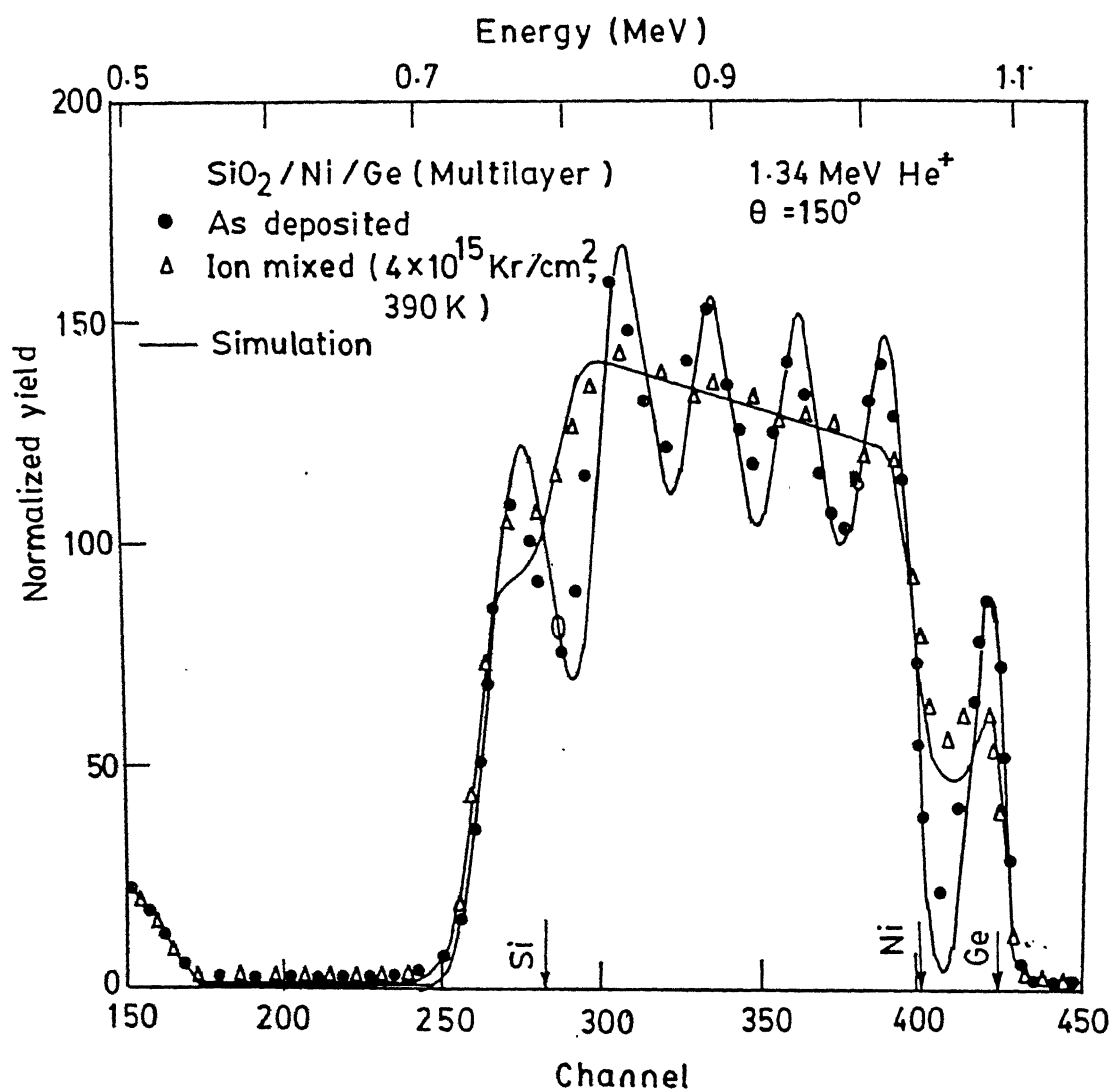


Figure 4.13: RBS spectra of Ni/Ge multilayer sample before and after ion-beam mixing at 390 K for a dose of $4 \times 10^{15} \text{ Kr}^+/\text{cm}^2$ showing formation of a uniformly mixed region of composition $\text{Ni}_{66}\text{Ge}_{34}$.

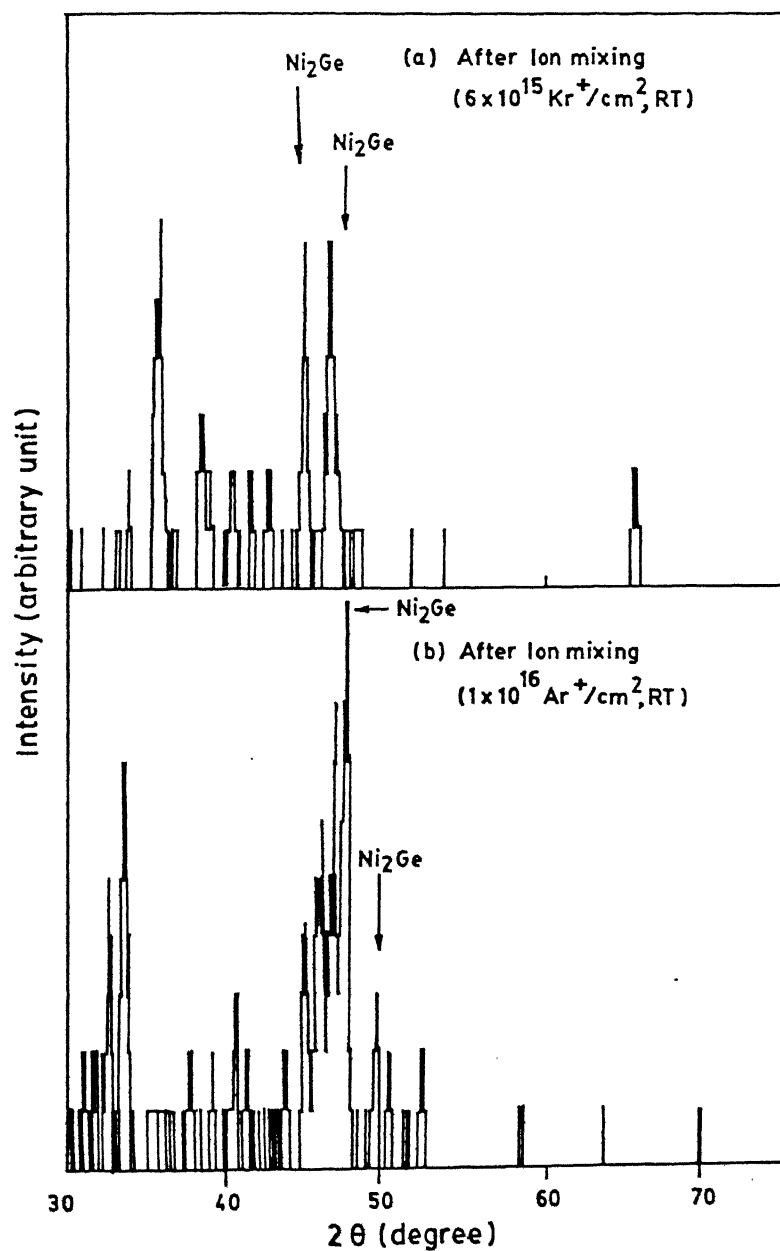


Figure 4.14: X-ray pattern of Ni/Ge multilayer sample after ion-beam mixing at for irradiation fluence of (a) $6 \times 10^{15} \text{ Kr}^+/\text{cm}^2$ (b) $1 \times 10^{16} \text{ Ar}^+/\text{cm}^2$.

Table 4.9: Comparison of experimentally obtained d-values of the observed Ni_2Ge phase with the one reported in literature.

Sample description	Experimental		Reported		
	Dose (ions/cm ²)	d_{hkl} (Å)	d_{hkl} (Å)	(hkl)	Phase
X-ray spectrum of Ni/Ge multilayer sample after RT ion-beam mixing	$6 \times 10^{15} \text{ Kr/cm}^2$	2.01	2.04	(211)	Ni_2Ge
		1.94	1.91	(020)	„
	$1 \times 10^{16} \text{ Ar/cm}^2$	1.91	1.91	(020)	Ni_2Ge
		1.834	1.836	(212)	„

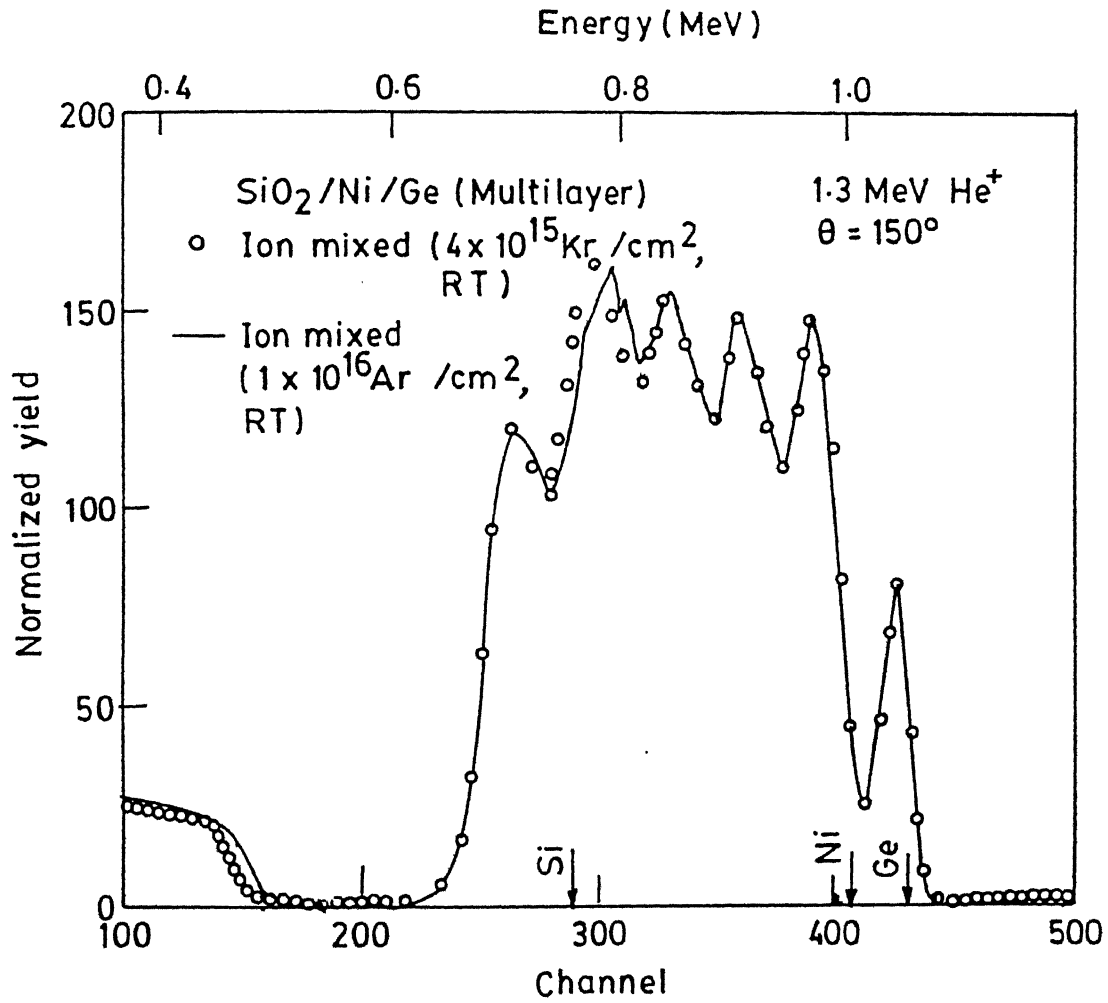


Figure 4.15: Comparison between the RBS spectra of Ni/Ge multilayer sample after ion-beam mixing at doses of $4 \times 10^{15} \text{ Kr}^+/\text{cm}^2$ and $1 \times 10^{16} \text{ Ar}^+/\text{cm}^2$.

Table 4.10: Summary of ion-beam mixing results in Ni/Ge multilayer systems using Kr and Ar ions at various doses and temperatures.

Sample description	Ion species	Temperature during Irrad.	Dose ions/cm ²	Phase obtained by IM	
				composition	Phase
Ni/Ge multilayer film deposited on SiO ₂	Kr	300	$(2 - 10) \times 10^{15}$	<i>Ni₆₆Ge₃₄</i>	<i>Ni₂Ge</i>
	Kr	100	$(6 - 10) \times 10^{15}$	„	*
	Kr	390	$(2 - 10) \times 10^{15}$	„	<i>Ni₂Ge</i>
	Kr	430	1×10^{16}	„	„
	Ar	300	$(5 - 10) \times 10^{15}$	<i>Ni₆₆Ge₃₄</i>	<i>Ni₂Ge</i>
	Ar	380	1×10^{16}	„	„

* Very low intensity x-ray peak.

Thermal annealing effects

The RBS spectrum for a multilayer Ni/Ge sample annealed at 580 K for 60 min. is shown in Fig 4.16 along with the corresponding as-deposited spectrum. As seen in the spectrum a uniform homogeneous composition has been obtained after annealing. The spectrum of annealed sample was simulated using a composition of $Ni_{66}Ge_{34}$ and some unreacted Ni and Ge. Similar results were obtained for other temperatures and annealing times. Figs 4.17a and 4.17b show the standard X-ray spectra for samples annealed at 580 K for 60 min. and 180 minutes. The analysis shows that the peaks correspond to the stable Ni_2Ge phase. The formation of Ni_2Ge phase was detected after annealing at temperature as low as 480 K by normal and glancing angle X-ray techniques.

Bilayer samples also show synthesis of the nickel germanide phases after annealing at various temperature. A typical RBS spectrum of an as-deposited bilayer sample is shown in Fig 4.18a. The simulated spectrum is shown by continuous line and the simulated structure is given in Table 4.11. The RBS spectrum after annealing at 480 K for 180 min. is also shown in Fig 4.18a along with its simulated spectrum. The simulation analysis shows the formation of two layers having compositions corresponding to NiGe and Ni_2Ge phases. The simulated structure is shown in Table 4.11. The XRD spectrum for this annealed sample is shown in Fig 4.18b which confirms the formation of NiGe and Ni_2Ge phases. Figure 4.19 shows the comparison of RBS spectra of three bilayer samples after annealing at 430 K for 90 min., 480 K for 60 min. and 530 K for 180 min. respectively. The detailed analysis show that only Ni_2Ge phase is produced at 430 K and both NiGe and Ni_2Ge are produced above 475 K. These results of RBS and XRD analysis of the thermally annealed multilayer and bilayer Ni/Ge samples are summarized in Table 4.12.

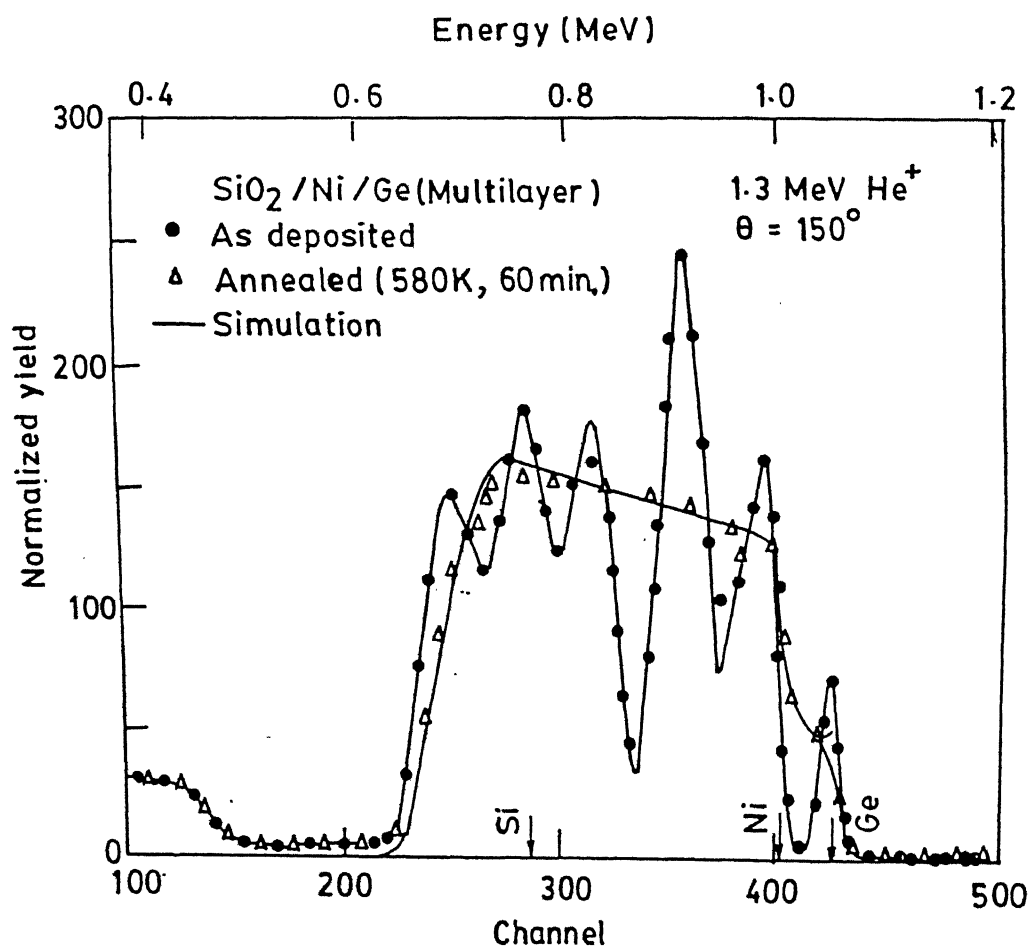


Figure 4.16: RBS spectra of Ni/Ge multilayer sample before and after annealing at 580 K for 60 min. along with simulations.

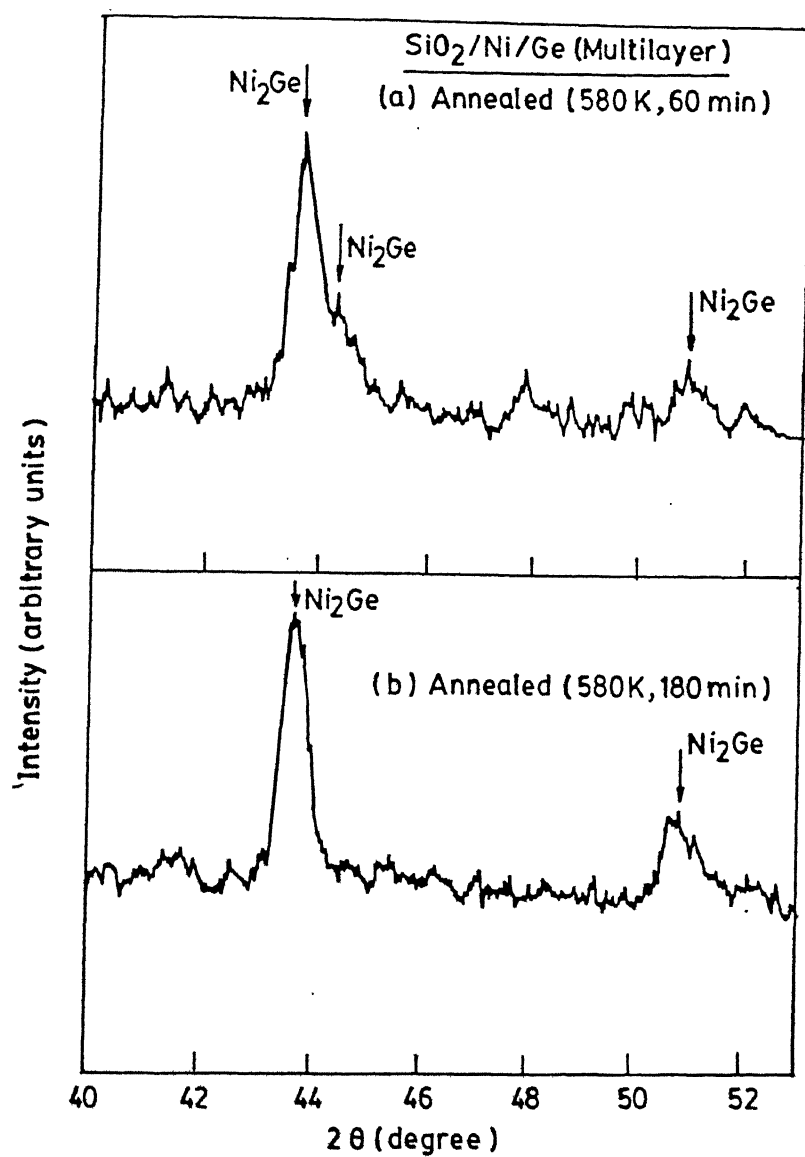


Figure 4.17: X-ray pattern of Ni/Ge multilayer sample after thermal annealing at 580 K for (a) 60 min. (b) 180 min.

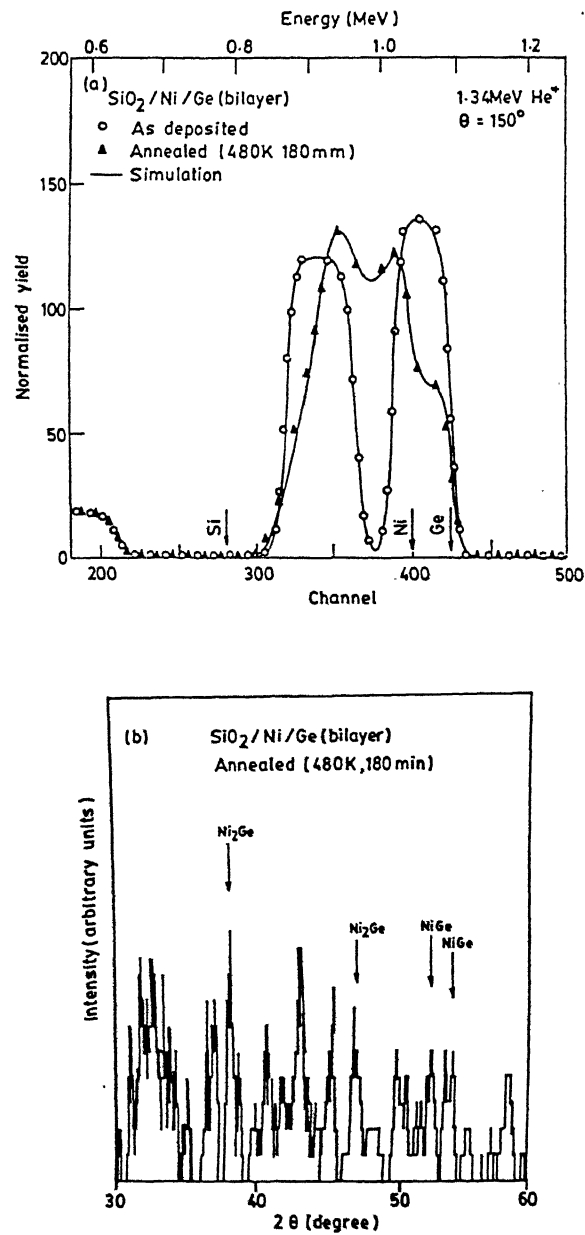


Figure 4.18: (a) RBS spectra of Ni/Ge bilayer sample before and after annealing at 480 K for 180 min. along with simulations (b) X-ray diffraction pattern confirms the formation of Ni_2Ge and NiGe phases.

Table 4.11: Description of the layer structures used for the simulations of RBS spectra of as-deposited and thermally annealed bilayer Ni/Ge bilayer sample shown in Fig 4.18.

Sample description	Layer structure used for simulation						
	Layer No.	Thickness (nm)	Composition				
Ni/Ge bilayer films deposited on SiO_2	1	106	Ge	1.00			
	2	71	Ni	1.00			
	3	1000	Si	1.00	O	2.00	
After annealing at 480 K for 180 min	1	2	Ge	1.00			
	2	80	Ge	0.50	Ni	0.50	
	3	30	Ge	0.34	Ni	0.66	
	4	50	Ge	0.50	Ni	0.50	
	5	1000	Si	1.00	O	2.00	

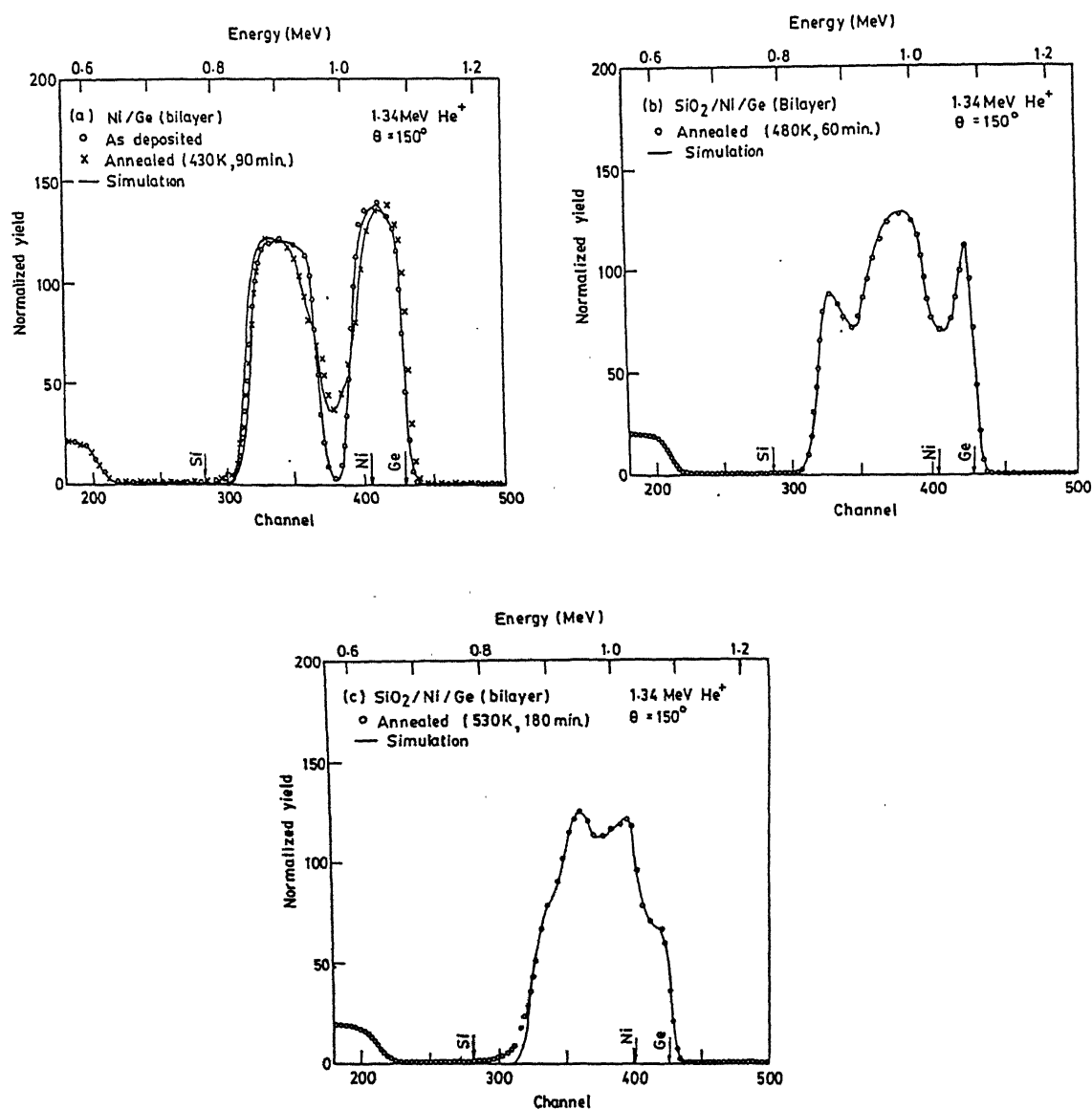


Figure 4.19: Comparison of RBS spectra of Ni/Ge bilayer samples annealed at three different temperatures (a) 430 K for 90 min. (b) 480 K for 60 min. (c) 530 K for 180 min.

Table 4.12: Summary of thermal annealing results of Ni/Ge sample

Sample description	Annealing temperature in K	Annealing time (in min.)	Phase obtained by annealing	
			Composition	Phase
Ni/Ge multilayer films deposited on SiO_2	480	60-180	$Ni_{66}Ge_{34}$	Ni_2Ge
	530	180	$Ni_{66}Ge_{34}$	Ni_2Ge
	580	60-180	$Ni_{66}Ge_{34}$	Ni_2Ge
Ni/Ge bilayer film deposited on SiO_2	430	60-180	$Ni_{66}Ge_{34}$	Ni_2Ge
	480	60-180	$Ni_{66}Ge_{34}+Ni_{50}Ge_{50}$	$Ni_2Ge+NiGe$
	530	90-180	$Ni_{66}Ge_{34}+Ni_{50}Ge_{50}$	$Ni_2Ge+NiGe$

4.3.3 Co/Ge system

Ion-beam induced effect

The multilayer Co/Ge samples were made with four pairs of cobalt and germanium layers each having total thickness of 110 nm. The RBS spectra in Fig 4.20 compare the backscattering yields of as-deposited sample with the one irradiated by 1 MeV Kr^+ ions at a dose of $1 \times 10^{16} \text{ ions/cm}^2$. The analysis of the irradiated sample shows the formation of mixed regions having composition of $Co_{66}Ge_{34}$ at the interface of each layer along with unreacted layers of Co and Ge. The simulated curves are shown by continuous line for both the cases. It may be noted that unlike Cu/Ge and Ni/Ge system the multilayers of Co/Ge do not mix completely for the irradiation dose of $1 \times 10^{16} \text{ Kr}^+/\text{cm}^2$. The SEM studies of as-deposited and irradiated sample do not show any noticeable change in surface features.

The effect of ion-beam mixing performed at elevated temperatures of 380 K and 420 K are depicted in Fig 4.21 and Fig 4.22 respectively for an irradiation dose of $1 \times 10^{16} \text{ Kr}^+/\text{cm}^2$ along with as-deposited spectrum. A single layer of composition $Co_{66}Ge_{34}$ was used for simulation of the mixed region in both the cases. The layer structures used for simulation for the irradiated samples as shown in Fig 4.21 is given in Table 4.13. It is also clear from these figures that at these elevated temperatures the mixing is more uniform across the thickness, nevertheless, a small amount of topside Ge film and the bottom side Co film still remain unreacted. The X-ray diffraction patterns of the irradiated sample shows many new diffraction peaks as compared to the as-deposited spectrum. Unfortunately, x-ray data for Co_2Ge is not available hence we could not identify x-ray diffraction peaks corresponding to this phase. However, the very fact that RBS gives uniform stoichiometry and that x-ray pattern indicate crystallinity of the film hence we conclude that the composition $Co_{66}Ge_{34}$ of the film belongs to the Co_2Ge phase and that the phase has formed after ion-beam mixing. The RBS results of ion mixing at different temperatures are summarized in Table 4.14.

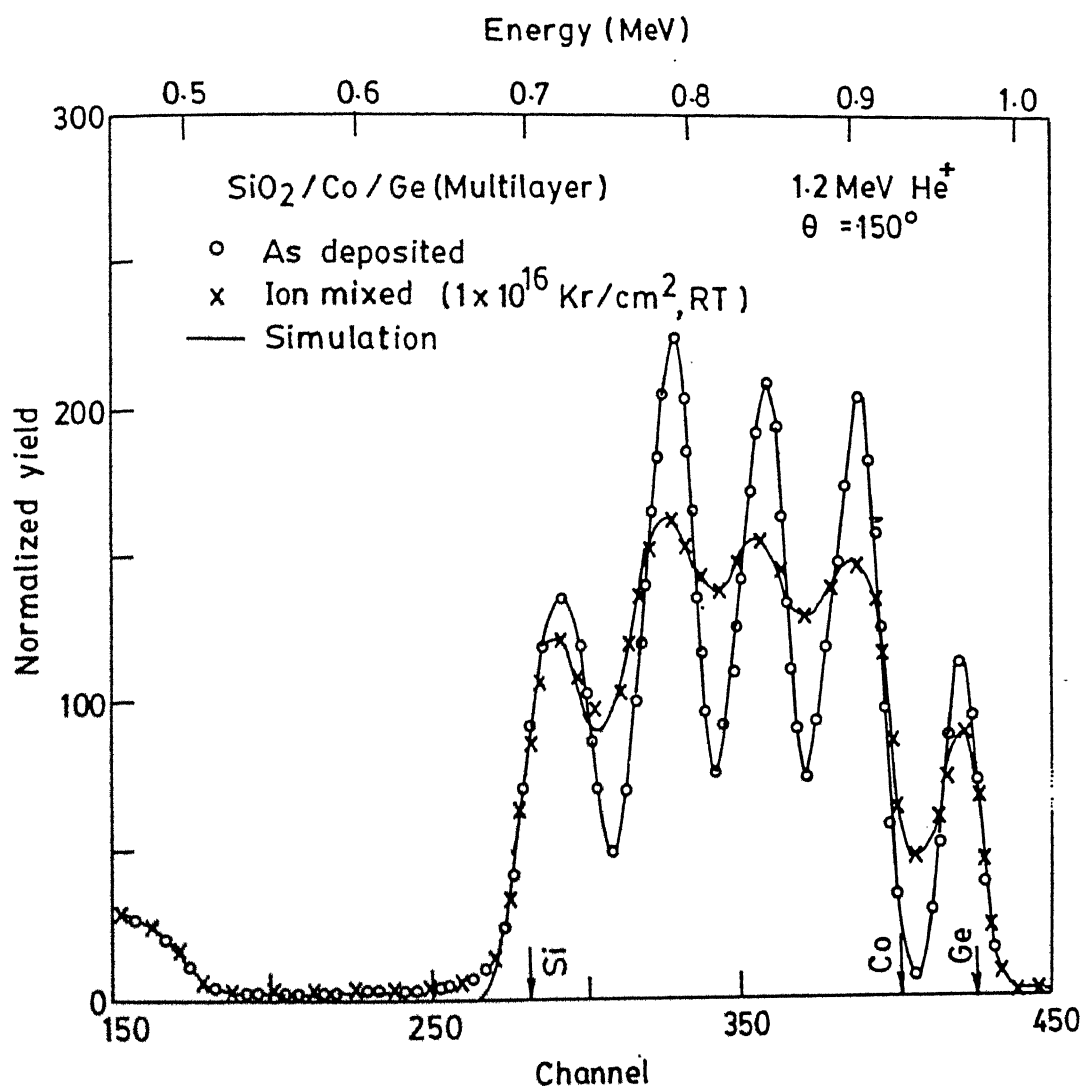


Figure 4.20: RBS spectra of Co/Ge multilayer sample before and after ion-beam mixing at RT for a dose of $1 \times 10^{16} \text{ Kr}^+/\text{cm}^2$. The simulated curves in both cases are shown by continuous line.

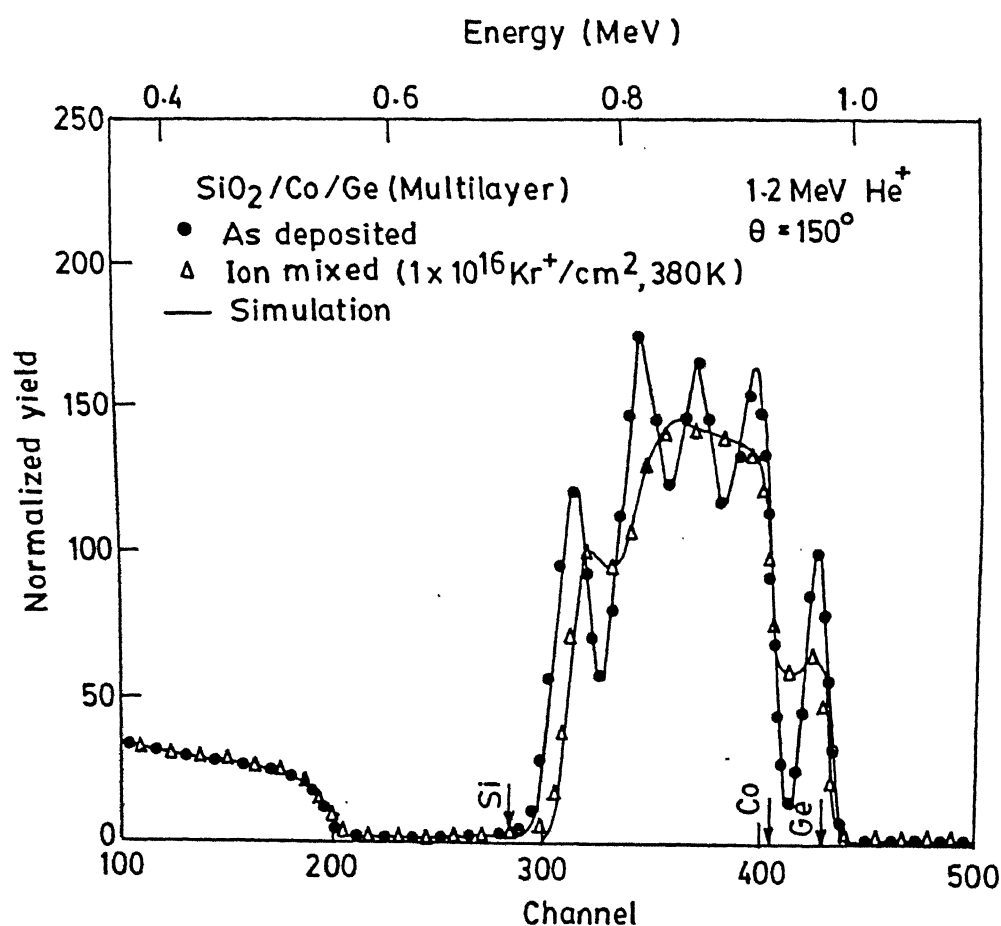


Figure 4.21: RBS spectra of Co/Ge multilayer sample before and after ion-beam mixing for a dose of $1 \times 10^{16} \text{ Kr}^+/\text{cm}^2$ at 380 K. In this case mixing leads to the formation of Co_2Ge phases. The simulated curve is shown by continuous line.

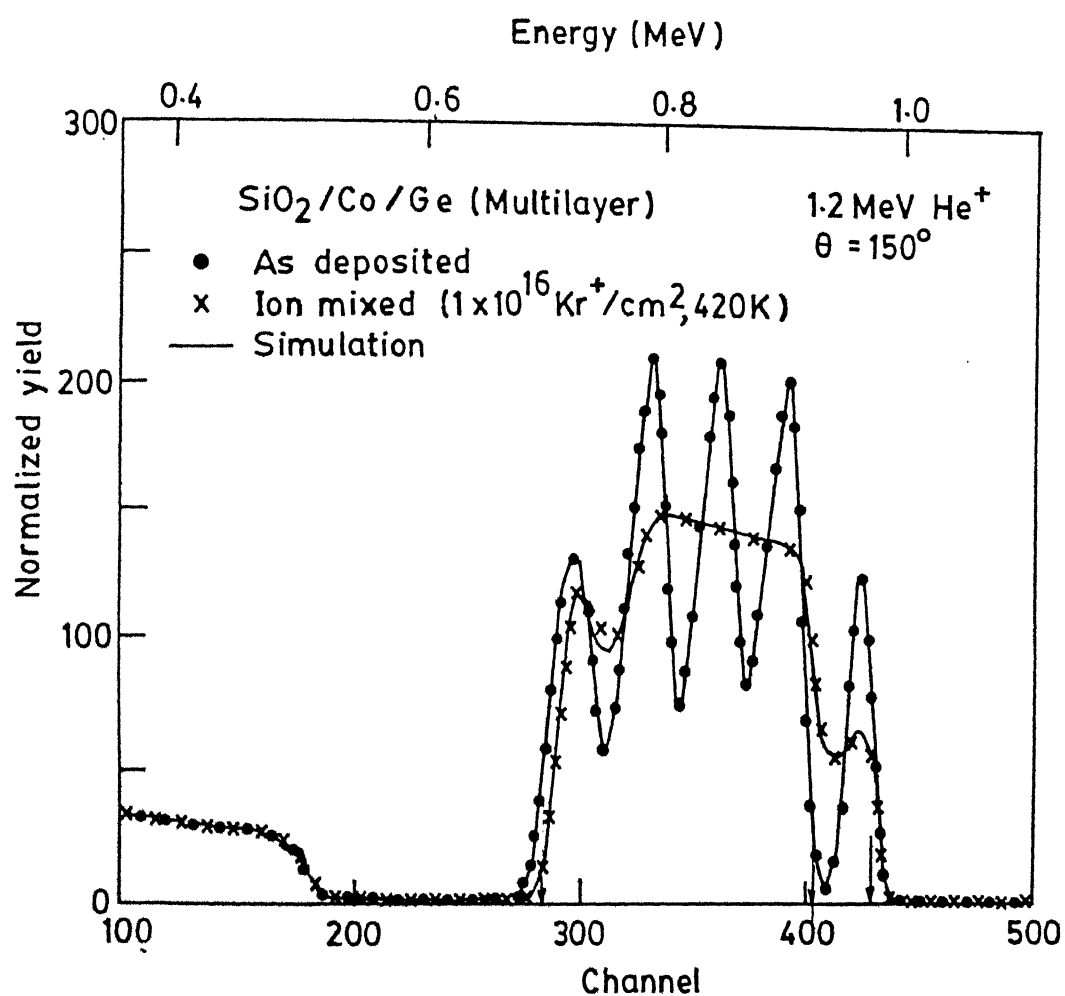


Figure 4.22: RBS spectra of Co/Ge multilayer sample before and after ion-beam mixing for a dose of $1 \times 10^{16} \text{ Kr}^+/\text{cm}^2$ at 420 K. In this case mixing also leads to the formation of Co_2Ge phases.

Table 4.13: Description of the layer structures used for the simulation of RBS spectrum of ion mixed Co/Ge multilayer sample shown in Fig 4.21.

Sample description	Layer structure used for simulation					
	Layer No.	Thickness (nm)	Composition			
Co/Ge multilayer sample after ion-beam mixing at 380 K for a dose of $1 \times 10^{16} \text{ Kr/cm}^2$	1	7	Ge	1.00		
	2	130	Ge	0.34	Co	0.66
	3	10	Co	1.00		
	4	1000	Si	1.00	O	2.00

Table 4.14: Summary of ion-beam mixing results of Co/Ge sample

Sample description	Ions	Temperature of Irrad (K).	Dose ions/cm ²	Phase obtained by IBM	
				Composition	Phase
Co/Ge multilayer sample deposited on SiO ₂	Kr	300	$(6 - 10) \times 10^{15}$	<i>Co₆₆Ge₃₄</i>	<i>Co₂Ge*</i>
	Kr	380	1×10^{16}	<i>Co₆₆Ge₃₄</i>	<i>Co₂Ge*</i>
	Kr	430	1×10^{16}	<i>Co₆₆Ge₃₄</i>	<i>Co₂Ge*</i>
	Ar	300	1×10^{16}	<i>Co₆₆Ge₃₄</i>	<i>Co₂Ge*</i>
	Ar	380	1×10^{16}	<i>Co₆₆Ge₃₄</i>	<i>Co₂Ge*</i>

* X-ray data for *Co₂Ge* phase are not available

Thermal annealing effects

In case of Co/Ge the thermal annealing experiments have been done for both bilayer and multilayer samples at 480 K to 680 K for different annealing durations. The RBS spectrum for a multilayer sample annealed at 530 K for 180 min. is shown in the Fig 4.23a along with the as-deposited spectrum. The spectrum of annealed sample can be simulated (shown by continuous line) by a layer of composition of Co_2Ge and some unreacted Co and Ge. The multilayer sample whose RBS spectrum is shown in Fig 4.23b completely reacts after annealing at 680 K for 120 min. duration and the simulation analysis shows the formation of uniform layer of composition Co_2Ge . The XRD analysis also shows a single sharp peak. The RBS spectra of Fig 4.24 compare the ion-beam mixing effect with the one induced by thermal annealing alone. It is seen from this figure that the sample annealed at 580 K for 60 min. matches quite well with the spectrum of the sample irradiated at 380 K for a dose of $6 \times 10^{15} Kr^+/cm^2$.

In case of bilayer samples, annealing at 480 K produces composition corresponding to Co_2Ge phase. Whereas at 530 K both Co_2Ge and $CoGe$ phases are formed at Co rich and Ge rich sides respectively. At still higher temperature of 580 K both of the layers react almost completely forming a uniform composition of CoGe. Figure 4.25 shows the comparison of RBS spectra corresponding to a bilayer sample annealed at three different temperatures. The detailed results of these bilayer and multilayer samples are tabulated in Table 4.15.

4.3.4 Resistivity measurements

The resistivity of the films after ion-beam mixing was measured by four probe method as described in Chapter 3. The measured resistances are shown in Table 4.16 for both ion mixed and thermally produced phases. In case of ion mixed phases, the resistivity values are reported for the minimum ion dose at which a uniform homogeneous layer is formed. The resistivity of the phases produced by ion-beam mixing are almost twice as compared to the phases produced by thermal annealing. This might be due to the

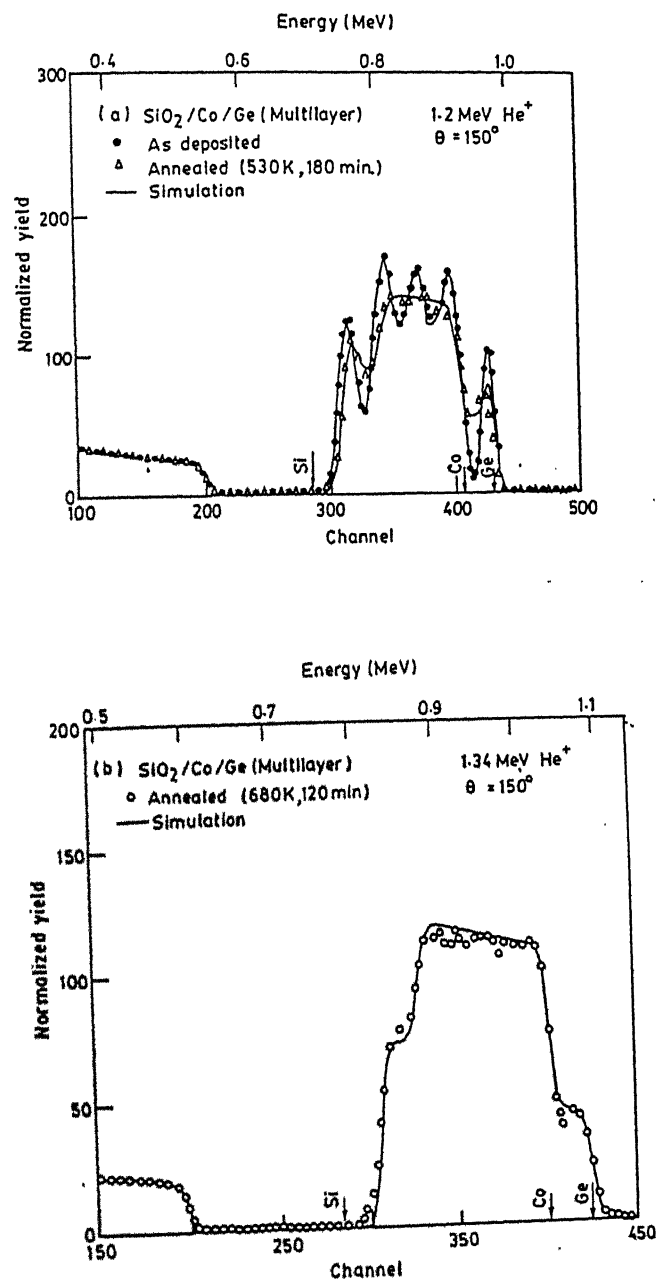


Figure 4.23: RBS spectra of thermally annealed Co/Ge multilayer samples (a) 530 K for 180 min. and (b) 680 K for 120 min. Simulated spectra are given by continuous lines.

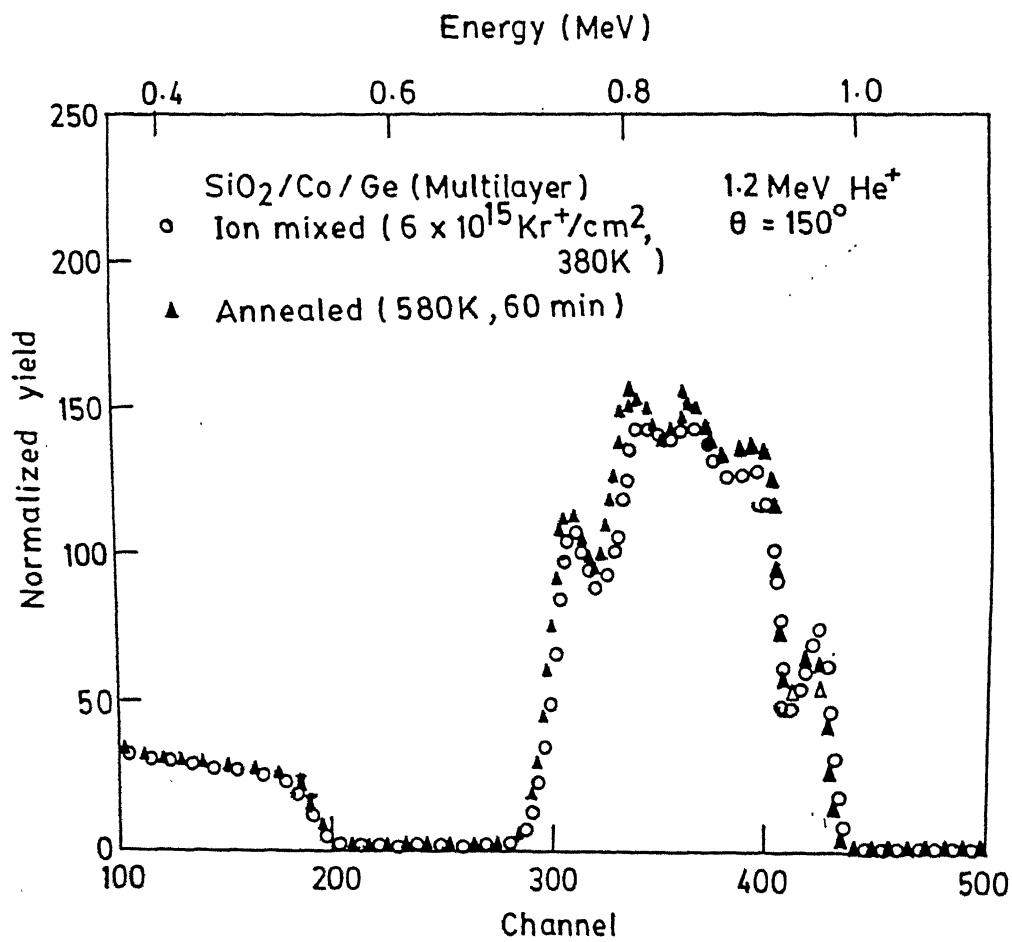


Figure 4.24: Comparison between RBS spectra of Co/Ge multilayer sample taken after ion-beam mixing at 380 K for a dose of $6 \times 10^{15} \text{ Kr}^+/\text{cm}^2$ and after thermal annealing at 580 K for 60 min.

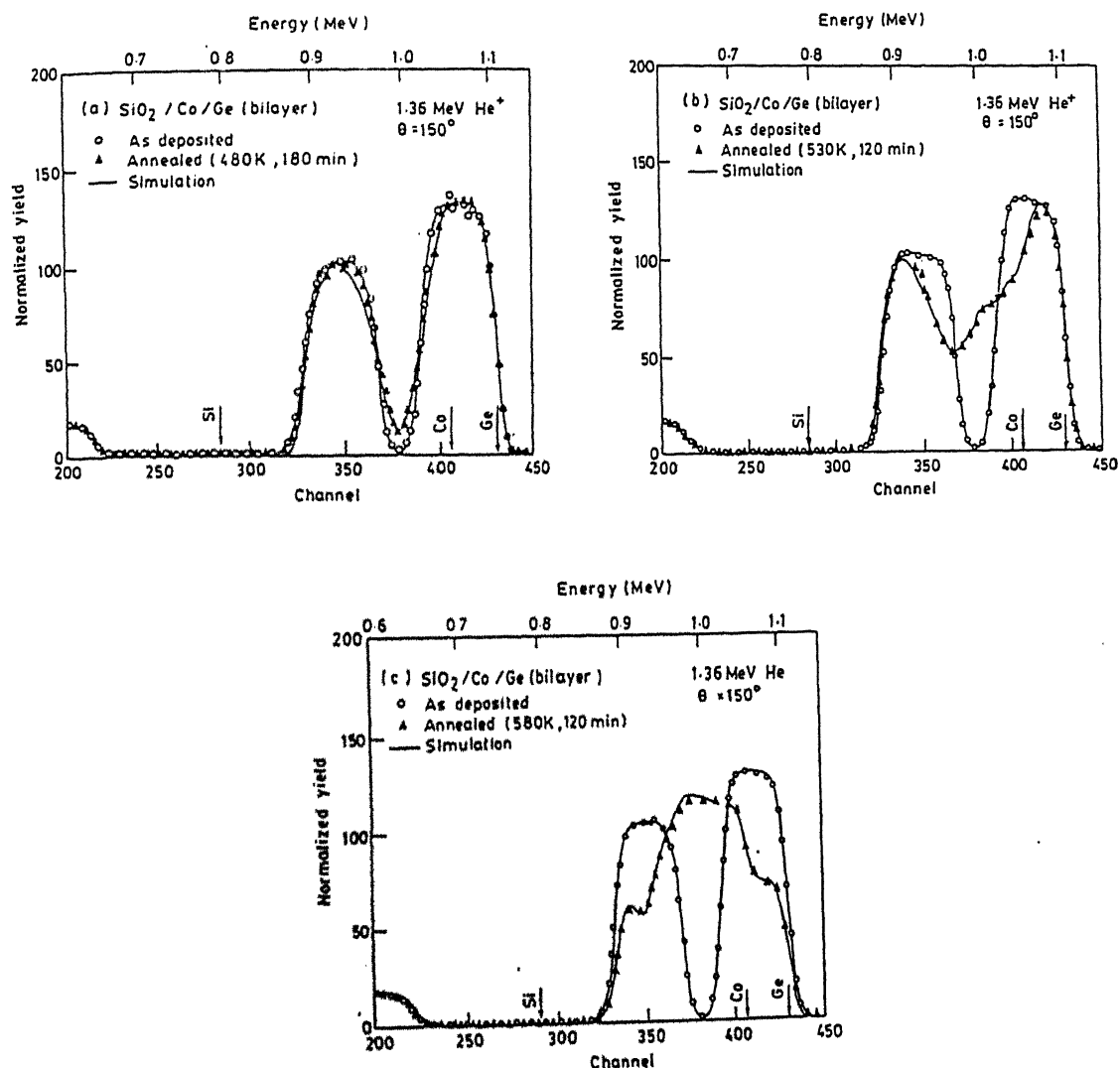


Figure 4.25: Comparison of RBS spectra of thermally annealed Co/Ge bilayer samples at three different temperatures (a) 480 K for 180 min. (b) 530 K for 120 min. (c) 580 K for 120 min.

Table 4.15: Summary of thermal annealing results of Co/Ge sample

Sample description	Annealing temperature in K	Annealing time in min.	Phase obtained by annealing	
			Composition	Phase
Co/Ge multilayer sample deposited on SiO_2	530	60-180	$Co_{66}Ge_{34}$	Co_2Ge^*
	580	60-120	$Co_{66}Ge_{34}$	Co_2Ge^*
	680	120	$Co_{66}Ge_{34}$	Co_2Ge^*
Co/Ge bilayer sample deposited on SiO_2	480	90-240	$Co_{66}Ge_{34}$	Co_2Ge^*
	530	60-240	$Co_{66}Ge_{34}$ +	Co_2Ge^* +
	580	60-120	$Co_{50}Ge_{50}$	CoGe

* see text (p 102)

Table 4.16: Resistivities measured on Cu_3Ge , Ni_2Ge and Co_2Ge layers produced by ion-beam mixing and thermal annealing.

Binary system	Phase synthesized by ion mixing		Phase prepared by thermal annealing	
	Dose Kr/cm^2	resistivity $\mu\Omega - cm$	Temperature and annealing time	Resistivity $\mu\Omega - cm$
Cu/Ge	8×10^{15}	20	350 °C, 150 min.	8.6
Ni/Ge	8×10^{15}	50	300 °C, 180 min.	23
Co/Ge	1×10^{16}	74	300 °C, 120 min.	50

presence of irradiation induced defects in the mixed regions. The resistivity of the Cu_3Ge phases compare reasonably well with the reported value of 6 μ -cm[49]. For the Ni_2Ge and Co_2Ge phases no resistivity data is available in the literature. Probably these are the first measurements to be reported. It is important to note that the resistivity values are lower as compared to metal silicides. Hence we believe that these germanide phases would become important for semiconductor industry.

4.4 Discussion

Before starting the discussion let us summarize the main points of the ion-beam mixing and thermal annealing results of Cu/Ge, Ni/Ge and Co/Ge systems presented in Tables 4.5, 4.7, 4.10, 4.12, 4.14 and 4.15 respectively.

- Both Kr and Ar ion irradiation induces mixing in the multilayer metal/Ge films at 100 K, RT and above. In all the cases the metal-rich compounds viz Cu_3Ge , Ni_2Ge and Co_2Ge form first in Cu/Ge, Ni/Ge and Co/Ge systems respectively after mixing at RT and above. Thermal annealing alone also produces the same phases which suggests that synthesis of the first phase is same for both ion-beam mixing and thermal reactions.
- At higher doses the ion-beam mixing also produces Cu_5Ge phase. In case of Ni/Ge and Co/Ge bilayer systems, higher annealing temperatures (above 475 K) produce $NiGe$ and $CoGe$ phases respectively.
- Ar ion induced mixing occurs at a much slower rate as compared to Kr irradiation.

4.4.1 Phase formation mechanism

In general, ion-beam mixing refers to the homogenization across the interfaces of multilayers or bilayers of two elements by energetic heavy ion beams. When the energetic ion passes through these layers (as described in Chapter 2) it loses most of its energy by soft atomic collisions and comes to rest within 10^{-15} s [14, 17]. During primary collisions the atoms of the target acquire sufficient energy and get dislodged from their original positions producing a number of secondary collisions. Thus within a short period of time, all the atoms in a small volume are set into random motion, which is commonly known as collisional cascade which lasts for about 10^{-13} to 10^{-11} s. During this short time period the displaced atoms interact in a collective fashion producing a significant amount of disorder. At the end of the collision cascade when the velocities of the moving atoms assume Boltzmann distribution one can invoke the notion

of temperature. Subsequently a relaxation process starts in which the excited mixture transits to a state of lower free energy. This process lasts for another 10^{-11} to 10^{-10} s and is called as thermal spike[14]. If we consider the temperature of the spike to be of the order of 1000 K the region cools down with rates of as high as 10^{14} K/s. It has been commonly accepted that the ion mixed alloys form during the relaxation process and not in the collisional process because the atoms are always in dynamically excited states in the cascade. In principle, if the temperature and time conditions during relaxation are sufficient for crystallization, the random mixture transforms to a stable or metastable crystalline state[13, 15]. However, if the conditions are not favorable then amorphous phase is formed.

This general picture described above has been found to be true for most of the metal/metal systems which form crystalline phases at high irradiation temperature and amorphous phases around room temperature and below. The characteristics of these binary metal/metal systems are (i) the non-reactive nature of the elements and (ii) their binary phase diagrams show equilibrium compounds which can be formed by thermal treatment at very high temperatures. On the other hand, many highly reactive systems like metal/semiconductor[15, 17, 30, 31, 41, 42, 57] and metal/Al[25, 58, 87] form simple as well as complex compounds around room temperature or below. It is interesting to note that these systems form compound by thermal treatment around 400-500 K. It should be mentioned over here that the thermal annealing at elevated temperatures also form the same phase as that formed by ion-beam mixing suggesting a common mechanism for the formation of the first phase in both the cases[57].

The emphasis here is to put the mixing processes on the scale of 'phase structure'. In this sense it is relevant to treat the relaxation process by invoking thermodynamics and kinetics of crystallization[13]. Apart from temperature, there are many other factors which influence the final phase formation. In general, the factors which are most likely to influence the formation of phase and its nature are the structure of the terminal solution[13], complexity of the compound phase[13, 56], width of phase fields[59, 60], atomic size[55, 62], atomic mobility[27, 56], heat of formation of various phases[56, 62],

the effect of substrate temperature[13] etc. All these factors act together in a complex manner. It has been mentioned earlier in Chapter 2 that several empirical rules[52–56] have been proposed from the knowledge of the final phase formed in a large number of binary systems. In turn, these rules have been used for predicting the formation of a phase and its nature for an unknown system. The literature shows that these rules are very successful (within their limitations) in most of the metal/metal and metal/Si systems[6, 13].

Since the chemical nature of Si and Ge is quite similar, one expects a similarity of results in producing silicide and germanide phases by ion-beam mixing as well as by thermal annealing[48]. This is indeed true and can be seen from Table 4.17 which compares the results of ion-beam mixing in Metal/Si with the results of this work on metal/Ge systems. We now test the predictions of the existing rules regarding phase formation with the finding of the present work.

4.4.2 Nature of Phase formation

Here we investigate the rules which predict the possible nature of the phases formed under different conditions by ion-beam mixing. Table 4.18 gives a summary of some of the widely used rules and their predictions in case of metal/Ge systems studied here.

The simple structure rule (column 1 of Table 4.18) proposed by Hung et al.[52] states that ion-beam mixing would produce crystalline compound having simple structure whenever the overall composition is close to that of a compound. Here simple structure means the fcc or bcc or hcp structures containing one or two atoms per unit cell. On the other hand, when the overall film composition is not close to an equilibrium alloy an amorphous phase would form. In the present case we have used samples having composition of one of the stable compounds present in the phase diagram. The equilibrium phase diagrams[91] of Cu/Ge, Ni/Ge and Co/Ge binary systems are shown in Figs 4.26, 4.27 and 4.28 respectively. The equilibrium phases present in the phase diagrams and other relevant information[63, 91–93] for these three systems are given

Table 4.17: Comparison of “first phase” formation in metal silicides and germanides by ion-beam mixing and thermal annealing.

Metal/Semiconductor system	Phase formed by IBM		Phase formed by thermal annealing	Ref.
	composition	phase		
Cu/Ge	Cu_3Ge	Cu_3Ge	Cu_3Ge	[this work]
Cu/Si	#	#	Cu_3Si	[48]
Ni/Ge	Ni_2Ge	Ni_2Ge	Ni_2Ge	[this work]
Ni/Si	Ni_2Si	Ni_2Si	Ni_2Si	[88]
Co/Ge	Co_2Ge	Co_2Ge^*	Co_2Ge	[this work]
Co/Si	Co_2Si	Co_2Si	Co_2Si	[89]
Pd/Ge	Pd_2Ge	Pd_2Ge	Pd_2Ge	[42]
Pd/Si	Pd_2Si	Pd_2Si	Pd_2Si	[30, 90]

Not reported in the literature

* X-ray data are not available.

Table 4.18: The nature of phases predicted by the existing empirical rules for the present case of metal germanide systems.

Emperical Rule	Parameters used	Predictions for present systems		
		Cu/Ge	Ni/Ge	Co/Ge
(1) Simple Structure rule[52]	Composition	C	C	C
(2) Hagg rule [55]	atomic radii the elements	C	C	C
(3) Structure difference rule[53]	Structure	C	C	A
(4) Extended structure rule[54]	Composition & Phase diagram	C	C	C

C = Crystalline phase

A = Amorphous phase

Table 4.19. This table shows that the Cu/Ge system has two stable metal rich phases viz., Cu_3Ge and Cu_5Ge . For this system we have used multilayer samples having composition close to the composition of Cu_3Ge phase. Simple structure rule of Hung's et al. that the Cu_3Ge phase should form, which is in accordance with our experimental results. The Ni/Ge system contains three stable phases Ni_2Ge , $NiGe$ and Ni_3Ge in equilibrium phase diagram. In this case we have used a composition close to the Ni_2Ge phase. This rule then predicts the formation of Ni_2Ge compound which also agrees with our experimental results. Similarly, Co-Ge phase diagram has three stable phases namely Co_2Ge , $CoGe$ and $CoGe_2$. Amongst these, we have chosen a composition of $Co_{66}Ge_{34}$ corresponding to Co_2Ge phase. The prediction of this rule to form Co_2Ge phase matches with our experimental findings. Table 4.19 shows that structure[92] of the Cu_3Ge phase is Cu_3Ti type whereas structures of the Ni_2Ge and Co_2Ge are that of Co_2Si type. There are many reports of formation of this kind of structures by ion-beam mixing. For example, Pd_2Si [56, 94], Co_2Si which have complex structures, are formed by ion-beam mixing at room temperature. Similarly, in case of aluminide systems the formation of complex phases like $AuAl_2$ [58, 95], Ni_3Al [25] at room temperature and below are reported in literature.

Hagg[55] and Rauschenbach[96, 97] have proposed (Column 2 of Table 4.18) that complex crystalline structures can be formed in a binary system if the ratio (R) of the radii of metalloid and metal atoms happens to be greater than 0.88 and compounds having simple crystalline structure would form if R is less than 0.59. Between these two limits amorphous phase formation takes place. This is shown in Fig 4.29. It can be seen from Table 4.19 and Fig 4.29 that in case of metal/Ge systems the ratio of radii[93] for all the three systems are greater than 0.88 thus suggesting the formation of compound phases in all the three cases. Thus both simple structure and radii ratio rule predict correctly the formation of compound at room temperature and above by ion-beam mixing. However, both these rules do not give any prerequisite of composition range under which these compound phases will be produced.

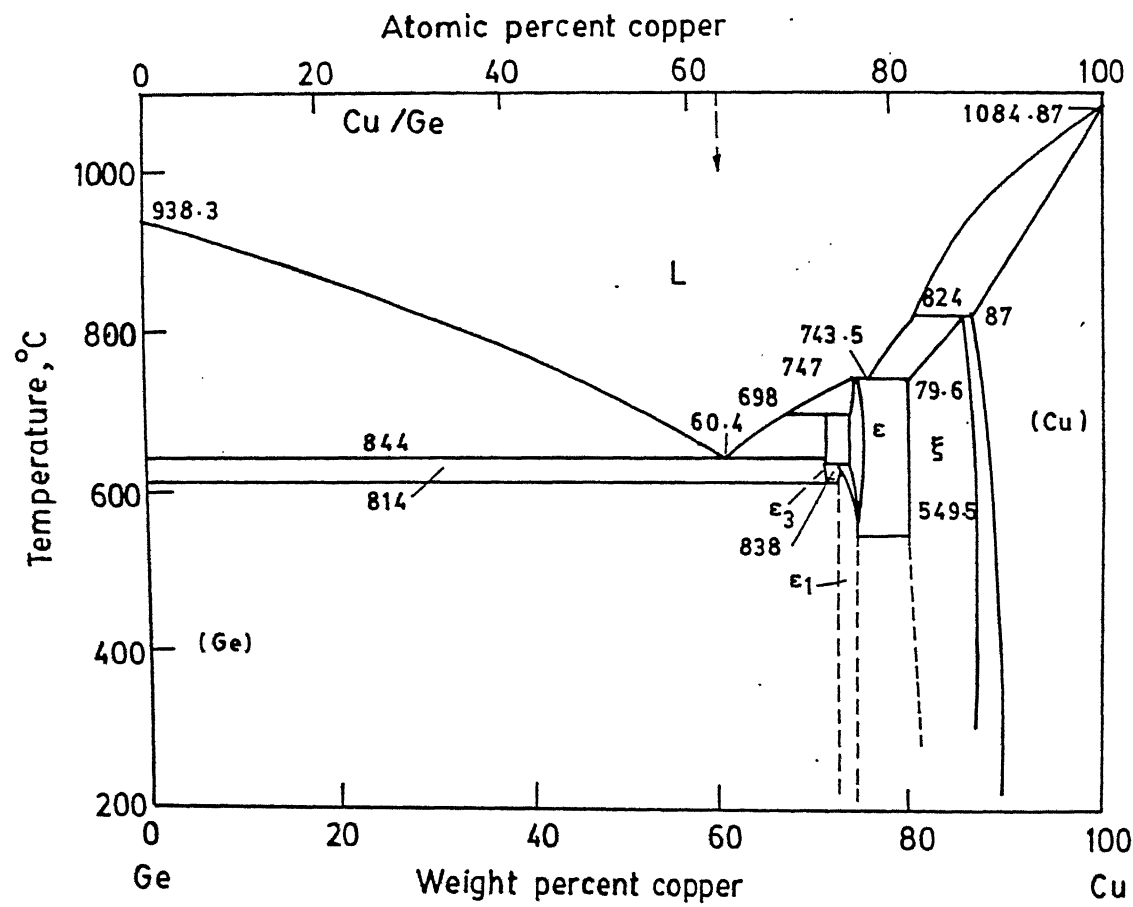


Figure 4.26: Equilibrium phase diagram of Cu-Ge system.

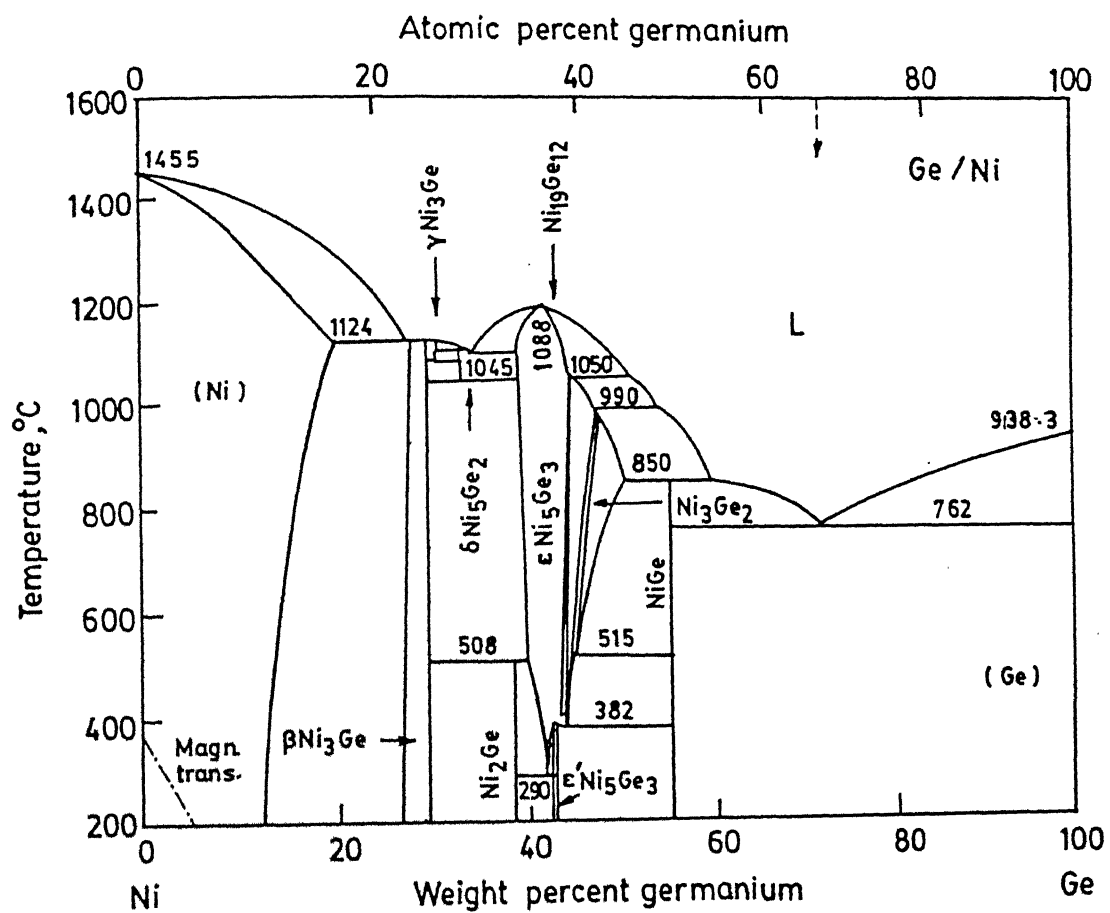


Figure 4.27: Equilibrium phase diagram of Ni-Ge system.

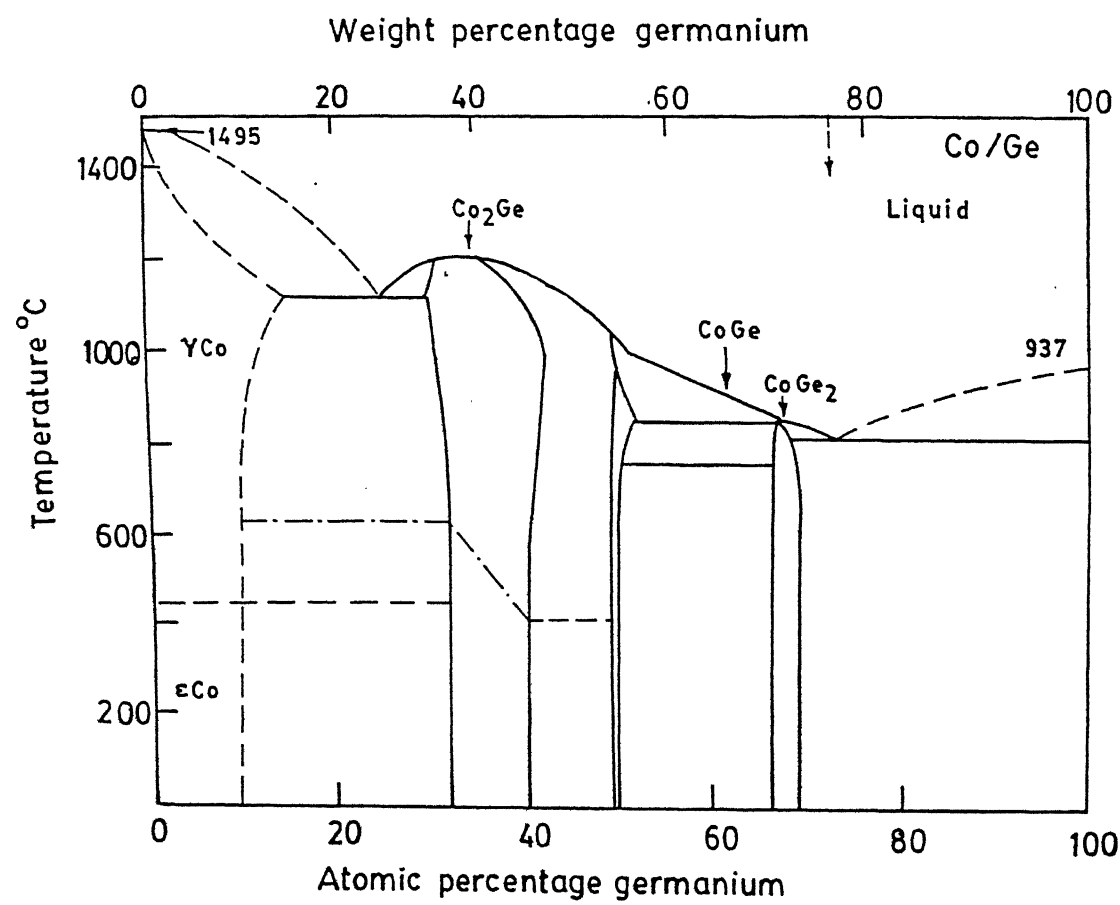


Figure 4.28: Equilibrium phase diagram of Co-Ge system.

Table 4.19: The different useful parameters of Cu/Ge, Ni/Ge and Co/Ge systems.

Binary system A/B	Lattice structure [92]	atomic radii ratio $R=r_B/r_A$ [93]	Equilibrium phase [91]	Width of phase field at% [91]	$-\Delta H_{for}$ kJ/mole [62]	Crystal structure [92]
Cu/Ge	fcc-fcc	0.95	Cu_3Ge	4	16	Cu_3Ti
			Cu_5Ge	8	> 16	Mg
Ni/Ge	fcc-fcc	0.98	Ni_2Ge	0	37	Co_2Si
			$NiGe$	0	32	MnP
			Ni_3Ge	2.5	25	Cu_3Au
Co/Ge	hcp-fcc	0.97	Co_2Ge	12	15	Co_2Si
			CoGe	3	16	$FeSi$
			$CoGe_2$	3	12	$PdSn_2$

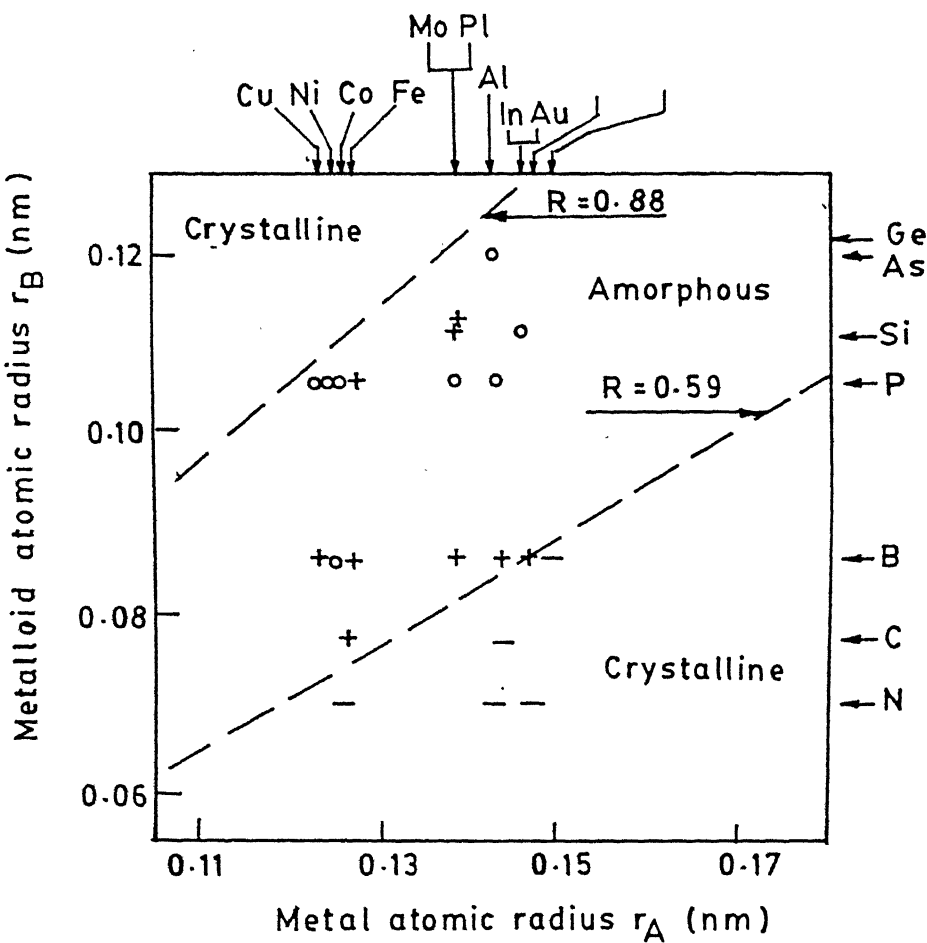


Figure 4.29: Hagg radii ratio diagram

The formation of phase can be also predicted by structure difference rule[53] of Liu (column 3 of Table 4.18). This rule states that an amorphous binary alloy will be formed by ion-beam mixing of multilayer samples when the two constituents are of different crystalline structures. Thus according to this rule in case of Co/Ge (hcp-fcc) one expects an amorphous phase but for Cu/Ge (fcc-fcc) and Ni/Ge (fcc-fcc) one expects a compound. Later Liu[54] proposed an extended structure difference rule based on the equilibrium phase diagram of the binary system under consideration (column 4 of Table 4.18).

The extended structure rule states that (1) if the overall composition is in the two phase region of the phase diagram, an amorphous phase is most likely to form, (2) if the overall composition is in or near the single phase region of the phase diagram and structure of this phase is not simple, an amorphous phase is likely to be formed and finally, (3) if the overall composition is in or near the single phase region of the phase diagram and the structure of the phase is simple, a crystalline phase is formed. From the phase diagram (Fig 4.26-Fig 4.28) of these systems it is evident that the composition of all multilayer samples of Cu/Ge, Ni/Ge and Co/Ge are within the stable single phase region therefore according to third rule a compound phase should be formed in each case.

Brimhall et al.[59] as well as others[60, 61] have pointed out that for better predictions, atomic mobilities and widths of the phase field width (ΔX) have to be taken into consideration. It has been found that the situation for a phase having large phase field is different than a line compound in the phase diagram. For example, Ni/Al system[61] has three phases in the phase diagram NiAl ($\Delta X = 50$ at.%), $NiAl_3$ (line compound, $\Delta X = 0$ at.%) and Ni_3Al (small phase field, $\Delta X = 4$ at.%). Room temperature ion-beam mixing in multilayer samples with composition 3:1 and 1:1 form a crystalline disordered cubic phase Ni_3Al and crystalline NiAl phase respectively. But for 1:3 composition an amorphous $NiAl_3$ phase is formed[25] as this is a line compound with complex (orthorombic) crystal structure. However, for Sb/Al systems[87] the SbAl rhombohedral phase is formed in case of bilayer sample at 77 K whereas in multilayer

case an amorphous phase is formed. It may be noted that Sb/Al system has a single line compound SbAl in the phase diagram. Brimhall et al.[59] have pointed out that the phase field wider than 10 at.% are stable whereas they become unstable below a few atom percent. In our case Cu_3Ge , Ni_2Ge and Co_2Ge phases have phase widths $\Delta X = 4$ at.%, 0 at.% and 9 at.% respectively. We suggest that the formation of stable compound phases due to irradiation at room temperature and above are probably due to the high atomic mobilities of the atoms. There are many other reports of stable compound phase formation (Co_2Si , Pd_2Ge , Pd_2Si etc.) for these kind of narrow phase fields. The lowest is the TiRu which has a phase field width 0.8 at%[60].

In summary, we have shown that the formation of crystalline phases is possible in these systems depending on certain conditions viz., temperature, structure, atomic size, phase width etc. In the following section we shall discuss the formation of “first phase” by ion-beam mixing and thermal annealing with the help of existing rules.

4.4.3 Formation of “First phase”

In many metal/semiconductor systems[42, 57, 88–90], it has been found that when one studies the sequences of phase formation by thermal annealing and ion-beam mixing the phase which synthesizes first in both processes is same in most of the cases. We have shown in Table 4.17 the comparison of the phases produced by ion-beam mixing and thermal annealing in metal/semiconductor systems. Our results for germanide systems (also presented in Table 4.17) clearly show that the “first phase” produced by thermal annealing and by ion-beam mixing are same for all the three systems.

Similarity of ion-beam mixing and thermal annealing results in metal/semiconductor systems can be viewed through the phase diagram. The correlation between “first phase” produced by thermal annealing in a bilayer sample and the phase diagram was proposed by Walser and Bene[98]. Their rule states that the phase to grow first upon thermal annealing of a bilayer sample is the highest congruently melting compound next to the lowest melting eutectic one in the phase diagram. On a similar line, for

ion-beam mixing in metal/Si systems, Lau et al.[57] proposed that the “first phase” which would produce, is the highest congruently melting compound next to the lowest melting eutectic in the phase diagram provided the atoms have sufficient mobility to form compound.

From Cu-Ge phase diagram (Fig 4.26) we find that the lowest temperature eutectic is at the position of 63 at.% of Cu shown by dashed vertical line. Therefore, it is expected that Cu_3Ge compound should form first. This is consistent with our thermal annealing and ion mixing results. In case of Ni/Ge system, the eutectic point is at 67 at.% of Ge so the first phase is expected to be Ni_3Ge_2 . But our experimental results of ion-beam mixing and thermal annealing show that it is the Ni_2Ge phase which forms first. Similarly for Co/Ge system this rule predicts that the $CoGe_2$ phase should form first whereas we obtained Co_2Ge phase in our experimental studies. Such violations of the prediction of Lau et al or Walser and Bene rule have been reported for other silicide systems viz. Co/Si[27] etc.

Let us consider the sequence of phase formation on the basis of thermodynamic point of view according to which “the phase corresponding to highest negative heat of formation has the largest chemical driving force and hence should form first”[27]. From Table 4.19 the heat of formation of Cu_3Ge phase is - 16 kJ/mole of atom[99] while the value for ζ phase is not available. From the phase diagram (Fig 4.26) it is seen that the melting temperature of ζ phase is slightly higher than that of Cu_3Ge phase signifying that the heat of formation of ζ phase should be higher than that of Cu_3Ge phase. Thus, from the thermodynamic point of view the ζ phase should form first. In case of Ni/Ge system the values of heat of formation of Ni_2Ge , NiGe and Ni_3Ge phases are -37, -32 and -25 kJ/mole of atom respectively (Table 4.19). Therefore, in this case Ni_2Ge is expected to form first which is in accordance with the ion-beam mixing and thermal annealing experimental results. For Co/Ge system, the values of heat of formation for CoGe, Co_2Ge and $CoGe_2$ being -16, -15 and -12 kJ/mole of atom respectively, CoGe phase should form first. But experimental results show that Co_2Ge has formed first. Similar deviations (like Cu/Ge and Co/Ge) from the heat of formation rule have been

reported in many metal/Si systems[27]. However, it is to be noted that the difference in energy values of the phases in all such cases being very close to each other, any phase can appear as a first phase. Thus the thermodynamics alone cannot predict the formation of phases in these cases. In short, none of the criteria mentioned above could simultaneously explain the formation of the “first phase” in all the three cases.

The similarity of ion-beam mixing and thermal annealing in the formation of equilibrium phases suggests that both thermodynamic and kinetic considerations[100] have to be taken into account since in case of thermal annealing, it is assumed that in determining the sequence of phase formation, kinetic factors dominate over the thermodynamic driving forces[27] where as in ion-beam mixing the kinetic restriction is normally relaxed. In the following, a rule proposed by Pretorius based on the calculation of effective heat of formation[56] which considers both thermodynamics and kinetics aspects will be discussed.

The kinetic barrier and effective heat of formation are both related to the number of atoms taking part in the reaction which in turn are related to the atomic mobility and supply of atoms during phase formation. The effective concentration at the reacting interface could be influenced by many other factors such as diffusivity, temperature etc. Pretorius et al. assumed that the effective concentration at the reacting interface is the concentration of the lowest temperature eutectic. Based on this concept the rules for phase formation proposed by Pretorius et al. are

1. The first compound phase to form during interaction of two elements is the phase having the largest negative effective heat of formation ($\Delta H'$).
2. The second phase to form at the interface between the phase and the remaining element is the next phase richer in the unreacted element which has the most negative heat of formation.

The effective heat of formation $\Delta H'$ i.e., the total heat released in the reaction is equal to the product of the heat of formation and the total number of atoms used in the reaction. One can write $\Delta H'$ as[27]

$$\Delta H' = \Delta H \times \frac{\text{The available concentration of the limiting element}}{\text{The compound concentration of the limiting element}} \quad (4.1)$$

It can be seen from the above expression that for each phase, the most negative $\Delta H'$ and therefore the release of the highest energy from the system occurs, when the atomic concentration matches with a particular compound i.e. $\Delta H' = \Delta H$. The effective heat of formation diagrams can be easily constructed by plotting the heat of formation ΔH and its compositional concentration and completing the triangulation by connecting those points to the end points of the concentration axis.

Figure 4.30a shows the $\Delta H'$ diagram calculated for Cu/Ge system. The ΔH value for Cu_3Ge is -16 kJ/mole. The maximum value of $\Delta H'$ is thus -16 kJ/mole which is shown by point 'a' in the figure. The triangle is constructed by connecting this point to 0 and 100 on the concentration axis. In the absence of the value of ΔH for Cu_5Ge phase we have assumed that the difference of ΔH between Cu_3Ge and Cu_5Ge phases is small because of the relatively small change in composition and melting temperatures[47]. For the purpose of estimation, we have considered a slightly higher ΔH value for Cu_5Ge phase than that of Cu_3Ge phase as shown by the point 'b'. The actual value might be different from this but certainly it is not below the value of Cu_3Ge phase. It may be noted that the value of $\Delta H'$ for Cu_3Ge phase is larger for Cu concentration below 76%. Therefore, according to the Pretorius' rule, in this case Cu_3Ge phase should form first as the effective heat of formation $\Delta H'$ is larger for Cu_3Ge at the eutectic concentration of 60% Cu. However, since the actual ΔH value of Cu_5Ge phase is not correctly known and for Cu concentrations below 76% the difference in the $\Delta H'$ values is small, it is possible that either Cu_3Ge or Cu_5Ge could form at the interface. In reality, the actual concentration of the limiting element available at the interface and the formation of first phase depends on several factors viz. diffusing species, their mobilities, presence of other impurities etc. It appears that, in the present case of Cu/Ge system these factors contribute in such a manner that the "available concentration of the limiting element" (i.e. Cu) favours the formation of Cu_3Ge phase at the interface.

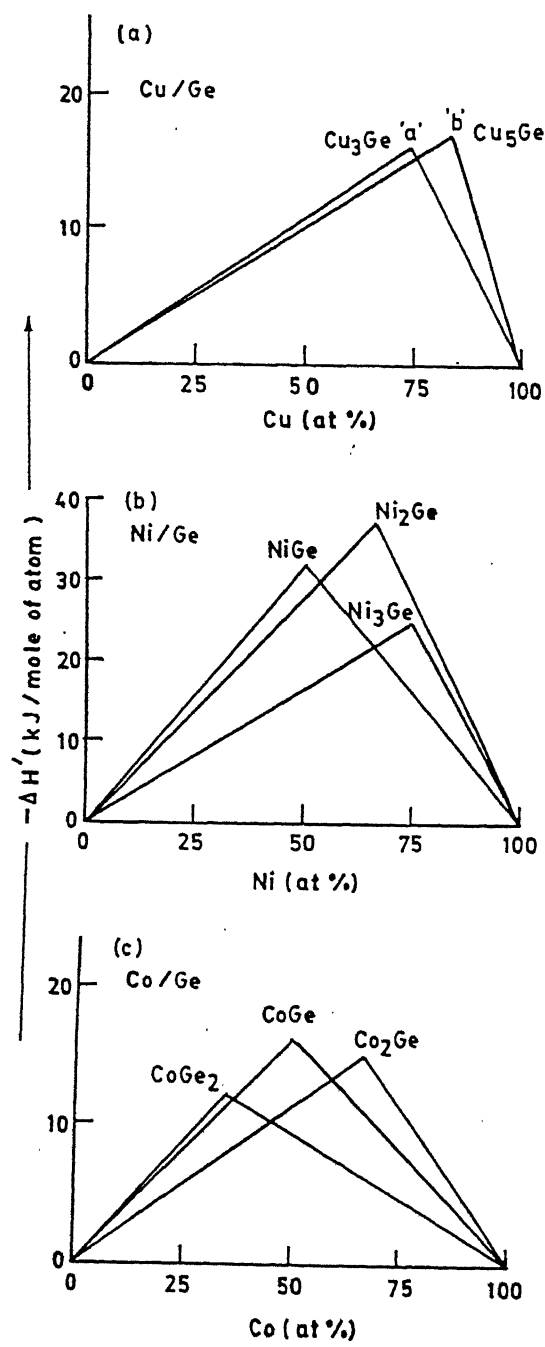


Figure 4.30: Effective heat of formation diagram for (a) Cu/Ge (b) Ni/Ge and (c) Co/Ge systems.

The $\Delta H'$ diagram for Ni-Ge system is shown in Fig 4.30b which shows that at the eutectic concentration of 66% Ge, $NiGe$ phase has the largest negative heat of formation and hence would form first. But we have observed that Ni_2Ge phase forms first in both ion-beam mixing or thermal annealing. The NiGe phase is produced subsequent to Ni_2Ge formation. This can be explained from the ΔH diagram by considering the supply of atoms which actually determine the available concentration across the interface. It is seen from Fig 4.30b that Ni_2Ge has largest negative heat of formation for Ge concentration of less than 47%. Above 47% Ge concentration NiGe has largest negative heat of formation. At 33% of Ge, Ni_2Ge phase has highest effective heat of formation. In this case, Ni and Ge are almost equally mobile (see Chapter 5). The occurrence of Ni_2Ge as a first phase can be seen from the following calculations. For illustration, we calculate the effective heat of formation $\Delta H'$ by considering that 25% of total Ge atoms are available for reaction at the reacting interface. The effective heat of formation for NiGe phase at the same interface is

$$\Delta H' = -32 (25\% / 50\%) = -16 \text{ kJ/mole of atom.}$$

For $NiGe_2$ phase the effective heat of formation at the same interface is

$$\Delta H' = -25 (25\% / 66\%) = -9.5 \text{ kJ/mole of atom.}$$

Similarly, for Ni_2Ge phase the effective heat of formation at the same interface is

$$\Delta H' = -37 (25\% / 33\%) = -28 \text{ kJ/mole of atom.}$$

The formation of Ni_2Ge phase is followed by the formation NiGe phase (which has second highest effective heat of formation for Ge concentration less than 47%) at the Ni_2Ge and Ge interface because at this interface Ge supply will be more.

For Co/Ge system, the $\Delta H'$ diagram is shown in Fig 4.30c. In this case Co_2Ge phase has the largest $\Delta H'$ for Ge concentration less than 41%, $CoGe_2$ has most negative heat of formation for the Ge concentration greater than 65% and CoGe phase has most negative heat of formation between 42% and 64% of Ge. The heat of formation for these three phases are almost equal. In this case Ge is the only moving specie. On the basis of calculations similar to the one performed for Ni/Ge system it can be shown that in case of Co/Ge system, Co_2Ge phase will appear first followed by the growth of

CoGe phase at the Ge and Co_2Ge interface.

To summarize, in this section it has been shown that the formation of first and subsequent phases in metal/Ge systems can be understood on the basis of effective heat of formation idea and the mobility of the species.

4.5 Conclusions

The conclusions of this chapter are given below.

1. It has been shown for the first time that MeV ion-beam mixing is an efficient low temperature process for producing stable equilibrium phases in Cu/Ge, Ni/Ge and Co/Ge systems.
2. In the case of multilayer samples, ion-beam mixing as well as thermal annealing lead to the formation of Cu_3Ge , Ni_2Ge and Co_2Ge as "first phase". In case of Cu/Ge system, another Cu rich phase Cu_5Ge , has also been observed at higher doses.
3. In case of bilayer samples, thermal annealing produces Cu_3Ge , Ni_2Ge and Co_2Ge phases as "first phase". At higher annealing temperatures above 475 K NiGe and CoGe phases have been observed as "second phase" in Ni/Ge and Co/Ge systems.
4. The "first phase" formed by thermal annealing and ion-beam mixing is same in all the cases.
5. The formation of crystalline phases by ion-beam mixing in these systems is in accordance with the prediction of the existing empirical rules.
6. The first and subsequent phase formation can be explained on the basis of the effective heat of formation rule and by considering the mobility of the atomic species.

7. The resistivity values of Cu_3Ge , Ni_2Ge and Co_2Ge layers produced by ion-beam mixing are 20, 50 and 74 $\mu\Omega - cm$ respectively. The resistivities of the phases produced by thermal annealing are 8.6, 23 and 50 $\mu\Omega - cm$ respectively. It is important to note that these resistivity values are lower as compared to metal silicides. Hence it is expected that these germanide phases would become important for semiconductor industry.

Chapter 5

Mobility of species during ion-beam mixing

5.1 Introduction

In the previous chapter we have shown the formation of compound phase by ion-beam mixing. It has also been argued that it is the dominant moving species that control the first and subsequent phase formation. In this chapter¹ we will describe the experimental results of the atomic movements across the M/Ge interface during the synthesis of germanide phases by ion-beam mixing.

¹Part of this work is published in Semiconductor Devices Ed. Krishan Lal, International conference on semiconductor devices, India, 1996 (Narosa Publishing House, New Delhi) p 502.

5.2 Experimental

Bilayer samples ($SiO_2/M/Au(marker)/Ge$) having a Au film of thickness less than 1 nm acting as a marker for monitoring the atomic motions across the interface, were prepared by e-beam evaporation technique. In all these samples Ge was deposited as the top layer.

The ion-beam mixing at different temperatures were performed by 1 MeV Kr^+ and Ar^+ ions for different doses in the range of $(2 - 20) \times 10^{15} \text{ ions/cm}^2$. At this energy most of the irradiating ions are transmitted through the bilayer structure. The deposited energy distribution was calculated using TRIM code[78]. The Rutherford back scattering (RBS) measurements with 1.3-1.5 MeV He^+ beam were carried out to study the composition of the mixed layers and movement of metal and Ge atoms across the interface by monitoring the position of the marker. The RUMP simulation code[81] was used to simulate all such RBS spectra.

5.3 Experimental results

Typical RBS spectra of a sample ($SiO_2/Cu/Au(marker)/Ge$) in the as prepared condition and after performing mixing at room temperature using Kr ions for a dose of $1 \times 10^{16} \text{ Kr}^+/\text{cm}^2$ are shown in Fig 5.1. The simulation analysis shows the composition of the mixed region as $Cu_{75}Ge_{25}$ (or Cu_3Ge). This type of growth of germanide phase requires a mass flow of one or both species across the marker leaving a different amount of material in front of the marker. This is equivalent to have a cover layer which results into an energy loss producing a shift in the position of the marker signal in the RBS spectrum. In this case Au marker has moved towards lower energy side after mixing. Also, there is a spreading in the Au peak which is due to the movement of Au atoms in Ge and Cu layers. However, the peak position is more important for evaluating the relative migration of the atoms of the two adjacent layers[101].

The movement of the marker signal is determined by measuring the energy dis-

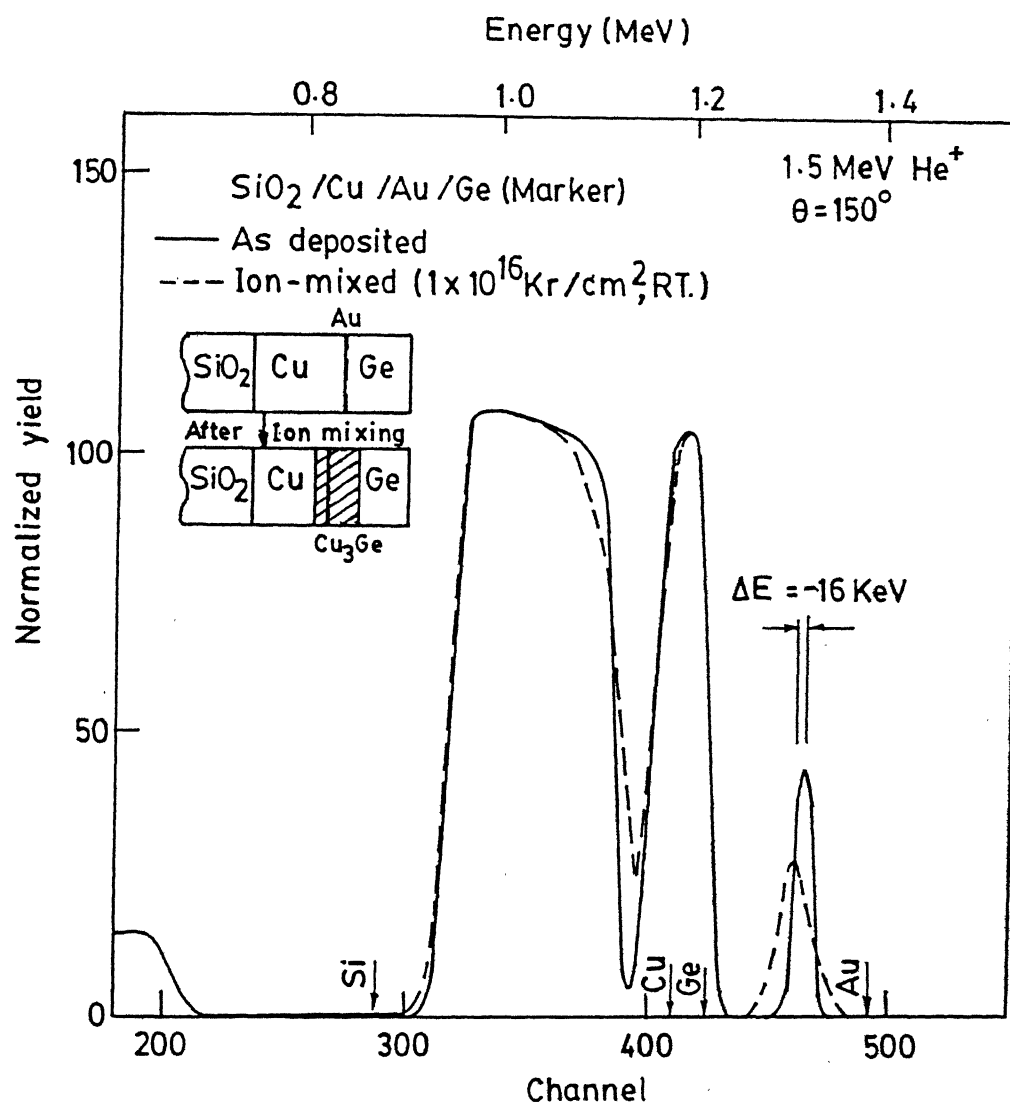


Figure 5.1: The RBS spectra of Cu/Ge sample embedded with Au marker layer at the interface. The continuous line shows RBS spectrum of as-prepared sample while the dashed line spectrum is taken after ion-beam mixing. The Au marker shifts towards low energy side suggesting dominating motion of Cu atoms.

placement (ΔE) of marker peak position. For measuring ΔE we have followed a sign convention since it can shift in either lower or higher energy side after mixing. The negative sign will be used for the marker movement towards the lower energy side and positive sign for movement towards the higher energy side. Analysis of the spectra presented in Fig 5.1 gives the energy shift of the marker position as -16 keV. The marker is located in the mixed region (Cu_3Ge) of total thickness 25 nm of which 17 nm is on the higher energy side of the marker as shown in Fig 5.1. This gives the ratio of the flux of Cu and Ge across the interface as 7:1. Other samples irradiated for different doses using Kr and Ar ions, whose RBS spectra are not shown here, also show marker movement towards the lower energy side. This shift increases with increasing ion dose. The shift in the marker position is plotted in Fig 5.2 as a function of the thickness of the germanide layer. The top(bottom) solid line is drawn from the calculated value for the extreme case where only Ge(Cu) atom is mobile. These results show that the Cu and Ge both are mobile but Cu is the dominant mobile species. d'Heurel et al.[47] have reported similar movements of Cu and Ge in thermal annealing experiments performed with Xe marker.

In case of Ni/Ge system, the marker position remains stationary which can be seen from RBS spectra of Fig 5.3 for a sample before and after irradiation at room temperature for a dose of $6 \times 10^{15} \text{ Kr/cm}^2$. This feature has been found for both Kr and Ar ion irradiations for all the doses used in this work. This implies that in case of Ni/Ge system both Ni and Ge are almost equally mobile during the growth of Ni_2Ge phase.

For Co/Ge system, the marker movement is just opposite to that of Cu/Ge system. The RBS spectrum of a Co/Ge sample after irradiation for a dose of $1 \times 10^{16} \text{ Kr/cm}^2$ is shown in Fig 5.4 along with the as-deposited spectrum. Here, the Au peak position has shifted towards higher energy side. The composition of the mixed region is Co_2Ge . The plot of ΔE versus thickness of the mixed (cobalt germanide) layers is shown in Fig 5.5. In this case, the experimental points coincide with the theoretical line calculated by assuming the movement of Ge only. This suggests that for Co/Ge system, Ge atom is

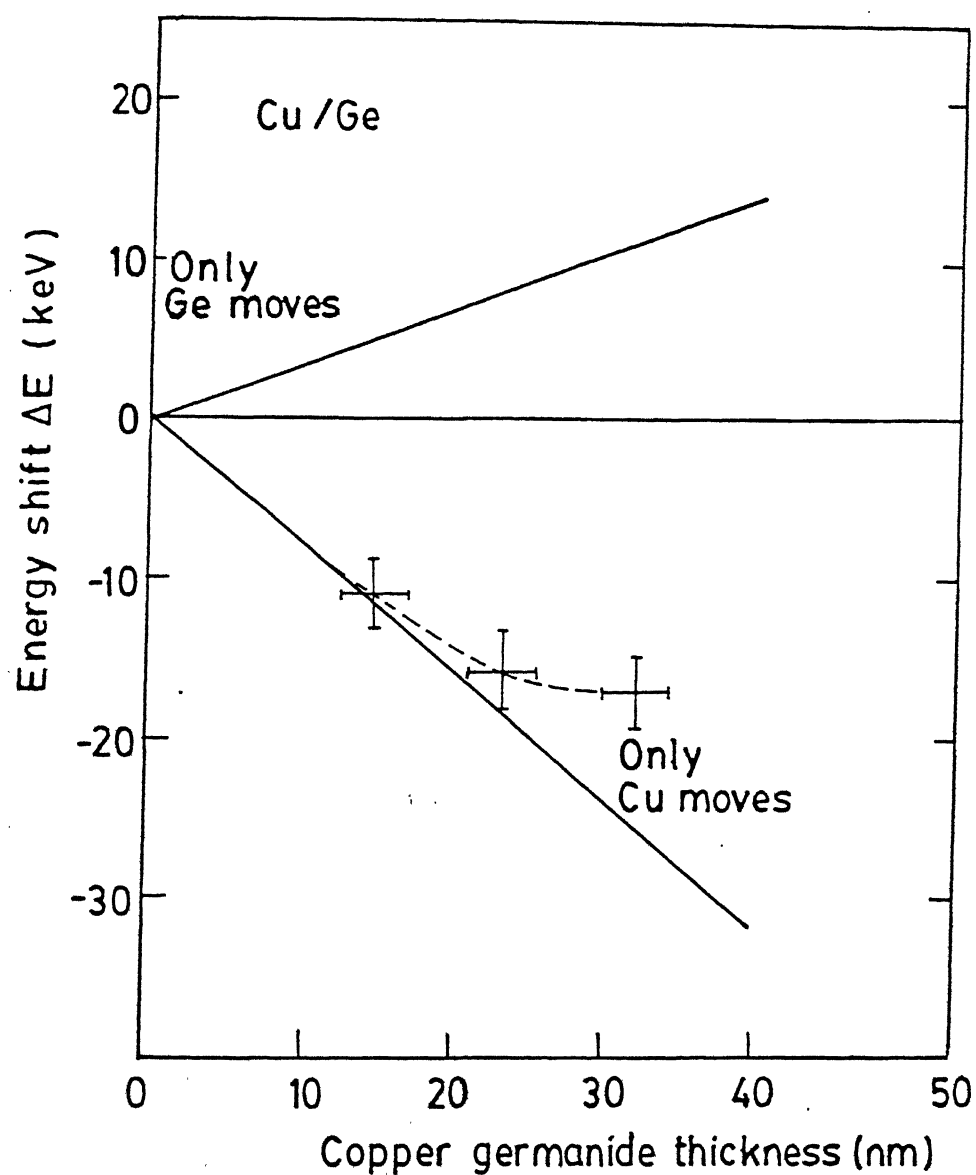


Figure 5.2: The plot of energy displacement ΔE of the marker versus thickness of the Cu_3Ge layers. The upper (lower) continuous line is obtained from the theoretical calculations by considering that only Ge (Cu) atoms are mobile.

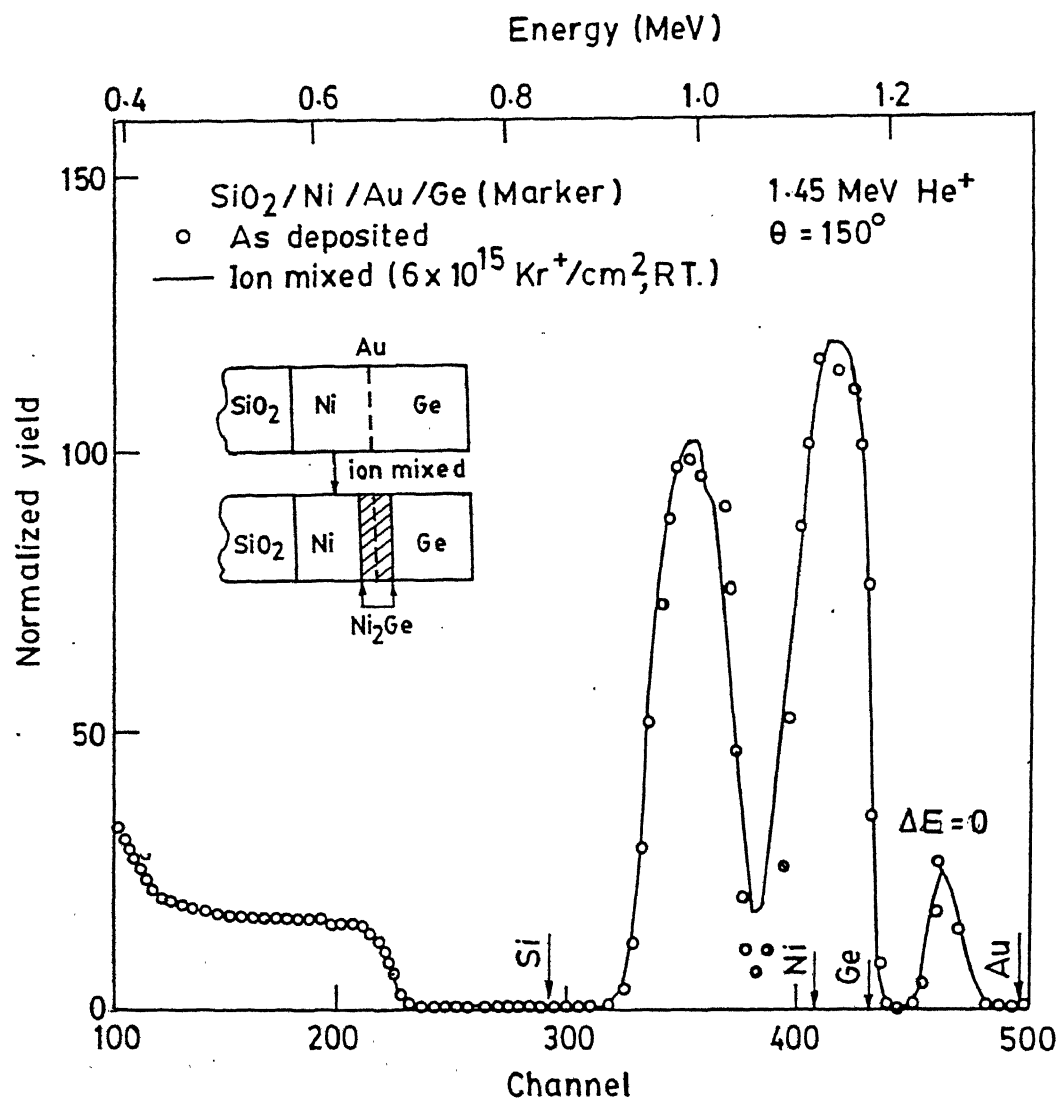


Figure 5.3: The RBS spectra taken before and after ion-beam mixing at RT for a dose of $6 \times 10^{15} \text{ Kr}^+/\text{cm}^2$ of Ni/Ge sample with a Au marker.

the only moving species. Figure 5.6 shows the comparison of RBS spectra of thermally annealed marker samples at different temperatures. Annealing at 480 K for 60 min. shows very little marker movement towards the surface (higher energy side) but at a higher temperature of 580 K when both the layers are completely consumed (forming a CoGe phase) the marker is found on the surface of the bilayer suggesting the movement of Ge atoms only.

5.4 Discussion

We have mentioned earlier that the ion-beam mixing process can be divided into two regimes (1) prompt regime (2) delayed regime. In the prompt regime the incident ions transfer energy to the target atoms producing number of primary recoils in the forward direction and is considered to have a negligible effect to ion-beam mixing[14]. Mixing in the prompt region is mainly due to the secondary recoils which are isotropic. In a collision cascade the lighter target atoms always have a larger displacement as compared to the heavier ones. The experimental results of Tao et al.[102] on twelve binary systems show that the lighter species tend to migrate towards the heavier elements and is correlated with the damage energy via inverse Kirkendall effect. This motion can also be seen from the spike point of view[103]. In a spike the temperature is instantaneously very high for a short duration within a small volume. The reaction in the spike may be treated as a normal thermal process for the duration of that high temperature. This temperature is much higher than the substrate temperature so the variation of ambient temperature should not affect the atomic motion in the spike. This has been shown for Ni/Si and Pt/Si systems[28].

Apart from these collisional effects the movement of atoms is also influenced by the thermodynamic forces[28, 102] which are similar to those operating during thermal annealing. However, the collisional effects are totally absent in the case of thermal annealing. In ion-beam mixing if the two components namely collisional and thermodynamic operate in the same direction then only one element is observed

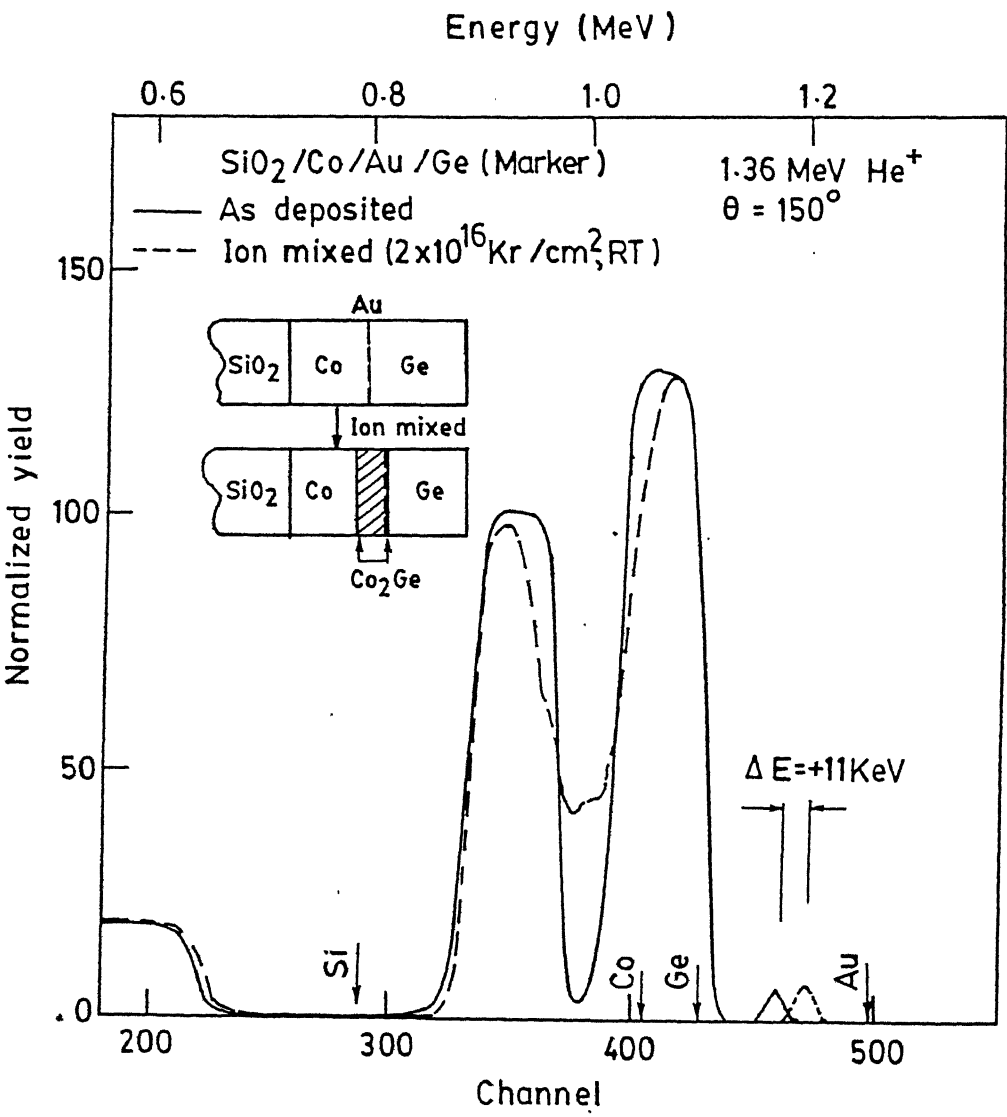


Figure 5.4: The RBS spectra of Co/Ge sample with a Au marker taken before and after ion-beam mixing at RT for a dose of $1 \times 10^{16} \text{ Kr}^+/\text{cm}^2$.

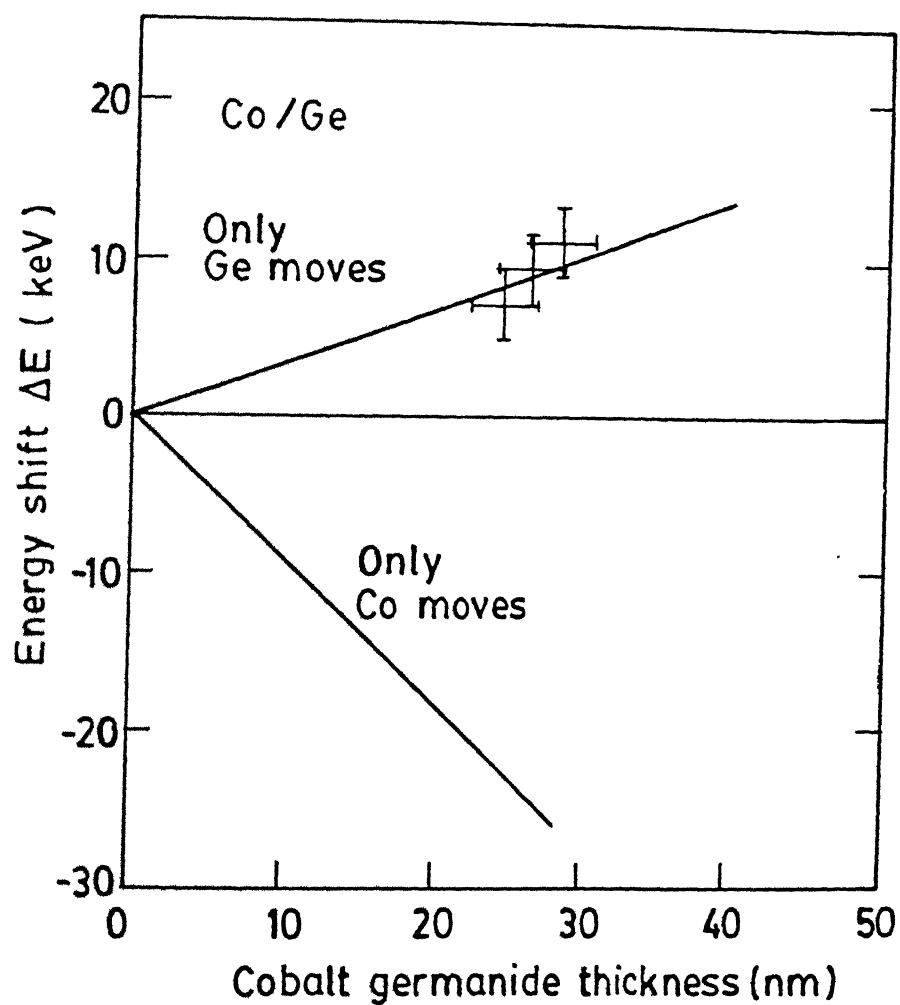


Figure 5.5: The plot of energy displacement ΔE vs. thickness of the cobalt germanide layers. The upper (lower) continuous line is obtained from the theoretical calculations by considering that only Ge(Co) atoms are mobile.

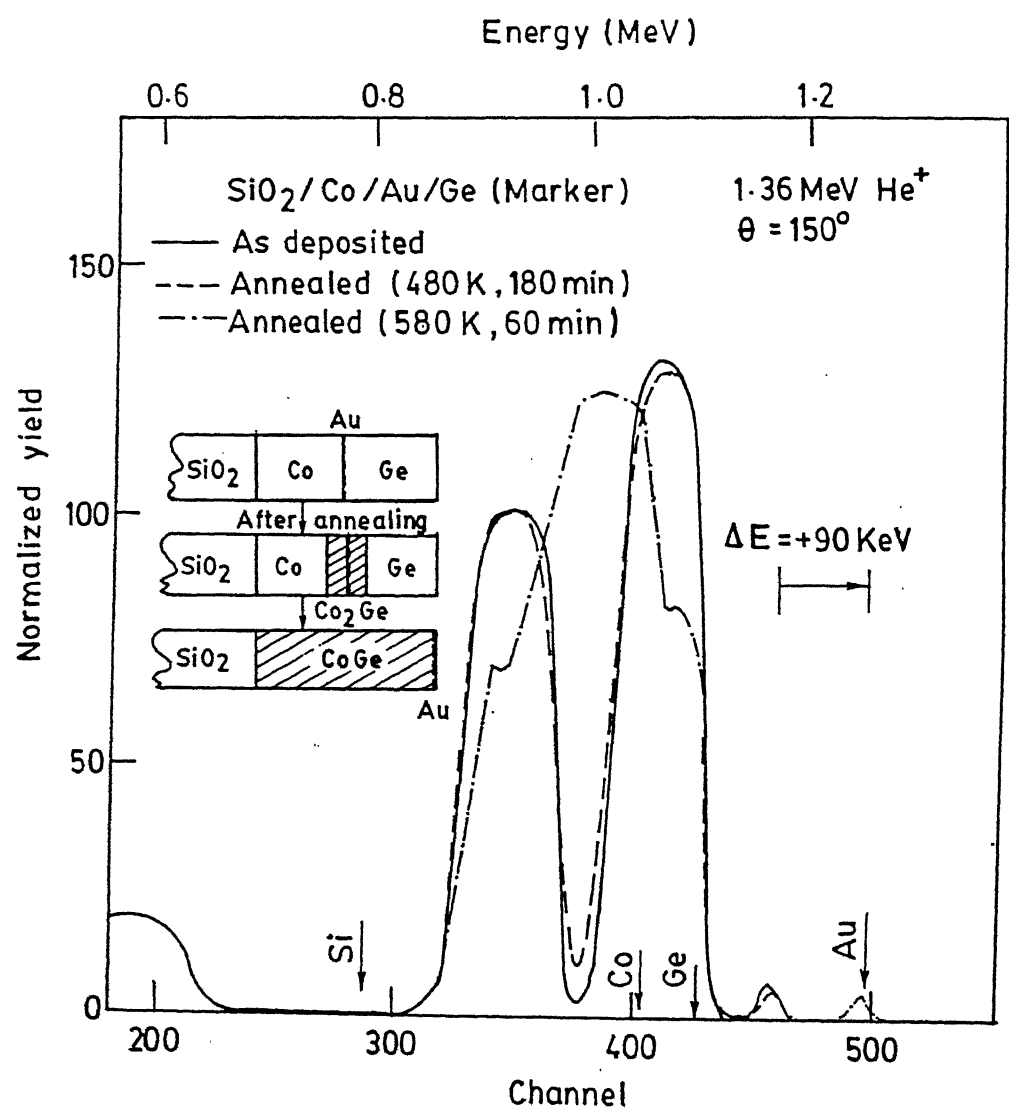


Figure 5.6: The comparison of RBS spectra of Co/Ge marker sample taken before and after thermal annealing at two different temperatures of 480 K and 580 K.

as the moving species and if they operate in opposite direction movement of both elements is expected[102]. This facts can be seen from the experimental data of metal/semiconductors systems given in Table 5.1.

In order to see the effect the collisional process, the distribution of damage energie obtained from the TRIM calculation[79] is shown in Fig 5.7a for Cu/Ge case. According to the inverse Kirkendall effect[102] it is expected that Ge atoms will move in the Cu layer. On the other hand, the results obtained from the thermal reactions[47] show that Cu is the only moving species for the Cu_3Ge phase formation. Thus, for Cu/Ge the two factors namely collisional and thermodynamic are acting in opposite direction resulting into the motion of both Cu and Ge. Our calculation of the ratio of the flux of Cu to Ge which is 7:1 which shows that the thermodynamic processes dominate during mixing as par as the mobility of the atoms is concerned. The equal mobility of Ni and Ge for the case of Ni/Ge systems can be explained in analogous manner.

In case of Co/Ge system Ge should be mobile under collisional effects as predicted by the damage distribution shown in Fig 5.7c. Motion of only Ge atoms has been revealed by thermally annealing experiments. These results suggest that both collisional and thermodynamic effects are acting in the same direction which result in the mobility of Ge atoms only which is in accordance to our observations.

5.5 Conclusion

In summary, we have shown that during the formation of Cu_3Ge phase by ion-beam mixing at room temperature, both Cu and Ge are mobile but Cu is the dominant moving species across the interface while for Ni/Ge system both Ni and Ge are equally mobile for the formation Ni_2Ge phase. However, for Co/Ge system only Ge atoms move to produce Co_2Ge phase.

Table 5.1: Reported results of marker movements in metal/Si systems during thermal annealing and ion-beam mixing

System	Marker	Moving species and flux ratio under thermal annealing	Ion-beam mixing			Phase formed
			Flux species and moving ratio	Atoms whose motion is rela- tive enhanced	Layer of lower damage density	
Si/Ni	W, Ag	Ni only	$\frac{Ni}{Si} \simeq \frac{1}{2} - \frac{2}{1}$	Si	Si	Ni_2Si
Si/Pt	Mo	$\frac{Pt}{Si} \simeq \frac{13}{1}$	$\frac{Pt}{Si} \simeq \frac{1}{1} - \frac{1}{2}$	Si	Si	Pt_2Si
Si/Pd	W	$\frac{Pd}{Si} > 1$	$\frac{Pd}{Si} \ll 1$	Si	Si	Pd_2Si
Si/Mo		Si only	Si only	Si only	Si	$MoSi_2$
Si/W		Si only	Si only	Si only	Si	WSi_2
Si/Cr	W	Si only	Si only	Si only	Si	$CrSi_2$
Si/Mg	W	Mg only	Mg only	Mg only	Mg	Mg_2Si
Ge/Ti	W	$\frac{Ge}{Ti} \simeq \frac{15}{1}$	$\frac{Ge}{Ti} \simeq \frac{7}{1}$	Ti	Ti	$\frac{Ti}{Ge} \leq \frac{6}{5}$
Ge/Mg	W	Mg only	Mg only	Mg only	Mg	Mg_2Ge
Cu/Ge (*)	Au	Cu only	$\frac{Cu}{Ge} \simeq \frac{7}{1}$	Ge	Ge	Cu_3Ge
Ni/Ge (*)	Au	$\frac{Ni}{Ge} \geq 1$	$\frac{Ni}{Ge} = 1$	Ge	Ge	Ni_2Ge
Co/Ge (*)	Au	Ge only	Ge only	Ge	Ge	Co_2Ge

* represents present work and other data from ref 101

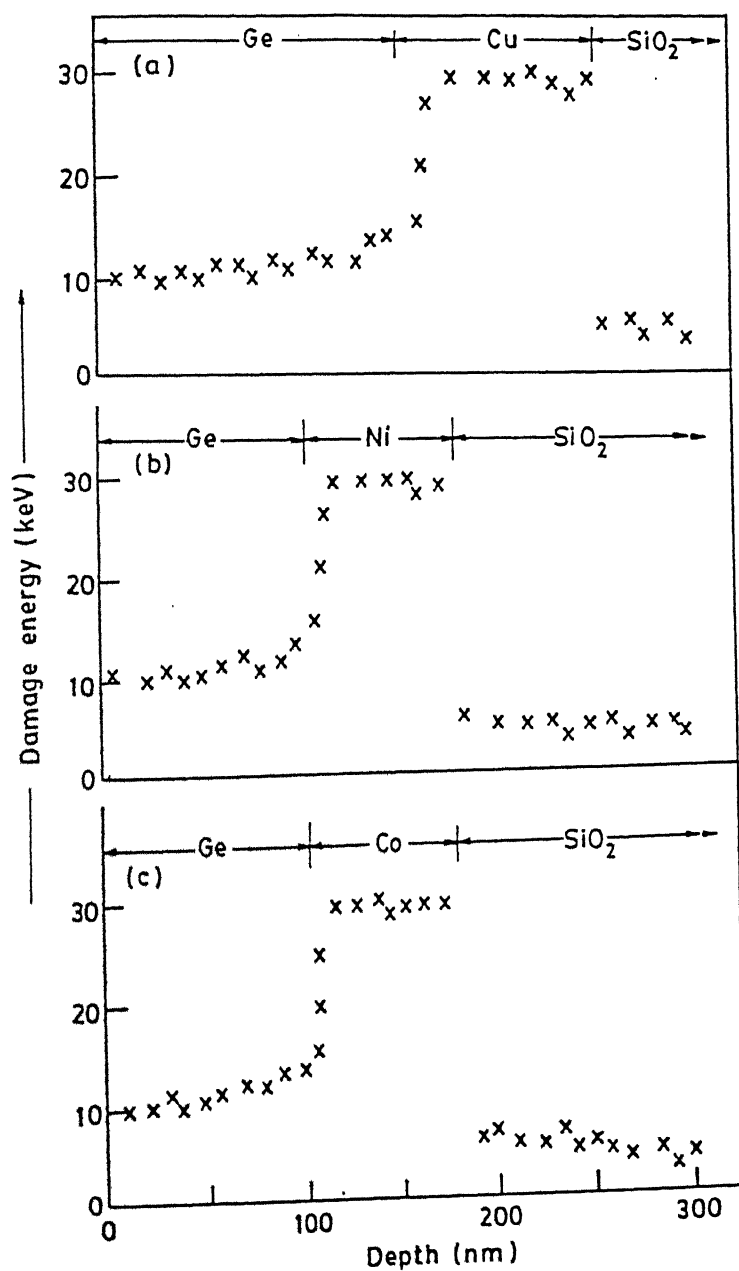


Figure 5.7: The distribution of damage energy due to 1 MeV Kr ion bombardment as a function of depth in (a) Cu/Ge and (b) Ni/Ge and (c) Co/Ge systems. Each point (x) corresponds to energy deposition in 10 nm.

Chapter 6

Mechanism of ion-beam mixing

6.1 Introduction

The formation of crystalline compounds in multilayer configuration of M/Ge ($M = \text{Cu, Ni, Co}$) systems by ion mixing has been dealt in Chapter 4. Some basic issues concerning the migration of the different species during mixing have been discussed in the last chapter in the light of the experiments performed using marker configurations. In this chapter¹, we discuss the mechanism of ion mixing in M/Ge systems on the basis of the experimentally determined parameters such as mixing rate, mixing efficiency etc. For this purpose bilayer configuration is the most suitable, since accurate quantification of these parameters is possible in this configuration only. To understand the basic processes of mixing mechanism, the prerequisite is to know the dependence of mixing on ion mass, ion energy, fluence, heat of mixing, cohesive energies, mobilities of the elements, composition of the mixed region etc.

In this chapter the experimental results of ion mixing of M/Ge bilayer systems by Kr and Ar ions at different temperatures are first described. The critical temperature

¹Part of this work is published in Phys. Rev. B 54 (1996) 5769.

T_c above which thermally activated processes set in for these systems, have been determined. Empirical models[20, 23, 51] which estimate the critical temperatures have been discussed.

The experimentally obtained room temperature mixing rates are then compared with the predictions of the existing phenomenological models[19, 22, 24, 31, 50] which show that the existing models cannot explain our results. A new model for compound formation has been proposed which considers mixing to occur under non-overlapping subcascades. The predictions of this model are shown to be in good agreement for highly reactive medium Z bilayer compound forming systems (such as Cu/Ge, Ni/Ge, Co/Ge etc.) where mixing rate is proportional to the deposition energy F_D . In addition, it has been shown that this model also able to explain the observed mixing rate of Ni/Si system reported in the literature[31].

6.2 Experimental

Metal/Ge samples having bilayer configuration (Fig 1.1d) were prepared by sequentially depositing high purity metal M (Cu, Ge, Co) and Ge films on clean fused quartz substrates, without breaking vacuum, using e-gun evaporation system. The total thickness of these bilayer samples was in the range of 150 nm to 270 nm with an overall composition in the vicinity of $M_{50}Ge_{50}$.

Ion-beam mixing was performed in the range of 100-450 K, using 1 MeV Kr^+ and Ar^+ in the dose range of $(2 - 20) \times 10^{15} \text{ ions/cm}^2$. The incident ion flux was kept low ($\leq 5 \times 10^{12} \text{ ions/cm}^2\text{s}^{-1}$) to minimize the rise in the sample temperature. It has been reported that MeV ion irradiations cause a typical rise of about 10 K of the film temperature and the temperature rise in SiO_2 substrate was believed to be higher by another ~ 10 K, suggesting actual rise of sample temperature by 20 K[74]. The values of range and deposited energy densities by the irradiating ions in the target were calculated by Monte Carlo computer program TRIM[78]. In the present case, most of the irradiating Kr and Ar ions (1 MeV) are transmitted through the bilayer

structure. Rutherford backscattering (RBS) measurements with 1.2-1.5 MeV He^+ beam were carried out to determine the composition and growth of the mixed region of irradiated samples. RUMP code[81] has been used to simulate all experimental RBS spectra. RBS spectra of all samples did not show any noticeable oxygen or carbon concentrations. X-ray diffraction measurements were performed using $Cu - k_\alpha$ source. However, the intensity of the peaks were very weak due to small volume of the mixed region. Therefore, the composition obtained from RBS analysis of these bilayer samples after mixing are used to infer about the nature of the phases formed by correlating with corresponding compounds (determined by X-ray analysis) obtained in these systems after ion mixing in multilayer configuration (presented in Chapter 4). The surface morphology for all the samples has been studied by scanning electron microscopy which did not show any noticeable feature before and after ion mixing.

6.3 Results

This section describes temperature dependence of ion-beam mixing in Cu/Ge, Ni/Ge and Co/Ge systems in the range 100 K to 450 K.

6.3.1 Cu/Ge system

The RBS spectrum of an as-deposited Cu/Ge bilayer sample is shown in Fig 6.1 along with the simulated spectrum. This sample consists of a top Ge layer of thickness 100 nm and bottom layer of Cu having a thickness of 50 nm. The simulated structure used for this is shown in Table 6.1. Figure 6.1 also shows the RBS spectrum of the sample taken after ion-beam mixing at room temperature (RT) for a dose of $6 \times 10^{15} Kr^+/cm^2$. The simulated spectrum for the irradiated case is obtained by using a layer structure shown in Table 6.1. The simulation analysis shows a stoichiometric composition of $Cu_{75}Ge_{25}$ across the interface which is indicated by the step in the copper signal at channel number 365. The formation of the stoichiometric composition

is clearly seen in Fig 6.2 which shows the RBS spectrum of the sample irradiated at a higher dose of $8 \times 10^{15} \text{ Kr}^+/\text{cm}^2$. The simulated spectrum is obtained by using two adjacent layers of the mixed region one with an overall composition of $\text{Cu}_{75}\text{Ge}_{25}$ and the other of composition $\text{Cu}_{83}\text{Ge}_{17}$. The layer structure utilized for simulation is given in Table 6.1. Similar results are observed for Ar ion irradiations performed at room temperature. However, the thickness of the mixed region in this case is lower as compared to the one obtained for Kr irradiated samples for the same dose.

The squared thickness (X^2) of the mixed layers of Cu_3Ge phase produced at room temperature due to both Kr and Ar ion bombardment is plotted as a function of dose in Fig 6.3. The slope of the linear dependence gives the value of mixing rates (X^2/Φ) as 20.6 nm^4 and 5.4 nm^4 for Kr and Ar ions respectively. It is to be noted that the thermal annealing of this bilayer samples also show (in Fig 6.4) a linear dependence of the square of the reacted region with annealing time[48] which suggests that the mixing process is like a diffusion controlled process. The variation of mixing rate with the deposited energy density (F_D) at the interface is shown in Fig 6.5 and it is observed that the mixing rate is linearly proportional to F_D . Similar behavior has been reported for many medium Z metal/metal[25, 66, 76] and metal/Si systems[31, 75]. The slope of this line gives mixing efficiency ($X^2/\Phi F_D$) of $13.1 \text{ nm}^5/\text{keV}$. This mixing parameter is a useful measure of the ion mixing since it normalizes the mixing rate with respect to deposited energy, thereby providing a convenient way to compare the results of different systems performed under different irradiation conditions.

The comparison of ion-beam induced effects in Cu/Ge bilayer samples irradiated for a dose of $4 \times 10^{15} \text{ Kr}^+/\text{cm}^2$ at different irradiation temperatures are shown by the RBS spectra of Fig 6.6. At sample temperatures above RT (300 K), mixing occurs at much higher rate. However, the mixing rate at 100 K occurs at almost similar rate as in the case of RT mixing. The mixing rates obtained at RT and 100 K do not differ by more than 20%. The temperature dependence of the mixing rates (normally referred to as Q curve) for Kr^+ ion is plotted in Fig 6.7a. This figure clearly shows that the mixing is nearly temperature independent up to 328 K with a steep increase at higher

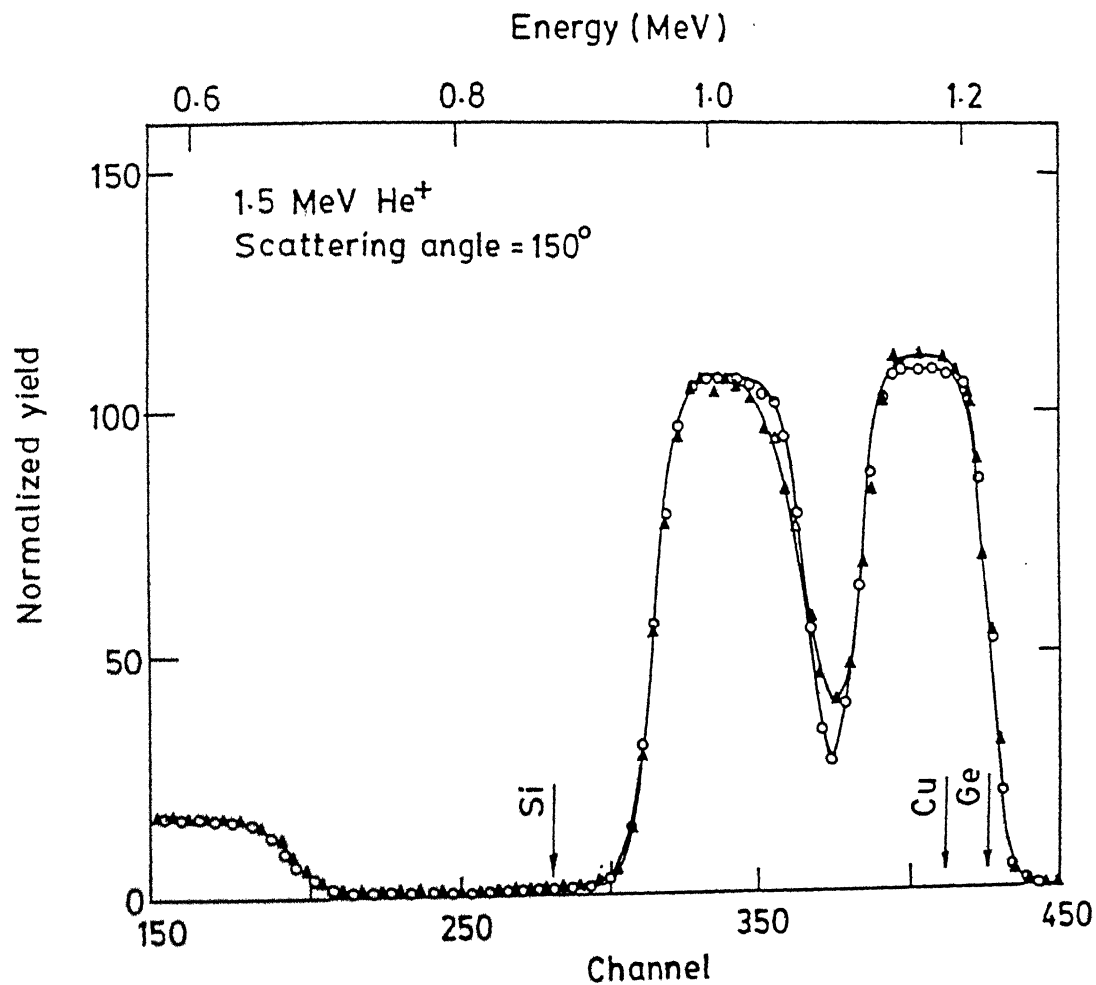


Figure 6.1: Rutherford backscattering spectra of Cu/Ge bilayer thin film on quartz substrate for as-deposited condition (○) and after room-temperature mixing (▲) with 1 MeV Kr ions at a dose of $6 \times 10^{15} \text{ Kr/cm}^2$. The corresponding simulated spectra are shown by solid lines. The arrows show the surface position of different elements.

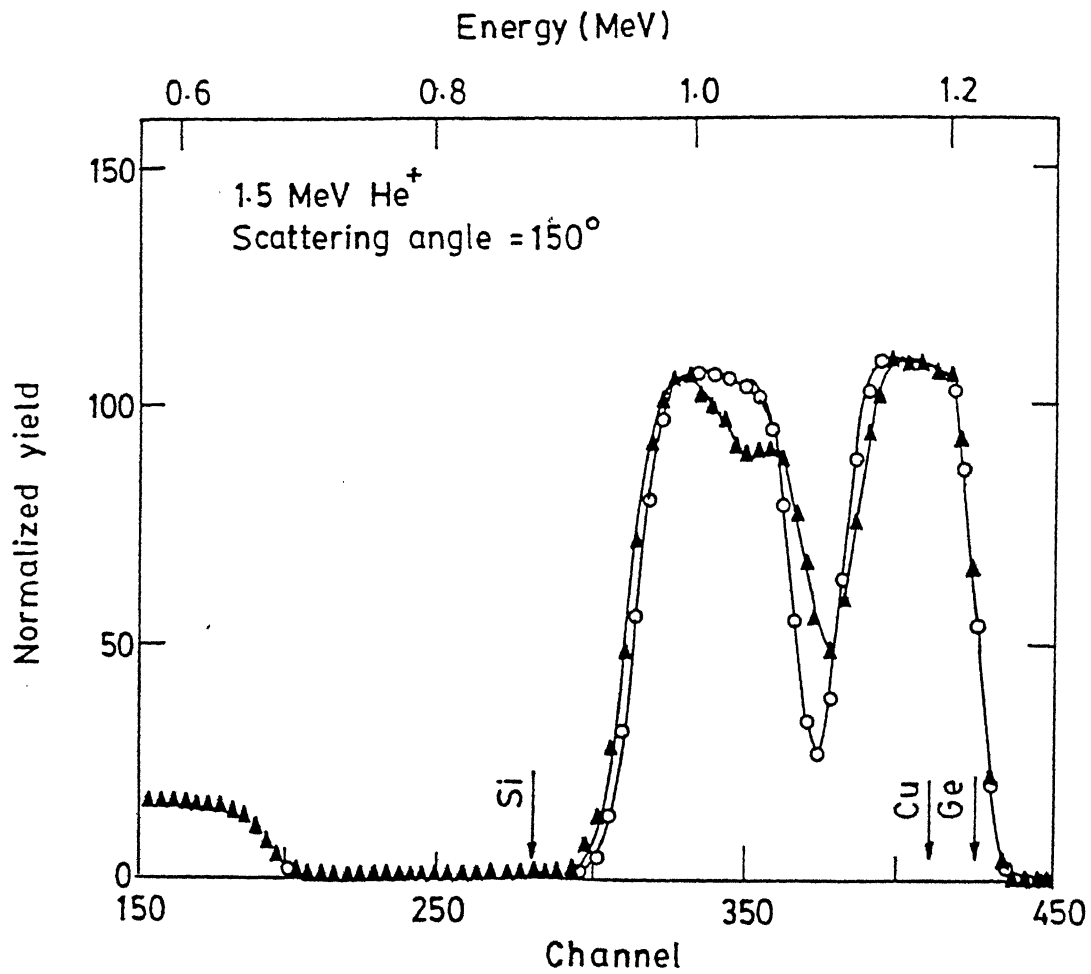


Figure 6.2: Rutherford backscattering spectra of Cu/Ge bilayer thin film on quartz substrate for as-deposited condition (○) and after room-temperature mixing (▲) with 1 MeV Kr ions at a dose of $8 \times 10^{15} \text{ Kr/cm}^2$. The corresponding simulated spectra are shown by solid lines.

Table 6.1: Description of the layer structure used for the simulation of RBS spectra of as-deposited and ion mixed Cu/Ge bilayer samples shown in Figs 6.1 and 6.2.

Sample description	Layer structure used for simulation						
	Layer No.	Thickness (nm)	Composition				
Cu/Ge bilayer film deposited on SiO_2	1	165	Ge	1.00			
	2	105	Cu	1.00			
	3	1000	Si	1.00	O	2.00	
After ion mixing at RT for a dose of $6 \times 10^{15} Kr/cm^2$	1	140	Ge	1.00			
	2	34	Cu	0.75	Ge	0.25	
	3	80	Cu	1.00			
	4	1000	Si	1.00	O	2.00	
After ion mixing at RT for a dose of $8 \times 10^{15} Kr/cm^2$	1	135	Ge	1.00			
	2	30	Cu	0.75	Ge	0.25	
	3	30	Cu	0.83	Ge	0.17	
	1	54	Cu	1.00			
	4	1000	Si	1.00	O	2.00	

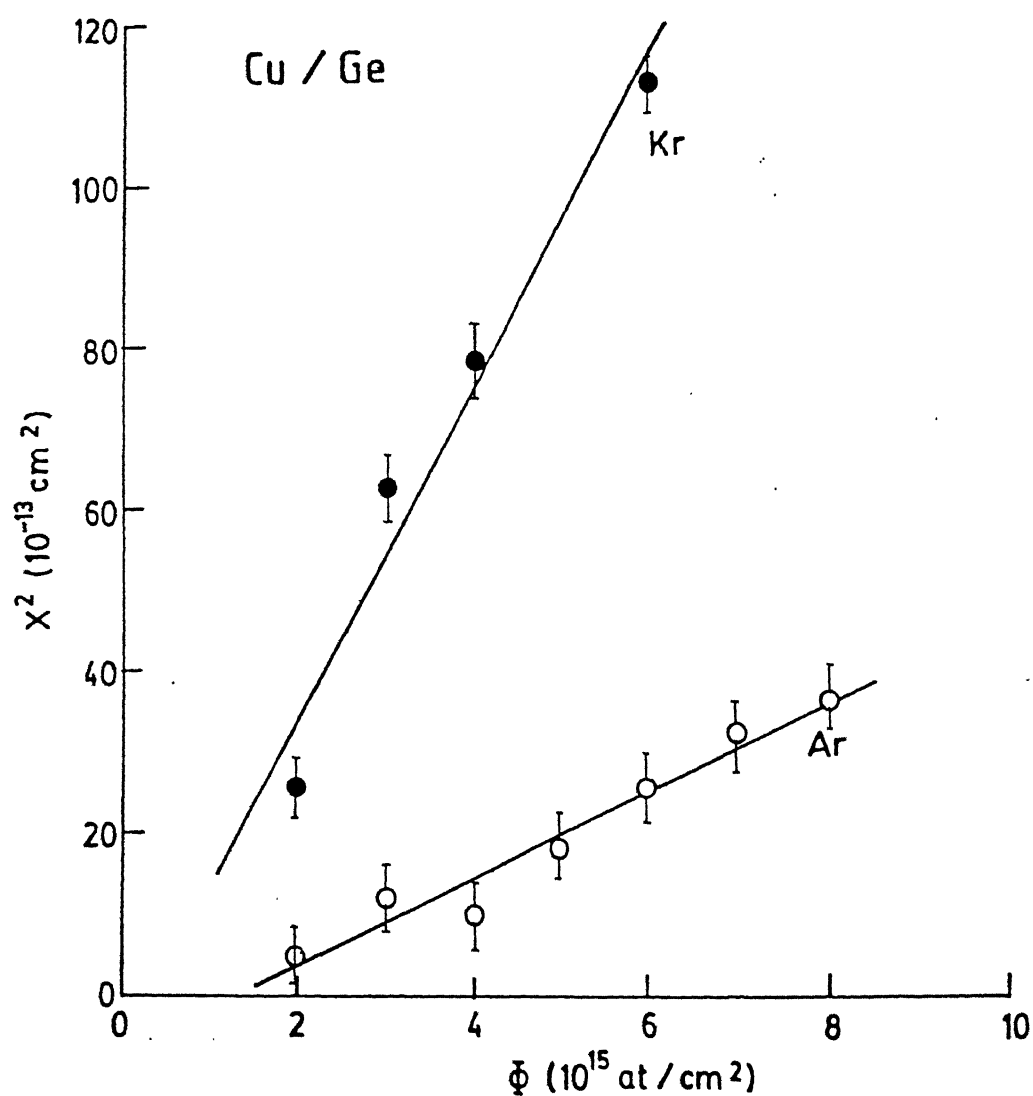


Figure 6.3: Dose dependence of squared thickness of mixed layers of composition Cu_3Ge formed across the interface of Cu/Ge bilayer system irradiated at room temperature with 1 MeV Ar ions (\circ) and Kr ions (\bullet) respectively.

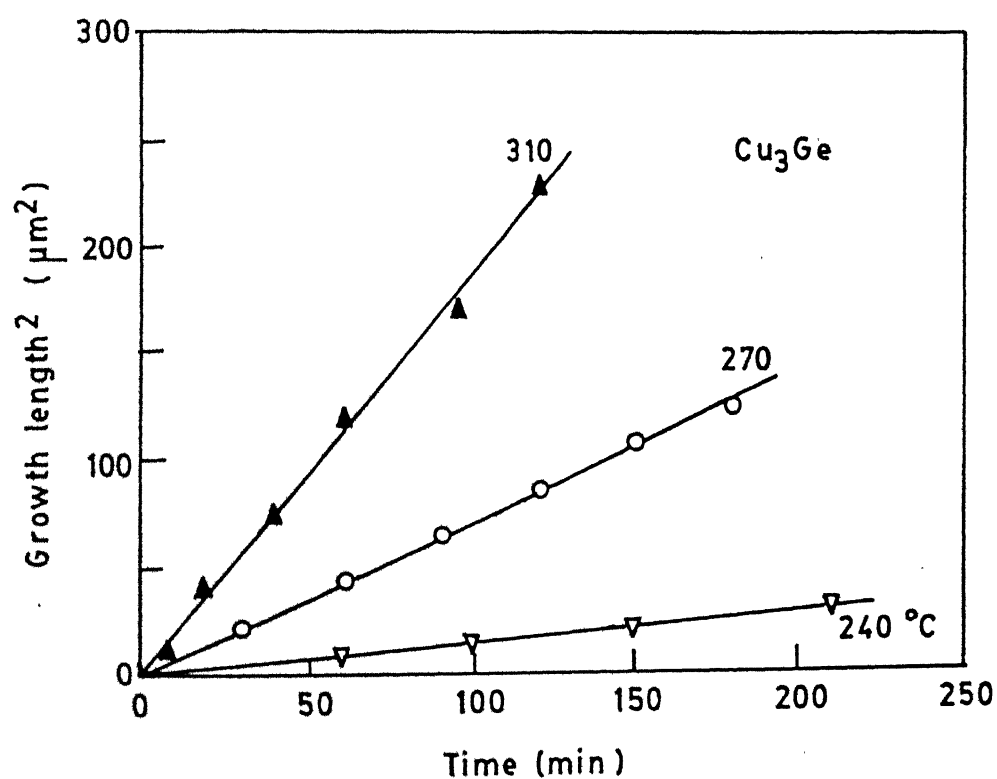


Figure 6.4: The squared thickness of the reacted layer of composition Cu_3Ge formed across the interface of Cu/Ge bilayer system after thermal annealing is shown as a function of annealing time for different temperatures (after ref 48).

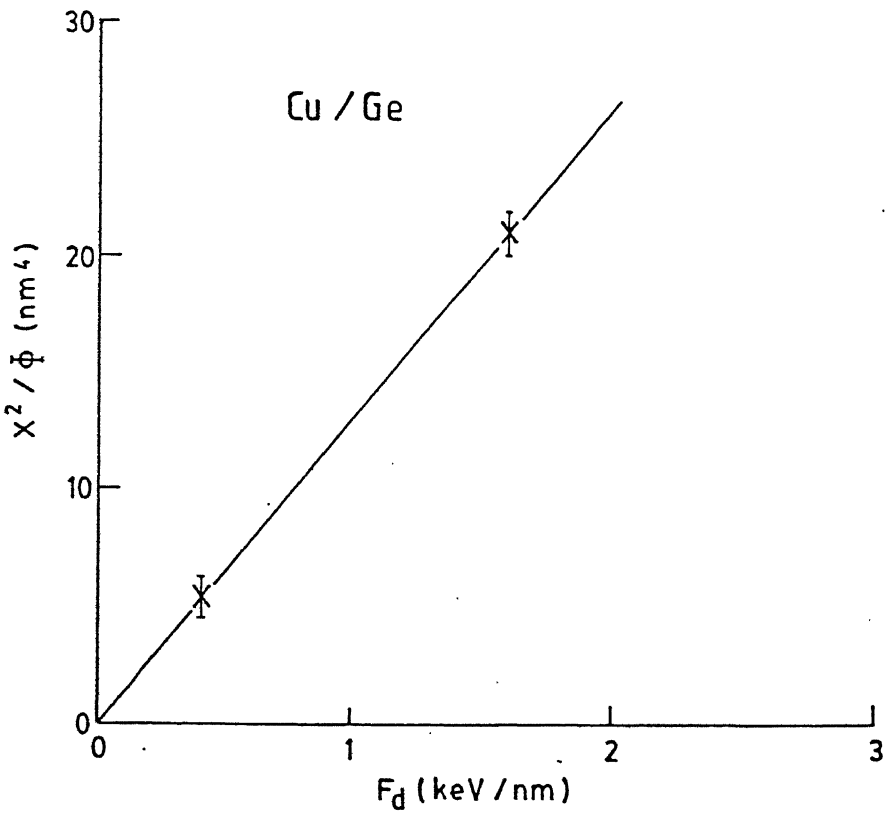


Figure 6.5: The variation of mixing rate measured in Cu/Ge bilayer system for different deposited energy F_D at the interface.

temperatures. The critical temperature which marks the beginning of the temperature dependent mixing is around 320 K. It is to be noted that for this system, the formation of the equilibrium phase after thermal treatment has been observed above 400 K[47]. However for Ar ions, mixing rate does not exhibit sharp temperature dependence as in the case of Kr. The values of the mixing rates in case of Ar are lower for similar doses but the critical temperature does not change appreciably. The thermally activated contribution can be obtained by subtracting the smallest mixing rate at the lowest irradiation temperature of the Q-curve from the remainder of the curve. The resulting plot for the temperature dependent contribution is shown in Fig 6.7b from which the activation energy E_A of ion mixing of approximately 1 eV is determined. This value is close to the one reported for thermal diffusion[48].

6.3.2 Ni/Ge system

Figure 6.8 shows the RBS spectrum of as-deposited Ni/Ge bilayer sample along with a spectrum taken after performing ion-beam mixing at RT at a dose of $8 \times 10^{15} \text{ Kr}^+/\text{cm}^2$. The step in the Ni signal at channel number 374 in case of irradiated spectrum indicates the formation of a stoichiometric composition at the Ni/Ge interface. The simulated spectra are shown by solid lines and the simulated structures are given in Table 6.2. The simulation analysis of the irradiated sample shows the formation of a composition of $\text{Ni}_{66}\text{Ge}_{34}$ similar to the multilayer Ni/Ge sample as described in Chapter 4. RBS analysis of ion mixed samples at other irradiation doses (at room temperature) by Kr and Ar ions show formation of mixed layer of similar composition. This composition belongs to one of the stable compound phases, Ni_2Ge in the equilibrium phase diagram (as shown in Fig. 4.27 of Chapter 4). Note that we have identified this compound in case of ion-beam mixing of multilayer samples as well.

The dose dependence of the squared thickness (X^2) of the mixed layers produced by Kr and Ar ion bombardments at RT are shown in Fig 6.9 where for both cases linear variation is observed which is similar to the case of Cu/Ge system. For comparison,

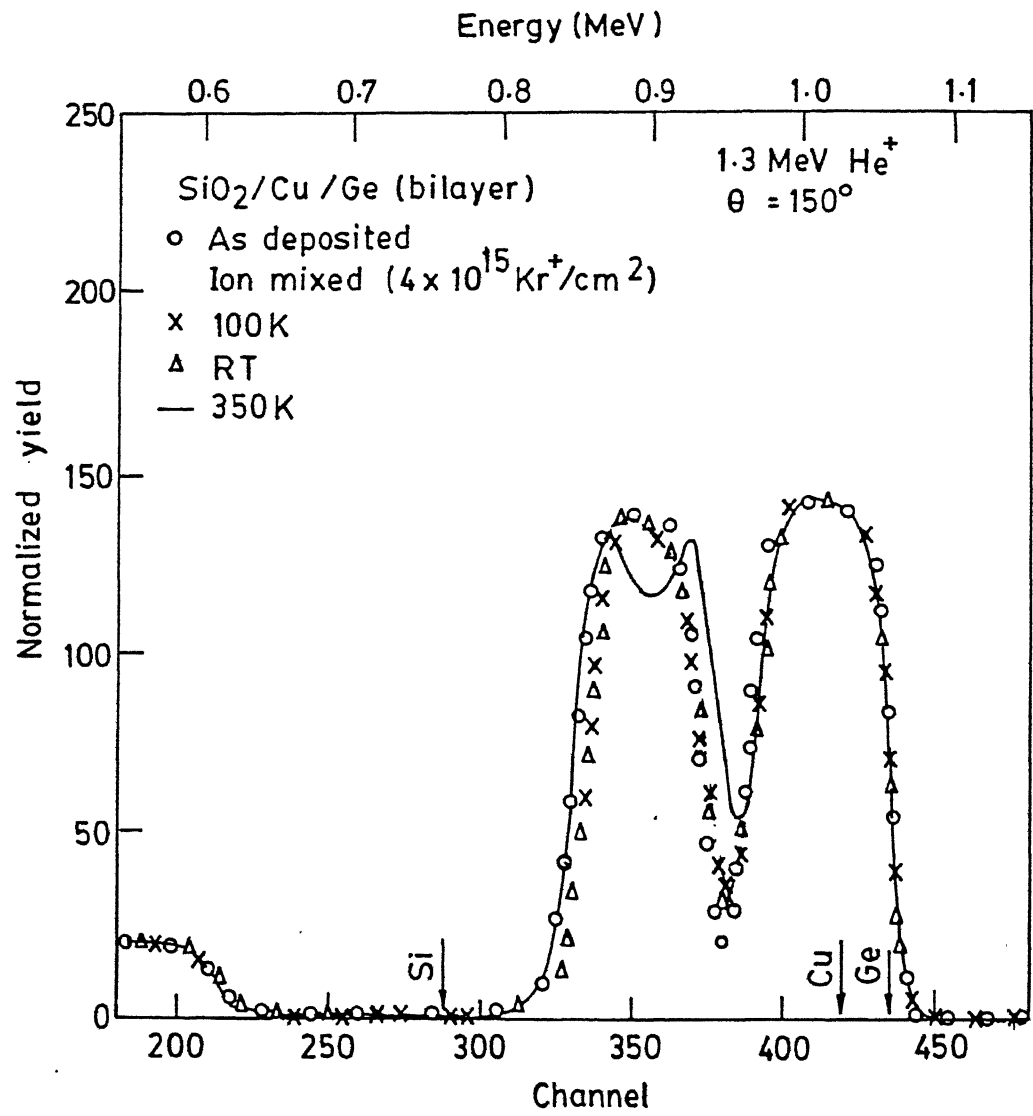


Figure 6.6: Rutherford backscattering spectra of Cu/Ge bilayer film on quartz substrate for as-deposited condition and after mixing for a dose of $4 \times 10^{15} \text{ Kr}/\text{cm}^2$ at 100 K, RT and 350 K.

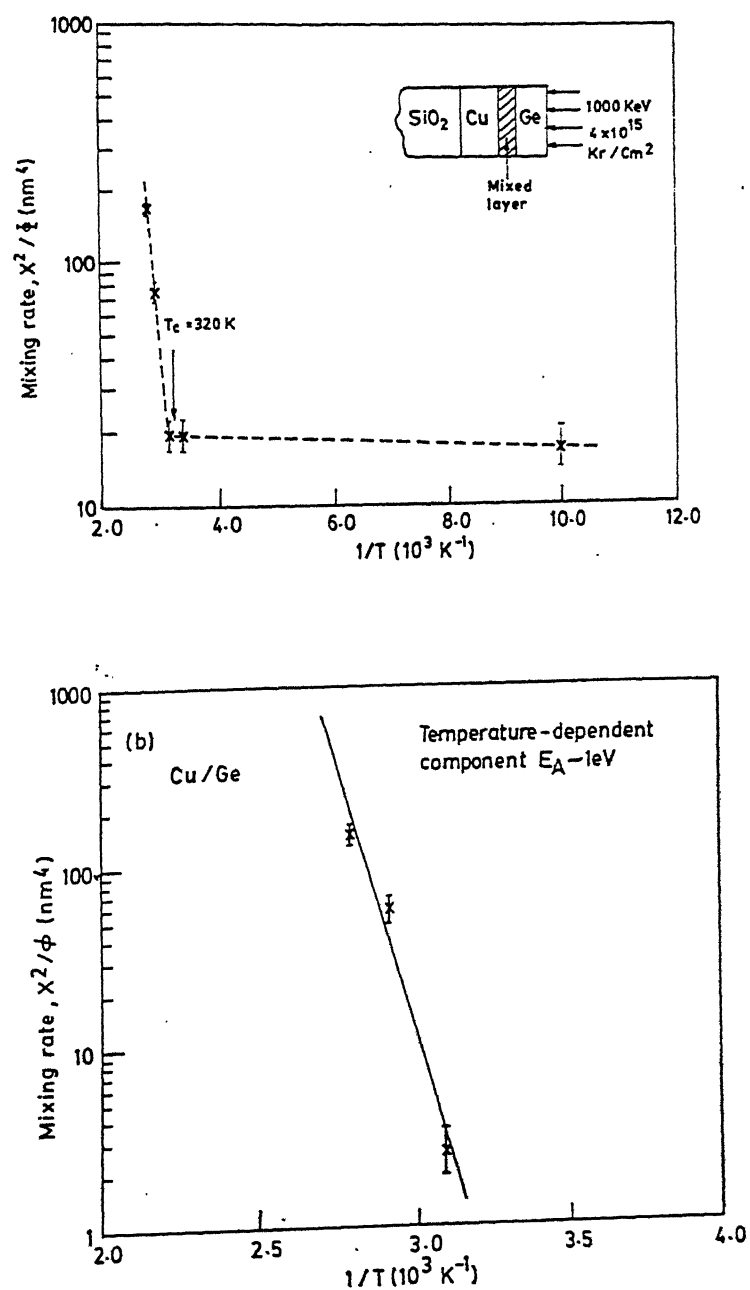


Figure 6.7: (a) The variation of mixing rate for Cu/Ge bilayer system as a function of reciprocal of substrate temperature for a dose of 4×10^{15} Kr/cm² (b) Arrhenius plot of the mixing rate as a function of reciprocal of substrate temperature extracted from Fig. 6.6a.

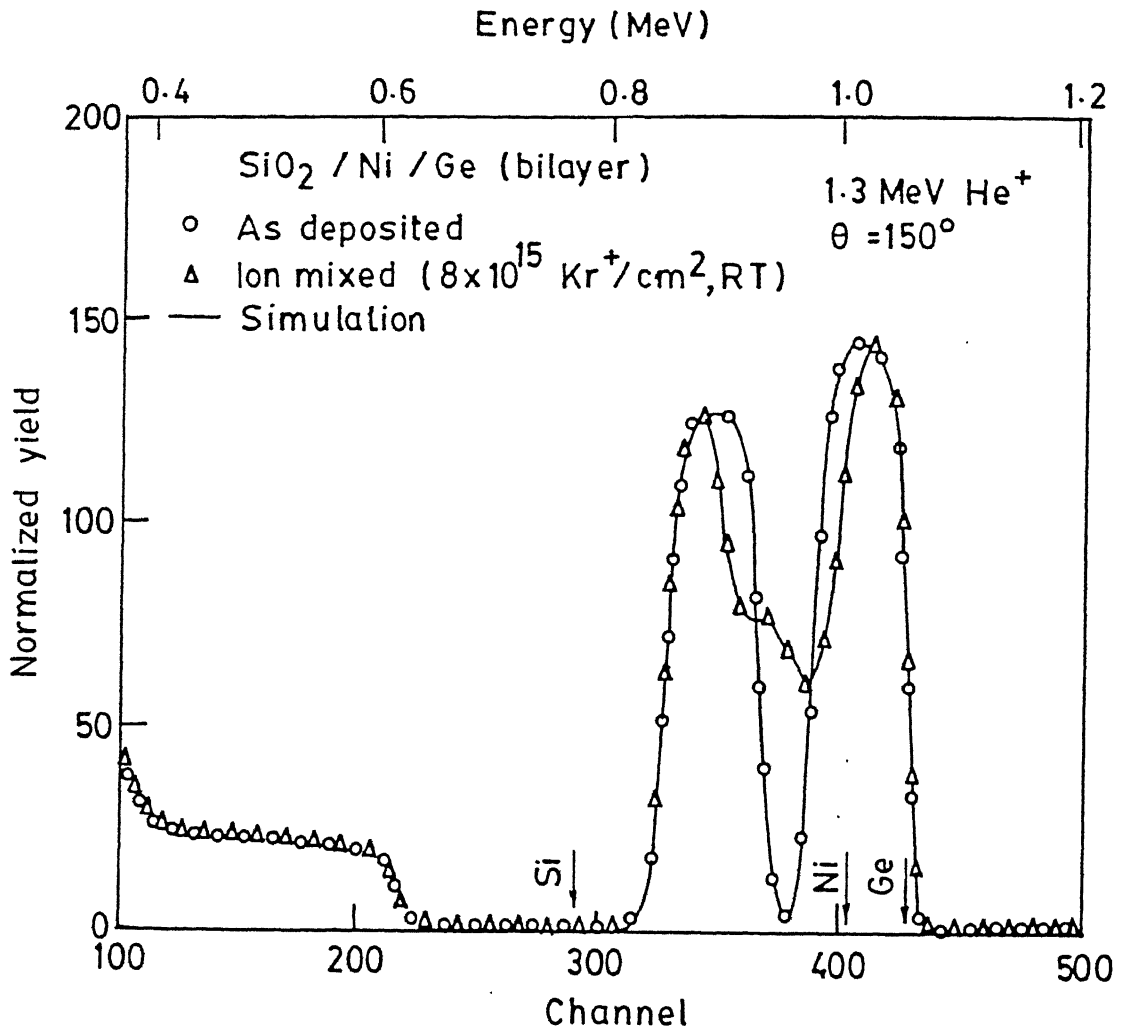


Figure 6.8: Rutherford backscattering spectra of Ni/Ge bilayer thin film on quartz substrate for as-deposited condition and after room-temperature mixing with 1 MeV Kr ions at a dose of 8×10^{15} Kr/cm². The corresponding simulated spectra are shown by solid lines.

Table 6.2: Description of the layer structure used for the simulation of RBS spectra of before and after ion mixing in Ni/Ge bilayer sample shown in Fig 6.8.

Sample description	Layer structure used for simulation					
	Layer No.	Thickness (nm)	Composition			
Ni/Ge bilayer film deposited on SiO_2	1	111	Ge	1.00		
	2	60	Ni	1.00		
	3	1000	Si	1.00	O	2.00
After RT ion mixing for a dose of $8 \times 10^{15} Kr/cm^2$	1	82	Ge	1.00		
	2	46	Ni	0.66	Ge	0.34
	3	37	Ni	1.00		
	4	1000	Si	1.00	O	2.00

Fig 6.10 shows the variation of square of the reacted layer thickness (X^2) as a function of different annealing durations at 480 K. The values of mixing rate (X^2/Φ) obtained from the studies of dose dependence are found to be 18.5 nm^4 and 5.6 nm^4 for Kr and Ar ions respectively. The dependence of mixing rate on the deposited energy density, F_D , at the interface is shown in Fig 6.11. The mixing rate varies linearly with F_D and mixing efficiency obtained from the slope of this curve is $11.3 \text{ nm}^5/\text{keV}$.

The RBS spectra of Fig 6.12 compare the effect of Kr irradiation at 400 K for a dose of $6 \times 10^{15} \text{ Kr}^+/\text{cm}^2$ with the as-deposited one. In this case the amount of mixing is much higher than that obtained at RT or 100 K for the same dose. The Q curves for Kr ion irradiations are plotted in Fig 6.13a. The critical temperature for this system is 326 K and is shown by an arrow. Only the temperature dependent part of mixing is shown in Fig 6.13b from which the value of activation energy E_A of 0.3 eV is obtained.

6.3.3 Co/Ge system

The RBS spectra of Fig 6.14 show the as-deposited Co/Ge bilayer sample along with the spectrum taken after ion-beam mixing at a dose of $1 \times 10^{16} \text{ Kr}^+/\text{cm}^2$. The simulated spectrum (solid line) for the irradiated case is obtained using a composition of $\text{Co}_{66}\text{Ge}_{34}$ which corresponds to the Co_2Ge phase (see Fig 4.28 of Chapter 4). The detail of the layer structure used for simulation of the as-deposited and irradiated samples are given in Table 6.3. The variations of X^2 as a function of incident Kr and Ar dose are shown in Fig 6.15 whereas Fig 6.16 shows the variation of (X^2) as a function of annealing duration. This suggest that the mixing process is like a diffusion controlled process. The dependence of mixing rate on F_D is shown in Fig 6.17. The value of mixing rates at room temperature are found to be 7.7 nm^4 and 1.6 nm^4 for Kr and Ar ions bombardment respectively. The slope of the line in Fig 6.17 gives mixing efficiency of $4 \text{ nm}^5/\text{keV}$. The Q curve for Kr ion irradiations is plotted in Fig.17. The critical temperature for this system is 347 K and is shown by arrow in Fig 6.18a. The activation energy E_A of 0.15 eV is obtained from the temperature dependent part as shown in Fig 6.18b.

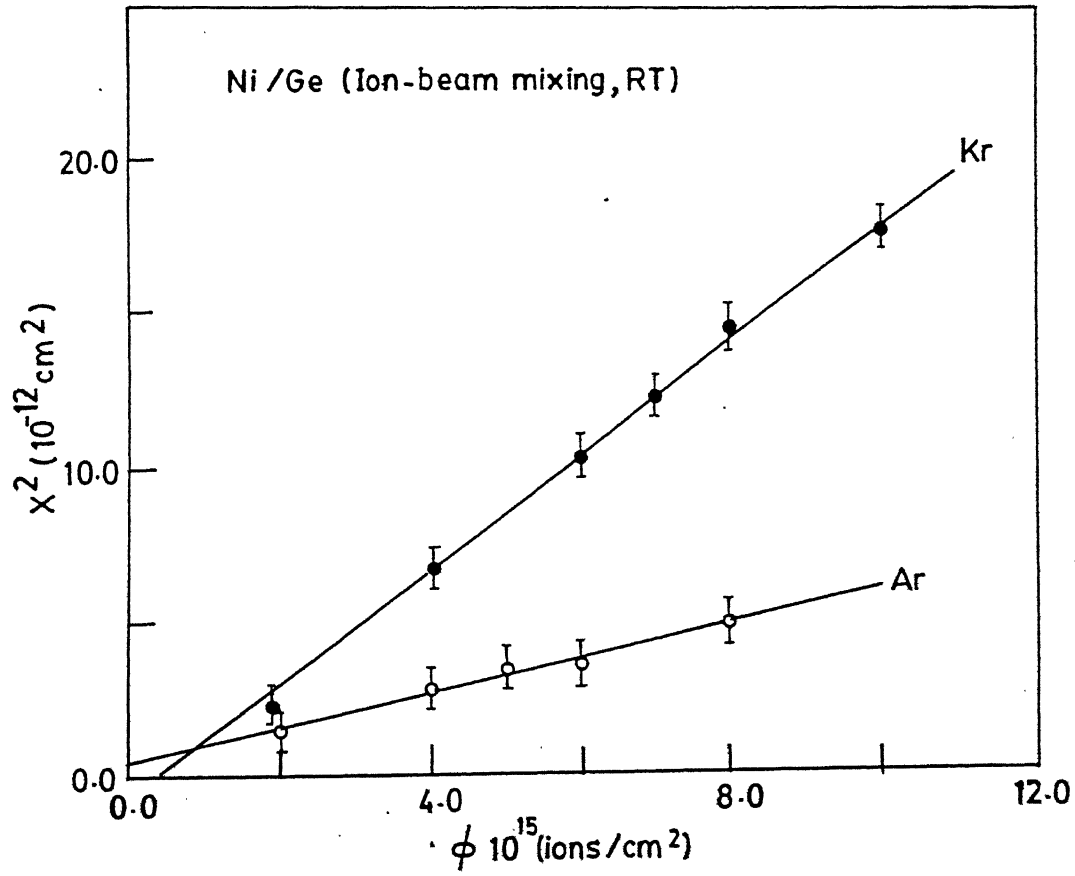


Figure 6.9: Dose dependence of squared thickness of mixed layers of composition Ni_2Ge formed across the interface of Ni/Ge bilayer system irradiated at room temperature with 1 MeV Ar ions (○) and Kr ions (●) respectively.

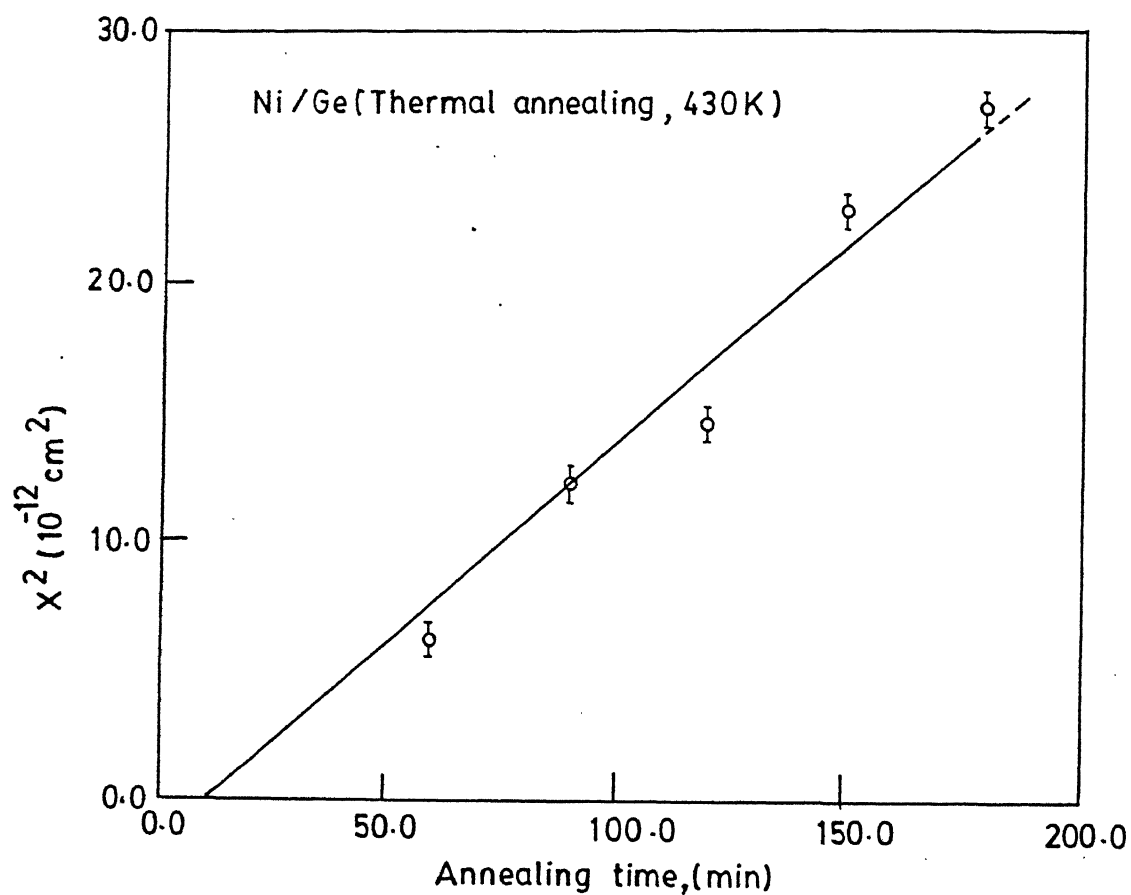


Figure 6.10: The squared thickness of the reacted layer of composition Ni_2Ge formed across the interface of Ni/Ge bilayer system after thermal annealing is shown as a function of annealing time.

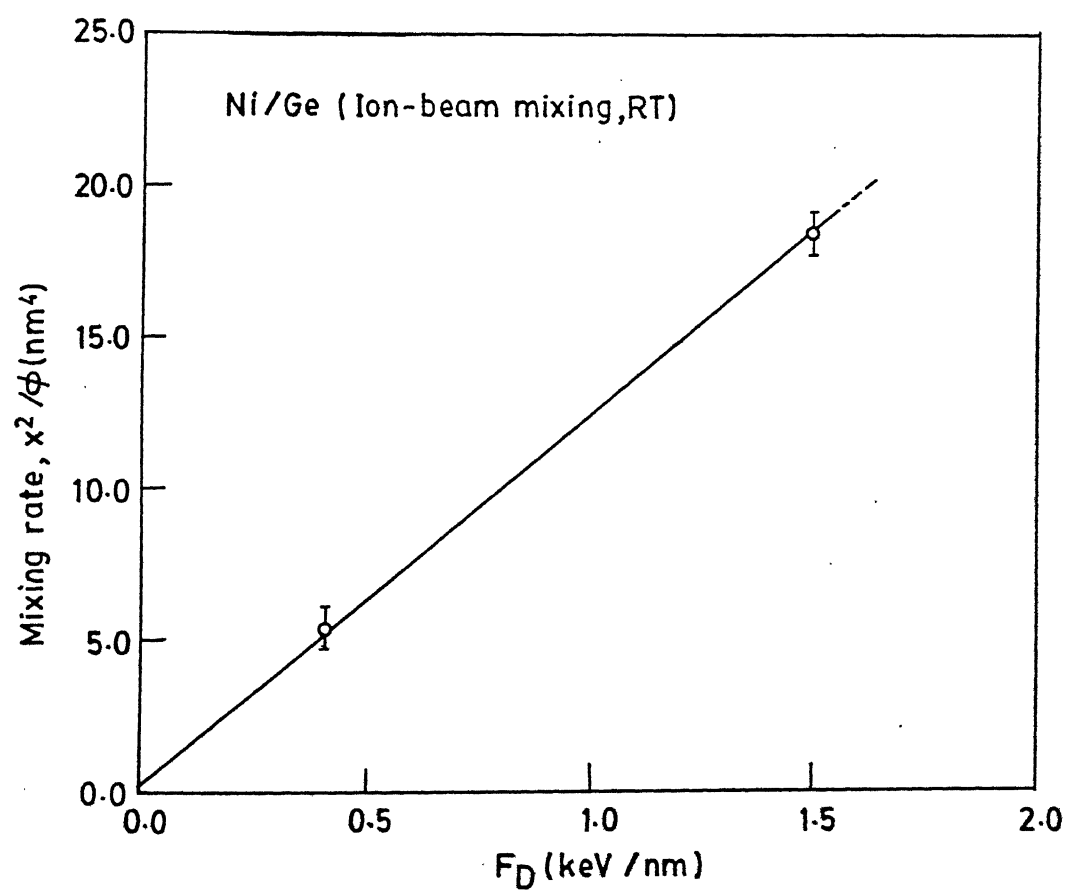


Figure 6.11: The variation of mixing rate measured in Ni/Ge bilayer system for different deposited energy F_D at the interface.

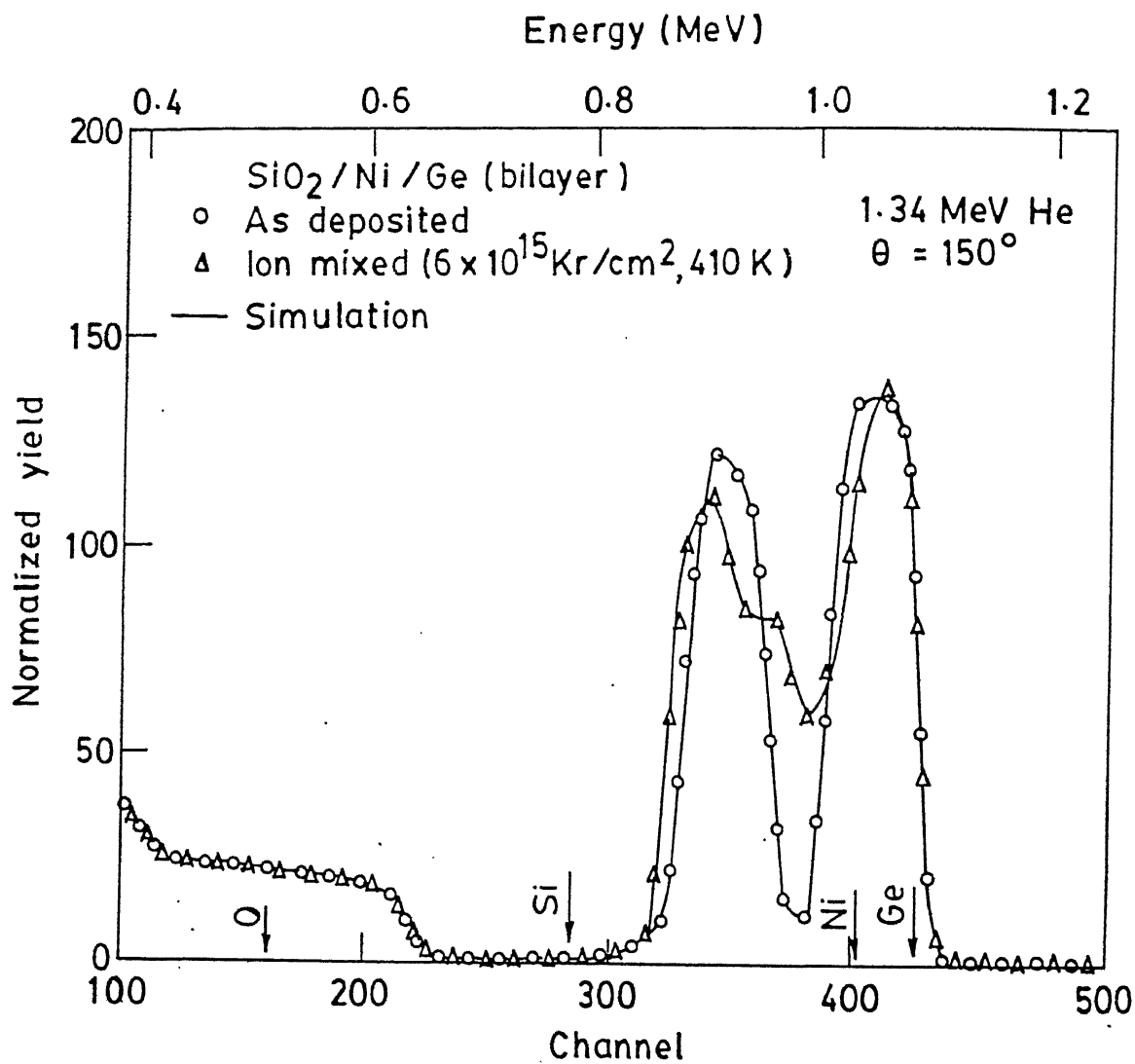


Figure 6.12: Rutherford backscattering spectra of Ni/Ge bilayer thin film on quartz substrate for as-deposited condition and after mixing for a dose of 6×10^{15} Kr/cm² at 410 K.

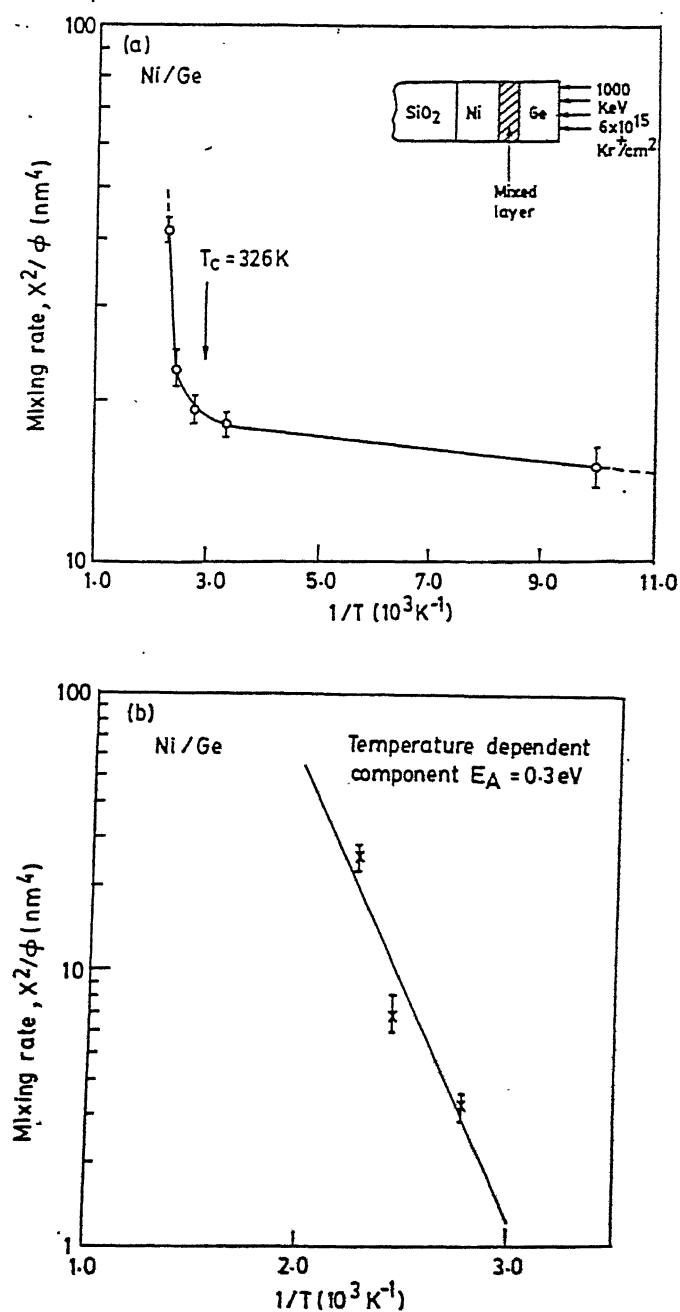


Figure 6.13: The variation of mixing rate for Ni/Ge bilayer system as a function of reciprocal of substrate temperature for a dose of 6×10^{15} Kr/cm² (b) Arrhenius plot of the mixing rate as a function of reciprocal of substrate temperature extracted from Fig.6.12a.

Table 6.3: Description of the layer structure used for the simulation of RBS spectra of as-deposited and ion mixed Co/Ge bilayer samples shown in Fig 6.13.

Sample description	Layer structure used for simulation						
	Layer No.	Thickness (nm)	Composition				
Co/Ge bilayer at film deposited on SiO_2	1	107	Ge	1.00			
	2	65	Co	1.00			
	3	1000	Si	1.00	O	2.00	
After RT ion mixing for a dose of $1 \times 10^{16} Kr/cm^2$	1	94	Ge	1.00			
	2	30	Co	0.66	Ge	0.34	
	3	45	Co	1.00			
	4	1300	Si	1.00	O	2.00	

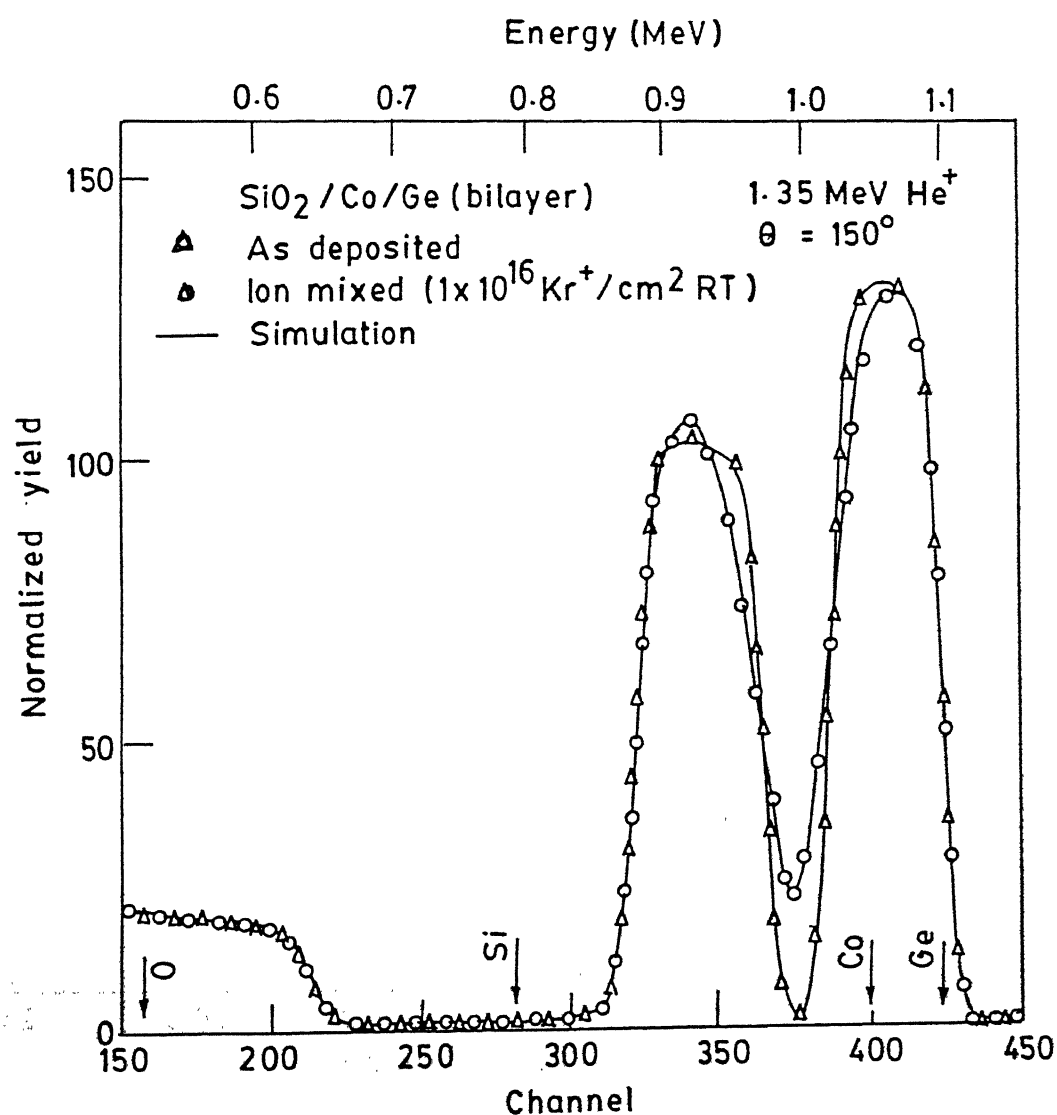


Figure 6.14: Rutherford backscattering spectra of Co/Ge bilayer thin film on quartz substrate for as-deposited condition and after room-temperature mixing with 1 MeV Kr ions at a dose of $1 \times 10^{16} \text{ Kr}/\text{cm}^2$. The corresponding simulated spectra are shown by solid lines.

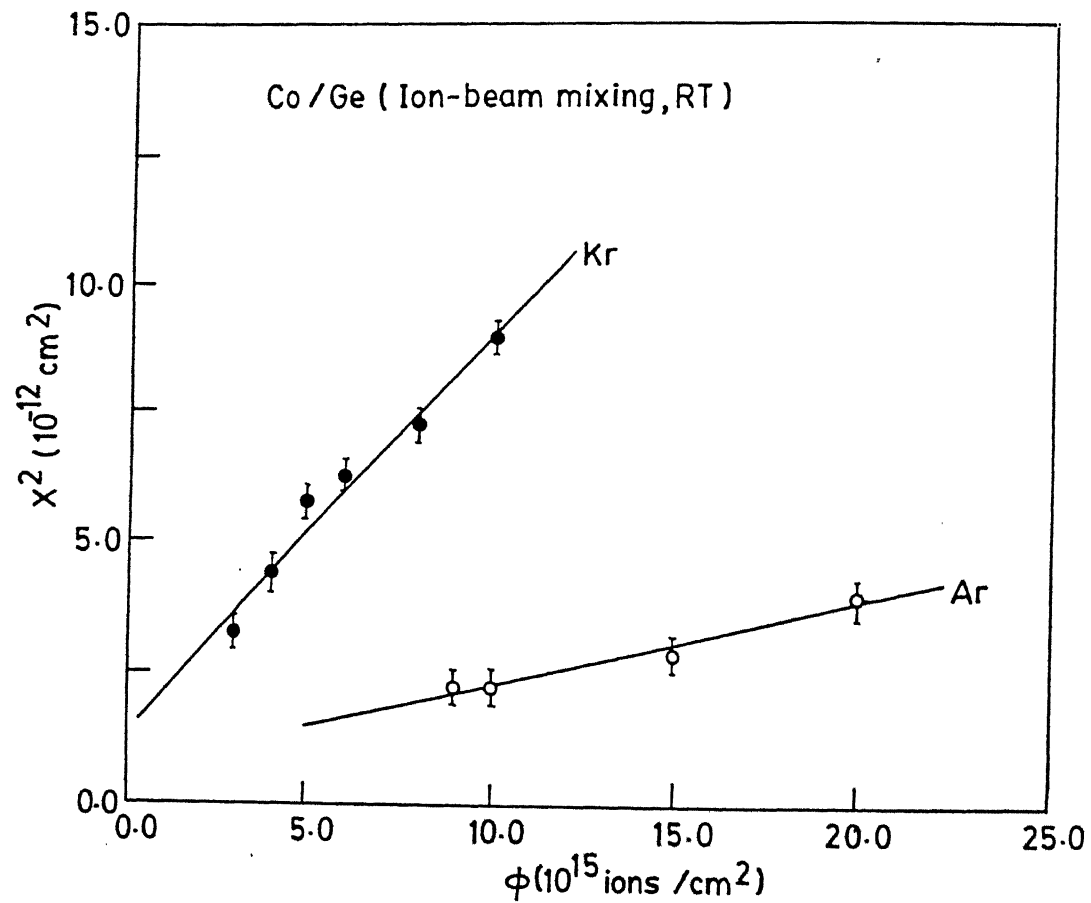


Figure 6.15: Dose dependence of squared thickness of mixed layers of composition Co_2Ge formed across the interface of Co/Ge bilayer system irradiated at room temperature with 1 MeV Ar ions (○) and Kr ions (●) respectively.

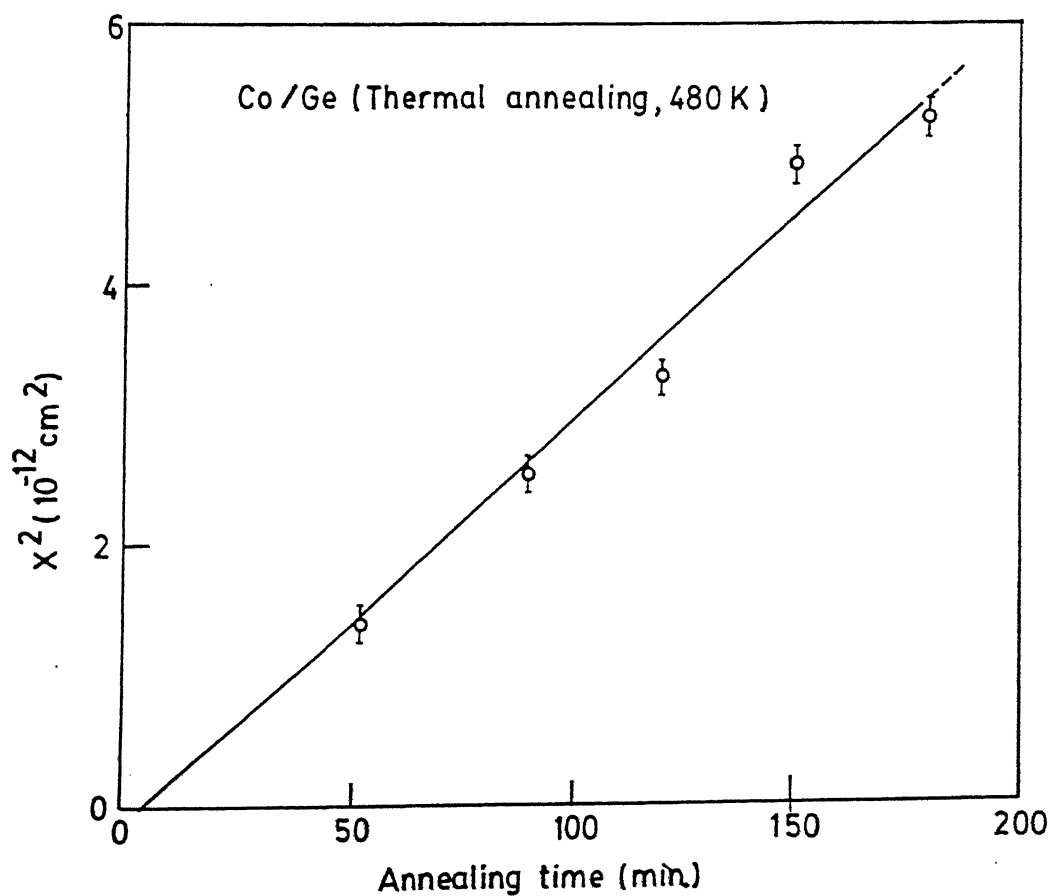


Figure 6.16: The squared thickness of the reacted layer of composition Co_2Ge formed across the interface of Co/Ge bilayer system after thermal annealing is shown as a function of annealing time.

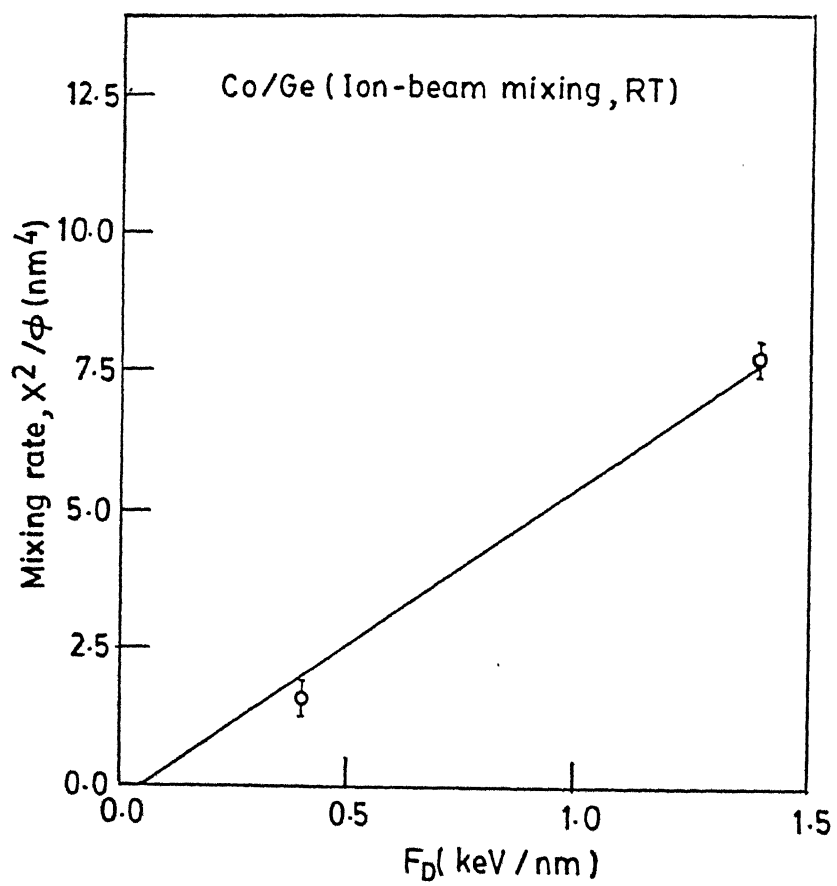


Figure 6.17: The variation of mixing rate measured in Co/Ge bilayer system for different deposited energy F_D at the interface.

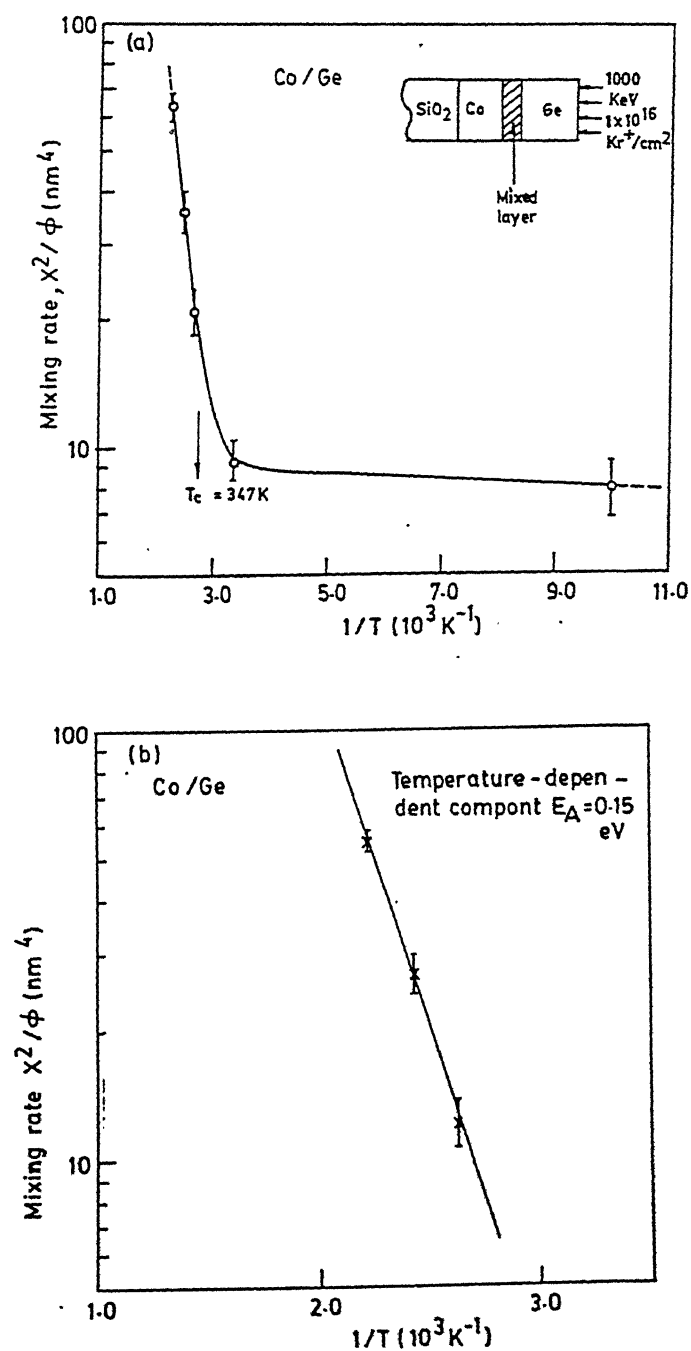


Figure 6.18: The variation of mixing rate for Co/Ge bilayer system as a function of reciprocal of substrate temperature for a dose of 1×10^{16} Kr/cm² (b) Arrhenius plot of the mixing rate as a function of reciprocal of substrate temperature extracted from Fig.6.17a.

6.4 Discussion

6.4.1 Critical temperature

At first we will discuss the nature of the mixed region on the basis of the Q curves presented in Figs 6.5, 6.13 and 6.18. It has been described in Chapter 2 that, in general, there exists two critical temperatures T_c and T_{eq} with $T_c < T_{eq}$ such that metastable phases are expected between T_c and T_{eq} and equilibrium phases are expected beyond T_{eq} . de Reus et al.[51] have correlated these temperatures with the energies required for creating a hole due to the smaller and the larger element in the compound. The smaller hole formation energy is related with T_c while the larger one with T_{eq} . These temperatures are predicted from the following expressions (Eqs.2.1 and 2.2 from Chapter 2)

$$T_c = 4.0 \times \Delta H_{Vsmall} \quad (6.1)$$

and

$$T_{eq} = 3.8 \times \Delta H_{Vlarge} \quad (6.2)$$

where the temperatures is given in Kelvin and the hole formation enthalpies in kJ/mole. The hole formation enthalpies ΔH_V for an alloy $A_{1-x}B_x$ are calculated from Miedema's formula described in Chapter 2 (Eq.2.3 and 2.4). For several systems the difference between T_c and T_{eq} is not so pronounced and in those cases there is only one transition temperature[51].

Cheng et al.[20] have correlated T_c with average cohesive energy of mixing elements. They have plotted experimentally determined T_c values against ΔH_{coh} and obtained a straight line whose slope is 100 K/eV. Thus from Eq. 2.5 of Chapter 2 we have

$$T_c = 100\Delta H_{coh} \quad (6.3)$$

For the present case of Cu/Ge system (see Fig 6.5) the value of T_c is 320 K. Theoretically, the models of de Reus et al. (Eq 6.1) and Cheng et al. (Eq 6.3) give T_c values of $253 (\pm 75)$ K and $373 (\pm 100)$ K respectively. According to the formulation of de

Reus et al. the value of T_{eq} is $330 (\pm 75)$ K. The comparison of calculated T_c and T_{eq} values with the experimental results is reasonably well and is presented in Table 6.4. The values of cohesive energy (ΔH_{coh}) for the present systems are given in Table 6.5. Similarly, the calculated values for Ni/Ge and Co/Ge systems are compared with the experimental one in Table 6.4. It is to be noted that in all the three cases the equilibrium phases have been observed around T_c . It has been found that several silicides form around T_c which could be due to the higher reactivity of these materials as compared to the metal/metal systems. For example, in Co/Si system the experimental[89] and theoretical[51] values of T_c and T_{eq} are both equal to 300 K. In this case the formation of equilibrium phase Co_2Si is reported to occur at room temperature under Xe ion bombardment[89]. In fact there are many more systems where an equilibrium phases are formed around T_c . Several such examples are shown in Table 6.4. Also note that the value of T_c depends on the mass of the irradiating ion[23, 29]. The value of critical temperatures increases with decreasing mass of the irradiating ion.

6.4.2 Mixing rate: Prediction of existing models

In this section the experimental values of mixing rates and mixing efficiencies will be compared with the values calculated for Cu/Ge, Ni/Ge and Co/Ge systems using empirical formulae proposed by different researchers (described in Chapter 2). The experimental values of mixing rates obtained at room temperature which is just below the critical temperature (see Table 6.4) for these systems. Each phenomenological model assumes certain mechanisms viz. cascade mixing, thermal spike etc. and usually expresses in the form of an empirical formula for the evaluation of mixing rate. Thus comparison of the experimentally obtained values with the ones calculated using these models can reveal the underlying mixing mechanism in the systems under consideration. It should be borne in mind that these models also assume certain conditions viz. unlimited supply of atoms of each species, size and shape of the collision cascade, thermodynamic parameters, mobility of the species involved etc. for their validity.

Table 6.4: Comparison of experimentally obtained critical temperatures with the one calculated from different empirical models

Bilayer system	Critical temperature T_c in K			Eq. temperature T_{eq} in K		Observed phase around RT or T_C	Ref.
	Exp.	Calculated from		Exp.	Cal. from		
		Cheng et al. model	de Reus et al. model				
		Eq 6.3	Eq 6.1				
Cu-Ge	320	368	253	320	330	Cu_3Ge^+	[this work]
Ni-Ge	326	414	338	326	455	Ni_2Ge^+	[this work]
Ni-Si	250	435	390	340	399	Ni_2Si^+	[ref 51]
Co-Ge	347	412	371	347	383	Co_2Ge^-	[this work]
Co-Si	300	451	356	300	410	Co_2Si^+	[ref 51]
Pd-Si	*	426	373	*	363	Pd_2Si^+	„
Ti-Si	380	474	392	390	426	$TiSi_2^-$	„
Pt-Si	*	524	416	320	429	Pt_2Si^+	„
Pd-Ge	*	387	371	*	383	Pd_2Ge^+	„
Nb-Si	550	610	425	570	490	$NbSi_2^-$	„

* Not available

+ Phase formed around RT or T_c

- Composition

Ballistic model

According to this model[50] the mixing rate is expressed as (Eq. 2.8 of Chapter 2)

$$\frac{X^2}{\Phi} \big|_{bal} = \frac{0.4 F_D \xi^{1/2} \lambda^2}{C E_d} \quad (6.4)$$

where C is the average atomic density, E_d is displacement energy or threshold energy for Frenkel pair production, $\xi = [4M_1M_2/(M_1 + M_2)^2]$ and $\lambda = 10 \text{ \AA}$ is the minimum separation distance for the formation of stable Frenkel pair[14]. The values of average atomic density C , displacement energy E_d and ξ for Cu/Ge, Ni/Ge and Co/Ge systems are given in Table 6.5. The deposition energy F_D for 1 MeV Kr and Ar ions in these three systems are given in Table 6.6. The mixing rates at room temperature for Kr and Ar irradiation calculated from this model for Cu/Ge, Ni/Ge and Co/Ge systems are compared in Table 6.7. It is seen from this table that the calculated ballistic mixing rates are one order of magnitude lower than that of the experimental ones. The calculated mixing efficiencies have been compared with the experimental ones in Table 6.8. Since all the three systems have similar masses and displacement energies, the collision process cannot account for more than 20% variation[14] in the observed mixing rate, whereas actual values varied by a factor of four for the systems under investigation.

Influence of chemical force and thermal spike

The low values of mixing rates predicted by the ballistic model suggest that the collisional effects alone are inadequate to produce the observed mixing and that there are driving forces of different nature which are also contributing to mixing[14]. These driving forces are termed as chemical forces since they depend on the heat of mixing, cohesive energy etc. We recall from Chapter 2 that the ion mixing rate of a Hf/Ni bilayer system is significantly larger than that for a Hf/Ti system. The collisional parameters for these two systems are similar but the heats of mixing for equal atomic concentrations are -62 and 0 kJ/gm.at. respectively showing the effect of chemical forces. The chemical forces act when thermal spikes are produced. On the basis of

Table 6.5: The values of average atomic number Z_{ave} , ξ , atomic density C , displacement energy E_d , heat of formation ΔH_{for} , cohesive energy ΔH_{coh} of Cu/Ge, Ni/Ge, Co/Ge and Ni/Si systems.

Bilayer system	Z_{ave}	ξ	C in $at./\text{\AA}^3$ [7]	E_d eV [67]	Equilibrium phase	$-\Delta H_{for}$ (kJ/gm.at.) [63]	$-\Delta H_{coh}$ (eV/at.) [73]	$\frac{\Delta H_{for}}{\Delta H_{coh}}$
Cu/Ge	30.5	1.00	0.075	17	Cu_3Ge	4.05	3.67	0.012
Ni/Ge	30	0.99	0.072	12	Ni_2Ge	12.3	4.30	0.022
Co/Ge	29.5	0.99	0.071	19	Co_2Ge	5.00	4.26	0.012
Ni/Si	21	0.94	0.078	20	Ni_2Si	16	4.5	0.036

Table 6.6: The values of deposited energy density F_D , critical energy F_D^c for global spike and the critical energy E_c for spike formation.

Bilayer system	Irradiating ion	F_D (keV/nm)	F_D^c (keV/nm)	E_c eV	Ref.
Cu/Ge	Ar	0.4	0.95	113	[this work]
	Kr	1.6	2.69	113	„
Ni/Ge	Ar	0.5	0.95	109	„
	Kr	1.6	2.68	109	„
Co/Ge	Ar	0.4	0.94	105	„
	Kr	1.4	2.64	105	„
Ni/Si	Au	4.8	5.53	47	[ref 31]

Table 6.7: Comparison between experimental ($\frac{X^2}{\Phi} |_{exp}$) and calculated mixing rates. The theoretical mixed rates calculated from ballistic model (Eq 6.4) ($\frac{X^2}{\Phi} |_{bal}$), model ($\frac{X^2}{\Phi} |_{loc}^{Borgesen}$) of Borgesen et al. (Eq 6.7), local spike model of Bolse (Eq 6.8) ($\frac{X^2}{\Phi} |_{loc}^{Bolse}$) and global spike model ($\frac{X^2}{\Phi} |_{glo}$) (Eq 6.9).

Bilayer system	F_D (keV/nm)	$\frac{X^2}{\Phi} _{exp}$ (nm ⁴)	$\frac{X^2}{\Phi} _{bal}$ (nm ⁴) Eq 6.4	$\frac{X^2}{\Phi} _{loc}^{Borgesen}$ (nm ⁴) Eq 6.7	$\frac{X^2}{\Phi} _{loc}^{Bolse}$ (nm ⁴) Eq 6.8	$\frac{X^2}{\Phi} _{glo}$ (nm ⁴) Eq 6.9
Cu/Ge	0.4	5.4	0.06	0.11	0.17	0.42
„	1.6	20.6	0.25	0.44	0.70	0.68
Ni/Ge	0.5	5.6	0.11	0.13	0.20	0.55
„	1.6	18.5	0.35	0.40	0.64	0.58
Co/Ge	0.4	1.6	0.06	0.09	0.13	0.03
„	1.4	7.7	0.22	0.32	0.47	0.48

Table 6.8: Comparison between experimental ($\frac{X^2}{\Phi F_D} |^{exp}$) and calculated mixing efficiencies from ballistic (Eq 6.4) model ($\frac{X^2}{\Phi F_D} |_{bal}$), Borgesen et al local (Eq 6.7) spike model ($\frac{X^2}{\Phi F_D} |_{loc}^{Borgesen}$) and Bolse local spike (Eq 6.8) model ($\frac{X^2}{\Phi F_D} |_{loc}^{Bolse}$) Global spike (Eq 6.9) model ($\frac{X^2}{\Phi F_D} |_{glo}$).

Bilayer system	$\frac{X^2}{\Phi F_D} ^{exp}$ (nm ⁵ /keV)	$\frac{X^2}{\Phi F_D} _{bal}$ (nm ⁵ /keV)	$\frac{X^2}{\Phi F_D} _{loc}^{Borgesen}$ (nm ⁵ /keV)	$\frac{X^2}{\Phi F_D} _{loc}^{Bolse}$ (nm ⁵ /keV)	$\frac{X^2}{\Phi F_D} _{glo}$ (nm ⁵ /keV)
Cu/Ge	13.1	0.16	0.20	0.39	0.73
Ni/Ge	11.3	0.22	0.25	0.3	0.73
Co/Ge	4.0	0.15	0.23	0.23	0.20

fractal geometry, Cheng[14] has shown that the Z_{ave} value should be larger than 20 for thermal spike to occur. He has demonstrated that the space filling cascades which embodies the idea of thermal spikes can be initiated if the recoil energies fall below the critical value E_c (in eV) given by the following equation

$$E_c = 0.039Z_{ave}^{2.23} \quad (6.5)$$

where Z_{ave} is the average atomic number of the target. The calculated values of E_c for Cu/Ge, Ni/Ge and Co/Ge systems are given in Table 6.6. These values are much higher than the displacement energies E_d (Table 6.5) for the atoms indicating the occurrence of thermal spikes in all these three systems. The thermal spikes are generally divided into two categories (i) those formed by overlapping subcascades (global spikes) and (ii) those formed by non-overlapping subcascades (local spikes).

As mentioned in Chapter 2, the density of spikes, and the conditions of their overlap as assumed by Johnson et al.[19], depend on the deposited energy density F_D and on the mass and energy of the incident ion. The threshold deposition energy[24] density also called as critical energy F_D^c above which the subcascades begin to overlap can be estimated from the formula (Chapter 3 Eq 2.15) given below.

$$F_D^c = k_m N \left[\frac{Z_i Z_t}{Z_i^{0.23} + Z_t^{0.23}} \right] \left[\frac{m_i}{m_i + M_t} \right] \quad (6.6)$$

Here, the constant k_m is of the order of $25 \times 10^{-2} \text{ ev-nm}^2$ [24, 65]. The values of F_D^c calculated for metal/Ge systems under investigation are compared with the F_D values (for Kr and Ar ions) used in this work and shown in Table 6.6. The experimental values are less than the threshold values required for overlapping of local spikes. Thus, it is expected that the mixing should occur under local spikes in the present cases.

Borgesen et al.[22] and Bolse[24] have separately suggested on the basis of their series of experimental results that the linear dependence of the mixing rate with F_D can be correlated with the formation of local spikes. Our experimental results also show a linear dependence of mixing rate with F_D (see Figs 6.5, 6.11, 6.17) suggesting the formation of local spikes in this systems.

6.4.3 Mixing in non-overlapping subcascade

By combining the effects of cohesive energy and heat of mixing under non-overlapping spherical spike condition and using regular solution approximation the mixing rate ($\frac{X^2}{\Phi} |_{loc}^{Borgesen}$) from the model of Borgesen et al.[22] can be written as (chapter 2 Eq 2.13)

$$\frac{X^2}{\Phi} |_{loc}^{Borgesen} = \frac{K_b Z_{ave}^{1.5} F_D}{C^{4/3} \Delta H_{coh}^{5/3}} \left[1 + \frac{5}{6} K_2 \frac{\Delta H_{mix}}{\Delta H_{coh}} \right] \quad (6.7)$$

where ΔH_{mix} and ΔH_{coh} are the heat of mixing and cohesive energy respectively. Here $K_b = 0.034 \text{ nm-eV}^{2/3}$ and $K_2 = 27.4$. Later Bolse[24] have shown that these spherical local spikes overlap and form local cylindrical spike. The mixing rate then becomes (chapter 2 Eq 2.14)

$$\frac{X^2}{\Phi} |_{loc}^{Bolse} = \frac{K_B Z_{ave}^{1.77} F_D}{C^{2/3} \Delta H_{coh}^2} \left[1 + K_2 \frac{\Delta H_{mix}}{\Delta H_{coh}} \right] \quad (6.8)$$

where $K_B = 0.0163 \text{ nm}^3 \text{ eV}$ and $K_2 = 41$ are empirical constants obtained by fitting the mixing rate of metal/metal systems[76]. Here (in Eq 6.7 or Eq 6.8) first factor is due to the non-overlapping subcascade and the second one is the Darken term which indicates the energy gained by forming AB pairs after 'freely moving' A and B atoms generated in the collision cascade[104]. The calculated mixing rate and efficiencies for all the systems are compared with the experimental results in Table 6.7 and Table 6.8. The values of ΔH_{mix} , ΔH_{coh} , C , Z_{ave} and F_D are given in Tables 6.5 and 6.6. Thus by taking into account the heats of formation, cohesive energies and deposited energies we find that the mixing rates calculated from the local spike models are higher than those obtained using the ballistic approach. However, these values are still about an order of magnitude lower than the experimental mixing rates.

6.4.4 Mixing under Overlapping subcascade

Johnson et al.[19] proposed this model for calculating mixing rates under regular solution approximation and is known as "global spike model". According to this model

mixing rate is given by (Chapter 2 Eq 2.12)

$$\frac{X^2}{\Phi} \big|_{glo} = \frac{K_1 F_D^2}{C^{5/3} \Delta H_{coh}^2} \left[1 + K_2 \frac{\Delta H_{mix}}{\Delta H_{coh}} \right] \quad (6.9)$$

where $K_1 = 0.00175$ nm and $K_2 = 27$ are empirical constants. Although the above formula is not applicable for present systems since the spikes are expected to be of non-overlapping nature, we have calculated the mixing rates for the sake of comparison. These values are given in Table 6.7 and are not very different as compared to the ones calculated from the local spike models.

6.5 Need for a new model

The inadequacy of all the above mentioned models indicates that there are some other factors which enhance mixing. There are many metal silicide[31] systems whose mixing rates are much higher than the ones calculated using above models. For example, recently, Desimoni and Traverse[31] have reported that the Pd_2Si occurs in Pd/Si system and the mixing rate varies linearly as a function of F_D^2 . They have found that the mixing rates calculated using the Johnson and Cheng model are 3 to 8 times lower than the measured mixing rates. All these results together with the results presented here strongly suggest that there are some other factors which contribute to the mixing process leading to compound formation. It may be noted that metal/Si and metal/Ge systems are strongly reactive. A formalism has been presented in the next section to calculate the mixing rates in such strongly reactive systems which is based on a mechanism in which the mobile species is driven to the growing interface where it gets consumed during compound formation along with simultaneous structural relaxation.

6.5.1 Model for compound formation under local spike mixing

It is now well recognized that thermodynamics has to be taken into account in describing ion-beam mixing and is normally manifested through heat of mixing. Johnson et al.[19] and Cheng[14] have shown that under regular solution approximation the diffusion coefficient can be expressed as

$$D = D_o (1 - 2\Delta H_{mix}/k_B T) \quad (6.10)$$

where D_o is a constant, k_B is Boltzmann constant, ΔH_{mix} is the heat of mixing and T is the local temperature. The term within the bracket is responsible for enhancing the diffusion coefficient and is known as Darken term.

However, in those cases where a chemical reaction also takes place at the interface of growing mixed layer, the reaction rate may strongly influence the concentration gradients and thus can become the dominant source of thermodynamically controlled modification of diffusion coefficient. This effect of reaction kinetics on mass transport coefficients is well known in the analysis of compound forming thermal diffusion couples[105–107]. Desimoni and Traverse[31] extended this analogy for thermally synthesized compounds for explaining the ion-beam mixing results of silicides.

This is best illustrated (see Fig 6.19) by considering a bilayer system A/B, where each layer is an infinite source of corresponding atoms; and for simplicity let only one atom, say A, be the moving species during compound formation. Assume that the solubility of A and B is very low but they are highly reactive resulting into a compound $A_a B_b$. On irradiation, initially the rate of the growth of the layer $A_a B_b$ is limited by the rate of reaction. However, at later times the supply of the mobile species to the reacting interface gets limited by its diffusion through the mixed layer[31]. If the reaction rate is high, then each atom arriving at the interface is consumed in the formation of the compound, and hence for the steady state growth, the flux (J_1) of mobile atoms due to diffusion must equal to the flux (J_2) participating in the formation of the compound

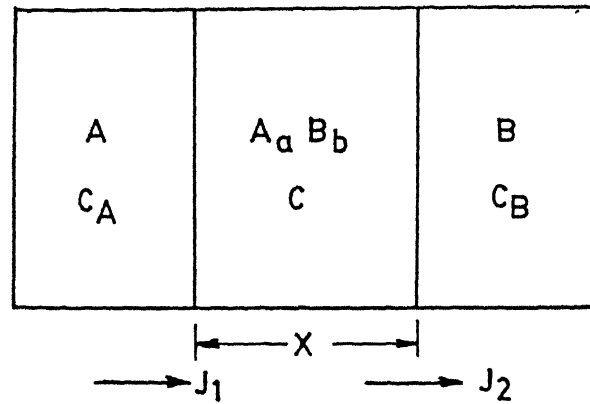


Figure 6.19: Bilayer sample configuration of two elements A and B where compound $A_a B_b$ grows across the interface under ion bombardment.

at the interface. Assuming a small layer of thickness X , this equality of steady state flux F_s can be written as,

$$F_s = D \frac{(C_A - C_i)}{X} = kC_i \quad (6.11)$$

where C_A is atomic density of layer A and C_i is the concentration of A atoms at the growing interface, k is the reaction rate and D is the diffusion coefficient. Note that the reaction rate coefficient determines "reaction kinetics" which in turn influences "transport kinetics" in a diffusion controlled process. The relationship between kinetics and thermodynamics in phase formation by ion-beam mixing has been discussed by Miotello and Kelly[26].

The time dependence of thickness X of the mixed layer can be expressed as steady state flux divided by the concentration of atom A in the compound,

$$\begin{aligned} \frac{dX}{dt} &= \frac{F_s}{N_A} \\ &= \dot{\Phi} \frac{dX}{d\Phi} \end{aligned} \quad (6.12)$$

where N_A is the concentration of A in the compound A_aB_b with atomic density C i.e., $N_A = [a/(a+b)]C$. The second equality is obtained by replacing time by dose assuming flux $\dot{\Phi}$ to be constant.

Using Eqs 6.11 and 6.12, eliminating C_i and solving for X with the initial condition, $X(t=0) \simeq 0$ one obtains,

$$(N_A \dot{\Phi} k) X^2 + (2DN_A \dot{\Phi}) X - 2DkC_A \dot{\Phi} = 0 \quad (6.13)$$

This gives two solutions for X of which the positive one is expressed as

$$X = \frac{D}{k} \left[\left(1 + 2D \frac{C_A \dot{\Phi} k^2}{N_A \dot{\Phi} D^2} \right)^{1/2} - 1 \right] \quad (6.14)$$

For diffusion limited process and *high reaction rate* k , X becomes independent of k giving rise to

$$X = \frac{D}{k} \left[\left(2D \frac{C_A \dot{\Phi} k^2}{N_A \dot{\Phi} D^2} \right)^{1/2} \right] \quad (6.15)$$

$$X^2 = 2 \frac{C_A}{N_A} D \frac{\dot{\Phi}}{\dot{\Phi}} = D_{eff} \frac{\dot{\Phi}}{\dot{\Phi}}$$

Note that though k does not explicitly appear in this equation, it is responsible for enhancement of D to some D_{eff} by a factor $2C_A/N_A$, whose origin can be attributed to the chemical driving force for formation of a compound[31]. In the approximation that there is no terminal solid solution, this is the only enhancement factor different from the Darken term in Eq 6.10. It is straight forward to extend Eq 6.15 to the case when both atomic species are mobile and is given by,

$$X^2 = 2 \left[\frac{C_A}{N_A} + \frac{C_B}{N_B} \right] D \frac{\dot{\Phi}}{\dot{\Phi}} \quad (6.16)$$

It is interesting to note that the enhancement factor appears as a ratio of concentration of mobile species to its concentration in the compound and is independent of the deposited energy[31]. However, under irradiation conditions the diffusion coefficient is

separately dependent on deposited energy F_D . This dependence is known to vary as F_D^2 in case of overlapping subcascades[14] and only as F_D in case of non-overlapping subcascades[22, 24]. It has already been mentioned that in case of non-overlapping subcascades/local spikes, under regular solution approximation, the mixing rate $\frac{X^2}{\Phi} \big|_{loc}^{Bols}$ for the later case is given by (Eq 6.8)

$$\frac{X^2}{\Phi} \big|_{loc}^{Bols} = K_B \frac{Z_{ave}^{1.77} F_D}{C^{2/3} \Delta H_{coh}^2} \left[1 + K_2 \frac{\Delta H_{mix}}{\Delta H_{coh}} \right] \quad (6.17)$$

The first factor is due to the spike effect and the second one is due to the effect of chemical driving force. In case of compound formation, this would be further enhanced by the factor in the square bracket in Eq 6.16. However, in the absence of terminal solution, the Darken term can be simply replaced in the above equation by the compound formation enhancement factor in Eq 6.16 and the mixing rate $\frac{X^2}{\Phi} \big|_{loc}^{com}$ would be given by

$$\frac{X^2}{\Phi} \big|_{loc}^{com} = K_s \left[\frac{C_A}{a/(a+b)} + \frac{C_B}{b/(a+b)} \right] \frac{2F_D Z_{ave}^{1.77}}{C^{5/3} \Delta H_{coh}^2} \quad (6.18)$$

where K_s is the proportionality constant. When atom A (B) is the only moving species during phase formation then the first (second) term within the bracket will be retained.

The quantitative success of the above formalism in predicting the experimental mixing rates for metal/Ge systems presented here as well as the mixing rate of Ni/Si system reported in the literature[31] is shown in the following subsection.

6.5.2 Comparison with experimental results

To calculate the mixing rates, the values of compound formation factor and thermal spike factors and the proportionality constant K_s are required. To determine the compound formation factor in Eq 6.18 for the present systems, it is essential to know whether only one or both the species are mobile during the formation and growth of the germanide phases. In order to investigate this we have studied the movement of

atomic species across the interface by marker experiments the results of which have been presented in the previous chapter. In Chapter 5 it has been shown that in case of Cu/Ge systems, both Cu and Ge are mobile but Cu is the dominant mobile species whereas in case of Ni/Ge system Ni and Ge both are equally mobile. However, in case of Co/Ge system Ge is the only mobile species.

The values of mixing rates calculated using Eq 6.18 for the metal/Ge systems are tabulated and compared with the experimental values in Table 6.9. The parameters used for these calculation are given in Tables 6.5 and 6.6. The calculated values are very close to the experimental mixing rates indicating excellent predictionability of the present model. The calculated mixing efficiencies for these systems are also quite close to the calculated values which are compared in Table 6.10.

For the sake of completeness, we shall now compare the experimental mixing rate with the calculated ones from the modified relation of the ballistic mixing rates. According to Desimoni and Traverse the ballistic mixing rate $\frac{X^2}{\Phi} |_{bal}^{com}$ can be written as (Chapter 2 Eq 2.16)

$$\frac{X^2}{\Phi} |_{bal}^{com} = \left[\frac{C_A}{a/(a+b)} + \frac{C_B}{b/(a+b)} \right] \frac{0.4 F_D \xi^{1/2} \lambda^2}{C^2 E_d} \quad (6.19)$$

The mixing rates obtained from this modified expression of ballistic model are compared with the experimental one in Table 6.9. This shows that mixing rates calculated from the modified ballistic model are one order of magnitude less than the experimental values. Now we shall calculate mixing rates using the modified global spike model[31] where mixing rate is proportional to F_D^2 . Although we have seen a linear dependence of mixing rate on F_D we would like to compare the predictions of this model with our experimental values. The mixing rate is given by (Eq 2.17 of Chapter 2)

$$\frac{X^2}{\Phi} |_{glo}^{com} = K_1 \left[\frac{C_A}{a/(a+b)} + \frac{C_B}{b/(a+b)} \right] \frac{2 F_D^2}{C^{3/3} \Delta H_{coh}^2} \quad (6.20)$$

The values calculated using the above relationship are also given in Table 6.9. The mixing efficiencies calculated from these two models are compared with the experimental one in Table 6.10. It is seen from both the tables that the model presented in this

Table 6.9: Comparison between experimental ($\frac{X^2}{\Phi} |^{exp}$) and calculated mixing rates. The theoretical mixed rates ($\frac{X^2}{\Phi} |_{loc}^{com}$) calculated from our model (Eq 6.18) agree well with the experimentally obtained mixing rates. Note the significant departures of the rates calculated from modified ballistic (Eq 6.19) model ($\frac{X^2}{\Phi} |_{bal}^{com}$) and global spike ($\frac{X^2}{\Phi} |_{glo}^{com}$) model (Eq 6.20).

Bilayer system	phase formed	Moving species	F_D (keV/nm)	$\frac{X^2}{\Phi} ^{exp}$ (nm ⁴)	$\frac{X^2}{\Phi} _{loc}^{com}$ (nm ⁴) Eq 6.18 *	$\frac{X^2}{\Phi} _{bal}^{com}$ (nm ⁴) Eq 6.19 #	$\frac{X^2}{\Phi} _{glo}^{com}$ (nm ⁴) Eq 6.20 #
Cu/Ge	Cu_3Ge	both	0.4	5.4	5.36	0.49	0.25
"	"	"	1.6	20.6	21.46	1.96	4.0
Ni/Ge	Ni_2Ge	both	0.5	5.4	4.14	0.78	0.25
"	"	"	1.6	18.5	13.25	2.49	2.51
Co/Ge	Co_2Ge	Ge	0.4	1.6	1.7	0.21	0.09
"	"	"	1.5	7.73	6.5	0.79	1.27
Ni/Si	Ni_2Si	Ni	4.8	11.8	8.92	2.04	9.27

* Model proposed in this work.

Model proposed in ref 31.

Table 6.10: Comparison between experimental ($\frac{X^2}{\Phi F_D} |_{exp}$) and calculated mixing efficiencies. The theoretical mixing efficiency ($\frac{X^2}{\Phi F_D} |_{loc}^{com}$) calculated from our model (Eq 6.18) agree well with the experimentally obtained mixing efficiency. The mixing efficiencies from modified ballistic (Eq 6.19) model ($\frac{X^2}{\Phi F_D} |_{bal}^{com}$) and global spike ($\frac{X^2}{\Phi F_D} |_{glo}^{com}$) model (Eq 6.20) are also shown for comparison.

Bilayer system	$\frac{X^2}{\Phi F_D} _{exp}$ (nm ⁵ /keV)	$\frac{X^2}{\Phi F_D} _{loc}^{com}$ (nm ⁵ /keV) *	$\frac{X^2}{\Phi F_D} _{bal}^{com}$ (nm ⁵ /keV) #	$\frac{X^2}{\Phi F_D} _{glo}^{com}$ (nm ⁵ /keV) #
Cu/Ge	13.1	13.4	1.23	1.56
Ni/Ge	11.3	9.3	1.56	1.01
Co/Ge	4.0	4.35	1.08	1.09
Ni/Si	2.46	1.86	0.42	1.93

* Calculated from the proposed model.

Calculated from the model presented in ref 31.

work provides the best agreement with the experimental results.

The formalism developed above is applied to calculate the mixing rate for Ni/Si system for which the experimental data is available in the literature[31]. Desimoni and Traverse have done mixing experiments on Ni/Si system to produce nickel silicide (Ni_2Si) phase and explained the experimentally obtained mixing rate by the modified global spike model for compound formation. Since, Ni/Si system consists of medium Z_{ave} elements, it is expected that the model proposed here is appropriate to explain the mixing rates in this case as well. Here, Ni is the only moving species during the nickel silicide phase (Ni_2Si) formation hence only the first term in the compound formation factor (Eq 6.18) is to be considered. The calculated mixing rate from our model and experimental mixing rate at low temperature are in close agreement as shown in Table 6.9. The experimental and calculated mixing efficiencies are compared in Table 6.10.

It is to be noted that we have used the same average value of the proportionality constant $K_s = 0.95 \times 10^{-6} \text{ nm}^3 - \text{keV}$ (Eq 6.18) in the present model for calculating the mixing rates for all the cases. A more general value of K_s of $0.99 \times 10^{-6} \text{ nm}^3 - \text{keV}$ has been obtained from the plot (see Fig 6.20) of the experimental mixing rate versus the product of the compound formation factor and thermal spike factor (the right hand side of Eq 6.18). In general, these results suggest that this new model should be able to explain the mixing rates for many other reactive medium Z_{ave} systems for which compound formations have been reported in the literature. Unfortunately, the information regarding mixing rates for compound formation for these systems are not available. The knowledge of mixing rates will be helpful for further validation of the proposed model.

Before concluding, it may be mentioned again that the growth of mixed layers at relatively low temperatures for highly reactive systems, such as silicides and germanides, must be viewed differently from those systems where a solid solution or amorphous phase is produced under ion irradiation prior to the formation of equilibrium compounds. In the later case long range atomic migration or overcoming of barrier to

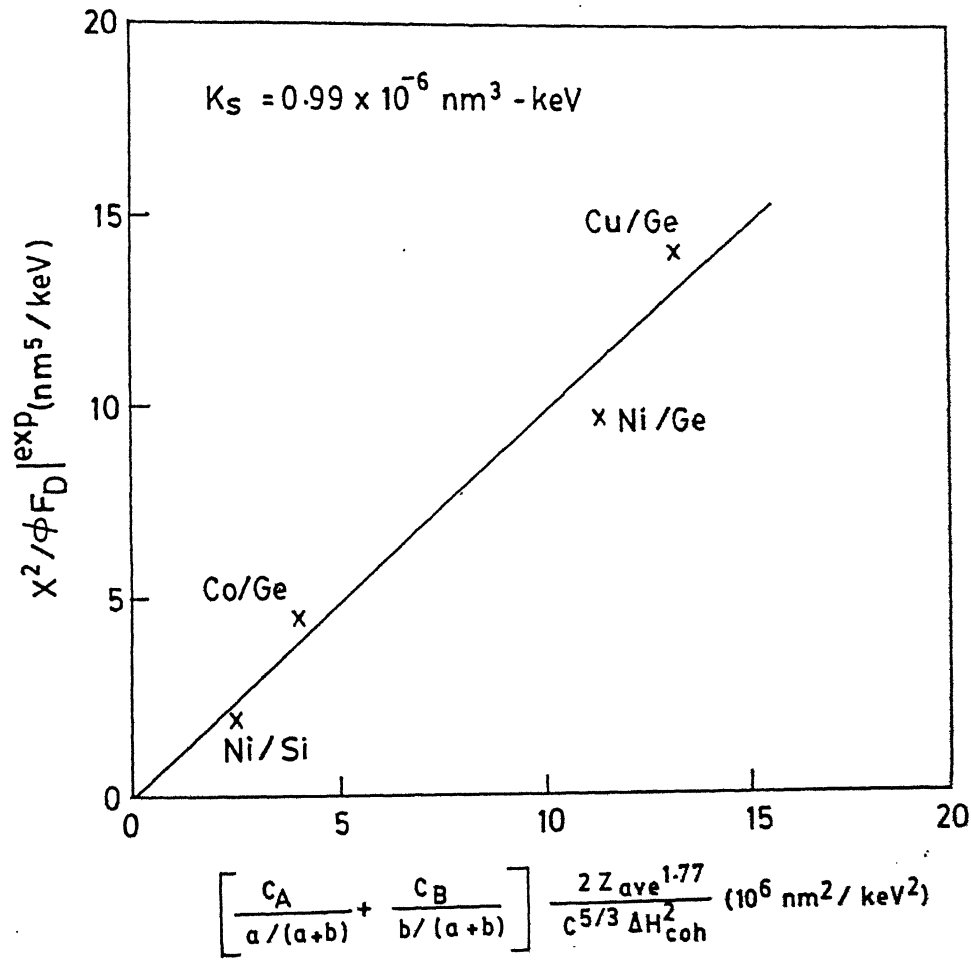


Figure 6.20: Determination of average value of the proportionality constant K_s , used in Eq 6.18 from the experimental mixing rates. The best fit gives a value $0.99 \times 10^{-6} keV - nm^3$.

nucleation is necessary. However, for reactive systems where the diffusive flux of the reacting species is controlled by the reaction rate k , such barriers are either absent or negligible so that the system can undergo structural relaxation to produce stable equilibrium compound. The role of ion irradiation is to provide the required flux of reacting species for incorporation into the compound at the reacting interface. Hence models such as the one presented here and of Desimoni and Traverse[31] or Miotello and Kelly[26], would be of general applicability for systems with high reaction rate coefficient and low solid solubility.

6.6 Conclusions

The main conclusions of this chapter are,

(1) For the bilayer structures of all the three Cu/Ge, Ni/Ge and Co/Ge systems, irradiation with Ar and Kr ions leads to the formation of Cu_3Ge , Ni_2Ge and Co_2Ge phases respectively. The square of the thickness of ion mixed layers is linearly proportional to the irradiation dose of Kr and Ar ions and the mixing rates too exhibit linear dependence on deposited energy density F_D . The thermal annealing experiments also exhibit similar compound formation and show linear variation of squared thickness of the reacted layer with the annealing duration.

(2) The room-temperature mixing rates for Ar ion irradiation in case of Cu/Ge, Ni/Ge and Co/Ge systems are found to be 5.4 nm^4 , 5.6 nm^4 and 1.6 nm^4 respectively. Similarly for Kr ion irradiations the mixing rates are 20.6 nm^4 , 18.5 nm^4 and 7.7 nm^4 respectively. The mixing efficiencies are independent of the deposited energy density in each case and the experimental values for Cu/Ge, Ni/Ge and Co/Ge are obtained as $13.1 \text{ nm}^5/\text{keV}$, $10 \text{ nm}^5/\text{keV}$ and $5 \text{ nm}^5/\text{keV}$ respectively.

(3) The temperature dependence studies of ion mixing in all the three systems show that the critical temperatures T_c , above which the mixing becomes temperature dependent, are just above the room temperature and are given by 320, 326 and 347 K for Cu/Ge, Ni/Ge and Co/Ge systems respectively. There is no distinction between

critical and equivalent temperature for crystallization. Compound formation in all the cases occurred around the critical temperature T_c .

(4) The calculated mixing rate from all existing models are much lower as compared to the experimental values.

(5) A new model has been proposed for medium Z_{ave} elements where compound formation occurs during ion-beam mixing under non-overlapping subcascades. In this model the mixing rate is enhanced by the compound formation factor in highly reactive systems, and it inherits the linear dependence on deposited energy density of non-overlapping subcascades. The predictions by this model are very close to the experimental results presented here and the model is also able to explain observed mixing rate of Ni/Si system reported in the literature. Hence it is demonstrated that this model would be applicable to the important class of silicide and germanide systems.

Chapter 7

Summary and Conclusions

The discovery of low resistivity Cu_3Ge phase, produced by solid state reaction at elevated temperatures, reported at the beginning of this decade has triggered a great interest in metal germanide phases since these materials have potential application as contact and interconnect in modern semiconductor technology. In the present thesis the syntheses of Cu_3Ge and other metal germanide phases in Ni/Ge and Co/Ge systems have been investigated using ion-beam mixing (directed energy deposition method) which has distinct advantages of spatial selectivity and low processing temperatures as compared to the conventional method of thermal treatment at elevated temperatures.

MeV Kr and Ar ions in the dose range of $(2 - 20) \times 10^{15} \text{ ions/cm}^2$ were used to induce mixing in the multilayer and bilayer films of the metal/Ge systems deposited on quartz substrate. Also the temperature dependence of ion-beam mixing in the range of 100-450 K was investigated. Syntheses of the germanide phases by thermal treatment in the range of 400-700 K were also studied for comparison. To study the atomic movement caused by irradiation or thermal treatment, ion beam mixing experiments on bilayer films embedded with a thin marker layer at the interface were performed.

The compositions and thicknesses of all samples before and after ion mixing or thermal treatment were determined using Rutherford backscattering spectroscopy (RBS).

The 2-MeV Van de Graaff accelerator at Indian Institute of Technology, Kanpur, was used for both irradiation and RBS measurements. X-ray diffraction techniques (conventional and small angle) were utilized for the identification of different phases produced after ion mixing or thermal annealing. The surface topography of the ion mixed and heat treated samples was examined after various doses and annealing treatments using scanning electron microscopy to detect the changes in surface features.

The information on the synthesis of the first and subsequent phases was obtained from experiments performed with both multilayer and bilayer samples. On the other hand, the values of mixing rates, mixing efficiencies and critical temperatures for the onset of thermally activated processes were obtained from the results of the bilayer experiments. The nature of the phases formed in these metal germanide systems was examined on the basis of existing empirical rules. The ion-beam mixing mechanisms have been discussed and a new phenomenological model based on chemical kinetics, applicable to reactive systems (silicides, germanides etc.) has been proposed to explain experimentally determined values of the mixing rates and efficiencies.

The important conclusions of these studies are summarized as :

1. We have found that MeV heavy ion irradiation technique is found to be a very efficient low temperature process for producing stable phases in Cu/Ge, Ni/Ge and Co/Ge systems. In case of Cu/Ge system, at lower doses, the equilibrium phase Cu_3Ge forms first, followed by the formation of Cu_5Ge phase at higher doses. In case of Ni/Ge system, only Ni_2Ge phase and in case of Co/Ge only Co_2Ge phase form at all doses. The "first phases" to form by thermal annealing in these systems are Cu_3Ge , Ni_2Ge and Co_2Ge respectively. These results show that for metal/Ge systems, as in the case of metal/Si systems, the first phase which is produced by ion-beam mixing is identical to the one produced by thermal annealing.
2. The resistivity values of Cu_3Ge , Ni_2Ge and Co_2Ge layers produced by ion-beam mixing are 20, 50 and 74 $\mu\Omega - cm$ respectively. The resistivities of the phases

produced by thermal annealing are 8.6, 23 and 50 $\mu\Omega - cm$ respectively. These resistivity values are lower as compared to metal silicides.

3. We have shown that during the formation of Cu_3Ge phase by ion-beam mixing at room temperature, both Cu and Ge are mobile but Cu is the dominant moving species across the interface while for Ni/Ge system both Ni and Ge are equally mobile for the formation Ni_2Ge phase. However, for Co/Ge system only Ge atoms are mobile to produce the Co_2Ge phase.
4. The first and subsequent phase formations in case of Cu/Ge and Co/Ge systems are correctly predicted by utilizing the concept of effective heat of formation and mobility of the participating atoms.
5. The squared thickness of the mixed region (compound) in all the three cases, obtained after ion-beam mixing of bilayers at room temperature show linear dependence on irradiated dose for both Kr and Ar irradiations. Mixing rates at room temperature also exhibit linear dependence on deposited energy density F_D . The growth of the mixed layer is like a diffusion controlled process. The thermal annealing experiments also exhibit similar compound formation and show linear dependence of the squared thickness of the reacted layers as a function of annealing time.
6. The temperature dependence studies of ion-beam mixing in all the three systems show that the critical temperatures T_c , above which the mixing becomes temperature dependent, are just above room temperature. The T_c values are about 320 K, 326 K and 347 K for Cu/Ge, Ni/Ge and Co/Ge systems respectively. There is no distinction between critical and equivalent temperature for crystallization. Compound formation in all the cases occur around the critical temperature T_c .
7. The room-temperature mixing rates for Ar ion irradiation in case of Cu/Ge, Ni/Ge and Co/Ge systems are found to be about 5.4 nm^4 , 5.6 nm^4 and 1.6 nm^4 respectively. Similarly for Kr ion irradiations the room temperature mixing rates

are about 20.6 nm^4 , 18.5 nm^4 and 7.7 nm^4 respectively. The mixing efficiencies are independent of the deposited energy density in each case and the experimental values for Cu/Ge, Ni/Ge and Co/Ge are obtained as $13.1 \text{ nm}^5/\text{keV}$, $10 \text{ nm}^5/\text{keV}$ and $5 \text{ nm}^5/\text{keV}$ respectively. These results and those for silicides reported in literature show that mixing rates and efficiencies are much higher than most of the metal/metal systems. The enhancement of mixing is attributed to the highly reactive nature of metal/semiconductor systems as compared to the metal/metal systems

8. The calculated mixing rates from all existing models are found to be much lower as compared to the experimental values. A new model has been proposed for systems composed of highly reactive elements where compound formation occurs during ion-beam mixing under non-overlapping subcascades. In this model the mixing rate is enhanced by the compound formation factor and it inherits the linear dependence of deposited energy density of non-overlapping subcascades. The predictions from the model are very close to the experimental results presented in this thesis as well as it predicts the mixing rate of Ni/Si system reported in the literature. It is expected that this model would be useful for predicting mixing parameters of other important silicide and germanide systems.

Scope of future work

The present work has demonstrated that metal germanide phases can be synthesized by ion-beam mixing at room temperature and above in Cu/Ge, Ni/Ge and Co/Ge systems. Several other metal/Ge systems such as Cr/Ge, Fe/Ge, Nb/Ge, Mn/Ge, Pt/Ge etc. can be investigated on similar lines. These systems have stable equilibrium phases which could be synthesized by ion-beam mixing and thermal annealing. It is expected that the ion-beam synthesis of these phases and the studies of their various properties viz. resistivity, electro-migration, diffusivity, oxygen affinity, atomic mobility

etc. would make these materials useful for technological applications.

With regard to the understanding of the mixing process, especially in reactive systems (or in other words easily compound forming systems) such as metal/Ge, metal/Si etc., the validity of the phenomenological model presented here and the models reported in the literature so far, has to be checked further by performing many more systematic experiments on mixing rates, mixing efficiencies, critical temperature etc.

Bibliography

- [1] J. Lindhard, M. Scharff, and H. I. Schiott, *Mat. Fys. Medd. Dan Vid Selsk* 18 (1963) 8.
- [2] G. Dearnaley, *Rep. Prog. Phys.* 32 (1969) 405.
- [3] J. H. Patterson, A. L. Turkevich. and E. J. Franzgrote, *J. Geophys Res.* 70 (1965) 1311.
- [4] G. Dearnaley, J. H. Freeman, R. S. Nelson and J. Stephen in "*Ion Implantation*" (Elsevier, NY) 1973.
- [5] J. S. Williams, *Rep. Prog. Phys.* 49 (1986) 491.
- [6] G.S. Was, *Prog. Sur. Sci.* 32 (1990) 211.
- [7] W. K. Chu, J. W. Mayer, and M. -A. Nicolet, *Backscattering Spectrometry* Academic Press, New York (1978).
- [8] L. C. Feldman and J. W. Mayer, *Fundamental of surface and thin film analysis* North-Holland, New York (1986).
- [9] S. Kalbitzer, *Nucl. Instr. and Meth.* B63 (1992) 1.
- [10] J. P. Riviere, *Nucl. Instr. and Meth.* B68 (1992) 361.
- [11] J. Asher, *Nucl. Instr. and Meth.* B89 (1994) 315.

- [12] D. H. Lee, R. H. Hart, D. A. Kiewit and o. J. Marsh, *Phys. Stat. Sol.* 15a (1973) 645.
- [13] B. X. Liu, *Phys. Stat. Sol.* 94a (1986) 11.
- [14] Y. -T. Cheng, *Mat. Sc. Rep.* 5 (1990) 45.
- [15] M. Nastasi and J. W. Mayer, *Mat. Sc. and Eng.* R12 (1994) 1.
- [16] F. A. Smidt and G. K. Hubler, *Nucl. Instr. and Meth.* B80/81 (1993) 315.
- [17] B. M. Paine and R. S. Averback, *Nucl. Instr. and Meth.* B7/8 (1985) 666.
- [18] M. Van Rossum, Y. -T. Cheng, M. -A. Nicolet and W. L. Johnson, *Appl. Phys. Lett.* 46 (1985) 610.
- [19] W. L. Johnson, Y. -T. Cheng, M. Van Rossum and M. -A. Nicolet, *Nucl. Instr. and Meth.* B7/8 (1985) 657.
- [20] Y. -T. Cheng, X. A. Zhao, T. Banwell, T. W. Workman, M. -A. Nicolet and W. L. Johnson, *J. Appl. Phys.* 60 (1986) 2615.
- [21] L. E. Rehn and P. R. Okamoto, *Nucl. Instr. and Meth.* B39 (1989) 104.
- [22] P. Borgensen, D. A. Lilienfeld and H. H. Johnson, *Appl. Phys. lett.* 57 (1990) 1407.
- [23] F. Rossi and M Nastasi, *J. Appl. Phys.* 69 (1991) 1310.
- [24] W. Bolse, *Nucl. Instr. and Meth.* B80/81 (1993) 137.
- [25] T. Weber and K. P. Lieb, *J. Appl. Phys.* 73 (1993) 3499.
- [26] R. Kelly and A. Miotello, *Thin Solid Films* 241 (1994) 192; A. Miotello and R. Kelly, *Surface Science* 268 (1992) 340 and 314 (1994) 275.
- [27] W. Xia, C. A. Hewett, M. Fernandes, S. S Lau, and D. B. Poker, *J. Appl. Phys.* 65 (1989) 2300.

- [28] W. Xia, M. Fernandes, C. A. Hewett, S. S. Lau, D. B. Poker and J. P. Biersack, *Nucl. Instr. and Meth.* B37/38 (1989) 408.
- [29] R. A. Collins, S.C. Edwards and G. Dearnaley, *Appl. Phys. Lett.* 43 (1983) 622.
- [30] J. Desimoni, A. Traverce and F. Xiangjun, *Nucl. Instr. and Meth.* B71 (1992) 22.
- [31] J. Desimoni and A. Traverse, *Phys. Rev.* B48 (1993) 13266.
- [32] G. J. Van Grum, *Semiconductor Silicon* ed H. R. Huff and E. Sirtl (Princeton, NJ: Electrochemical Society) p342.
- [33] *Thin Film Interdiffusion and Reactions* ed J. M. Poate, K. N. Tu and J. W. Mayer (Princeton, NJ: Electrochemical Society).
- [34] A. H. Reader, A. H. van Ommen, P. J. W. Weijs, R. A. M. Wolters and D. J. Oostra, *Rep. Prog. Phys.* 56 (1992) 1397.
- [35] J. B. Butcher, *MIEL Proceeding* (Elsevier, 1989), Vol.1, p 1.
- [36] *VLSI Electronics Microstructure Science*, ed. N. G. Einspruch (Academic Press, 1981) , Vol.1, p 18.
- [37] J. W. Mayer, B. Y. Tsaur, S. S. Lau and L. S. Hung, *Nucl. Instr. and Meth.* 182/183 (1981) 1.
- [38] S. S. Lau, B. Y. Tsaur, M. von Allmen and J. W. Mayer, *Nucl. Instr. and Meth.* 182/183 (1981) 97.
- [39] T. L. Alford, P. Borgesen, J. W. Mayer and D. A. Lilienfeld, *Appl. Phys. Lett.* 58 (1991) 1848.
- [40] B. R. Appelton, O. H. Holland, D. B. Pokar, J. Naroyan and D. Fathy, *Nucl. Instr. and Meth.* B7/8 (1985) 639.

- [41] E. Jaroli, N. Q. Khanh, G. Mezey, E. Zsoldos, B. Kovacs, I. Mojzes, T. Lohner, E. Kotai, A. Manuaba, M. Fried and J. Gyulai, *Nucl. Instr. and Meth.* B15 (1986) 703.
- [42] J. Li, Q. Z. Hong and J. W. mayer, *J. Appl. Phys.* 66 (1989) 3600.
- [43] N. S. Saleh, J. A. Al-Saleh and A. A. Saleh, *Nucl. Instr. and Meth.* B47 (1990) 263.
- [44] M. O. Aboelfotoh, C. L. Lin, and J. M. Woodall, *Appl. Phys. Lett.* 65 (1994) 3245.
- [45] M. O. Aboelfotoh, H. M. Tawancy, and L. Krusin-Elbaum, *Appl. Phys. Lett.* 63 (1993) 1622.
- [46] M. O. Aboelfotoh and H. M. Tawancy, *J. Appl. Phys.* 75 (1994) 2441.
- [47] F. M. d'Heurle and J. Gupta, *Appl. Surf. Sci.* 73 (1993) 214.
- [48] S. Q. Hong, C. M. Comrie, S. W. Russell, and J. W. Mayer, *J. Appl. Phys.* 70 (1991) 3655.
- [49] L. Krusin-Elbaum and M. O. Aboelfotoh, *Appl. Phys. Lett.* 58 (1991) 1341.
- [50] P. Sigmund and A. Gras-Marti, *Nucl. Instr. and Meth.* B182/183 (1981) 25.
- [51] R. de Reus, A. M. Vredenberg, A. C. Voorrips, H. C. Tissink and F. W. Saris, *Nucl. Instr. and Meth.* B53 (1991) 24.
- [52] L. S. Hung, M. Nastasi, J. Gyulai and J. W. Mayer, *Appl. Phys. Lett.* 42 (1983) 622.
- [53] B. X. Lau, W. L. Johnson, M. -A. Nicolet and S. S. Lau, *Appl. Phys. Lett.* 42 (1983) 45.
- [54] B. X. Liu, *Phys. Stat. Sol.* 75a (1983) K77.

- [55] G. Hagg, *Z. Phys. Chem.* B12 (1931) 3.
- [56] R. Pretorius, A. M. Vredenberg and F. W. Saris, and R. D. Reus, *J. Appl. Phys.* 70 (1991) 3636.
- [57] S. S. Lau, B. X. Lau and M. -A. Nicolet, *Nucl. Instr. and Meth.* 209/210 (1983) 97.
- [58] L.S. Hung and J.W. Mayer, *Nucl. Instr. Meth.* B7/8 (1985) 676.
- [59] J. L. Brimhall, H. E. Jissinger and L. A. Charlot, *Radiat. Eff.* 77 (1983) 237.
- [60] D.A. Lilienfeld, L.S. Hung and J.W. Mayer, *Nucl. Instr. Meth.* B19/20 (1987) 1.
- [61] D.M. Follstaedt, *Nucl. Instr. and Meth.* B7/8 (1985) 11.
- [62] J. A. Alonso and S. Simozar, *Sol. Sta. Comm.* 48 (1983) 765.
- [63] F. R. de Boer, R. Boom, W. C. M. Mattens, A. R. Anderson, Maidema and A. K. Niessen, "*Cohesion in Metals*", eds. F. R. de Boer and D. Pettifor (North-Holland, Amsterdam) 1988.
- [64] T. L. Alford, P. Borgesen, J. W. Mayer and D. A. Lilienfeld, *Appl. Phys. Lett.* 58 (1991) 1848.
- [65] F. Shi, W. Bolse and K. P. Lieb, *Nucl. Instr. and Meth.* B89 (1994) 332.
- [66] P. Borgesen, D. A. Lilienfeld and H. Msaad, *Nucl. Instr. and Meth.* B59/60 (1991) 563.
- [67] H. H. Anderson, *Appl. Phys.* 18 (1979) 131.
- [68] K. Jopannessen and P. Sigmund, *Nucl. Instr. and Meth.* B19/20 (1987) 85.
- [69] I. Koponen and M. Hautala, *Nucl. Instr. and Meth.* B47 (1990) 375.

- [70] Y. -T. Cheng, M. Van Rossum, M. -A. Nicolet and W. L. Johnson, *Appl. Phys. Lett.* 45 (1984) 185.
- [71] M. Van Rossum, U. Shreter, W. L. Johnson and M. -A. Nicolet, *Mater. Res. Soc. Symp. Proc.* 27 (1984) 127.
- [72] G. H. Vineyard, *Radiat. Eff.* 29 (1976) 245.
- [73] C. Kittel, *"Introduction to Solid State Physics"*, 5th Ed. (Wiley, NY, 1976).
- [74] P. Borgensen, T. L. Alford, D. A. Lilienfeld and H. H. Johnson, *Appl. Phys. A* 50 (1991) 161.
- [75] T. L. Alford, P. Borgesen and D. A. Lilienfeld, *J. Appl. Phys* 69 (1991) 7528.
- [76] F. Shi, W. Bolse and K. P. Lieb, *J. Appl. Phys.* 78 (1995) 2303.
- [77] K. Ramakrishnan, *M.Tech Thesis, 1994, IIT, Kanpur.*
- [78] J. F. Ziegler, *Nucl. Instr. and Meth.* B6 (1985) 270.
- [79] G. K. Mehata et al., *Technical Report, IIT, Kanpur VDG/13/1976.*
- [80] V. N. Kulkarni and R. M. Singru, *Technical Report, IIT, Kanpur TR/CNF/1987.*
- [81] L. R. Doolittle, *Nucl. Instr. and Meth.* B9 (1985) 344.
- [82] D. K. Schroder, *Semiconductor Material and Device Characterization* (John Wiley, 1990).
- [83] S. A. Joshi, *Ph.D. Thesis* University of Poona.
- [84] Powder diffraction file, *JCPCS, International Centre for Diffraction Data, Pennsylvania, USA, 1995.*
- [85] P. Nath, V. Dutta and K. L. Chopra, *Thin Solid Films* 64 (1979) 59.

- [86] B. M. Clemens, *Phys. Rev.* B33 (1986) 7615.
- [87] F. Shi, W. Bolse, K. P. Lieb and J. -P. Wilbrandt, *Nucl. Instr. and Meth.* B89 (1994) 382.
- [88] B. Y. Tsaur, Z. L. Liao and J. W. Mayer, *Phys. Lett.* 71A (1979) 270.
- [89] A. H. Hamdi and M. -A. Nicolet, *Thin Solid Films* 119 (1984) 357.
- [90] B. Y. Tsaur, S. S. Lau and J. W. Mayer, *Appl. Phys. Lett.* 35 (1979) 225.
- [91] *Alloy Phase Diagrams* (ASM International, 1992) vol.3.
- [92] P. Villars and L. D. Calvert, *Pearson's Handbook of Crystallographic Data for Intermetallic Phases*, (American Society for Metals, Oh, USA, 1995) vol.1 & 2.
- [93] L. V. Azaroff, *Introduction to Solids* (TMH, Bombay, 1990) p437.
- [94] B. Y. Tsaur and C. H. Anderson Jr., *J. Appl. Phys.* 53 (1982) 940.
- [95] I. J. R. Baumvol, *Nucl. Instr. and Meth.* B80/81 (1993) 369.
- [96] K. Hohmuth, B. Rauschenbach, A. Kolitsch and E. Richter, *Nucl. Instr. and Meth.* B209/210 (1983) 249.
- [97] B. Rauschenbach, K. Hohmuth, *Phys. Stat. Sol. (a)* 72 (1982) 667.
- [98] R. Walser and R. Bene, *Appl. Phys. Lett.* 28 (1976) 624.
- [99] S. V. Meschel and O. J. Kleppa, *Met. Trans. A* 22 (1991) 2162.
- [100] K. N. Tu, G. Ottaviani, R. D. Thompson and J. W. Mayer, *J. Appl. Phys.* 58 (1985) 4125.
- [101] K. T. Ho, C. -D. Lien, U. Shreter and M. -A. Nicolet, *J. Appl. Phys.* 57 (1985) 227.

- [102] K. Tao, C. A. Hewett, S. S. Lau, Ch. Buchal and D. B. Poker, *Appl. Phys. Lett.* 50 (1987) 1343.
- [103] U. Shreter, C. T. So. Frank, B. M. Paine and M. -A. Nocolet, *Mater. Res. Soc. Symp. Proc.* 27 (1984) 31.
- [104] K. P. Lieb, W. Bolse, M. Uhramacher, *Nucl. Instr. and Meth.* B89 (1994) 277.
- [105] U. Gosele and K. N. Tu, *J. Appl. Phys.* 53 (1982) 3252.
- [106] U. Gosele and K. N. Tu, *J. Appl. Phys.* 66 (1989) 2619.
- [107] S. W. Russell and S. Q. Wang, *J. Appl. Phys.* 76 (1994) 264.